A Fundamental Study of Relationships Among Fuel Properties, Combustion Characteristics and Emissions with Normal and Synthetic Diesel Fuel

by

Jeremy T. Llaniguez

Bachelor of Science in Mechanical Engineering
University of California, Berkeley
2001

Submitted to the Department of Mechanical Engineering
in Partial Fulfillment of the Requirements for the Degree of
Master of Science in Mechanical Engineering

at the

Massachusetts Institute of Technology

September 2003

Signature of Author: _____
Department of Mechanical Engineering
August 2003

Certified by: _____
Doctor Victor W. Wong
Principle Research Scientist and Lecturer in Mechanical Engineering
Thesis Supervisor

Accepted by: _____
Ain A Sonin
Professor, Department of Mechanical Engineering
Chairman, Department of Graduate Committee

(This page left intentionally blank.)

A Fundamental Study of Relationships Among Fuel Properties, Diesel Combustion Characteristics and Emissions with Normal and Synthetic Diesel Fuel

by

Jeremy T. Llaniguez

Submitted to the Department of Mechanical Engineering
September 2003 in Partial Fulfillment of the Requirements
for the Degree of Master of Science in Mechanical Engineering

ABSTRACT

The allowable emission levels for diesel engines are becoming more and more strict. In the past, improvements in fuel quality like increases in cetane number and reductions of the fuel sulfur content helped keep engines abreast of regulations. With fuel quality standards slowly evolving, in recent years, engine manufacturers have had to push the engine design envelope to meet regulations by employing advanced engine subsystems like common-rail fuel injection systems, cooled-EGR systems, and variable geometry turbochargers, all controlled by sophisticated algorithms in a computer. As a result of these advancements, the emission levels leaving the engine are now more a function of engine technology than fuel properties. As a result, reducing emissions through engine design is increasingly getting more and more difficult.

Fischer-Tropsch (FT) diesel fuels have been proposed as a means of meeting future emission levels. These synthetic fuels have drastically different properties than normal diesel fuel, all of which have been shown to be beneficial in reducing emissions. However, recent studies have tested FT fuels in old engines and at conditions that were not representative of future market use. Thus, the understanding of how FT fuels behave in modern engine systems is limited. The knowledge base of FT combustion was extended through engine tests in a Model Year 2002 (MY02) Cummins ISB 300 engine run with FT diesel fuel provided by the Syntroleum Corporation. A technology sweep matrix was developed to ascertain FT fuel behavior under modern engine running conditions.

Emission reductions were immediately seen when the FT diesel fuel was run using the stock calibration map for normal diesel. Further experiments revealed that reductions in emissions, with little loss in performance, could be achieved by recalibrating the engine computer to take advantage of FT fuel properties. FT fuel gives freedom back to the engineer to push the envelope with engine technology to reduce emissions.

Thesis Advisor: Doctor Victor Wong
Title: Principle Research Scientist and Lecturer in Mechanical Engineering

(This page left intentionally blank.)

Acknowledgements

The sandbox pipe dream

Gatorade hydrates and cools

Marble floors throughout

(This page left intentionally blank.)

Table Of Contents

List Of Figures

List Of Tables

Nomenclature

ABBREVIATIONS and SYMBOLS

API	American Petroleum Institute
aBDC	After Bottom Dead Center
aTDC	After Top Dead Center
bTDC	Before Top Dead Center
BMEP	Brake Mean Effective Pressure
BSFC	Brake Specific Fuel Consumption
bsHC	Brake Specific Hydrocarbon Output
$bsNO_x$	Brake Specific NO_x Output
bsPM	Brake Specific Particulate Matter Output
CA	Crank Angle
CN	Cetane Number
CNI	Cetane Number Index
CARB	California Air Resource Board
Da	Damköhler Number
DEE	Diethylether
DMM	Dimethoxymethane
DOC	Diesel Oxidation Catalyst
Dp	Particle Diameter Based on Electrical Mobility
DPF	Diesel Particulate Filter
EGR	Exhaust Gas Recirculation
EOI	End Of Injection
EOC	End Of Combustion
EVC	Exhaust Valve Close
EVO	Exhaust Valve Open
FT	Fischer-Tropsch
HC	Hydrocarbon
HEPA	High Efficiency Particulate Arrestance
HFID	Heated Flame Ionization Detector
LII	Laser-Induced Incandescence
LIF	Laser-Induced Fluorescence
NO_x	Oxides Of Nitrogen
PAH	Polycyclic Aromatic Hydrocarbon
PLRS	Planar Laser Rayleigh Scattering
PM	Particulate Matter
PPM	Parts Per Million
Q_{LHV}	Lower Heating Value
Re	Reynolds Number
RPM	Revolutions Per Minute
RTD	Resistance Temperature
SI	Spark Ignition
SOC	Start Of Combustion
SOF	Soluble Organic Fraction
SOI	Start Of Injection
TC	Thermocouple
TDC	Top Dead Center
VGT	Variable Geometry Turbocharger
ζ_{st}	Percent of Stoichiometric Air
ϕ	Fuel-Air Equivalence Ratio
γ	Ratio Of Specific Heats
$\eta_{f,i}$	Indicated Fuel Conversion Efficiency
α	Pressure Ratio In Limited-Pressure Cycles
β	Volume Ratio In Limited-Pressure Cycles
τ_d	Ignition Delay

Chapter 1 Background and Introduction

1.1 Diesel Engine Overview

In 1893, Rudolf Christian Karl Diesel was awarded a German patent for the design of what he called the "rational heat engine" [1] that became the technological basis for internal combustion engines that now bear his name. In his patent, Diesel outlined his plan to incorporate the constant-temperature energy addition of the Carnot cycle in a four-stroke engine [1]. This idea was realized by initiating combustion through the injection of liquid fuel into air that was solely heated by the compression process. This fundamental concept is what sets the diesel combustion process apart from spark-ignition (SI) engines.

Generally, diesel engines are favored over SI engines since they do not run into the same combustion limitations that SI engines inherently have. Unlike a diesel engine, the combustion of the homogenous fuel-air mixture in an SI engine is initiated by an auxiliary energy source, usually in the form of a spark from the engine's ignition system. As the initial flame kernel grows and expands outward, the unburned, surrounding mixture – called the end gas – is further compressed leading to a denser, hotter unburned mixture. The chemical kinetics governing the reactions within the end gas mixture may accelerate to produce large amounts of radicals that may lead to the autoignition of the unburned mixture, the spontaneous and rapid release of a large part or all of their chemical energy [2], before the initiated flame has propagated outward to consume the unburned mixture. When autoignition occurs, the end gas burns very rapidly, releasing its energy up to 25 times faster [2] than a normal propagating flame. This rapid heat release leads to a sudden increase in pressure within the cylinder, causing high-frequency pressure-wave oscillations that result in the audible sound known as knock. To limit the chance of knock, the compression ratios of SI engines are limited to about 12 or less, limiting their efficiency through a congruous reduction of the allowable expansion ratio[1].

As stated earlier, the combustion process in diesel engines begins as the hot, compressed air within the cylinder evaporates, heats, and ignites the injected fuel. As this fuel-air mixture burns, it expands outwards, but now only compressing and heating air. This is in direct contrast to the operation of an SI engine explained above. Therefore, with no fuel in the surrounding mixture, the possibility of

---

[1] Although the compression ratio is highlighted in engine specifications, it is actually its identical sibling, the expansion ratio that is more important in describing an engine's efficiency. The expansion ratio gives an idea of how much work can be extracted from the burned gas mixture before the exhaust valve opens. Thermodynamically, as gases are expanded over a larger volume change, more work is extracted since the change in gas temperatures are much greater.

autoignition is eliminated. As a result, diesel engines can run with compression ratios from 16 – 24, the main limitation being the maximum allowable pressure in the cylinder.

1.1.1 Technical Merits of the Diesel Engine

As stated above, the main differentiation between diesel and SI engines is in the manner of combustion initiation. Although this is the only difference from a combustion point of view, its application gives the diesel engine a few technological advantages over the SI engine. These include better fuel efficiency, better exchange of gases into and out of the cylinder, and an increase in torque output versus a comparably sized SI engine.

In general, diesel engines are more efficient in converting fuel energy to mechanical energy. Since fuel is injected into the cylinder of a diesel engine just before the desired start of combustion, separate from the compression process, diesel engines are not affected by the knocking limits that plague SI engines. As a result, diesel engines run with much higher compression ratios. Examining Equation 1.1, one can see that higher compression ratios lead to higher fuel-conversion efficiencies [2]:

Equation 1.1

$$\eta_{f,i} = 1 - \frac{1}{r_c^{\gamma-1}}\left[\frac{\alpha\beta^{\gamma} - 1}{\alpha\gamma(\beta - 1) + \alpha - 1}\right]$$

where $\eta_{f,i}$ is the indicated fuel conversion efficiency, r_c is the compression ratio, γ is the ratio of specific heats, and α and β are pressure and volume relationships. Not only are diesel engines more fuel efficient, they are also more efficient in pumping air into and out of the combustion chamber. In SI engines, a throttle that effectively chokes the engine of fuel and air controls engine load. Thus, depending on the output of the engine, an SI engine's volumetric efficiency can vary between its minimum and maximum allowable values. On the other hand, diesel engines control their load by adjusting the amount of fuel injected into the cylinder and therefore do not need a throttle. Without added airflow restrictions in the intake system, the airflow through a diesel engine is almost constant at a given engine speed, regardless of engine load, resulting in an almost constant volumetric efficiency. This results in less work lost in diesel engines throughout the overall gas exchange process (i.e. pumping loop losses), especially at part loads where comparable SI engines have low volumetric efficiencies.

In general, to prevent emitting excessive amounts of black smoke, diesel engines operate with overall lean mixtures, usually with fuel/air equivalence ratios (ϕ) between 0.2 - 0.8. As the equivalence ratio is decreased below the stoichiometric value, ϕ = 1.0, the indicated fuel conversion efficiency increases. This occurs due to the fact that the extra air present, acting as a diluent since it does not react with any fuel, reduces the overall burned-gas temperature at the end of combustion. Also, the dominant

products in very lean combustion are nitrogen (N_2) and oxygen (O_2) (above $\phi = 0.6$, carbon dioxide (CO_2) and water (H_2O) become dominate over oxygen). Based on the kinetic theory of gases, lower gas temperatures result in lower specific heats for each species present in the gas since the vibrational excitation mode is unexcited. The kinetic theory of gases also predicts that diatomic molecules have lower specific heats versus polyatomic molecules. The combination of these two factors lead to decreased burned-gas specific heats and thus increases the effective value of γ during the expansion process [2]. Revisiting Equation 1 and replacing r_c with r_e to describe the expansion ratio, we see that an increased γ results in an increased indicated fuel conversion efficiency. Thermodynamically speaking, for a given expansion ratio, a gas with a higher γ will expand through a larger temperature ratio prior to the exhaust valve opening, resulting in more work extracted per mass of fuel burned [2].

The combination of higher fuel conversion efficiencies through lean operation and higher compression ratios along with increased volumetric efficiencies from throttle-less operation is clearly seen in Figure 1.1. The throttle-less operation and lean combustion is especially evident at low loads where the fuel consumption rate between SI and diesel engines diverges quickly. Further part-load efficiencies are achieved in diesel engines due to a related reduction in combustion duration which helps increase the cycle efficiency [3].

Lastly, operating with higher compression ratios leads to higher in-cylinder pressures in diesel engines. Since the amount of torque produced by an engine is a function of the pressure force on the piston head acting upon the effective lever arm of the crankshaft, diesel engines produce more torque than an SI engine of comparable displacement. The combination of higher fuel conversion efficiency, higher volumetric efficiency, and higher torque output make the diesel engine the favored primary mode of power in the transportation industry, where fuel consumption is very important to total operating costs.

1.1.2 Technical Challenges of the Diesel Engine

Although having very good performance characteristics, diesel engines have significant problems when it comes to emissions. Hydrocarbons (HCs) are not a problem in diesel engines since the compression of air during the compression stroke only allows fresh air into the crevice volumes, removing the significant contribution that HCs from crevice volumes (~40%) [4] can play in SI engines. Carbon monoxide is not a problem in diesel engines due to the overall-lean mixture in the cylinder. The two major pollutants from diesel engines are oxides of nitrogen (NO_x) and particulate matter (PM), with emission levels much greater than those found in SI engines [2].

The reason NO_x and PM outputs are significant in diesel engines lies in how combustion proceeds in diesels. Although overall lean, the fact that combustion occurs as a heterogeneous, multi-phase process poses many problems. The current phenomenological model of diesel combustion (see Chapter 2

provides clues as to where the problems lie with respect to each major pollutant. Essentially, the regions of fuel-rich vapor in the interior of a diesel flame contribute to large amounts of soot while the diffusion flame that establishes around the fuel-rich mixture leads to conditions that form significant amounts of NO_x. Furthermore, the excess air from operating lean not only freezes NO formation chemistry making it difficult for NO_x to reduce through chemical equilibrium in the cylinder, but also through aftertreatment systems that must reduce NO_x in an oxidizing environment.

Concern about these emissions developed in the 1960s, particularly in the city of Los Angeles, as atmospheric reactions between NO_x and HCs lead to the formation of photochemical smog [3] and ozone [5] in urban air. NO_x can also participate in a chain reaction removing ozone from the stratosphere, allowing increased ultraviolet radiation to reach the earth's surface [5]. Recently, PM has been shown to have adverse respiratory affects when inhaled, depending on the length of exposure. Short-term exposure leads to the inflammation and irritation of the respiratory system [6] while long-term exposure can lead to an increase in lung-cancer risk [7], the exacerbation of existing allergies and asthmatic symptoms, or genetic alterations by gene mutations, deletions, translocations (transfer of a chromosomal segment to a new position), aneuploidy (incomplete chromosome sets), or gene amplification (production of multiple copies of a gene to amplify its traits, good or bad) [6].

1.2 Emissions And Fuel Quality Standards

To curb the adverse environmental and health impacts from burning petroleum fuels, the United States Environmental Protection Agency (EPA) and its counterparts in other states (such as the California Air Resource Board) and countries have steadily imposed increasingly stricter absolute emission outputs for new production engines. Figure 1.2 shows the relative changes between allowable emission levels over the years 1990 to 2007. The permissible range of emissions is getting increasingly smaller and smaller, making it harder and harder for engine manufacturers to meet the mandated levels. The 2002 and 2007 emission levels are special cases. The 2002 level was actually set to come into effect in 2004. However, due to various engine manufacturers using special fueling programs for testing that would pass emissions but not be used in actual on-road use, a 1998 court settlement forced engine manufacturers to meet the future deadline 15 months ahead of time [8]. For the 2007 limits, only the PM cap will be enforced right away while the NO_x cap will be phased in from 2007 to 2010 [8].

In order to keep abreast of the imposed limits, engine manufacturers have redesigned and optimized the combustion chambers in diesel engines and incorporated advanced subsystems to control fueling and EGR precisely (see Section 1.3). However, as the emission limits will decrease by an order of magnitude between 2002-limits to 2007-limits, engineers are finding it more and more difficult to meet emission levels through in-cylinder optimizations. Aftertreatment systems like diesel oxidation catalysts

(DOC), diesel particulate filters (DPF), NO_x adsorber catalysts, and selective catalytic reduction (SCR) and non-catalytic reduction (SNCR) of NO systems are available but are very expensive and require user upkeep (for example, refilling of ammonia or urea for SCR and SNCR systems) [10].

Further complicating the emission story are the increasing regulations on fuel properties (see Figure 1.3). Studies have shown that large changes in fuel sulfur levels and aromatic content can lead to lower NO_x and PM emissions (see Chapter 3). The EPA has finalized legislation that will lower the sulfur content of available diesel fuel to no more than 15 PPM beginning June 1, 2006 [8]. The World-Wide Fuel Charter has asked for the harmonization of fuel-quality standards worldwide, proposing requirements that will enable advanced technology to reduce fuel consumption and reduce engine-out emissions [9]. Petroleum refineries also predict that ultimately, requirements will eventually reach levels where fuels must contains less than 1% aromatics by volume and 5 PPM of sulfur by weight [10].

1.3 Trends In Emission Reduction

Due to the high cost of aftertreatment systems, most engine manufacturers have focused on in-cylinder optimizations and advanced subsystems to reduce the emissions exiting the engine. In-cylinder optimizations include advanced bowl-in-piston designs to increase squish flow and intake area shaping to increase the amount of swirl, all in attempt to increase the mixing of fuel and air. Also, fuel injection timing is usually retarded to reduce peak cylinder temperatures and pressures. Advanced subsystems include exhaust gas recirculation (EGR) and cooled-EGR systems that lower combustion temperatures and reduce the oxygen concentration; variable geometry turbochargers (VGT) that are required to drive EGR at low loads; and high pressure, common-rail (CR) fuel injection systems that allow for better mixing and atomization, while allowing advanced injection strategies like pilot-, main-, and post-injection coupled with injection rate shaping algorithms.

Similarly, advances are occurring in petroleum-based fuels that are currently available today. Leading the way in diesel fuel quality in the United States is California, whose California Air Resource Board (CARB) rated diesel fuel requires no more than 10% aromatics (20% from small refineries) and sulfur contents below 500 PPM. In Europe, Swedish Environmental Class 1 (EC-1) fuel is available with less than 0.02% polyaromatics and 10 PPM of sulfur. However, even with fuels with such good properties, engine out emissions may not be lowered, especially in modern engines [35].

1.4 Fischer-Tropsch Fuels

In the late 1890s, S.M. Lasanitsch and M.Z. Jovitschitsch from Germany converted carbon monoxide gas (CO) and hydrogen gas (H_2) to liquid products using an electrical discharge [10]. In 1902,

P. Sabatier and J.B. Senderens from France used nickel catalysts to convert CO and H_2 to methane [10]. These early pioneering experiments in converting synthesis gases (CO and H_2) to liquid hydrocarbons laid the groundwork for the well-known Fischer-Tropsch synthesis process still in use today. First reported in 1923, then patented in 1925 in Germany by Franz Fischer and Hans Tropsch, the Fischer-Tropsch (FT) synthesis combined the production of liquid products, notably alkanes, from CO and H_2 gas, using cobalt (Co), iron (Fe), and ruthenium (Ru) catalysts all at normal pressures [10]. The use of these catalysts and the ability to run at lower pressures increased the yield and safety of plants producing synthetic hydrocarbons.

The Fischer-Tropsch process, depicted in Figure 1.5, consists of four major steps. The first step (pictorials 1 – 3 in Figure 1.5) is concerned with the generation of the synthesis gas. In early years, especially in Germany during World War I where liquid petroleum was in short supply, synthesis gas was made by the gasification of coal with steam at temperatures of about 900°C. Nowadays, the feedstock has changed from coal to natural gas, including subquality[2] natural gas. Natural gas is reformed with oxygen or air to produce synthesis gas. The general chemical reaction for synthesis gas generation is [10]:

Equation 1.2

$$CH_n + O_2 \xrightarrow{Catalyst} \tfrac{1}{2n} H_2 + CO$$

The second step in the process is synthesis gas purification. Since the Fischer-Tropsch process relies heavily on catalysts in the main step of the process, any sulfur in the synthesis gas will poison the reaction sites on the catalysts, reducing the overall yield. Thus, as depicted in pictorial 4 in Figure 1.5, H_2S and organic sulfur is removed from the synthesis gas stream.

The next step in the Fischer-Tropsch process (pictorial 5 in Figure 1.5) is the heterogeneous surface reaction (see Figure 1.4) that converts the synthesis gas to a primary product of heavy, straight chain liquid hydrocarbons (oils) and waxes. The step provides the first possibility of tailor-making a product through the proper choice of reactor type and reactor conditions. The general reaction at the catalyst surface is:

Equation 1.3

$$2nH_2 + CO \xrightarrow{Catalyst} (CH_2)_{n,(liq)} + nH_2O$$

---

[2] Low quality, or "subquality" natural gas is that gas that has one or more impurities that disallow its use without first going through a pretreatment process to remove the impurities. Subquality natural gas is defined as having equal to or more than 2% carbon dioxide, 4% nitrogen, or 4 parts per million of hydrogen sulfide. Based on this criteria, approximately one third of U.S. reserves, or about 53 trillion cubic feet, in the lower 48 states are subquality [11].

The quality of the heavy liquids and waxes is heavily dependent upon the catalysts used in the reactor and the temperatures and pressures the reactions take place.

The final step in the manufacture of liquid hydrocarbons using the Fischer-Tropsch process is primary product refining. Hydrocracking of the primary product uses thermal cracking to break down the heavy hydrocarbons into lighter ones and hydrogenation to increase saturation by removing double and triple carbon-carbon bonds. Isomerization rearranges the chemical structure to upgrade the physical properties such as viscosity. Finally, fractionation and distillation separates the final product by weight, allowing gasoline, diesel fuel, lubricants, waxes, and even margarine to be separated and stored for shipping [10].

The advantages of FT fuel are threefold, the first dealing with fuel properties, the second its economic viability, and third its ability to extend the useable petroleum reserves. First, with respect to fuel properties, since the final specifications of the synthesized product can be controlled, desirable fuel properties can be enhanced. For example, the cetane number and aromatic content of a diesel fuel can be determined *a priori*. Also, as a consequence of the synthesis gas purification in the FT process, fuel properties are guaranteed to be virtually sulfur free. Furthermore, FT fuel has similar physical properties, such as viscosity, density, flammability, and energy density to petroleum-based diesel fuel. Additionally, FT fuel is liquid phase at ambient conditions; it is transportable in the existing infrastructure, requiring no changes to existing facilities to market the fuel. Finally, since it is miscible in diesel fuel, blends of FT fuel and normal diesel can be used, where research has shown that emission benefits with blended fuels are at most in proportion to the amount of FT fuel in the blend [12].

The overall FT process shown in Figure 1.5 seems long, complicated, and costly, depending upon the type of reactor and catalysts used in the process. However, depending on the volume of product produced, the production costs is comparable to petroleum-based fuels [13][14][43]. Lastly, since the FT process can use any quality of feedstock due to the synthesis gas preparation, the potential for extending the reserves of fuel is substantial. United State Department of Energy (DOE) data [15] show that the proven reserves of crude oil and natural gas are about $1x10^{12}$ barrels and $140x10^{12}$ m^3 respectively. These proven reserves of natural gas, if converted to synthetic fuel through the FT process can increase the reserves by about $500x10^9$ barrels. Studies of discovered, undeveloped and un-marketable gas suggests that about $400x10^{12}$ m^3 of subquality gas may be available worldwide, potentially extending the proven reserves by about $1.4x10^{12}$ barrels. This would more than double the world's current oil reserves, if these subquality gases are converted to synthetic crude oil using the FT process [13].

1.4.1 Current Understanding Of Emissions Benefits With Fischer-Tropsch Fuels

A recent literature review of past research of light-duty and heavy-duty engines running with various FT fuels shows considerable promise [16]. In that review, Alleman et al. state, "The results of these tests have consistently shown reductions of regulated pollutants." However, further investigations of the quoted research show that much more needs to be done in order to fully understand how FT fuels behave in modern combustion systems. For the most part, heavy-duty research on FT fuels has been done on outdated engines, at low loads, and without engine or computer modifications. Furthermore, researchers have usually looked at engine-out characteristics, rarely correlating emissions to in-cylinder behavior.

One of the first heavy-duty engine studies using FT fuel was done in 1997 [12]. In that study, a old, 1988 Detroit Diesel Series 60 engine, rebuilt to meet 1991 EPA standards, was run on the FTP cycle using two Sasol Slurry Phase Distillate FT fuels. The average load factor of the FTP cycle is about 20% – 25% of maximum power at any given speed with exhaust temperatures ranging from 250°C – 350°C to a maximum of 450°C [8]. Furthermore, a timing sweep was done by retarding timing by 3°, 6°, and 8° from the stock point. The results of the transient tests showed an average reduction of 27% in NO_x and 21% in PM levels compared to No. 2 diesel fuel. The timing sweep test showed typical NO_x-PM tradeoff behavior [2] as NO_x decreased while PM increased as timing was retarded

In 1998, Norton et al. ran neat Shell FT and FT/diesel blends in unmodified engines [14]. A 1994 International Navistar engine was run on an FTP cycle and three 1996-1997 Caterpillar 3176B engines were run on the West Virginia University 5-mile route. Compared to No. 2 diesel, the Navistar engine reduced NO_x and PM by 14% and 13% respectively. Compared to CARB diesel, the Caterpillar engines showed reductions of 12% in NO_x and 24% in PM.

In 1999, researchers in West Virginia again used the unmodified 1994 International Navistar engine mentioned above, running on the FTP cycle, to compare various fuels such as federal low-sulfur diesel, CARB diesel, Malaysian FT fuel, soy-derived Biodiesel, and high aromatic content FT from Mossgas [17]. Compared to No. 2 diesel, the Malaysian FT fuel reduced NO_x by 14.3% and PM by 13.3%. The high aromatic content Mossgas FT only reduced NO_x by 5%, while reducing PM by 14.2%. This is expected, as the cetane number (CN) of the Malaysian FT is significantly higher than the Mossgas FT (73.7 versus 51.3), due to the high aromatic content in the Mossgas FT fuel. Clark et al. also state that unlike normal and biodiesel, FT fuels do not suffer from the usual NO_x-PM tradeoff characteristics.

The only in-cylinder characterization of FT combustion characteristics was done in 1999, again by researchers from West Virginia University [18]. The same 1994 International Navistar engine described previously, instrumented with PCB Piezotronics, Inc. pressure transducers, was used in steady state, modal testing using a natural gas derived FT fuel. The maximum BMEP during the steady-state

tests was 1070 kPa. Compared to No. 2 diesel fuel, NO_x was reduced by 20% on average while PM was reduced 31% on average. Researchers at WVU also did heat-release characterization of the in-cylinder pressure traces they recorded. They reported that FT has a shorter ignition delay but longer combustion duration, a 35% average lower maximum burn rate, and lower peak combustion pressures. They also found that for the same exhaust gas temperature, NO_x emissions were the same for No. 2 diesel and FT fuel, and concluded that, "These results show great promise in the further reductions of exhaust emissions in an engine with optimized injection timing."

Researchers from UC Berkeley used an unmodified 1993 Cummins B5.9 engine running steady state points to test CARB diesel, Shell FT, and oxygenated CARB fuel using dimethoxymethane (DMM) and diethylether (DEE) [19]. The timing on the Cummins engine was mechanically set to 11.5° before top dead center (bTDC). With timing kept constant, steady state tests were run with BMEPs ranging from 100 kPa to 910 kPa. Compared to CARB fuel, the Shell FT reduced NO_x by 9% and PM by 28%.

More recently researchers at Sasol Oil and Southwest Research Institute ran experiments comparing results from a modern engine to an older engine [20]. A 1999 Detroit Diesel Series 60 engine meeting 1998 EPA standards was run on an FTP cycle and compared to a similar engine run previously on an FTP cycle [12]. Compared to No. 2 diesel on the hot-start FTP cycle, the modern engine reduced NO_x by 7% and PM by 27%. The NO_x reduction was much less than the 1991 engine due to the stock timing being more retarded in the modern engine. As timing moves closer and closer to TDC, where pressures and temperatures are higher, the fuel CN plays less of a role in influencing the initial premixed burn fraction. PM dropped much more in the newer engine due to the more advanced injection system. The researchers concluded that, "despite changes in engine technology which have generally been found to reduce the effects of fuel properties on exhaust emissions, significant reductions in emission levels can still be achieved with Fischer-Tropsch diesel, particularly in the case of PM emissions."

The first tests with EGR systems and FT fuel was done in 2001 using a 2000 International Power Stroke engine with an EGR system [21]. The base engine was not fitted with an EGR system, so a custom-designed, although un-optimized, system was put together. Steady-state tests were run, with BMEPs ranging from 100 kPa to 1120 kPa. The researchers found that even with an improperly matched turbocharger to drive the EGR, large reductions in NO_x (~56%) were realized with minimal increases in PM (~5%).

In all the available literature, researchers at Luleå University of Technology have run the highest load conditions using FT fuel in diesel engines [22]. Steady state tests on a 2000 Valmet 620 DWRE engine running on commercially available FT fuel, Eco-Par, were run with loads ranging from idle to a BMEP of 1270 kPa. Unlike most Fischer-Tropsch fuels, Eco-Par fuel has a relatively low CN of 52.2. Compared to Swedish EC-1 fuel, the Eco-Par reduced NO_x emissions by 7.1%.

1.5 Project Objectives

Based on the literature review presented above, most research on FT fuels in diesel engines has been run on older engines (pre-2002 EPA specification). Since the mechanical operation of injection systems in older engines made it difficult to change injection timing, researchers were forced to run tests only on the stock operating conditions optimized for No. 2 diesel. Furthermore, these older engines prevented investigations of the effects advanced systems such as common-rail injection systems and EGR systems can play when used in conjunction with Fischer-Tropsch fuels.

More importantly, only one paper in the last six years has published data on the in-cylinder characteristics of Fischer-Tropsch combustion, along with a characterization of the rate of heat release from in-cylinder data. This lack of understanding of the combustion characteristics of FT fuels prevents the proper analysis of emission data and subsequent theoretical reasoning on why FT fuel reduces emissions. Combined with the lack of technology sweeps (timing and EGR) and how they affect emissions with Fischer-Tropsch fuel, the lack of a fundamental knowledge base of Fischer-Tropsch combustion hampers further development of engine technologies and control algorithms that can optimize engines to run on FT fuel.

The focus of this research was then to build up the fundamental knowledge base of Fischer-Tropsch combustion in modern engines. A matrix of operating conditions based on fuel injection timings and EGR rates was used to compare the performance and emissions of a model year 2002 (MY02) Cummins ISB 300, 6-cylinder engine using No. 2 diesel and an FT diesel developed by the Syntroleum Corporation. The engine was fully instrumented including a pressure transducer in cylinder number 6. The cylinder pressure measurements permitted the calculation of combustion characteristics that were used to interpret performance and emission results.

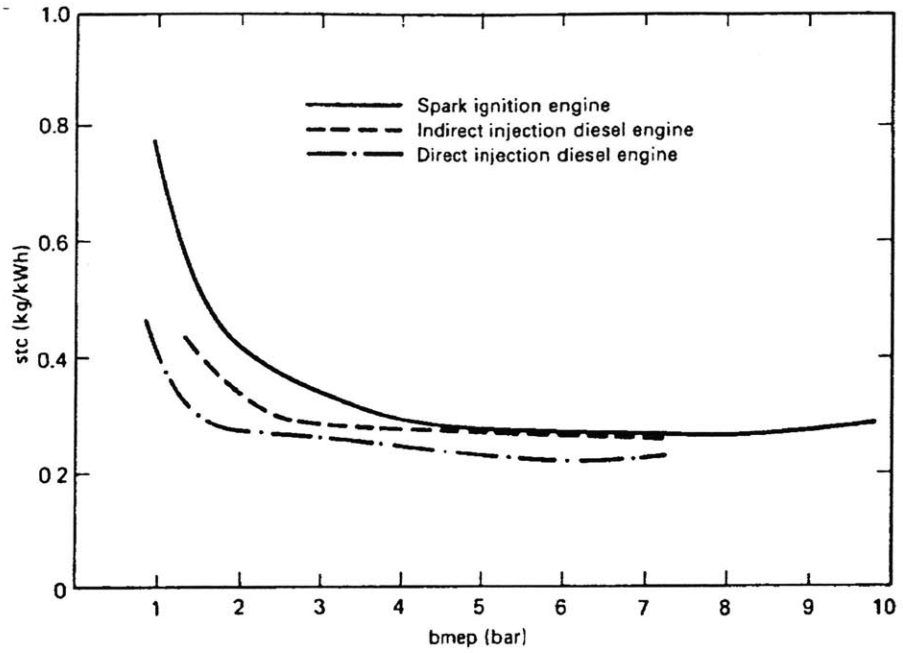

Figure 1.1 Comparison of the part-load efficiency of spark ignition and diesel engines at 2000 RPM [3].

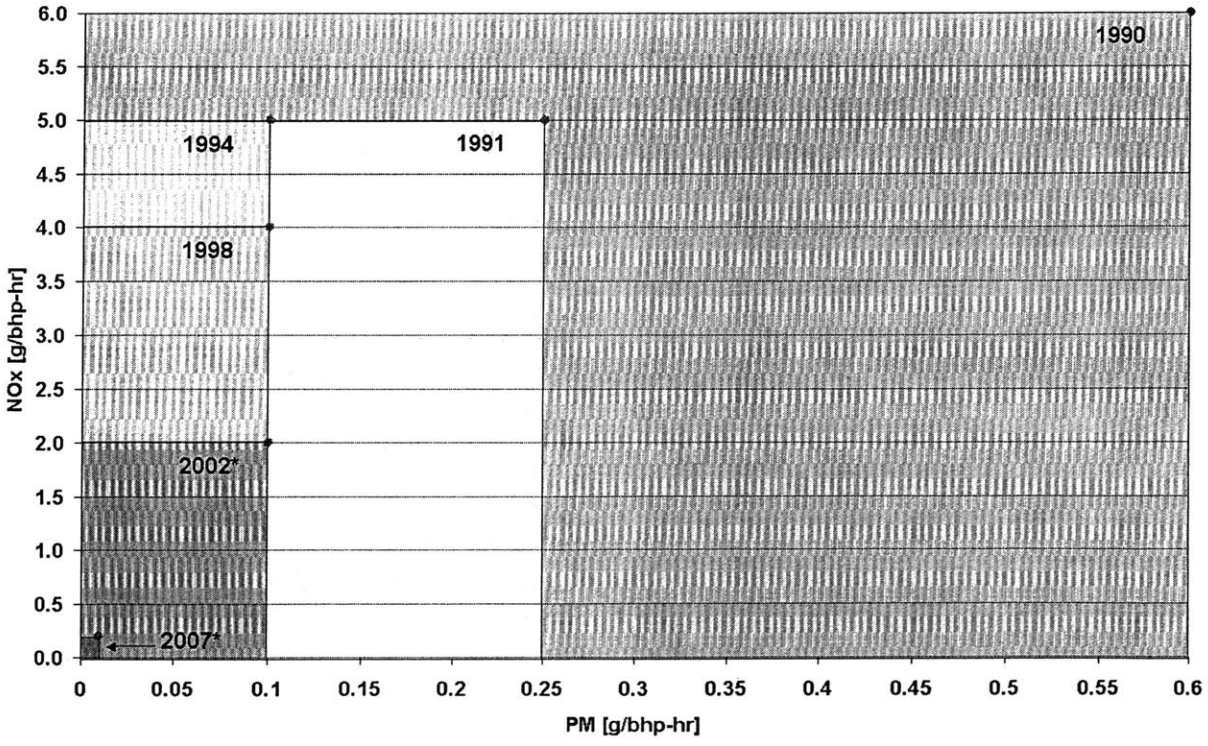

Figure 1.2 Allowable-emission map for heavy-duty, on-highway diesel engines based on EPA limits. Figure shows relative reductions in allowable emission levels as EPA limits become stricter. Data from [8].

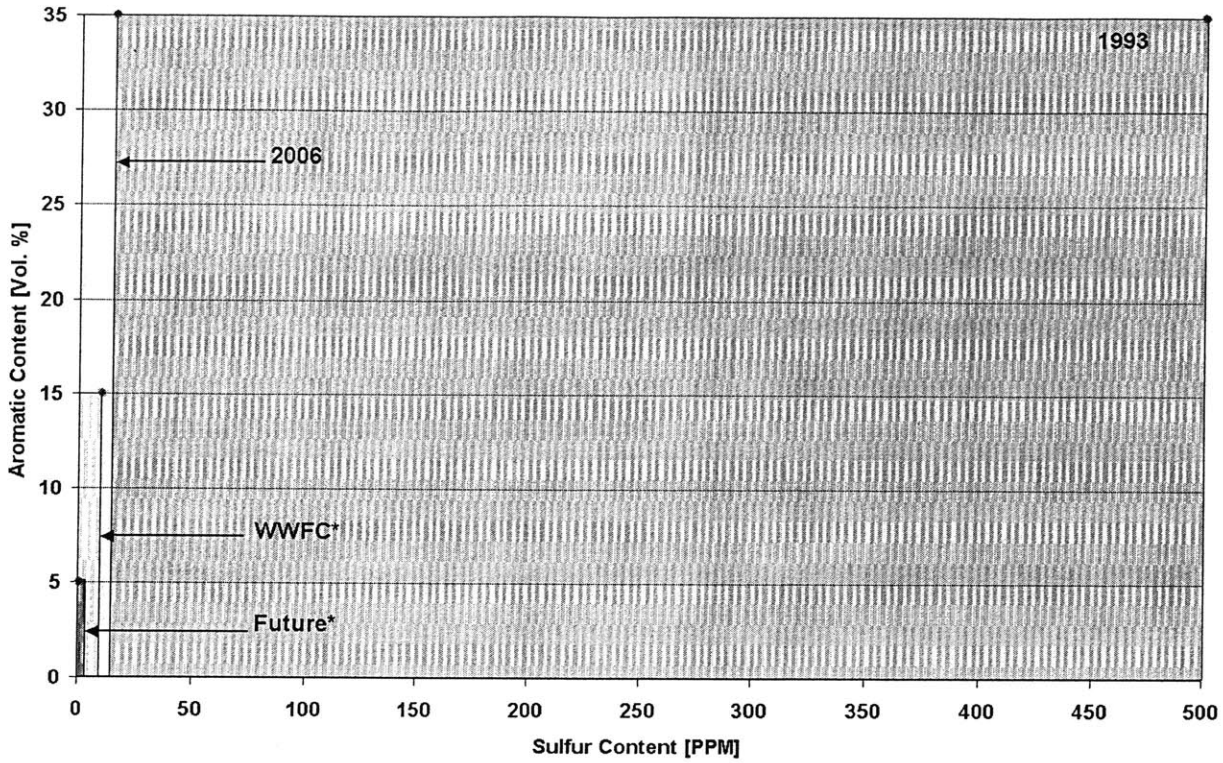

Figure 1.3 Allowable-property map for heavy-duty engine fuel standards. The 1993 and 2006 data points are from established EPA limits, the World-Wide Fuel Charter values are given in [9], whereas the future projection is given by www.fischer-tropsch.org.

$$CO + (1+m/2n)H_2 \longrightarrow 1/n\ C_nH_m + H_2O\ (R_{FT})$$

$$CO + H_2O \rightleftharpoons CO_2 + H_2O\ (R_{WGS})$$

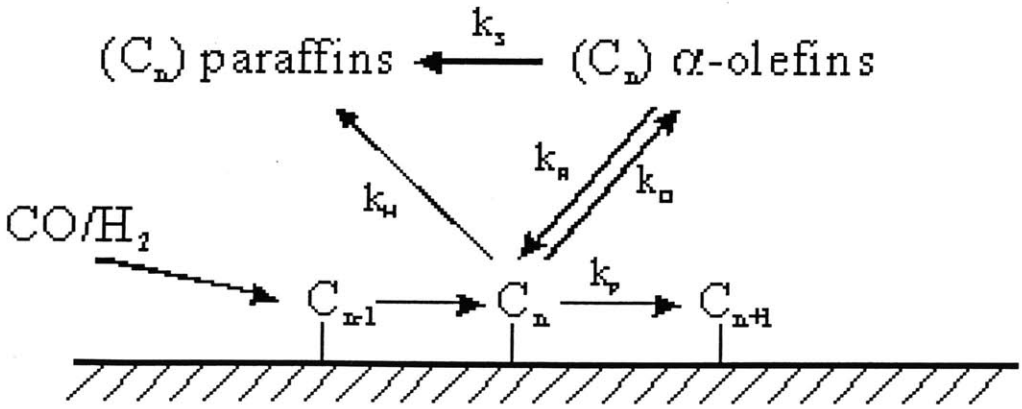

Figure 1.4 Schematic of heterogeneous chemical reactions taking place within a Fischer-Tropsch reactor.

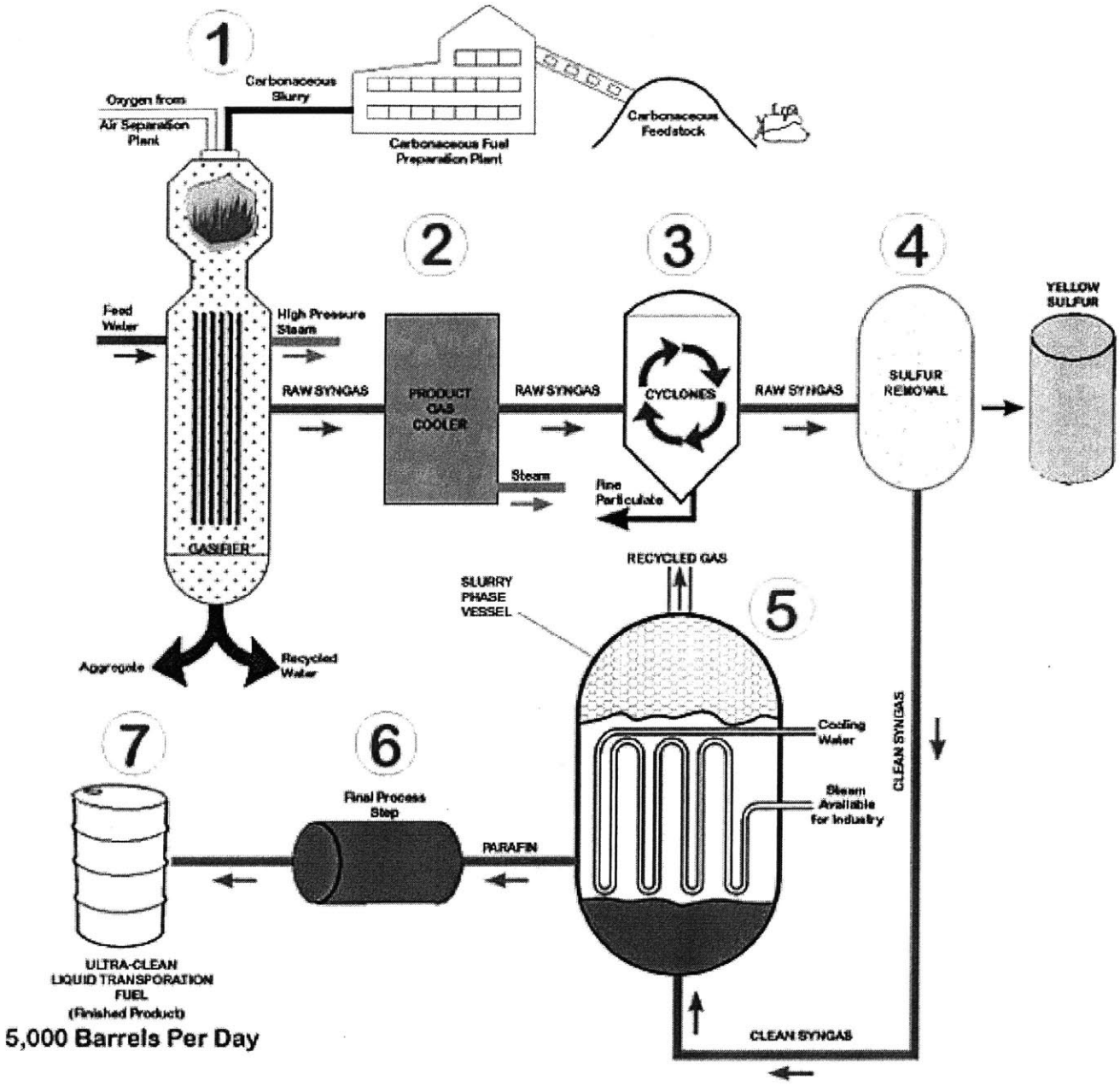

Figure 1.5 General schematic of the Fischer-Tropsch synthesis, www.hydrocarbons-technology.com

(This page left intentionally blank.)

Chapter 2 Diesel Combustion And Emissions

2.1 Diesel Combustion

Diesel combustion is a highly complex, turbulent, three-dimensional, multiphase process involving fluid dynamics, heat transfer, mass transfer, and chemical kinetics, all before a flame is even established. Unlike the homogenous mixtures in spark ignition engines, the two-phase constituents (liquid fuel and air) must be properly mixed relying on fluid dynamics to atomize the fuel at the injector while shear forces at the liquid-fuel boundary layer in the spray further break up the fuel jet, all the while turbulent convection is mixing the fuel and air. Heat transfer plays an important role in vaporizing and mixing the liquid fuel, allowing it to form a gaseous, combustible mixture with the surrounding air. Mass transfer helps to further mix the fuel and air by diffusing the fuel outward from the liquid-fuel jet. Lastly, the "cool" chemistry of autoignition is governed by the relative concentrations of fuel and oxidizer, along with the prevailing conditions within the combustion chamber.

Until recently, the combustion process in diesel engines was thought to occur in two distinct stages, with the diesel fuel burning in either the unsteady, autoignition of a stoichiometric premixed flame or the quasi-steady combustion of a diffusion flame. Recently, researchers at Sandia National Laboratories developed a drastically different conceptual model of diesel combustion after combining data from various advanced imaging experiments from an optically accessible heavy-duty, direct injection diesel engine [24] - [29]. This new concept of diesel combustion now proposes that all of the fuel injected into the cylinder goes through a two-stage oxidation, beginning with a fuel-rich (ϕ = 2 – 4) premixed combustion followed by a diffusion-controlled combustion. Contrasting the new conceptual model with the old phenomenological model has provided different insights into the pollutant formation pathways, leading to a better understanding of combustion characteristics that affect the level of emissions.

2.1.1 "Old" Diesel Combustion Model: Two Stages Of Fuel Oxidation

Before the advent of advanced laser diagnostics and other innovative optical imaging techniques, the diesel combustion process was poorly understood. Previous direct measurement techniques included high-speed backlight, schlieren, and natural-flame-emission cinematography to study flame structure and sampling probes that dumped out cylinder contents at various crank angles to study the temporal formation and destruction of species during the combustion and expansion process [2]. However, these simple techniques lacked the necessary temporal resolution and species differentiation to give precise

details such as the spatial distribution of species at specific crank angles within the developing liquid-vapor fuel jet.

Without precise details of the combustion process, early diesel engine researchers interpreted heat-release rate curves from direct pressure measurements using theory from spray combustion in furnaces and gas turbines [26]. Armed with only intuition and spray combustion theory, some researchers thought that the unsteady, autoignition stage occurred at stoichiometric, or near-stoichiometric conditions within the cylinder [2] and the separate quasi-steady part of diesel combustion occurred as a reacting jet with a nearly pure, liquid-fuel core feeding a diffusion flame occurring around individual droplets or as a sheath around the jet [26]. Schematics showing the early models of diesel combustion can be found in Figure 2.1, Figure 2.2, Figure 2.3 and Figure 2.4.

Attempts to describe the production of the major pollutants in diesel engine exhaust with this previously accepted model of diesel combustion led to the following interpreted conclusions. First, it was commonly believed that NO_x emissions were determined by the amount of fuel reacting in the high-temperature, stoichiometric, or near-stoichiometric autoignition stage of combustion (initial premixed burn) [27]. Intuitively, this was the only way high-temperature regions would exist to drive the thermal mechanism of NO_x formation (see Section 2.2.1). Second, since soot forms from fuel pyrolysis at temperatures above about 1300 K [26], soot was believed to only form on the rich side of the diffusion flame that established after the transient autoignition process. Temporally, the diffusion flame, burning stoichiometrically, was the only region after the autoignition event that would supply the necessary temperatures and residence times to form soot.

The previously accepted model of diesel combustion separated the two accepted aspects of diesel combustion, the transient (everything prior to autoignition) and quasi-steady (everything following ignition) portions into two separate events. The autoignition event was thought to occur on the periphery of the developing liquid-fuel jet after the fuel had mixed with enough hot air to reach an ignitable temperature at stoichiometric or near-stoichiometric fuel-air equivalence ratios. Furthermore, as fuel in the interior continued to evaporate after autoignition to feed the surrounding diffusion flame, vaporizing droplets of fuel were believed to exist up until the rich-side of the diffusion flame, further supporting the idea of soot production occurring just on the inside of the diffusion flame.

2.1.2 New Combustion Model: Two-Stage Fuel Oxidation

Recently, the combination of various laser-imaging tests that tracked various aspects of the reacting fuel jet such as fuel distribution and chemical species such as hydroxyl (OH) radicals and nitrous oxide (NO) spatially and temporally have led to a more complete understanding of the development of the diesel combustion process. The major difference between the old model and the new phenomenological

model is that all of the fuel goes through two oxidation stages, first partially oxidizing in a fuel-rich premixed flame and then completing oxidation in a stoichiometric, or very-near stoichiometric diffusion flame. As such, the physical characteristic of the spray is very different from the previously believed model for diesel combustion (see Figure 2.5 and Figure 2.6).

Studying the temporal development of the new combustion model shows that the differences between the two combustion models arise from the misrepresentation of the development of the liquid-vapor regions. The temporal development of the diesel fuel jet based on the new combustion model is shown in Figure 2.7. The pictorials shown in Figure 2.7 were derived from an engine running at 1200 RPM using a static injection timing of 11.5° bTDC. At these conditions, each crank angle represents 0.139 ms. The intake air was prepared to give TDC conditions of T_{TDC} = 992 K and P_{TDC} = 5.0 MPa (realistic diesel-engine TDC conditions). Finally, the CN of the fuel used was 42.5.

In the initial jet development period (0.0° – 4.5° after the start of injection [ASI]) the dark regions near the fuel injector (small circle near crank-angle labels) show that liquid exists only near the fuel injector; no liquid fuel exists near the diffusion flame. As soon as 2.0° ASI, a vapor-fuel region begins to grow around the liquid core, thickening as the jet continues to penetrate further into the combustion chamber. After about 3.0° ASI, the liquid reaches its maximum penetration distance, about 20 mm downstream of the injector. Enough hot air has been entrained and mixed to vaporize all the fuel by this point. The vaporized fuel-air mixture continues to moves downstream due to the momentum of the fluid, and by 4.5° ASI have reached a combustible, although rich, condition. Autoignition occurs somewhere in this region, between 3.0° – 5.0°, the exact point not very well defined temporally or spatially [26]. Comparing the temporal development of the fuel jet to the appropriate heat release curve (see Figure 7.33 and Figure 7.34) shows the first part of the premixed burn spike occurs around 4.0° – 6.5° ASI. As the premixed flame continues to burn, its products feed a diffusion flame that begins to establish around 5.5° – 6.5° ASI (in Figure 2.5, Figure 2.6 and Figure 2.7, the diffusion flame envelopes the small mushroom cloud of fuel-rich vapor surrounding the liquid fuel and the larger plume of partially oxidized fuel downstream). The dominance of the premixed flame begins to decrease around 7.0° – 9.0° ASI, as the diffusion flame begins to dominate (9.0° ASI to end of injection [EOI]). Based on this differing model of the temporal development of the fuel-jet and diffusion flame structure, the new model for diesel combustion looks vastly different. The regions where the two concurring stages of fuel oxidation are shown in Figure 2.5, along with estimated temperatures in each region.

The old diesel combustion model was quickly questioned, even from very early experiments in 1995 [24], where the direct measurement of soot using laser-induced incandescence (LII) showed that soot formed in the central regions of the fuel jet, well away from the jet periphery. Later, in 1998, planar laser-induced fluorescence showed that the initial premixed burn fraction did not produce any NO_x [27].

Combining fuel-spray dispersion studies [31] further showed that the fuel-air equivalence ratios originally thought to exist throughout the fuel jet are in actuality vastly different, helping to corroborate the above observations of pollutant formation.

Studies on fuel spray behavior into diesel-like combustion bombs show the premixed burn of the autoignition stage is fuel-rich (ϕ = 2 – 4), supporting the fact that soot is found to form in the central regions of the jet, while the lack of oxygen in rich combustion does not support any appreciable NO_x production. Also, tracking the fuel distribution throughout the jet using LII and planar laser Rayleigh scattering (PLRS) shows the premixed flame to continually exist throughout the entire combustion process. The premixed flame is then divided into two stages; the transient, initial premixed flame and the quasi-steady, standing premixed flame. Furthermore, the products of the rich premixed combustion are shown to form the precursors for soot. These soot precursors combine and grow to form actual soot particles that continue to increase in size before they are oxidized at the periphery of the fuel jet where the diffusion flame is established. Similar to the old model, the diffusion flame surrounds the fuel jet and reacts where the mixture is stoichiometric, or very near stoichiometric. See Figure 2.6 for a graphical representation of where various species and pollutants are likely forming during diesel combustion.

Based on the above findings, the diffusion flame is the determining factor for diesel engine emissions. Since the diffusion flame establishes itself where the rate of mixing and reaction are equal (where the Damköhler number, Da, is of the order of one), its stoichiometric equivalence ratio leads to high adiabatic flame temperatures next to a large source of nitrogen and oxygen, prime conditions for the production of NO_x. Furthermore, it is proposed that in the soot formation-destruction process within the fuel-vapor plume, the quenching of the final oxidation stage at the diffusion-flame boundary is the main contributor for diesel soot emissions [29].

2.1.3 Flame Lift-Off

The proposed equivalence ratios in the standing premixed flame outlined by the new two-stage oxidation model described above cover a large range in the rich regime. Applying theory about lifted, turbulent diffusion flames from gas jets allows one to make relative estimates about how rich the standing premixed flame is based on engine operating conditions. Research done on these types of flames shows that stoichiometric, or near stoichiometric combustion occurs at the flame stabilization location [30]. The distance away from the fuel injector where the diffusion flame "sits" and reacts is called the lift-off length, denoted as H. Due to the two-stage combustion process, the transient and quasi-steady injection events are considered separately when applying flame lift-off theory.

Based on research done in quiescent combustion bombs, both ambient gas temperature and gas pressure have strong effects on the size of the standing, premixed flame that forms in the transient startup

of injection, eventually affecting the flame lift-off length. Reducing either temperature or pressure leads to an increase in lift-off length once autoignition occurs. With respect to temperature, the lift-off length increases as temperature decreases since heat transfer to the liquid fuel affects autoignition chemistry. Ignition delay is exponentially dependent upon ambient gas temperature (see Equation 7.1). Therefore, as cylinder temperature decreases, the amount of time required for a fuel to autoignite increases, allowing more time for mixing, leading to an increased lift-off length as shown in Figure 2.8.

Reducing the cylinder pressure does not reduce the size of the standing premixed flame by itself. Rather it is the increased pressure difference between the fuel leaving the nozzle and the cylinder that governs the size of the rich fuel-air mixture. Assuming the fuel leaves the injector nozzle at a constant pressure, reducing the cylinder pressure increases the relative momentum of the fuel with respect to the ambient gas, increasing the air-entrainment rate, resulting in a larger lift-off length. Similarly, lower in-cylinder pressure leads to lower gas densities. The flame lift-off length increases as the lower density gas has a smaller heat capacity per volume, requiring more air to transfer energy to the fuel before autoignition occurs. Data in [30] shows the flame lift-off length is linearly dependent upon fuel-injection velocity, implying a square-root dependence on the differential pressure between the injector and cylinder (based on Bernoulli's equation). The linear dependence of flame lift-off length to fuel-injection velocity occurs because the turbulent fuel-air mixing rate increases in proportion to injection velocity, but decreases in proportion to the axial distance from the injector tip to the flame lift-off point. Thus, to maintain a balance between the local mixing rate and the local reaction rate of the surrounding diffusion flame (i.e. keep a constant turbulent Damköhler number of order one), the increase in fuel-injection velocity forces the lift-off length downstream, as seen in Figure 2.9 (see Figure 2.10 for injection pressure analogue). Therefore, with modern fuel-injection systems having large injection pressures, the fuel spray will have a physical appearance resembling the schematic on the right of Figure 2.12.

In the quasisteady portion of diesel combustion (after ignition occurs), heat transfer and its corresponding effect on the ignition delay are no longer important. While the diffusion flame is being fueled by the standing premixed flame, the laminar flame speed and thermal diffusivity become the dominant parameters that describe the local flame reaction rate, and hence the lift-off length.

As cylinder temperature increase, both the laminar flame speed and thermal diffusivity increase, raising the local flame reaction rate. Data from several hydrocarbon fuels with varying fuel/air equivalence ratios show the following dependence of laminar burning velocity on in-cylinder temperature and pressure:

Equation 2.1

$$S_L = S_{L,0}\left(\frac{T_u}{T_0}\right)^{\alpha}\left(\frac{p}{p_0}\right)^{\beta}$$

where T_0 is the reference temperature (298 K), p_0 is the reference pressure (1 atm), and $S_{L,0}$, α, and β are constants for a given fuel, equivalence ratio, and burned gas diluent fraction [2]. The exponents in the above equation are not available for diesel fuel, but they are not drastically different for typical hydrocarbon fuels as the following correlations apply to propane (C_3H_8), isooctane (C_8H_{18}), and methanol (CH_4O), fuels having drastically different physical and chemical properties [2]:

Equation 2.2 $$\alpha = 2.18 - 0.8(\phi - 1)$$

Equation 2.3 $$\beta = -0.16 + 0.22(\phi - 1)$$

Equation 2.4 $$S_{L,0} = B_m + B_\phi(\phi - \phi_m)^2$$

where ϕ_m is the equivalence ratio where $S_{L,0}$ is a maximum, B_m is the maximum value of $S_{L,0}$ at ϕ_m, and B_ϕ is a fuel constant. Therefore, increasing the in-cylinder temperature increases the laminar burning velocity. With respect to pressure, although the above equation shows increasing the in-cylinder pressure will slow down the laminar burning velocity, the overall dependence on pressure is weak compared to temperature due to the small value of β.

The thermal diffusivity in and around the diffusion flame describes how well heat can diffuse through the fuel-air mixture. As the in-cylinder temperatures increase, the thermal diffusivity increases, allowing the fuel-air mixture to respond more quickly to prevailing ambient conditions. Thus, as combustion progresses, heating of the surroundings by high-temperature combustion products and compression of the unburned mixture helps raise the unburned mixture temperature, accelerating the chemical kinetics governing combustion. Together, both the increased thermal diffusivity and laminar flame speed allow the flame to anchor closer to the injector tip, shortening the lift-off length.

Gas density again has an inverse relationship with lift-off length after ignition has been established since high density gas slows down the mixing rate as momentum in the fuel jet decays more quickly when entraining heavier air. Thus, the diffusion flame moves closer to the injector to keep the Damköhler number to an order of magnitude of one. Based on power-law fits to experimental data in [30], the effects of both gas temperature and density are non-linear, having dependencies of $H \alpha T^{-3.74}$ and $H \alpha \rho^{-0.85}$.

As mentioned in the section above, the flame lift-off length is linearly dependent upon the fuel-injection velocity. The linear dependence of the flame lift-off length to fuel-injection velocity is further corroborated by the fact that the local reaction rate, determined by the laminar flame speed and thermal diffusivity, does not change with the fuel-injection velocity.

For applications of flame lift-off theory to diesel engine combustion, see Section 7.1.2.1.

2.2 Pollutant Formation Pathways in Diesel Engine Exhaust

As stated earlier, the major pollutants in diesel exhaust include oxides of nitrogen (NO_x) and particulate matter (PM). Due to the overall-lean operation and direct-injection of fuel in diesel engines, the formation mechanisms for CO, CO_2, and HCs are not included (see Figure 2.11).

2.2.1 NO_x Formation Mechanisms

Four different routes have been identified that can lead to the formation of NO_x during combustion [5]. These routes include the thermal route (Zeldovich mechanism), the prompt route (Fenimore mechanism), the N_2O route (Wolfrum mechanism), and the fuel-bound nitrogen route. Given that the near-stoichiometric, high-temperature diffusion flame dominates in diesel combustion after about 10° ASI, the thermal mechanism is the most important pathway for NO_x formation in diesel engines. Generally, the Fenimore mechanism is favored in rich flames; the Wolfrum mechanism is favored in the lean premixed combustion in gas turbine engines; NO_x from fuel-bound nitrogen is mainly observed in coal combustion [5].

The elementary reactions that form NO through the extended[3] Zeldovich mechanism are [2]:

Equation 2.5 $$O + N_2 \underset{k_1^-}{\overset{k_1^+}{\Leftrightarrow}} NO + N$$ Reaction 1

Equation 2.6 $$N + O_2 \underset{k_2^-}{\overset{k_2^+}{\Leftrightarrow}} NO + O$$ Reaction 2

Equation 2.7 $$N + OH \underset{k_3^-}{\overset{k_3^+}{\Leftrightarrow}} NO + H$$ Reaction 3

The rate constants for the forward and reverse reactions are given in Table 2.1, in m^3/mol-s.

Table 2.1 Forward and reverse rate constants for the elementary reactions in the extended Zeldovich NO formation mechanism.

Reaction	Forward Rate Constant [m^3/mol-s]	Reverse Rate Constant [m^3/mol-s]
1	$1.8 \times 10^8 \exp(-38{,}370 / T\ [K])$	$3.8 \times 10^7 \exp(-425 / T\ [K])$
2	$1.8 \times 10^4 \exp(-4680 / T\ [K])$	$3.8 \times 10^3 \exp(-20820 / T\ [K])$
3	$7.1 \times 10^7 \exp(-450 / T\ [K])$	$1.7 \times 10^8 \exp(-24{,}560 / T\ [K])$

[3] Y.B. Zeldovich originally proposed (1946) only the first two listed elementary reactions, Reaction 1 and 2 [5]. Lavoie et al. (1970) later added the third mechanism, Reaction 3 [2].

The Zeldovich mechanism earns its "thermal" moniker because the forward rate constant for Reaction 1 has a very high activation energy due to the strong triple bond in the N_2 molecule, and is thus sufficiently fast only at high temperatures [5]. Reaction 1 is thus the rate-limiting step in the extended Zeldovich mechanism.

The rate of formation of NO based on the above reactions (applying the quasi-steady state approximation for N atoms, i.e. d[N]/dt ~ 0) is:

Equation 2.8
$$\frac{d[NO]}{dt} = 2k_1^+[O][N_2]$$

Thus it can be seen that reducing k_1^+ (by reducing combustion temperatures) or the concentrations of N_2 and/or O will decrease the overall formation rate of NO. The concentration of N_2 can be easily measured with gaseous-emissions equipment or calculated accurately assuming equilibrium; the oxygen radical, however, poses a problem. Assuming equilibrium between oxygen and the oxygen radical will underpredict the [O] concentration by up to a factor of 10 [5]. A better approximation for [O] is [5]:

Equation 2.9
$$[O] = \frac{k^+_{H+O_2} k^+_{OH+H_2} [O_2][H_2]}{k^-_{OH+O} k^-_{H_2O+H} [H_2O]}$$

The rate constants in the oxygen-radical concentration relation are based on the partial equilibrium approximation in hydrogen combustion [5]:

Equation 2.10
$$H + O_2 \underset{k^-_{OH+O}}{\overset{k^+_{H+O_2}}{\Leftrightarrow}} OH + O$$

Equation 2.11
$$O + H_2 \underset{k^-_{OH+H}}{\overset{k^+_{O+H_2}}{\Leftrightarrow}} OH + H$$

Equation 2.12
$$OH + H_2 \underset{k^-_{H_2O+H}}{\overset{k^+_{1OH+H_2}}{\Leftrightarrow}} H_2O + H$$

2.2.2 Particulate Formation Mechanisms

The particulate matter that is exhausted out of a diesel engine consists primarily of carbonaceous material, commonly referred to as soot, on which organic and inorganic compounds adsorb and condense. Organic compounds include unburned hydrocarbons, aromatic hydrocarbons (ketones, esters, ethers, organic acids) and polynuclear aromatic hydrocarbons (PAHs). Inorganic compounds include sulfur

dioxide, nitrogen dioxide, and sulfuric acid (sulfates) [2]. Although a myriad of compounds end up as PM, the main building block is the carbon core.

The physical processes that contribute to the formation of soot include: particle nucleation or inception; particle growth by reaction with gas-phase molecules that adsorb or condense onto the newly-nucleated particle; agglomeration of large particles through particle-particle sticking collisions such as coagulation and aggregation; mass removal from particles by pyrolytic elimination of functional groups along with dehydrogenation and structural rearrangement of the condensed matter; mass removal through oxidation. The most important step in the entire process is the particle nucleation/inception step, without which the rest of the process cannot proceed.

Although researchers have claimed various mechanisms of how soot is formed in the past, it is now agreed that the molecular precursors to soot are heavy PAHs. The growth of heavy PAHs relies on reactions between the smallest aromatic 2 – 3 ring structures, recombining to form molecules with ten or more rings. Therefore, aromatic structures with 1, 2, and 3 rings are the most important building blocks in the entire soot formation process.

1-, 2-, and 3-ring structures initially form from acetylene (C_2H_2), present as combustion starts due to the thermal breakdown of hydrocarbon fuels. Acetylene can go through further pyrolysis and form the propargyl radical (C_3H_3) that can recombine with another propargyl radical to form the simplest ring structure, benzene (C_6H_6). Further reactions with benzene and acetylene can easily lead to 2 ring structures through a process called cyclization. The process continues on the free sites of the aromatic structure: acetylene attaching to a free site, then reacting with another acetylene molecule to close the ring to form bigger and bigger PAHs.

Based on collision theory, as the PAHs grow larger and larger, the possibility of them colliding with another large molecule increases. As soon as molecules begin to collide with one another, soot growth proceeds rapidly as the increased surface area not only allows for more frequent collisions, but it also provide more sites for gas phase species to adsorb and condense. Furthermore, acetylene continues to grow PAHs that then attach to the soot particle, while also reacting directly with the surface of the large particles, speeding up the surface growth rate.

After soot has formed within the interior of the plume (see Section 2.1.2), it can be oxidized as it moves towards the diffusion flame boundary. Oxidation is the only pathway available that removes soot mass, in contrast to the many ways soot can grow. Thus, only by allowing the diffusion flame to burn to completion can soot be reduced in-cylinder.

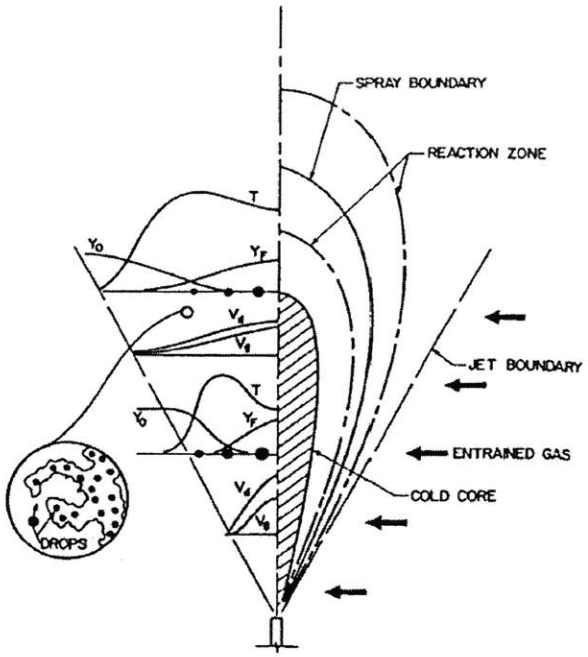

Figure 2.1 Schematic representation of a coaxial spray diffusion flame. Uses as an early model of quasi-steady portion of diesel combustion [26].

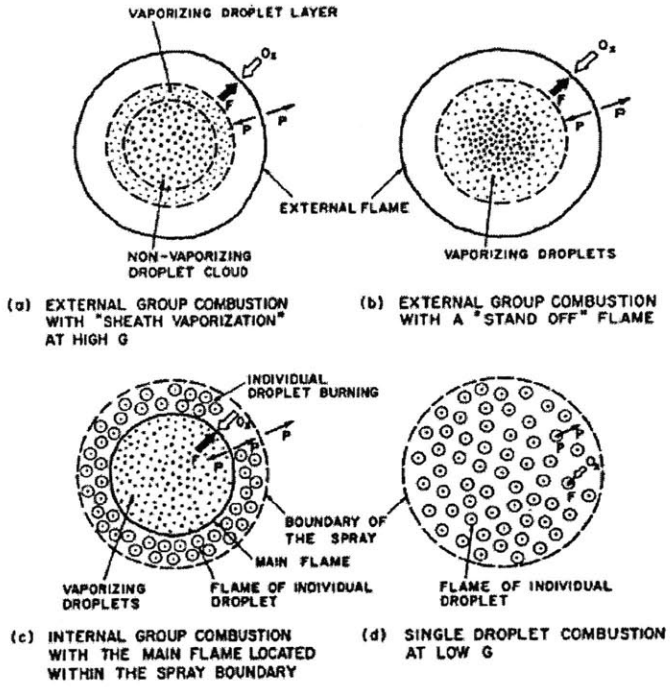

Figure 2.2 Schematic of combustion modes in a developing liquid-fuel spray. Used as an early model of flame development and combustion around liquid fuel droplets [26].

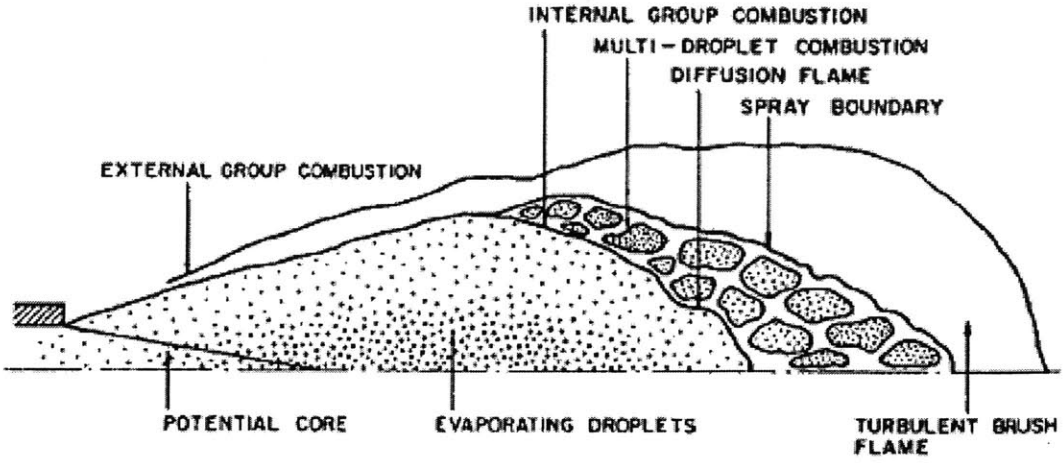

Figure 2.3 Schematic of various group combustion modes scattered spatially in a reacting liquid-fuel spray. Combustion is shown to occur as a sheath around the spray on the exterior and around individual droplets within the evolving spray cloud [26].

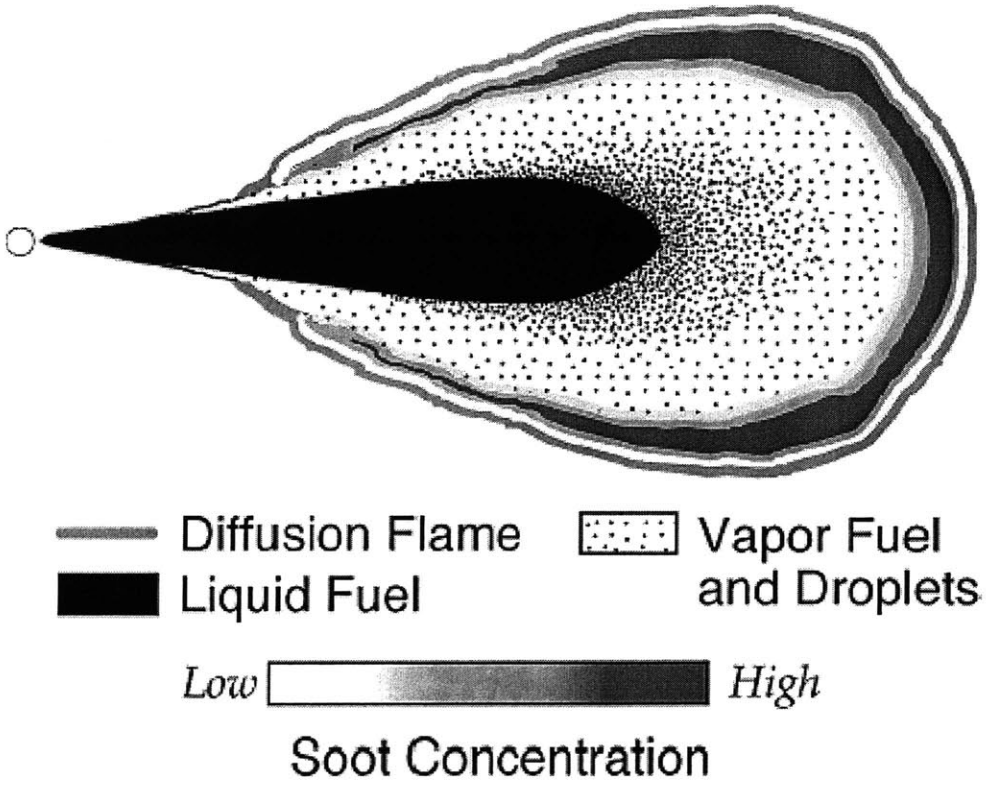

Figure 2.4 General schematic of the "old" view of diesel combustion that intuitively combined droplet and spray combustion theory.

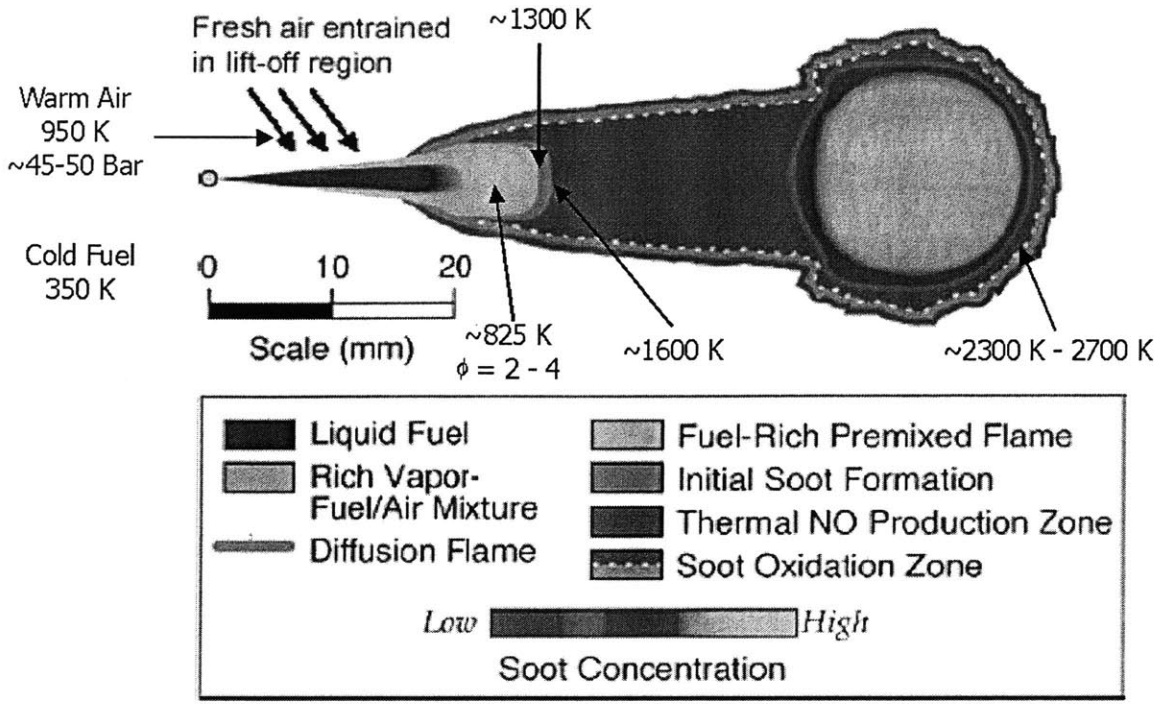

Figure 2.5 Schematic of new phenomenological model of diesel combustion with proposed temperatures throughout the developing plume. Adapted from [26] and [29].

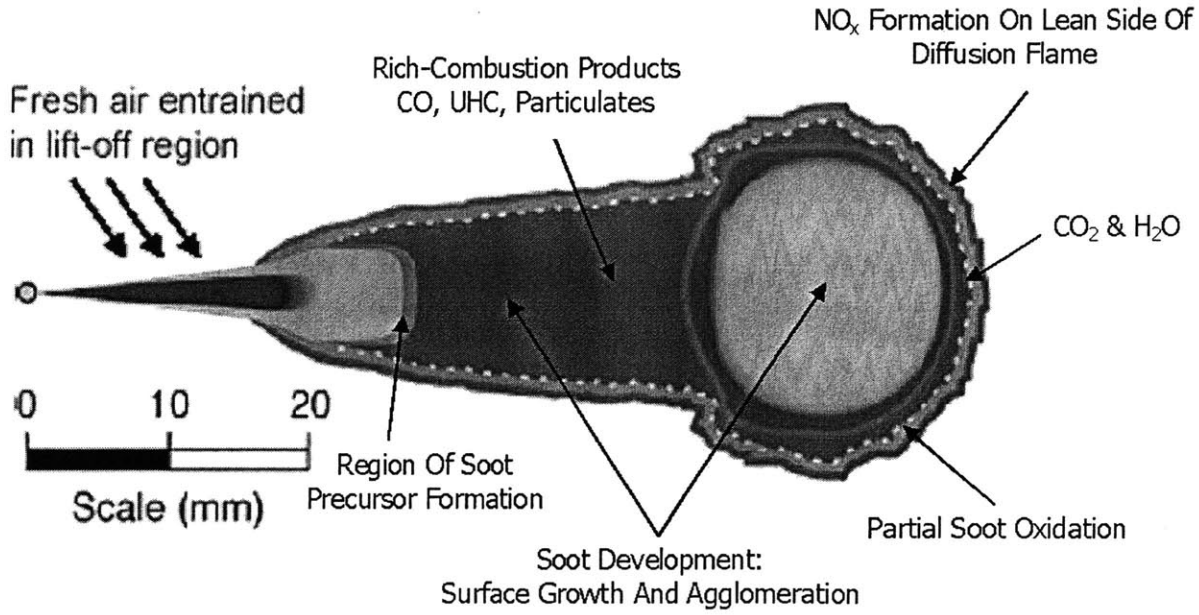

Figure 2.6 Schematic of new phenomenological model of diesel combustion showing spatial distribution of combustion products. Adapted from [26] and [29].

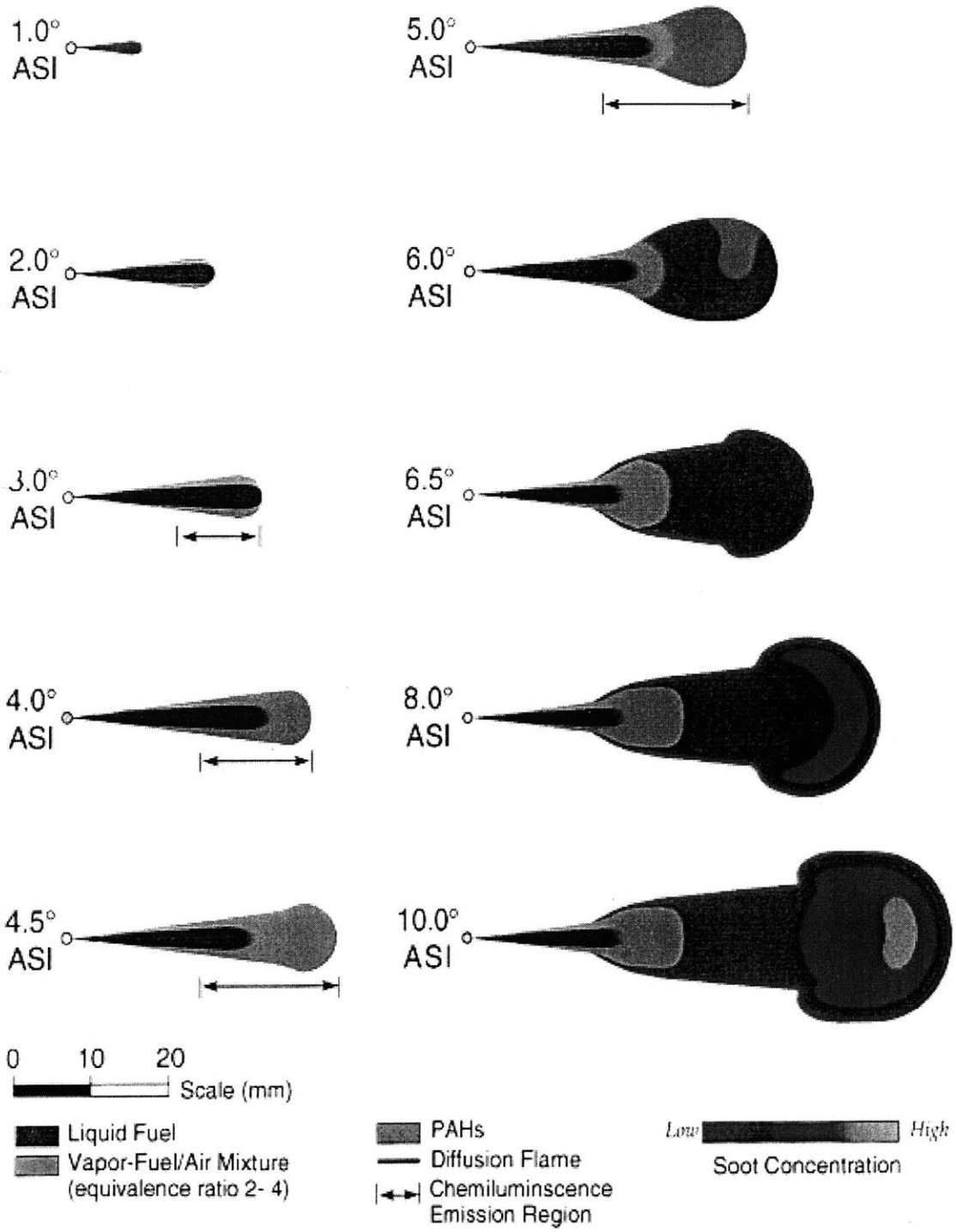

Figure 2.7 Temporal development of the transient and beginning quasi-steady portion of the diesel flame structure based on the new two-stage phenomenological model of diesel combustion. The figures are drawn using data recorded from a Cummins N14 engine, running at 1200 RPM, with intake temperatures and pressures that give realistic diesel-engine TDC conditions (992 K, 5.0 MPa @ TDC) [29]. Each crank angle represents 0.139 ms at this RPM.

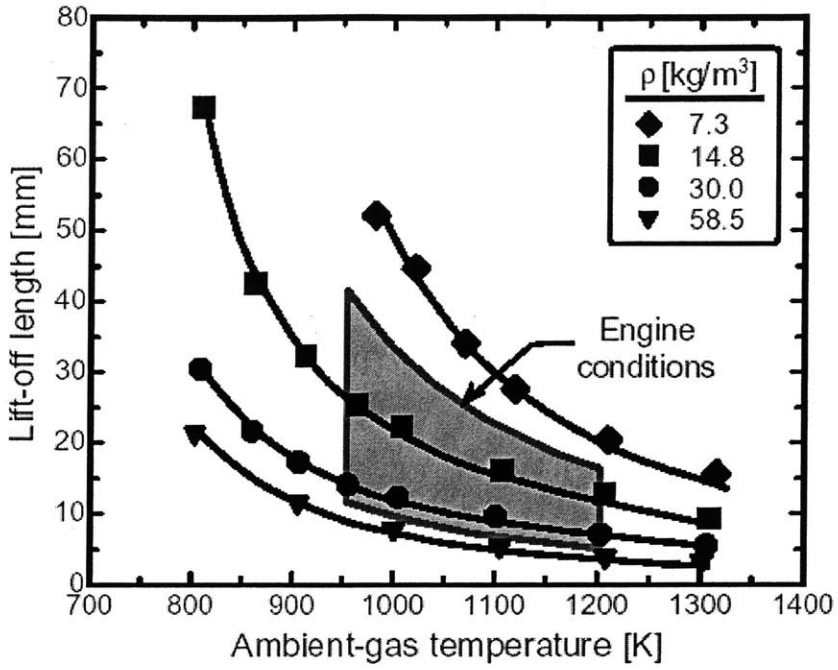

Figure 2.8 Flame lift-off length versus ambient gas temperature for a range of ambient gas densities. The pressure drop across the injector orifice and the orifice diameter are 138 MPa and 180 μm. The gray region is the expected lift-off length in quiescent diesel engines [30].

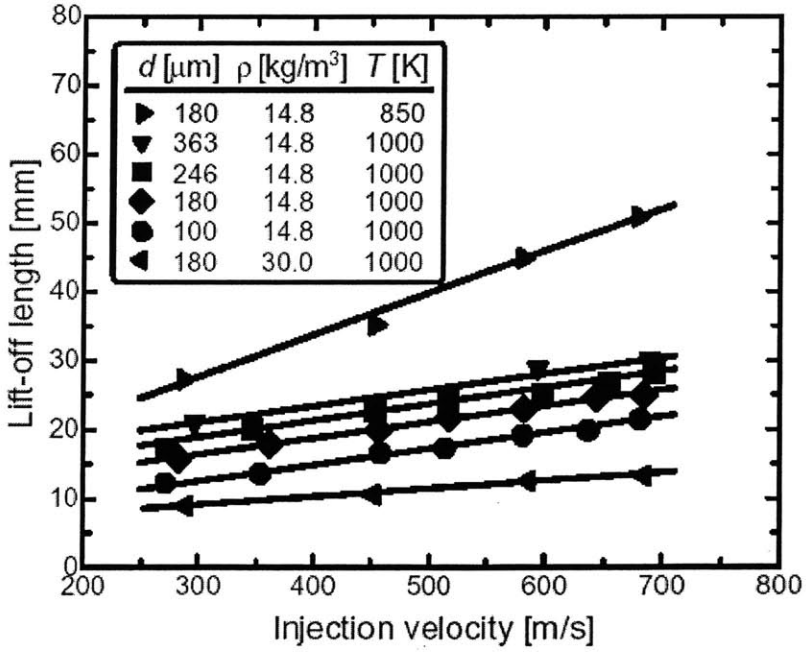

Figure 2.9 Flame lift-off length versus injection velocity for a range of injector orifice diameters, ambient gas densities, and ambient gas temperatures [30].

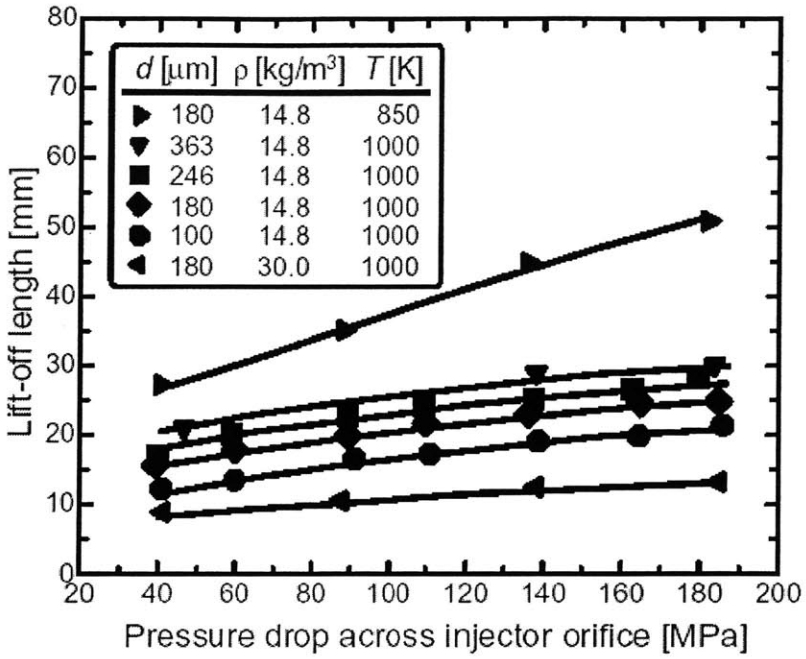

Figure 2.10 Flame lift-off length versus injection pressure for a range of injector orifice diameters, ambient gas densities, and ambient gas temperatures [30].

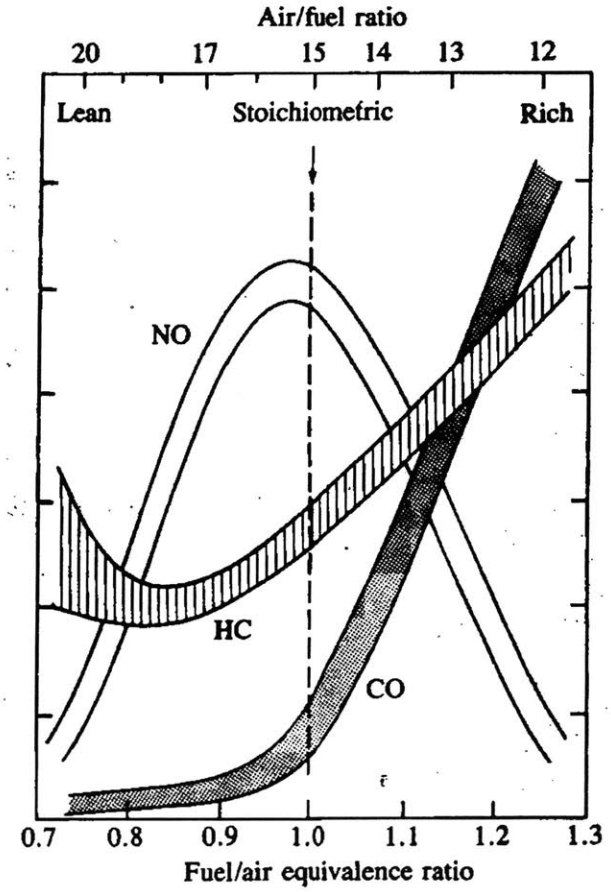

Figure 2.11 Relative emission concentrations in the exhaust versus fuel/air equivalence ratio [2].

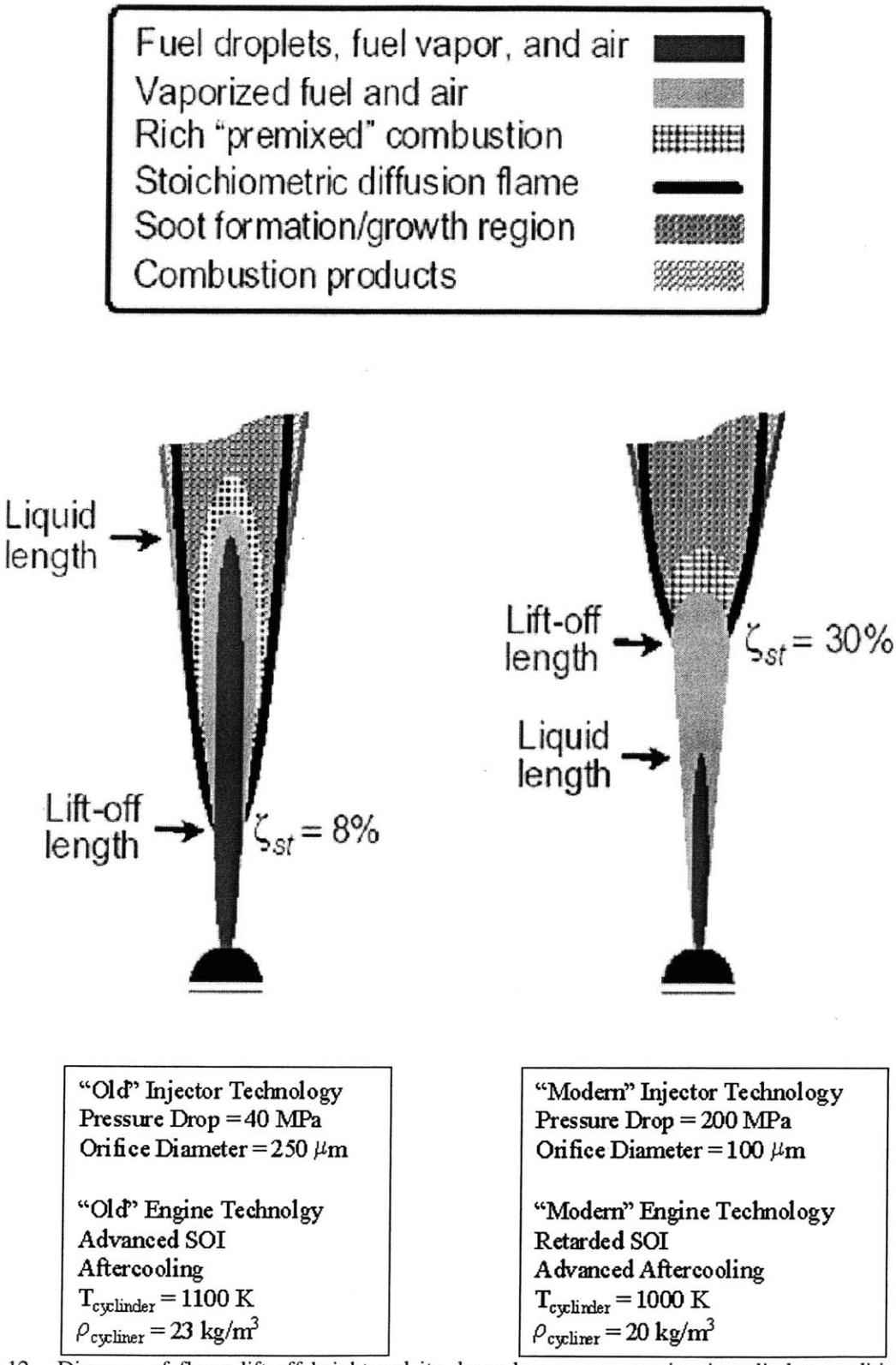

Figure 2.12 Diagram of flame lift-off height and its dependence upon varying in-cylinder conditions and injection parameters. Adapted from [30].

Chapter 3 Impact of Fuel Properties on Diesel Emissions

3.1 Current Understanding

The large variations in engine technology found in older engines led to contradicting claims and understandings of what fuel properties affected engine-out emissions [32]. Researchers claimed that some properties affected emissions more than others, whereas engine technology might have been playing a role as well. In recent years, in-cylinder optimizations and advanced subsystems such as modern fuel injection equipment and cooled-EGR systems in modern engines have decreased the effect diesel fuel properties play in governing engine-out emission levels as they did in older engines [35]. However, some fuel properties still play a role such as those described below.

3.2 Cetane Number

A fuel's cetane number (CN) is a general description of its tendency to autoignite. This fuel parameter gives a relative rating of a fuel's ignition quality based on the chemical interactions occurring within the fuel during the fuel injection process. As described in the phenomenological model of diesel combustion, ignition occurs in a region where the fuel has already vaporized and mixed with air. Therefore, a fuel's CN indicates the magnitude of the oxidation reactions occurring in the liquid fuel droplets and the likelihood of the large hydrocarbons thermally cracking into smaller molecules [2] such that autoignition can occur.

Since a fuel's CN describes its ignition quality, the CN is also a relative indicator of the amount of fuel that autoignites in the initial premixed burn fraction. Low CN fuels require longer times before autoignition occurs, resulting in more fuel mixing with the surrounding air. Consequently, the added time for mixing helps to lean the initial premixed burn mixtures. On the other hand, high CN fuels autoignite quickly, limiting the amount of fuel and air that mixes before ignition occurs. As a result, the fuel-air mixture in the initial premixed flame will be richer compared to a low CN fuel. Thus, based on the two-stage diesel combustion model detailed in Chapter 2, the initial premixed burn fraction of a low CN fuel will contain a relatively large amount of vaporized fuel and air with an equivalence ratio on the leaner side of the proposed $\phi = 2 - 4$ by the time it autoignites while a high CN fuel will have comparatively small amount of fuel-air mixture towards the richer side of the proposed equivalence ratio range.

According to new models for diesel combustion, the premixed burn fraction is no longer a proper indication of potential NO_x emissions since it occurs in regions too rich to support NO production. The main culprit is the diffusion flame, burning stoichiometrically next to a large source of oxygen. Still,

however, the combustion characteristics of the diffusion flame are coupled with the behavior of the initial premixed burn fraction. The characteristics of the initial premixed burn fraction (the initial premixed burn fraction is differentiated from the premixed flame that coexists with the diffusion flame) and it's relative proportion versus the diffusion flame leads to cylinder characteristics that affect NO production in the diffusion-flame dominated phase of combustion. The initial premixed burn fraction leads to a rapid and substantial pressure rise in cylinder pressure following the start of fuel injection, further compressing the fresh mixture surrounding the jet of fuel. The increased cylinder temperature leads to higher diffusion flame temperatures. Furthermore, the elevated temperature and pressure of the cylinder increase the kinetics of the diffusion flame, leading to more pronounced NO_x production [27].

Engine technology has a large effect on the size of the initial premixed burn fraction in combustion. In early engines, fuel injection occurred anywhere from 20 to 30° BTDC in order to ensure operation away from the smoke limit (poor mixing of fuel resulted in high HC and PM outputs). In newer engines, higher injection pressures have improved mixing and allowed for more retarded timing to reduce NO_x (diesel engines nowadays inject fuel from –5 to 15° BTDC). Based on recent studies, a cetane number improvement of 10 points results in up to a 5% reduction in NO_x in older engines (1998 and older) with a reduction of about 2% in newer and future engines [33].

Consistent with the NO_x-PM tradeoff characteristic (see [2]) of diesel engines, an increase in cetane number has been shown to increase PM [34][35]. According to the new two-stage oxidation model for diesel combustion from Sandia National Laboratories, the rich, premixed standing flame is the main source of soot precursors due to the "cool" temperatures of the rich, premixed combustion resulting in the partial oxidation and pyrolysis of the diesel fuel forming PAHs. As cetane numbers increase, the proportion of fuel mass found in the initial premixed burn and the subsequent proportion of fuel mass at any given time during combustion in the standing premixed flame in the diesel fuel spray decreases while the proportion of fuel mass found in the surrounding vapor and diffusion flame boundary increase. Furthermore, since duration of combustion is approximately equal in modern engines (1994 and newer) regardless of fuel cetane number (see Section 7.1.2 and reference [18] which shows No. 2 Diesel with CN = 48.7 & F-T fuel with CN = 73.7 having combustion durations within 1.5° in a total of between 25 – 30°) a higher cetane-numbered fuel allows more time for the soot precursors formed in the standing premixed flame to undergo particle growth through surface growth and agglomeration before reaching the diffusion flame. In summary, the decreased size of the fuel-rich, standing premixed flame as a result of higher cetane numbers may possibly lead to a decrease in the number of soot precursors that are guaranteed to form. This may lead to a drop in the number of soot particles, but each particle's respective mass may increase due to longer residence times for growth as explained above.

For heterogeneous reactions like the oxidation of soot, the overall rate depends on the mass transport of reactants (oxygen) to and products from the surface of the particle along with the chemical kinetics governing the reaction at the surface. Usually, for particles smaller than 1 μm, the diffusional resistance is negligible [2]. However, as soot particles grow, the oxidation rate decreases as mass transport becomes important. Also, the oxidation time is a linear function of the initial soot diameter. These factors can eventually lead to higher PM out of the engine as a result of a higher cetane number.

Another reason a higher cetane-numbered fuel may lead to more PM is in the fact that less air entrainment occurs during fuel injection before the initial premixed burn occurs. With less oxygen available, this initial burn fraction is much more rich, resulting in the formation of even more soot precursors. Soot precursors are formed in richer conditions due to an unfavorably high C/O atomic ratio. Without enough oxygen to form CO, the carbon atoms are forced to form other carbonaceous species, such as soot precursors.

As described above for NO_x reductions with cetane number, engine technology again plays a major role in determining how the cetane number affects PM emissions output. A literature review on the fuel quality impact on diesel emissions concluded that the effect of changing the cetane number of a fuel on PM emissions is engine specific [35]. Also, a more recent paper compounds this fact by stating that diesel engine emissions are primarily determined by engine design [36]. In engines designed to emit less pollutants, engine out emissions are insensitive to cetane number changes, while older engines designed to emit pollutants at higher levels tended to show improvements as the fuel cetane number was increased. The insensitivity to cetane number found in newer engines comes from the fact that cylinder temperatures are much higher at the time of injection due to retarded timing strategies and higher compression ratios, reducing the initial premixed burn fraction, and that mixing has been increased due to higher injection pressures and velocities allowing for better soot oxidation.

3.2.1 Cetane Number Ratings

Cetane number is usually defined through test procedure ASTM D 613 [37]. However, this method has a limit of determining CN only up to 74, and is only reliable in determining CN in the range of 30 – 65. Fischer-Tropsch fuels thus rely on a cetane number index (CNI), which correlates fuel properties to a cetane-like number. Two methods are available for determining the cetane number index, ASTM D 976 and ASTM D 4737 [37], using distillation curve properties and fuel density to calculate the CNI. The ASTM D 976 correlation is:

Equation 3.1 $$CI_{976} = 454.74 - 1641.416 * D + 774.74 * D^2 - 0.554 * T50 + 97.803 * [\log_{10}(T50)]^2$$

where D is the fuel density [g/ml] at 15° C (given by test method ASTM D 1298) and T_{50} is the temperature corresponding to the 50% point on the distillation curve (given by test method AST D 86). The ASTM D 4737 correlation is:

Equation 3.2
$$CI_{4737} = 45.2 + 0.0892(T_{10N}) + [0.131 + 0.901B](T_{50N}) + [0.0523 + 0.420B](T_{90N}) + 4.9x10^{-4}[(T_{10N})^2 - (T_{90N})^2] + 107B + 60B^2$$

where $T_{10N} = T_{10} - 215$; $T_{50N} = T_{50} - 260$; and $T_{90N} = T_{90} - 310$ with T_{10}, T_{50}, and T_{90} are the temperatures corresponding to the 10%, 50%, and 90% points on the distillation curve (by ASTM D 86); and B is given by B = [exp(-3.5DN)] – 1, where DN = D – 0.85 (D as above).

Research done by a lab in New Zealand labs has tried to correlate CNI_{976} and cetane number. The best equations thus far are [38]:

Equation 3.3
$$CI_{976} = 0.951922 * CN + 4.12858 \quad [r^2 = 0.70]$$

Equation 3.4
$$CI_{976} = 0.99849 * CN + 2.41224 \quad [r^2 = 0.75]$$

The equations used above were based on diesel fuels found in New Zealand. From this study, CI_{976} is a better representation for CN, however neither of the ASTM equations is suitable for fuels containing pure hydrocarbons (i.e. FT diesel) or non-petroleum based fuels derived from coal.

3.3 Aromatic Content

The effects of aromatic content on PM and NO_x emissions is uncertain, but the overall trend seems to show that reducing the aromatic content of a fuel has a small, if any, benefit in reducing the aforementioned emissions. In a recent report by researchers at the National Research Council Canada [36] and Equilon Enterprises [35], test results showed that the total aromatic type or content had no effect on diesel engine PM emissions. RCM research [39] corroborates this claim even in non-engine applications where the fuel-air mixing process is limited. Although mono-, di-, and poly-aromatics have higher C/H ratios than a zero-aromatic fuel (~ 0.57 vs. 0.48 in [39]) that presumably would lead to more PAH soot precursors, aromatics also have higher adiabatic flame temperatures due to the increased C/H ratio. Thus, although more PAHs may form as nucleation sites for soot, the elevated flame temperatures help oxidize the soot at the diffusion flame and during post-combustion oxidation in the expansion stroke.

With respect to NO_x formation, increasing aromatic content increases NO_x due to the elevated adiabatic flame temperatures in aromatic-containing fuels. It is well known that the extended Zeldovich

NO mechanism is highly temperature dependent, so any increase in cylinder temperatures will affect NO_x formation. Researchers from NRC showed that the aromatic type did not affect NO_x emissions, but the total aromatic content did [36]. NO_x emissions increased monotonically as the total aromatic content was raised from 10% to 30%.

3.4 Fuel-Sulfur Content

Fuel sulfur reacts with oxygen during combustion to form SO_2. Further oxidation in the port and exhaust system leads to the formation of SO_3. This can react with water in the post-combustion products to produce sulfuric acid. The sulfuric acid droplets can then condense on soot precursors, contributing to the increased mass of soot particles. This accounts for the sulfate contribution of PM, which can be on the order of a few percent.

Large engine out reductions were seen in the past when the sulfur content of on-road diesel fuel was reduced from 3000 PPM to 500 PPM [35]. However, this reduction diminishes as the sulfur content approaches zero, as seen in the following correlation relating sulfur content to sulfate emissions [40]:

Equation 3.5
$$SO_4[g/bhp-hr] \approx 5.5x10^{-5} + 4.9x10^{-6} * [S, PPM]$$

An increasingly important drawback with sulfur in diesel fuel is its deleterious effects on emission control technology. In engines with EGR systems, sulfur oxides from the exhaust gas have been shown to increase engine wear, especially in the piston rings [41]. Properly designed diesel oxidation catalysts (DOCs) can be poisoned when using fuels with sulfur contents above 500 PPM [16] and can contribute to further PM levels by helping to oxidize sulfur dioxide (SO_2) to sulfur trioxide (SO_3) which leads to sulfuric acid as described above [42]. The sensitivity to fuel sulfur content increases with diesel particulate filters (DPFs) that require fuels with sulfur content levels below ~30 PPM and NO_x adsorber catalysts that need levels as low as ~3 PPM to continue to be effective [16].

3.5 Fuel Density

The density of diesel fuel affects emissions by describing the volumetric energy content of a fuel. Most hydrocarbon-based fuels have a lower heating value of about 44 MJ/kg. However, diesel fuels can have specific gravities ranging from 0.74 – 0.85. As fuel density increases, the volumetric energy content similarly rises. Since an engine's ECM is only calibrated to inject for a certain time, unless an engine is recalibrated when a different fuel is used, the mass of fuel energy injected will also change, being linearly dependent upon a fuel's density.

As such, reducing density decreases the mass of fuel injected into the cylinder. This can lead to reductions in NO_x and PM emissions due to lower cylinder temperatures and less fuel to turn into soot precursors. However, an engine's sensitivity to fuel density is also dependent upon its state of tune and the technology it uses to meet emissions standards. According to Lee et. al [35] the development of improved air-fuel mixing technology (common-rail system with higher injection pressures) and fueling strategies (pilot, main, and post injection, along with injection rate-shaping) has significantly reduced the influence of density on diesel emissions.

3.6 Summary of Fuel Property Impacts On Emissions

According to a 2001 ASME Spring Technical Paper [43], small changes in individual fuel properties result in only small benefits in modern heavy-duty diesel engines. However, the same paper argues that making multiple or large changes in fuel properties may provide for emissions reductions, paving the way for Fischer-Tropsch fuels. Fischer-Tropsch fuels embody almost all desirable fuel characteristics (low sulfur to reduce PM, high cetane number to reduce NO_x, and zero aromatic content to reduce NO_x). Thus, since multiple fuel properties change greatly, large emissions benefits can be seen, or achieved by enabling the use of advanced after-treatment systems. However, a fundamental understanding on the fuel effects of these and other premium fuels can only come from more detailed investigations at the combustion characteristics of each fuel type.

Chapter 4 Experimental Fuels

4.1 Base Number 2 Diesel Fuel

The No. 2 diesel fuel to create a performance and emission baseline was supplied by Fleetline, distributed by Dennis K. Burke Inc. Based on the product information brochure, this fuel is formulated with anti-oxidants to reduce volatility and prevent fuel degradation, inhibitors to fight gum and deposit formations in the fuel system, viscosity improvers for fuel injector lubrication and correct spray pattern, and additives for low-temperature operation. Although the base diesel fuel has a fuel-sulfur content of 400 PPM (see Table 4.1), it still meets the EPA Low-Sulfur Fuel requirement (<500 PPM). Also, since it meets the ASTM D 975 specifications for No. 2 diesel fuel, it should contain a high aromatic content, although no more than 35% as required by law (see Table 4.3). As this is a typical worst-case fuel currently allowed and available to on-road heavy-duty diesel engines, it should give a good baseline to compare the improvements seen when running with FT fuel.

The lower heating value of the No. 2 diesel fuel is not listed in the table provided by Fleetline. In order to compare the lower heating value of the No. 2 diesel fuel to the Syntroleum Fischer-Tropsch fuel used in the experiments, the lower heating value for an EPA No. 2 diesel fuel given by Syntroleum's S-2 brochure was used [54]. The value reported in the brochure is: $Q_{LHV,No.2}$ = 129,400 Btu/gal. Converting this to SI units on a mass basis requires the density of the fuel. Table 4.1 lists the API (American Petroleum Institute) gravity obtained using the ASTM D 287 method. The ASTM D 287 method lists API gravity at 16°C as:

Equation 4.1

$$API\,@16^{\circ}C = \frac{141.5}{s.g.@16^{\circ}C} - 131.5$$

Using the above equation and an average API gravity of 35, (34 –36 listed in Table 4.1), we get a fuel density of $\rho_{No.2}$ = 840 kg/m^3. Finally, converting the lower heating value appropriately leads to a lower heating value of $Q_{LHV,No.2}$ = 42.9 MJ/kg. This checks closely to data about general light diesel fuels listed as $Q_{LHV,No.2}$ = 43.2 MJ/kg in [2].

In order to make combustion-characteristic comparisons between No. 2 diesel and Syntroleum S-2 FT diesel, a simplified chemical composition of $CH_{1.8}$ and molecular weight of 170 g/mol [2] was used in order to write the ideal combustion equation (using the simplified chemical composition) for No. 2 diesel as follows:

Equation 4.2 $$12.3CH_{1.8}+\frac{17.835}{\phi}(O_2+3.773N_2)\rightarrow 12.3CO_2+11.07H_20+17.835\left(\frac{1}{\phi}-1\right)O_2+\frac{67.29}{\phi}N_2$$

Using Equation 4.2, the air/fuel ratio of No. 2 diesel fuel is 14.50:1.

4.2 Syntroleum Fischer-Tropsch Fuel

The Syntroleum Corporation provided the Fischer-Tropsch fuel (Syntroleum S-2) used in the experiments. Unlike the process outlined in Figure 1.5 and the synthesis-gas-production process described in Equation 1.2 that require pure oxygen, obtained from peripheral equipment that strip oxygen from the air, Syntroleum S-2 fuel is synthesized using the Syntroleum Process™ (see Figure 4.1), which consists of a special reformer (auto-thermal-reformer, ATR) that produces synthesis gas using untreated air. This reduces the overall production costs, making S-2 fuel economically marketable.

Due to the zero-sulfur content (not listed in preliminary specifications, but found in [54]) of the S-2 fuel, the lubricity properties of the fuel are low, increasing the likelihood of wear and tear in the fuel injection system. To pass lubricity tests, 300 PPM of a lubricity additive from Lubrizol was added to the fuel before shipping to MIT. The Lubrizol additive should not affect the combustion characteristics of the S-2 fuel. Lubricity additives contain polar groups that attracts to metal forming a thin surface film on the injector surfaces that are subject to wear [54].

Like many other FT diesel fuels available, the S-2 fuel has a combination of advantageous properties. The S-2 fuel has a very high cetane index (CNI = 74.4), zero aromatic content, and zero olefin content. Furthermore, it has a similar viscosity to No. 2 diesel, preventing any modifications to the fuel injection system to properly handle the fuel.

The lower heating value of Syntroleum S-2 was calculated using information from Syntroleum Corporation's product brochure and values listed in Table 4.2. The product brochure lists a lower heating value of $Q_{LHV,S-2}$ = 121,500 Btu/gal. Converting this to a mass basis with the S-2 density listed in Table 4.2 as r_{S-2} = 775 kg/m^3 results in a value of $Q_{LHV,S-2}$ = 43.7 MJ/kg.

Correspondence with Syntroleum provided further S-2 properties, necessary to do combustion calculations. The molecular weight of the FT fuel is 205 gm/mol with a chemical composition of 84.9% carbon and 15.1% hydrogen, with no other impurities detectable (i.e. oxygen and nitrogen). This composition gives a reduced chemical formula of $CH_{2.12}$ for the S-2 diesel fuel. Using this simplified composition, the ideal combustion formula for Syntroleum S-2 is:

Equation 4.3 $$14.49CH_{2.12}+\frac{22.17}{\phi}(O_2+3.773N_2)\rightarrow 14.49CO_2+15.36H_20+22.17\left(\frac{1}{\phi}-1\right)O_2+\frac{83.65}{\phi}N_2$$

Using the above equation nets an air/fuel ratio of 14.95:1 for Syntroleum S-2 diesel.

4.3 Fuel Property Comparisons

The heating value of a fuel gives the overall magnitude of the heat of reaction at constant standard conditions ($T_0 = 298$ K, $p_0 = 101.325$ kPa) for the complete combustion of a unit mass of fuel (as written in Equation 4.2 and Equation 4.3). Comparing the lower heating values of the two fuels shows that No. 2 diesel has less energy per mass of fuel compared to Syntroleum S-2 diesel, suggesting that the adiabatic flame temperature with No. 2 diesel should be lower than Syntroleum S-2 diesel even though the No. 2 diesel contains significant amounts of aromatics. However, the ideal-combustion equations and air/fuel ratios for the two fuels show that more air is required to burn a unit mass of Syntroleum S-2, reducing the adiabatic flame temperature since more products need to be heated in the case of the S-2 diesel. Based on a flame temperature correlation that uses a fuel's H/C ratio [48] and the first-law of thermodynamics, the adiabatic flame temperatures for the fuels are very similar (see Section 7.2.2 and Appendix C).

Table 4.1 Manufacturer's specifications for No. 2 diesel used in experiments.

FLEETLINE® **PRODUCT SPECIFICATIONS**

PREMIUM LOW-SULFUR DIESEL FUEL

TEST DESCRIPTION	ASTM METHOD	ASTM NO. 2-D STANDARD (D 975)	TYPICAL ANALYSIS
Cetane Number	D 976	40 min.	47
API Gravity at 16°C (60°F)	D 287	30 min.	37
Pour Point, °C (°F)	D 97	-7 (20) max.	-11 (12)*
Cloud Point, °C (°F)	D 2500	--	-10 (14)*
Flash Point (Pensky-Martens), °C (°F)	D 93	52 (125) min.	66 (151)
BTU/Gallon (gross)	--	--	139,200
Sulfur, Weight %	D 1552	0.05 max.	0.04
Viscosity, Saybolt, SUS at 38°C (100°F)	D 2161	32.6-40.1	34.5
Viscosity, Kinematic, cSt at 40°C (104°F)	D 445	1.9-4.1	2.52
Copper Strip Corrosion, 3 Hrs. @ 50°C (122°F)	D 130	3 max.	1
Distillation (Evap.), °C (°F)	D 86		
10% Recovered		--	206 (402)
50% Recovered		--	260 (500)
90% Recovered		282-338 (540-640)	335 (635)
End Point		--	353 (667)
Recovery %		--	98.0
Residue %		--	1.5
Loss %		--	0.5
Carbon Residue, Ramsbottom (10% Bottoms, Weight %)	D 524	0.35 max.	0.05
Water and Sediment, Vol. %	D 1796	0.05 max.	0.001
Ash, Weight %	D 482	0.01 max.	<0.001
Color (Visual)	--	--	Clear to Amber
Date Approved: 3/15/00 (Specification valid only if dated)			

Typical test data are average values only. Minor variations which do not affect performance may occur.

Table 4.2 S-2 fuel properties. Fuel used in experiments was from a preliminary run in Syntroleum's pilot plant.

Sample Data & Preliminary Product Specification — Syntroleum®

S-2 — RDIL 4047

S-2 is an additized, highly paraffinic, high-cetane distillate product suitable for use as a fuel cell fuel and in compression ignition engines. S-2 combustion emission characteristics are superior to petroleum-based diesel fuels.

SYNTHETIC DIESEL FUEL (CONTAINS ADDITIVES)

PHYSICAL PROPERTIES	TEST METHOD	UNITS	SPECIFICATION VALUE	TYPICAL VALUE	SAMPLE PROPERTIES
Specific Gravity, 15°C	ASTM D-4052	°C		0.771	0.775
API	ASTM D-4052	°		52.0	51.1
Flash Point	ASTM D-93	°F, (°C)		148, (64)	142, (61)
Cloud Point	ASTM D-5771	°F, (°C)		<0, (<-18)	-13, (-25)
Color	ASTM D-1500			L0.5	L0.5
Viscosity	ASTM D-445	cSt @ 40°C		2.1	2.2
		cSt @100°C		1.0	1.0
Copper Strip	ASTM D-130			1a	1a
Bromine Index	ASTM D-2710	mg/100g			179
Cetane Index	ASTM D-976			>74	74.4
Distillation, IBP, vol%	ASTM D-86	°F(°C)		320 (160)	347 (175)
10		°F(°C)		390 (199)	395 (202)
50		°F(°C)		493 (256)	487 (253)
90		°F(°C)		601 (316)	601 (316)
FBP		°F(°C)		662 (350)	648 (342)
Ash	ASTM D-482	wt%		<0.001	
Aromatics	ASTM D-1319	vol%		nd*	
Olefins	ASTM D-1319	vol%		nd*	
Saturates	ASTM D-1319	vol%			
Carbon Res.	ASTM D-524	wt%		nd*	
Total Insolubles		mg/100ml		0.0	
Lubricity	ASTM D-6079	mm		<0.37	

*nd indicates Not Detectable by the prescribed test method. Result is either below method detection limit or outside of method range.

Health and Safety: The product(s) described herein may require precautions in handling and use. If deemed necessary, Material Safety Data Sheets (MSDS) for Syntroleum products are included with this document. You may also obtain this information by visiting our website or writing to us at the address below. Always consult the Material Safety Data Sheet for products you consider using.

Contact: Syntroleum
1350 South Boulder Avenue, Suite 1100
Tulsa, OK 74119-3295
www.syntroleum.com

Table 4.3 ASTM D 975 requirements for diesel fuel oils.

ASTM D 975 Requirements for Diesel Fuel Oils

Property	Test Method*	Low Sulfur No. 1-D	No. 1-D	Low Sulfur No. 2-D	No. 2-D	No. 4-D
Flash point, °C, min	D 93	38	38	52	52	55
Water and sediment, % vol, max	D 2709 D 1796	0.05	0.05	0.05	0.05	0.50
Distillation temperature, °C, 90% vol recovered min max	D 86	 288	 288	 282 338	 282 338	
Kinematic viscosity, 40°C, cSt min max	D 445	 1.3 2.4	 1.3 2.4	 1.9 4.1	 1.9 4.1	 5.5 24.0
Ash, % mass, max	D 482	0.01	0.01	0.01	0.01	0.1
Sulfur, % mass, max	D 2622	0.05	0.50	0.05	0.50	2.00
Copper strip corrosion, 3 hr at 50°C, max rating	D 130	No. 3	No. 3	No. 3	No. 3	
Cetane number, min	D 613	40	40	40	40	30
One of the following: 1) Cetane index, min 2) Aromaticity, % vol, max	 D 976 D 1319	 40 35		 40 35		
Ramsbottom carbon residue on 10% distillation residue,	D 524	0.15	0.15	0.35	0.35	

* All "Dxx" methods are ASTM standards.

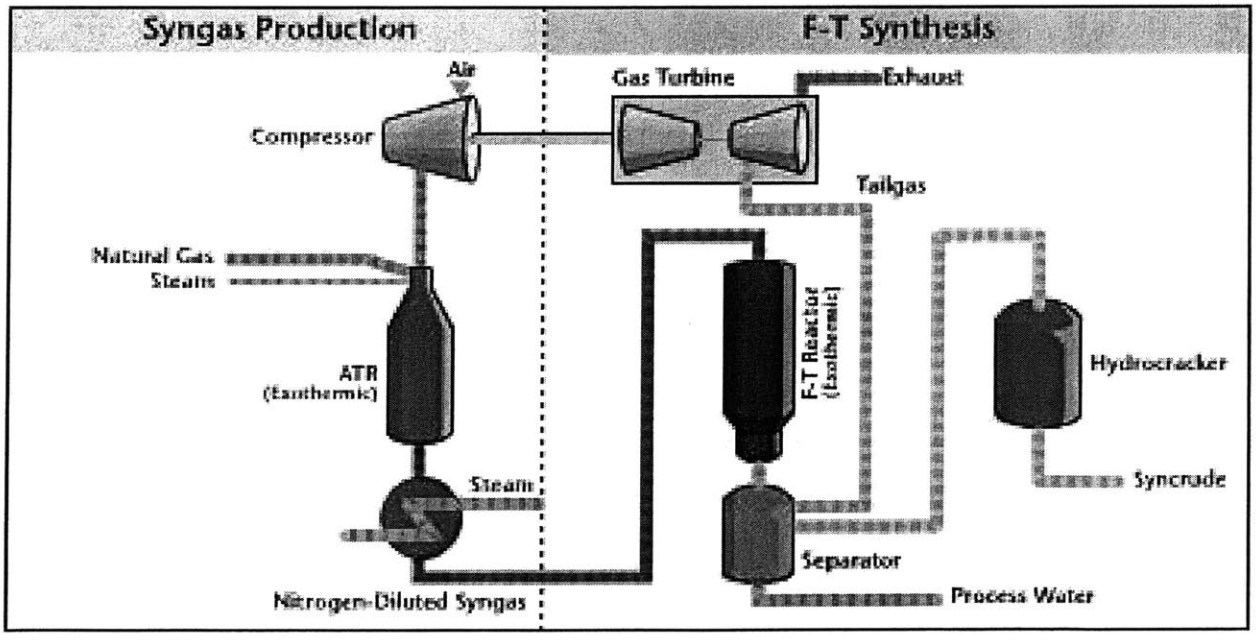

Figure 4.1 The Syntroleum Process™, showing the production of synthesis gas with just air. Available at www.syntroleum.com

Chapter 5 Experimental Setup

5.1 Engine

Cummins supplied a close-to-production development engine based on the model year 2002 (MY02) ISB 300. The ISB 300 is a turbocharged, 6-cylinder, 5.9-liter direct injection diesel engine. The engine is rated at 224 kW (300 hp) at 2500 RPM and 890 N-m (660 lb-ft) at 1600 RPM. In order to meet 2002 EPA standards, the engine has advanced subsystems like a Bosch common-rail fuel injection system, Holset variable geometry turbocharger, and cooled-EGR system. To control these devices, the ISB 300 has an electronic control module (ECM) (version CM 850) that has been calibrated to meet emissions when operating with an EPA No. 2 diesel fuel. Table 5.1 contains further detailed information of engine specifications and geometry.

To control load, a Watlow Series 96 process controller was wired into the engine's ECM. The ECM expects voltages between 0.5 ± 0.25 VDC at idle and 3.75 ± 0.25 VDC at wide-open throttle, so the 0 – 5 VDC process output on the Watlow controller was connected to the appropriate pins on the ECM.

The engine was left mostly in stock form. No provisions were installed to pre-heat the oil or coolant since the engine can be motored and warmed up relatively quickly. Powering the engine's subsystems are two Interstate Batteries Workaholic Model 8D-MHD (12VDC, 1440 CCA) commercial batteries hooked in series. A Charles Industries Ltd. Model 5000 battery charger supplies continuous current to the batteries when the engine is running and charges the batteries when the engine is off.

5.2 CalTerm

The pre-production ISB 300 engine came equipped with an unlocked ECM, allowing for engine calibration changes and real-time monitoring and modification of engine parameters. To communicate and link to the engine's ECM, Cummins provided their in-house software, CalTerm (Calibration Terminal) version 7.63. Once the engine was installed, the stock 300-horsepower calibration, based on No. 2 diesel and provided by Cummins was uploaded into the ECM. This was done to ensure the engine would run on the 2002 EPA-emission-certified performance maps.

CalTerm allows for the monitoring and modification of hundreds of engine parameters. The important parameters modified in the experiments include the start of main injection and EGR fraction. The response time after commanding an injection timing change is trivial, since the electronic control of fuel injection with the common-rail system provides a response time dependent only upon the speed of the signal from the ECM. For adjustments to the EGR fraction, changes take a few seconds to settle (if it

settles at all) since the ECM tries to find the best path to move to a different state. The coupling of engine load, turbine inlet pressure, turbine exhaust backpressure, intake manifold boost pressure, and EGR valve position required the ECM to optimize changes to prevent the system from reaching an unstable state. One last commanded parameter that was changed enabled cylinder cut out. During engine shakedown and TDC determination (see 5.4.1.1), the engine parameter FSI_x_ExtCylMask_c was set to 001F (hexadecimal representation of cylinder 6) in order to cut fueling to the cylinder so that motoring pressure traces could be recorded.

Various other parameters were monitored and logged, including charge flow, pilot injection quantity and timing, post injection quantity and timing, and common-rail accumulator pressure.

5.3 Dynamometer Setup and Dynamometer Controller

A Digalog AE 250 eddy current dynamometer, able to absorb up to 250 kW, was used to load the engine. The dynamometer came instrumented with thermocouples monitoring the temperatures of the inner and outer loss plates along with the two bearings supporting the load shaft. A Maywood Instruments U4000, 500 kg load cell measures torque by resisting the rotation of the outer casing. A differential pressure switch on the cooling-water outlet protects the dynamometer from failing if the cooling water supply happens to shut off. Before the dynamometer was able to operate properly, the load cell wiring was redone to match the factory settings and one side of the differential pressure switch's diaphragm was exposed to ambient conditions such that a pressure difference would be detected. Initially, both pressure taps were monitoring the same pressure.

Connecting the engine to the dynamometer is a driveshaft assembly made with two Spicer 1710 Series flange yokes attached to a 4" O.D. tube. The flange yokes are rated to withstand up to 1220 N-m at steady state or spikes of up to 6500 N-m. The driveshaft is installed at about an 8° to relieve stresses in the flange yokes as they rotate.

On the dynamometer side, the Spicer flange yoke bolts directly to the flange on the dynamometer's load shaft. The flange on the dynamometer has a pilot surface that centers the driveshaft. Drilled-body grade 8 bolts were used along with cotter pins and castle nuts in order to provide a safe, positive-lock system. On the engine side, a Voith Küsel flexible coupling was first attached to the engine's flywheel. The Voith Küsel flexible coupling is designed to absorb torque fluctuations and prevent the rotating system from reaching a point of resonance that could lead to component failures in the driveshaft, flanges, or dynamometer. One side of the Voith Küsel coupling bolts directly to the engine's SAE 11-1/2 flywheel. Drilled head bolts were connected in pairs with 0.032" O.D. safety wire to again provide a positive-lock system. The other side of the coupling has a DIN 150. An adapter plate was machined to mate the Spicer 1710 flange yoke and DIN 150 flange on the flexible coupling.

A Digalog Model 1022A-STD dynamometer controller was used to control engine speed while reading out the load from the Maywood Instruments load cell. The PID settings in the dynamometer controller were also adjusted to reduce load fluctuations when the commanded throttle setting changes. Before any tests were run, the controller and dynamometer were calibrated at two points, the 50% and 100% loads of the engine.

5.4 Data Acquisition System

A full complement of National Instruments data acquisition (DAQ) hardware and software was used to measure and record various temperatures, pressures, and flows. The heart of the system is the high-speed DAQ board, a National Instruments PCI-6024E. This board can read up to 200,000 samples per second. The high-speed DAQ board is limited to 16 single-ended channels (signals with a common ground) or 8 differential channels (signals with separate grounds). In order to get around this limitation, an SCXI-1000 multiplexing chassis was also used. The SCXI-1000 chassis can house up to 4 special modules, containing various signal amplification, isolation, and noise suppression circuitry. The multiplexing chassis works by quickly scanning, one after another, all the channels of each module installed streaming the data into one differential channel of the DAQ board.

A special 32-channel module for thermocouples (SCXI-1102B) containing a fixed low-pass filter of 200 Hz was installed into the multiplexing chassis. The SCXI-1102B allows for gain and filter settings to be programmed on a per-channel basis. Most slow-speed signals were connected to this module. Attached to the SCXI-1102B is a TBX-1303 terminal block. The TBX-1303 provides a convenient location for the sensors to wire into while also containing a cold-junction-compensation sensor to provide a reference voltage to correctly scale any thermocouples plugged into the terminal block. A general 32-channel module (SCXI-1100) was used for mixed measurements. This module has user-selectable low-pass filter settings (4 Hz, 10 kHz, and no filter) that apply to all channels. Since high-speed cylinder measurements (see Section 5.4.1) were recorded through this module along with various slow-speed signals, the 10 kHz filter setting was used to provide some noise filtering while preventing the possibility of introducing phase errors into the high-speed signals due to poor low-pass filter response. Another TBX-1303 terminal block is attached to the SCXI-1100 module to facilitate sensor wiring.

5.4.1 High Sampling Rate Measurements

High-speed measurements taken during the experiments consisted of in-cylinder pressure, intake manifold pressure, and engine-position-indexing signals. Since in-cylinder pressures in a diesel engine can rise very rapidly after the autoignition event, a high-resolution crank-angle encoder was installed onto the tone wheel to act as an external clock to the DAQ system. An 1800-pulse-per-revolution BEI encoder

provides a 0.2° resolution for the high-speed data. The BEI encoder also has another channel that gives out one digital pulse per revolution. This once-per-revolution signal was used to trigger the high-speed DAQ measurements, ensuring the data recording started at the same point of an engine revolution, although not always on the same stroke. This removed the need to superimpose a reference signal to the cylinder pressure data.

The pre-production ISB 300 engine installed at MIT was actually used at Cummins to perform development work on the engine currently available on the market. When the engine was shipped to MIT, an AVL QC33C heavy-duty pressure transducer was already installed in cylinder number 6 (cylinder closest to flywheel). The QC33C is a quartz, piezo-electric pressure transducer that is actively liquid-cooled to reduce the effects of thermal shock. A Bernard Model 2500SS MIG welder cooler is plumbed into the pressure transducer and circulates and cools a 50:50 mixture of distilled water and ethylene glycol. The transducer's small current output is converted to a voltage using a Kistler Model 5010B charge amplifier. The charge amplifier's output is fed into the DAQ system.

Since piezo-electric pressure transducers only measure changes in pressure, a method of referencing the pressure is required. The intake manifold pressures recorded along with the in-cylinder pressure provide a value to peg the cylinder pressure. The in-cylinder pressure signal is usually averaged around BDC and then scaled to equal the intake manifold pressure.

In order to provide precise fueling, the engine's ECM not only must know where the pistons are in relation to TDC, it also needs to differentiate which aspect of the four-stroke cycle each piston is going through. To provide engine-position data, the engine has Hall-effect sensors on both the camshaft and tone wheel. The tone wheel is a 60 (-1) design, originally containing 60 equally spaced teeth with one removed to provide a point of reference. The signal from the tone-wheel sensor was also fed into the DAQ system to check the phasing of the in-cylinder pressure signal.

5.4.1.1 High Sampling Rate, Crank-Angle Resolved Data Integrity

The proper phasing of in-cylinder pressure signals is important if further analyses such as IMEP calculations are done with the data. Various checks are available to test for the proper phasing of the data, such as the linearity of the compression and expansion stroke curves in log-P vs. log-V graphs and confirmation that the two curves do not cross each other.

Cummins engineers suggested two ways to correctly phase the start of high-speed data recording with respect to TDC. The first suggestion was to adjust the crank angle encoder such that the reference signal on the tone wheel (the point where the signal goes from high to low after the missing tooth) occurs 60.0° bTDC. Another suggestion was to find the peak pressure during a motoring pressure trace (see Section 5.2 for cylinder cut-out information), then add 0.4° due to heat transfer and blow-by effects. A

combination of both techniques was used to check both methods. Initially, the first suggestion was tried, and the crank angle encoder was adjusted such that the high-to-low transition following the gap occurred at 300° as TDC intake was chosen as 0° (see Figure 5.1). Triggering the crank-angle encoder with this setup resulted in a peak motoring pressure at 361.2° with the addition of heat transfer and blow-by giving an actual engine-TDC of 361.6° (see Figure 5.2). Although the peak pressure occurred 61.2° after the reference signal, this is still within the anticipated uncertainty of the tone-wheel/crankshaft sensor setup.

With the knowledge of the correct phasing of engine-TDC and the crankshaft reference signal, the crank-angle encoder was finally adjusted such that engine-TDC occurred at 360.0°, as everything is referenced with TDC intake as 0.0°. This necessitated encoder adjustments such that the crankshaft reference signal occurs at 298.4°, or 61.6° bTDC (see Figure 5.3). Motoring pressure traces were tested with this final crank-angle encoder setup as a last check for correct phasing. The log-pressure versus log-volume curve is found in Figure 5.4.

Figure 5.4 shows the motoring pressure trace results in linear sections during the compression and expansion stroke. The slope of each line corresponding to the compression and expansion stroke provides the ratio of specific heats of the gas during each process. The ratio of specific heats are: $\gamma_{compression} = 1.297$ and $\gamma_{expansion} = 1.334$. The exhaust process has a higher ratio due to heat transfer and mass loss through blow-by. Also, the compression and expansion lines do not cross, revealing the data is not out of phase in the advanced direction. Thus, Figure 5.4 shows the pressure data is correctly phased. If the pressure data is off, the amount of crank-angle phase error can be determined by examining where the reference signal occurs, and the data can be offset accordingly.

5.4.2 Low Sampling Rate Measurements

The test engine and dynamometer is heavily instrumented with various thermocouples and transducers. Table 5.2 lists the type of sensor, its location in the test setup, and which channel and module it is connected to. The following sections provide further details about special sensors used during the experiments.

5.5 Fueling System

To measure fuel flow, two Exact Flow Model EFM84 single-rotor turbine flow meters are used, one measuring fuel supplied to the lift pump that supplies the high-pressure common-rail fuel pump, and the other measuring fuel returning to the fuel tank. Each flow meter has an Exact Flow IFC-14 flow computer calibrated with fuel flow rates versus fuel viscosity. Temperatures from a thermocouple in the flow meter allow the flow computer to correctly read out fuel flow even as fuel temperatures fluctuate. To help keep fuel temperatures steady, a liquid-liquid heat exchange was installed upstream of each fuel

flow meter. Exact Flow provided flow computer calibrations for each fuel based on viscosity information from the specification sheets show in Chapter 4 The stock fuel filter on the engine was retained so no filter elements were installed upstream of the flow meters.

In order to prevent cross contamination of sulfur and aromatics between the two fuels used in the experiments, two 22-gallon ATL Inc. SP122B racing fuel cells were installed on the engine test bed. Two bulkhead connections near the engine allow switching between the individual fuel tanks. Another bulkhead allows for fuel to bypass the return system in order to drain the entire system or purge standing fuel in various fuel galleries in the engine when changing fuels. The entire fuel system uses Teflon lines since diesel fuel is a strong solvent, while stainless-steel overbraids over the Teflon protect them from physical wear and tear.

5.6 Intake Air Measurement and Preparation

An Eldridge Products, Inc. Series 8732 thermal mass flow meter measures airflow into the turbocharger's compressor inlet. The inline-style flow meter consists of a sensing element, installed into a flow section. The flow section has a laminar flow element to ensure fully developed flow by the time the air reaches the sensing element. The sensing element uses two RTDs (resistance temperature detector) to measure airflow. One RTD measures the temperature of the incoming. The second RTD is forced through self-heating to maintain a constant temperature above the incoming gas. The sensing element's signal processor takes both the required current to heat the second sensor and the initial temperature read by the first RTD to calculate the mass of air flowing through the flow section. A K&N paper filter fitted upstream of the thermal mass flow meter filters the ambient air in the test cell before it flows into the engine.

After being compressed by the turbocharger, the pressurized air leaving the turbocharger is extremely hot. To reduce peak pressures in the engine, the compressed air is cooled once it leaves the compressor. A Spearco Universal Air/Liquid Intercooler was used to cool the fresh charge leaving the turbocharger. The amount of charge-air cooling is controlled by a gate valve on the liquid side of the charge-air cooler that controls the flow of water through the core of the charge-air cooler. Connections between the engine and aftercooler are made with 3" I.D. silicone rubber hose, capable of withstanding temperatures up to 450 K.

5.7 Gaseous Emissions Analyzers

A Thermo Environmental Instruments (TEI) Model 42C-HL (High Level) chemiluminescence analyzer was used to measure the oxides of nitrogen from various sample streams. For engine-out NO_x, a

sample point about 30" away from the closest exhaust elbow (54" total distance from turbine exhaust) was installed. This point is about 10 pipe diameters away from the elbow, ensuring fully developed flow at the sample point. For intake-mixture NO_x (for EGR fraction calculations), a sample point 4" downstream from the closest elbow (12" from EGR valve) was installed. The intake sample point was installed in the middle of the intake air heater, the heating elements within the flow stream acting as guide vanes, helping to distribute the flow uniformly. For dilution ratio measurements, a sample point was installed about 30" away from the transfer tube, again ensuring fully developed flow at the sampling point. To calibrate the Model 42C-HL, a calibration gas of 998 PPM of NOx and zero gas of pure N_2 was used to create a linear voltage output between the two concentrations. This output of is fed into the DAQ system, and the voltage read is converted back to a PPM concentration and recorded. For the chemiluminescent reaction, pure oxygen is fed into the meter, converted to ozone, and then used in the reaction chamber. The Model 42C-HL was kept on the 0 – 1000 PPM range for all tests.

The TEI Model 42C-HL uses a Vacuubrand MD4 three stage, four head diaphragm pump to provide the proper vacuum for the reaction chamber. Also, to prevent clogging the capillary tubes inside, a Universal Analyzers Model 530SS single channel sample cooler is used to condense out any water in the exhaust stream. The sample chiller uses a thermoelectric cooler operating on the Peltier effect to bring gas temperatures down to about 4.5° C, removing most of the water that can condense within the temperatures found in most gas analyzers. Thus, all NO_x measurements are on a dry exhaust basis.

To measure hydrocarbon emissions, a California Analytical Instruments (CAI) Model 300-HFID was installed. The Model 300-HFID was calibrated with 300 PPM propane (C_3H_8), so the effective range was 0 – 900 PPM of C_1. During experiments, the Model 300-HFID was left on the 0 – 30 PPM range since HC emissions from diesel engines are low. To measure HC, a flame ionizes the sample stream and electrodes in the instrument measure the particles. The flame in the Model 300-HFID is fueled by HC-free air and a fuel mixture of 40%/60% H_2/He.

The Model 300-HFID takes gas samples from the same points as the Model 42C-HL. All engine and dilution sample points are connected to a bulkhead holding various 3-way valves to switch between various sample points. The engine-out gas stream is transferred to the bulkhead using a 25' heated sample line while the two cooler sample points use stainless-steel-overbraid Teflon tubes. All samples from the bulkhead are moved using a 10' heated sample line to a Universal Analyzers Model 270S heated stack filter that removes any large particulate matter that can also clog sample and capillary tubes within the gas analyzers. To move the gases through all the filters and gas analyzers, two vacuum pumps were used. With the engine-out and intake samples, the gases are above atmospheric pressure, requiring a less-robust vacuum pump to move samples. A Gast Model IVAF-10-M100X rotary-vane vacuum pump was first used in these applications. However, the flow rate with this pump was not sufficient to supply the

sample requirements for both gas analyzers. An Air Dimensions Incorporated (ADI) Model 01620TC high-vacuum, double-head diaphragm vacuum pump was installed in series with the Gast pump to increase sample flow rates and reduce the lag time when changing between sample points. The two heads on the ADI vacuum pump were connected in series, effectively giving the system a three-pump arrangement.

5.8 Mini Dilution Tunnel

The EPA defines particulate matter as all solid matter and condensable species that can be collected on a paper filter from a diluted exhaust sample held at no higher than 52°C [49]. The EPA defines particulate matter in such a way since it forces the sampling system to employ some form of a dilution tunnel that helps simulate particle transformations (i.e. agglomeration, adsorption, and nucleation) that would normally occur outside of the laboratory. Dilution tunnels can be designed to condition the entire exhaust flow or can be arranged in such a way as to only take and dilute a small sample of the exhaust.

The mini dilution tunnel used with the experimental setup is based on the dilution of a fraction of the exhaust stream. The dilution tunnel is predominantly made of 3" O.D. stainless steel 304 tubing. The exhaust gas sample is transferred, due to a positive pressure differential, through a ¾" O.D. tube with a high-temperature resistant ball valve in place to regulate exhaust gas flow. The transfer tube introduces raw exhaust into the dilution tunnel 30" away from the sample point, allowing the dilution air and raw exhaust to mix and become fully developed before being sampled. The pressure in the dilution tunnel is held below atmospheric conditions by connecting the exit of the dilution tunnel to the intake of a Spencer Model 1001-½SS blower. As air is drawn through the mini dilution tunnel, the pressure drops due to losses within the tubing. A Solberg FS-31P-250 air filter holder with a HEPA filter element is installed at the inlet of the dilution tunnel system, providing an additional pressure drop within the tunnel. The dilution ratio is measured by comparing the NO_x readings in the tunnel to the NO_x readings in the raw exhaust.

5.9 Gravimetric Particulate Matter Sampling System

The gravimetric particulate matter sampling system used to sample raw and dilute gas samples employs a Pall Corporation stainless steel 47mm filter holder that housed Pall Corporation Pallflex® Fiberfilm glass filters (Model T60A20-47 MM). Made with borosilicate glass fibers and a moisture-resistant fluorocarbon (TFE) coating, the Pallflex Model T60A20 brand of filters resist moisture uptake and prevent moisture-gas reactions, eliminating the need for lengthy drying times when using normal

hygroscopic glass fiber filters. As such, the EPA recommends the Model T60A20 brand of filters for use in gravimetric filter measurements [50]. The Model T60A20 filters can also withstand very high temperatures, up to 315.5°C, making it ideal for raw exhaust gas sampling as well.

To measure sample flow through the filter, an Omega FVL-1611 volumetric flow meter was installed downstream of the filter/filter holder assembly. The Omega FVL-1611 sensor body houses a differential pressure transducers, a thermocouple, and a laminar flow element that the flow computer uses to measure flow rates up to 250 SLPM. The flow computer output is fed into the National Instruments DAQ system, so flow rates over time can be recorded, then averaged. This helps account for the variation in flow rates as the filter paper is loaded. A Millipore Model 6675 piston-driven vacuum pump was used to draw the raw or dilute sample through the sampling lines, filter paper, and mass flow meter. To prevent condensation of particles on the walls with raw exhaust samples, the stainless steel lines from the raw exhaust sample point were insulated with silicon-rubber based tubing insulation. Also, a rope heater was installed from the sample point to a position 5 feet downstream.

To weigh filtered samples, an Ohaus Explorer E11140 microbalance, accurate to 0.1 mg was used. It was left on for at least one hour to warm up before any filters were weighed.

5.10 SMPS System

For a detailed description of the Scanning Mobility Particle Sizer (SMPS) system, see Hallgren [51]. Backgrounds scan with and without the HEPA filter installed upstream of the dilution tunnel is found in Figure 5.6, showing the effectiveness of the HEPA filter. Other than the HEPA filter, no other dilution-air preparation was done.

Due to the short supply of FT fuel available (one 55-gallon drum), no runs with the SMPS system were recorded when the data presented in Chapter 7 was recorded. However, since the test engine has an EGR system, some characterizations of the effects of EGR on PM size distribution were done with No. 2 diesel while the test setup was being shaken down. Please see Section 7.2.3 for a discussion of these scans.

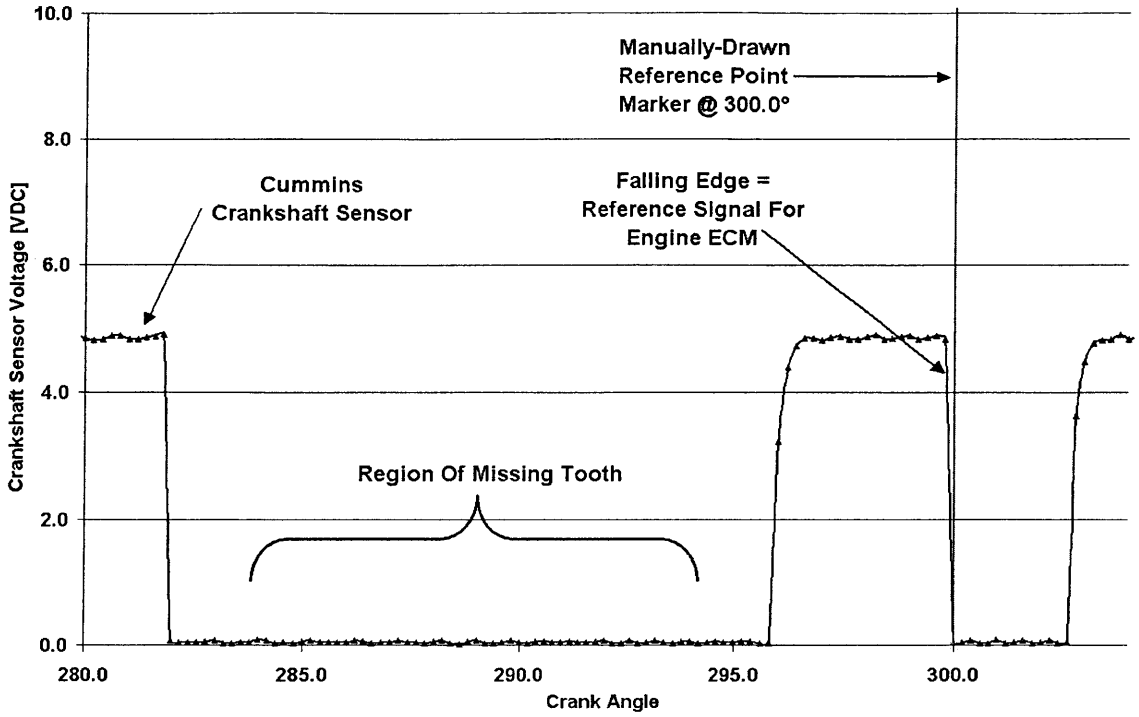

Figure 5.1 Initial adjustment of crank angle encoder to test for TDC. Reference signal from encoder believed to be 60° bTDC. Encoder was set to trigger data acquisition 60° bTDC such that TDC lined up with 360.0°.

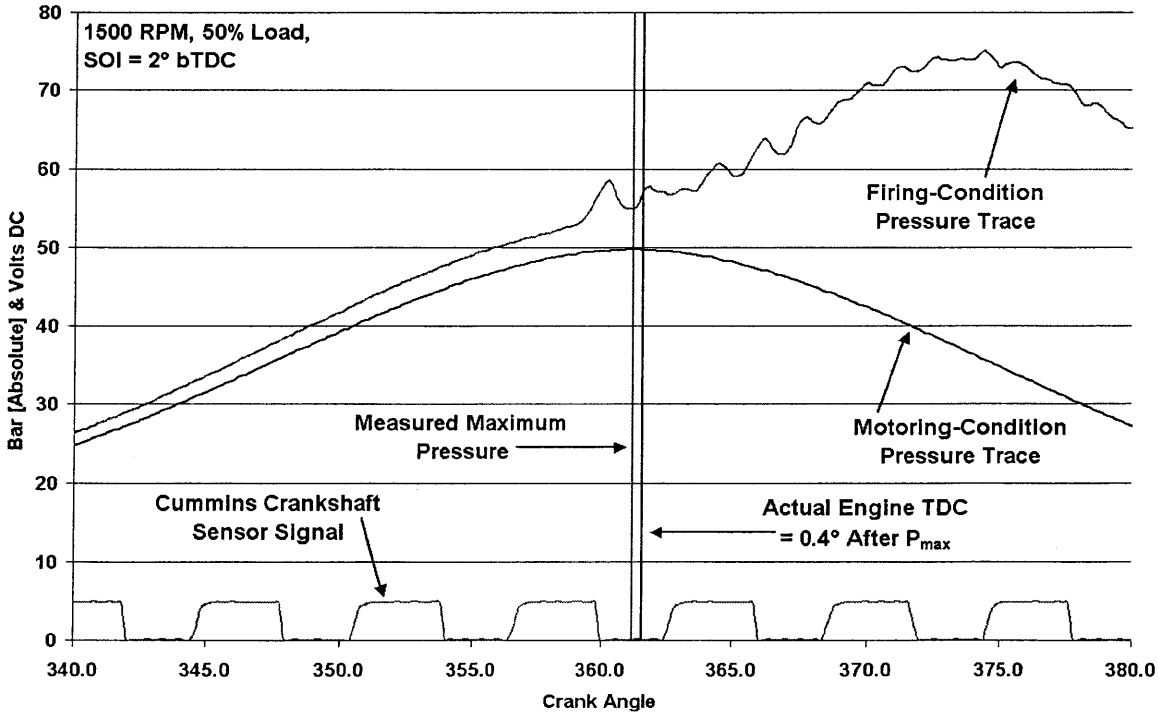

Figure 5.2 Firing- and motoring-pressure traces with crank-angle encoder triggered to start data acquisition such that crankshaft reference signal occurs 60° bTDC. Tests show reference signal is near the expected value and within the anticipated uncertainty.

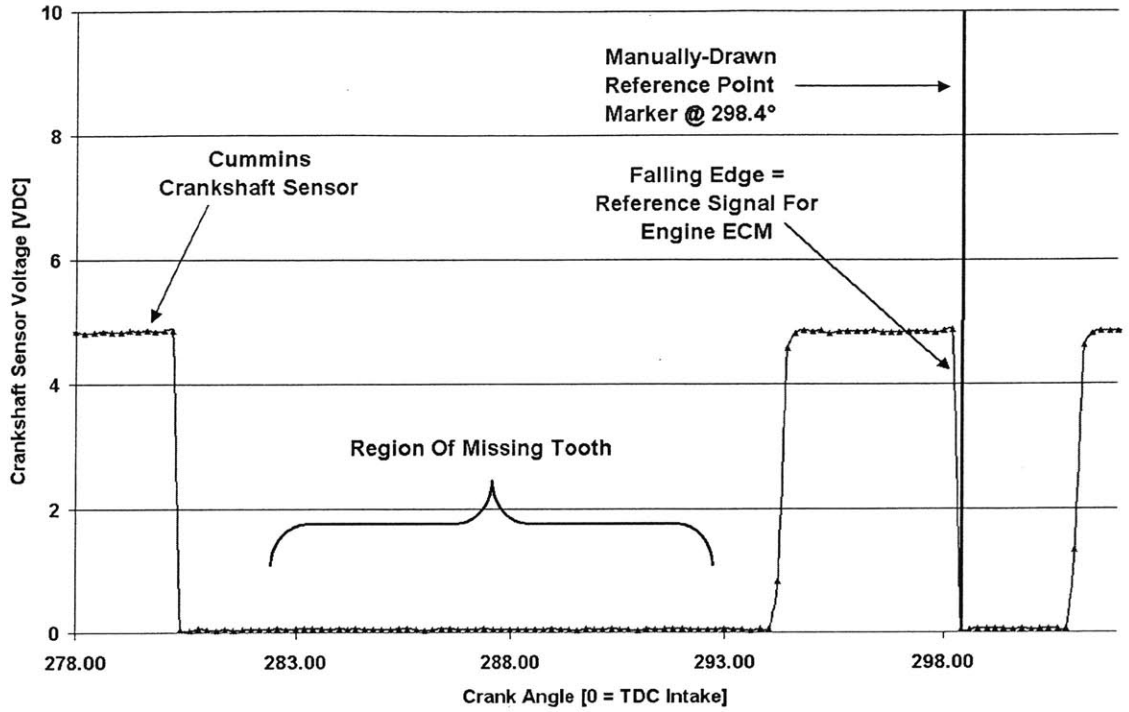

Figure 5.3 Final crank-angle encoder adjustment to set engine TDC on compression stroke to be 360.0° after start of data-acquisition.

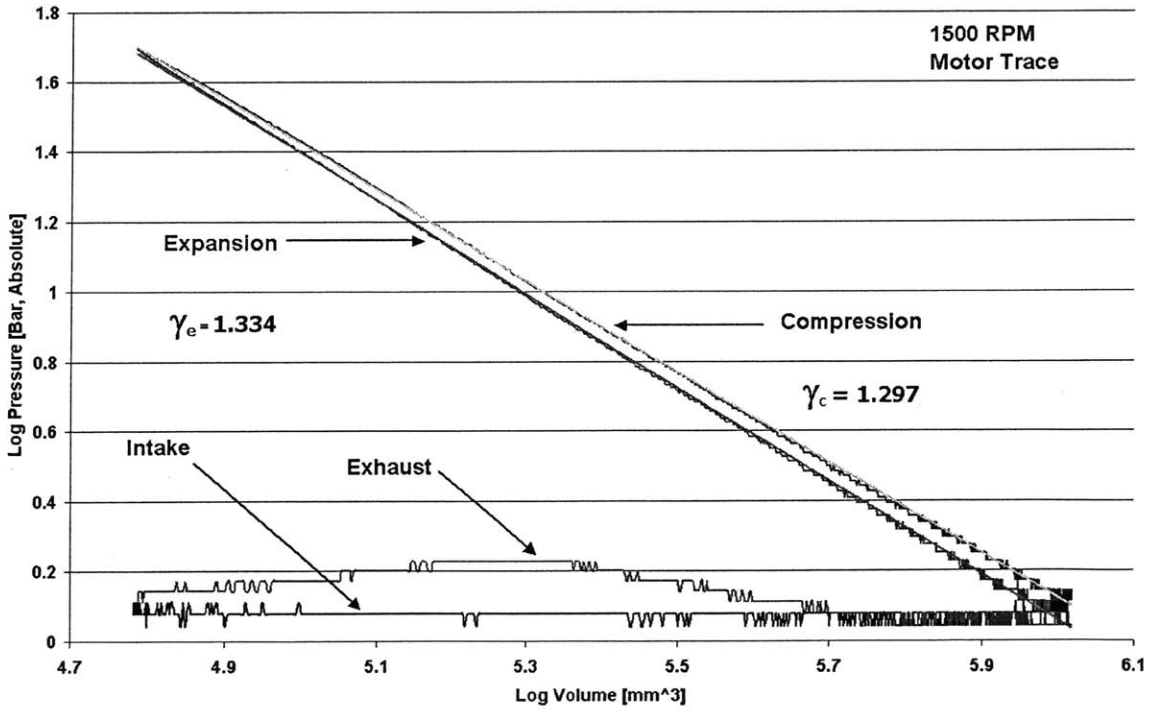

Figure 5.4 Log-pressure versus log-volume of motoring pressure trace with correct phasing. Pressure trace taken from cylinder running at 1500 RPM, 50% load before fuel was cut. Reference signal from crankshaft sensor must be at 298.4° aTDC intake, or 61.2° bTDC compression for correct pressure-data phasing.

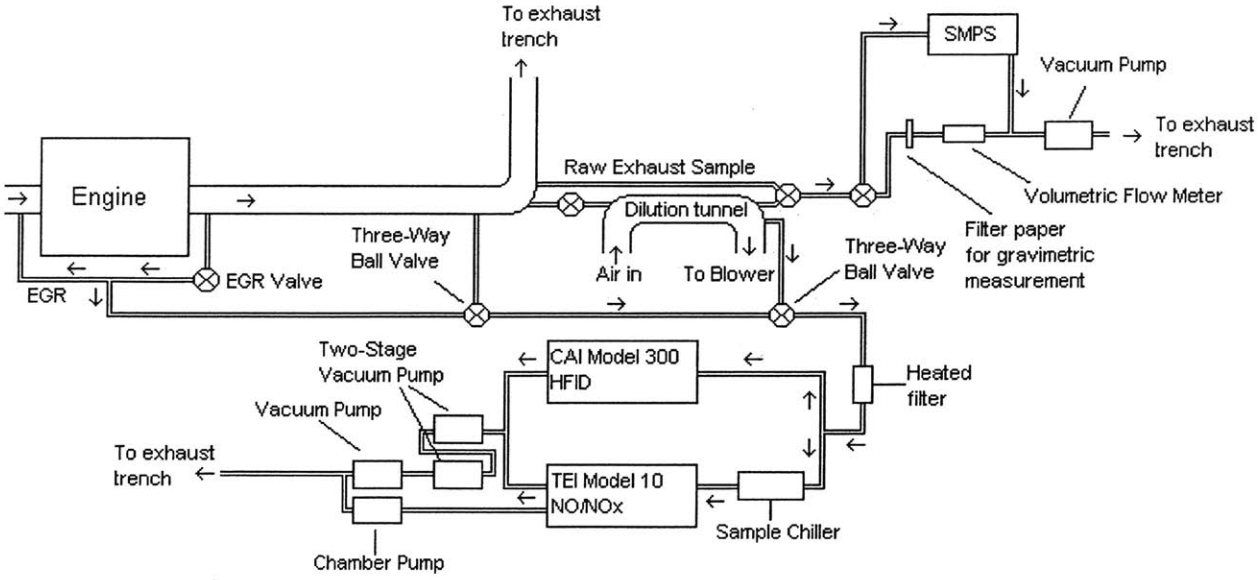

Figure 5.5 Emission sampling system schematic.

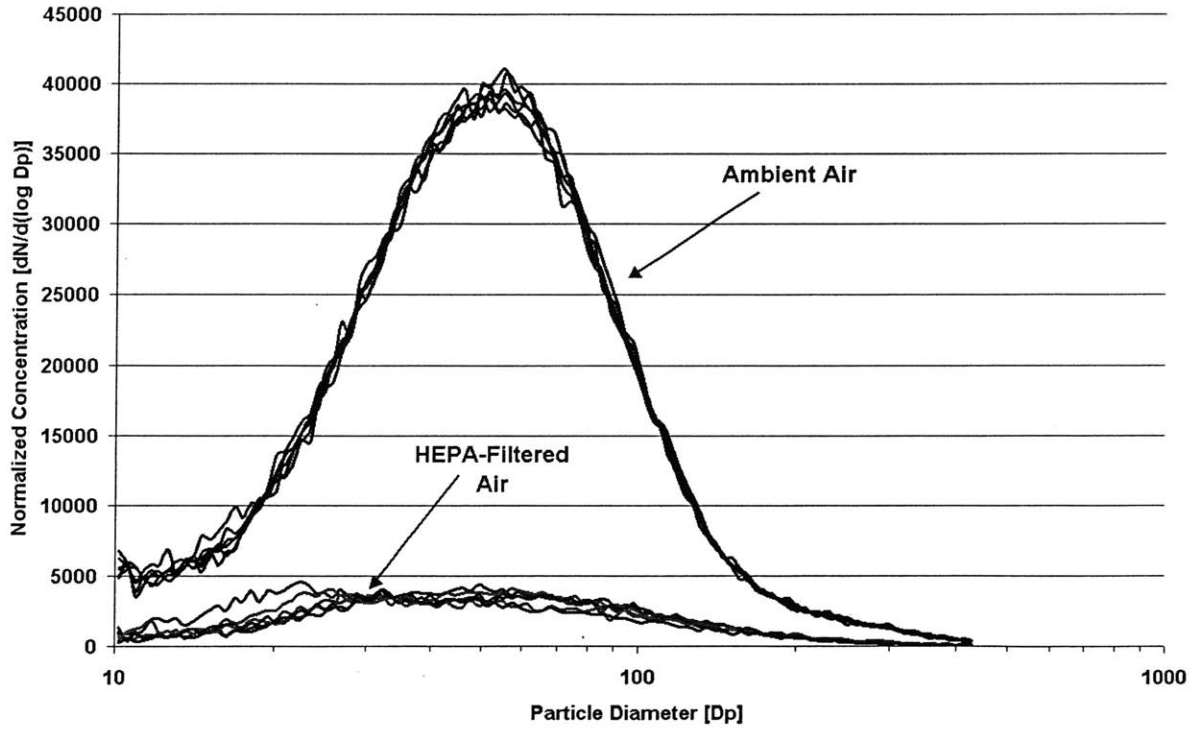

Figure 5.6 SMPS background scans with and without the HEPA filter installed.

Table 5.1 Pre-production ISB 300 engine details.

Model	Cummins ISB 300
Number Of Cylinders	6
Combustion System	Direct Injection
Aspiration	Turbocharged
Stroked (Displaced) Volume [liters]	5.9
Bore [mm]	102.02
Stroke [mm]	120
Connecting Rod Length [mm]	192
Crank Radius [mm]	60
Compression Ratio	17.2
Valve Timing	IVO = 9.5° bTDC | IVC = 23.5° aBDC
	EVO = 142.0 °aTDC | EVC = 18.0° aTDC
Injection Nozzle	O.D. = 158 μm, L = 1.00 mm
	8 Sac-less (VCO) Nozzles Per Injector

Table 5.2 Sensor, sensor location, and module/channel it is wired to.

DAQ Measurement	Instrument Type	Module 1	Module 4	PCI-6024E
Cylinder 1 Exhaust TC	Type K TC	0	N/A	N/A
Cylinder 2 Exhaust TC	Type K TC	1	N/A	N/A
Cylinder 3 Exhaust TC	Type K TC	2	N/A	N/A
Cylinder 4 Exhaust TC	Type K TC	3	N/A	N/A
Cylinder 5 Exhaust TC	Type K TC	4	N/A	N/A
Cylinder 6 Exhaust TC	Type K TC	5	N/A	N/A
EGR TC - Before Cooler	Type K TC	6	N/A	N/A
EGR TC - After Cooler	Type K TC	7	N/A	N/A
Heat Exchanger - City Water Out	Type K TC	8	N/A	N/A
Heat Exchanger - Engine Coolant In	Type K TC	9	N/A	N/A
Turbine Outlet TC	Type K TC	10	N/A	N/A
Intake Manifold TC	Type K TC	11	N/A	N/A
Exhaust Manifold TC	Type K TC	12	N/A	N/A
Coolant Reservoir TC	Type K TC	13	N/A	N/A
Heat Exchanger - Engine Coolant Out	Type K TC	14	N/A	N/A
Heat Exchanger - City Water In	Type K TC	15	N/A	N/A
Engine Block Oil TC	Type K TC	16	N/A	N/A
Compressor Outlet TC	Type K TC	17	N/A	N/A
Fuel Supply TC	Type K TC	18	N/A	N/A
Dynamometer TC - Inner Loss Plate	Type K TC	19	N/A	N/A
Dynamometer TC - Outer Loss Plate	Type K TC	20	N/A	N/A
Dynamometer TC - Bearing #1	Type K TC	21	N/A	N/A
Dynamometer TC - Bearing #2	Type K TC	22	N/A	N/A
Dynamometer Water Pressure	Pressure Transducer	23	N/A	N/A
Exact Flow Fuel Flow Meter - Return	Turbine Flow Meter	24	N/A	N/A
Exact Flow Fuel Flow Meter - Supply	Turbine Flow Meter	25	N/A	N/A
Engine Block Oil Pressure	Pressure Transducer	26	N/A	N/A
Turbine Exhaust Pressure	Pressure Transducer	27	N/A	N/A
Intake Manifold Pressure	Pressure Transducer	28	N/A	N/A
Fuel Lift Pump Pressure	Pressure Transducer	29	N/A	N/A
Exhaust Manifold Pressure	Pressure Transducer	30	N/A	N/A
Coolant Reservoir Pressure	Pressure Transducer	31	N/A	N/A
Cylinder 6 Pressure Transducer	Pressure Transducer	N/A	0	N/A
Fluke Current Probe	Hall-Effect Sensor	N/A	1	N/A
Intake Air Flow	Dual RTD	N/A	2	N/A
Dilution Tunnel - Pre Dilution	Type K TC	N/A	3	N/A
Dilution Tunnel - Post Dilution	Type K TC	N/A	4	N/A
Ambient Temperature	Type K TC	N/A	5	N/A
Post-Filter TC	Type K TC	N/A	6	N/A
Pre-Filter TC	Type K TC	N/A	7	N/A
Engine Torque	Digalog Controller	N/A	10	N/A
Engine RPM	Digalog Controller	N/A	11	N/A
Charge Air Cooler	Type K TC	N/A	13	N/A
Heated Sample Line - Short	Type K TC	N/A	14	N/A
Heated Sample Line - Long	Type K TC	N/A	15	N/A
HFID Range 1 - 8	0 - 5 VDC	N/A	16 - 23	N/A
HFID Voltage	0 - 5 VDC	N/A	25	N/A
HFID Oven Temperature	0 - 5 VDC	N/A	26	N/A
PM Sample Flow Rate	0 - 5 VDC	N/A	29	N/A
NOx Voltage	0 - 10 VDC	N/A	30	N/A
NO Voltage	0 - 10 VDC	N/A	31	N/A
Cummins Crankshaft Sensor	Hall-Effect Sensor	N/A	N/A	2

Chapter 6 Experimental Procedure

6.1 Engine Operation

Since the test engine is a close-to-production design incorporating advanced subsystems to control emissions, a proper test matrix was designed to include the effects of engine technology on fuel properties. Therefore, only the start of main injection and EGR fraction parameters was varied. The ECM was left alone in every other respect letting it command the values for such parameters as charge flow, pilot and post injection quantities, and pilot and post injection timings and execute the correct algorithms to move between states that are contained in the original No. 2 diesel calibration. This provides the worst-case scenario for a modern engine that switches to FT fuel without properly calibrating the ECM to account for the change in fuel properties.

6.1.1 Experimental Test Matrix

To certify their engines, Cummins uses the European Stationary Cycle outlined by the Euro-III directive that came into effect October 2000 [8]. The test modes are found in Table 6.1. In general, high average load factors and very high exhaust gas temperatures, simulating actual on-road driving conditions quite well, characterize the ESC test. The engine speeds A, B, and C are defined by the following: 1) the high speed RPM, RPM_{high}, is defined by calculating the highest engine speed (above the rated speed) where 70% of the declared maximum net power occurs, 2) the low speed RPM, RPM_{low}, is defined by calculating the lowest engine speed (below the rated speed) where 50% of the declared maximum net power occurs, 3) the following formulas are then used to calculated each mode speed:

Equation 6.1 $$A = RPM_{low} + 0.25*(RPM_{high} - RPM_{low})$$

Equation 6.2 $$B = RPM_{low} + 0.50*(RPM_{high} - RPM_{low})$$

Equation 6.3 $$C = RPM_{low} + 0.75*(RPM_{high} - RPM_{low})$$

Using the above equations with the torque and power curves of the test engine give the following values for the above mode speeds: A = 1682 RPM, B = 2013 RPM, and C = 2345 RPM.

To help shake down the experimental setup, Cummins provided data for the entire ESC test in order to validate important parameters like air flow and fuel flow values measured by the sensors described in Chapter 5 . Since the data for the ESC tests was on hand, combined with the fact that the ESC test simulates actual on-road engine operation, the ESC test modes were chosen as a basis to design an experimental test matrix. Another factor that lead to the decision to replicate some of the ESC test

modes is the fact that outside of the ESC test regime, the VGT and EGR system can reach points where they can not change mass flows or EGR flows even with completely open or closed compressor-intake nozzle or EGR valve settings. This is a function of the mechanical limitations of the systems themselves.

Governing the design of the test matrix was the limited supply of FT fuel. The Syntroleum Corporation could only supply one barrel of S-2 FT fuel during the time period this thesis covers. Therefore, with a large supply of No. 2 diesel available, multiple experimental conditions and exhaust sampling methods were tested and rated based on the total fuel consumption of each test. A full timing and EGR sweep consisting of 5 timing points and 4 EGR rates was initially chosen to calculate the overall fuel consumption values to accomplish a full test-matrix sweep. After a couple months of designing the experiments, it was decided to keep five timing points and three EGR rates, running the A25 point and a slightly modified A50 point, with raw PM sampling methods.

The five timing points chosen to run injection sweeps consists of the stock timing for each mode point, the stock timing ± 3°, and the stock timing ± 7°. The maximum advance (and hence retard) was determined from the modified A50 tests. An injection advance of 7° increased in-cylinder pressures to values (~13.0 MPa) within 15% of safe maximum operating pressures (15.3 MPa). Further injection advances increased in-cylinder pressure significantly. The ±3° advance/retard was chosen as it is not a multiple of ±7°. Graphing data with unevenly spaced intervals will help highlight trends, if any happen to appear. The three EGR rates chosen for the EGR sweep consist of the stock EGR rate and the stock EGR rate ± 10% of the total charge flow (i.e. if stock EGR rate was 20%, the sweep included 10%, 20%, and 30% EGR rates).

For the load and speed points, the A25 test mode (1682 RPM, 25% load) was chosen since it has a low fuel consumption rate (Cummins reports $\dot{m}_{fuel} = 9.7\ [kg/hr]$ or $\dot{V}_{fuel} = 11.6\ [L/hr]$) and a high PM output (Cummins data PM = 0.167 g/kW-h) reducing the time needed to load filters and consequently, the overall consumption of fuel. The BMEP at this point is about 480 kPa. The modified A50 point consists of running the engine at the A speed (1682 RPM) but at a slightly higher load rating than 50%. The reasoning for a slightly modified load is based on the literature review in Section 1.4.1 showing a lack of high BMEP tests in recent FT diesel fuel experiments. Thus, the load/BMEP at the A speed was increased until the fuel consumption rate became too great to run 15 timing/EGR test points. This resulted in a BMEP of 1000 kPa or a load of 53%.

The operating conditions defined by these timing, EGR, and speed/load combinations were given shortened labels to simplify data presentation. The low load tests with No. 2 diesel begin with the letter "L", while the high load tests begin with the letter "H." For the S-2 FT diesel test, the low load tests are denoted by "FTL" while the high load tests are defined by "FTH." Please see Table 6.2 for the naming convention that describes the speed/load, injection timing and EGR combination.

6.1.2 Unmodified Fuel-Injection System

Since the viscosity of the FT diesel and No. 2 diesel used in the tests are comparable (S-2 FT = ~2.2 mm^2/s vs. No. 2 diesel = ~2.5 mm^2/s, see Chapter 4), the fuel injectors did not have to be modified or changed between tests to keep the spray characteristics constant. According to Payri et al. [52] who used GOPSA diesel fuel, representative of the standard diesel fuel distribute in Europe with a viscosity of 2.5 mm^2/s and Sasol FT diesel fuel with a viscosity of 2.1 mm^2/s, there are no significant variations in either macroscopic and microscopic spray behavior between FT fuels and standard diesels. Payri et al. go on further and say the atomization process is not affected by the physical characteristics of FT fuel, although an improvement is seen with respect to the evaporation process due to the lower evaporation temperatures of FT fuel. However, the increased evaporation rate, and thus air/fuel mixing process, is offset by the higher stoichiometric air fuel ratio of FT fuels. Therefore, since the macroscopic behavior of the fuels is the same (the proportions of mixed and entrained air in both cases is similar), it allows for the comparison of performance and emissions solely on fuel characteristics, without having to worry about normalizing to a certain spray pattern or amount of swirl.

FT fuel's lower density does affect the volumetric and mass injection rates into the cylinder. These can be quantified by using the following equation [2]:

Equation 6.4

$$\dot{m}_{fuel} = C_D A_n \sqrt{2\rho_{fuel}\Delta p} \propto \rho_{fuel}^{1/2}$$

where fuel $\dot{m}_{fuel}$ is the mass flow rate injected through the nozzle, C_D is the discharge coefficient of the nozzle, ρ_{fuel} is the fuel density, and Δp is the pressure drop across the nozzle. Based on the above equation, we can also write:

Equation 6.5

$$\% \ d\dot{m}_{fuel} = \frac{(\rho_{fuel}^{1/2})_{FT} - (\rho_{fuel}^{1/2})_{No.2}}{(\rho_{fuel}^{1/2})_{No.2}} \cdot 100$$

Based on the density information given in Chapter 4 , under constant injector conditions, the 7.7% reduction in density with FT fuel results in a 3.9% reduction in mass flow rate through the injector. Using this value of mass flow reduction, along with the values given in Chapter 4 for the lower heating values, the total power derate can be calculated:

Equation 6.6

$$\% \ Power = \frac{\dot{m}_{fuel,FT}}{\dot{m}_{fuel,No.2}} \cdot \frac{Q_{LHV,FT}}{Q_{LHV,No.2}}$$

Using the known values, under constant injection characteristics, 2.2% less energy is injected when running with FT diesel versus No. 2 diesel. Due to this slight power derate, the injection durations when operating with FT diesel are slightly longer. The largest difference in injection duration is about 0.5°. See Figure 6.1, Figure 6.2, Figure 6.3 and Figure 6.4.

6.1.3 Inlet Conditions

To simulate on-road conditions and keep cylinder pressures reasonable, the air temperature leaving the liquid-air aftercooler was adjusted by metering the water flow through the cooler. For the low-load tests (25% load), the charge air temperature was kept around 34°C. For the high-load tests (53% load), the charge air temperature was kept around 37°C. No other intake air preparation was done during the tests. The ambient humidity and barometric pressure readings were not taken, since the amount of water in the intake manifold due to the EGR system takes precedence over the water present in ambient air.

6.2 Particulate Matter Sampling Conditions

Due to the limited quantity of S-2 FT diesel fuel, the majority of PM samples were taken by filtering raw exhaust. However, the gravimetric sampling system was shaken down using dilute samples with No. 2 diesel fuel at the A25 test condition in order to gain confidence with the sampling system setup. A few runs with FT fuel at the A25 operating mode were taken for comparison to the shakedown data.

6.2.1 Dilute Exhaust Sampling

Multiple dilution tunnel conditions were run with No. 2 diesel fuel at the A25 condition in order to characterize the sampling system. Dilution ratios from 5 – 10 (determined through NO_x readings) were used in order to keep sampling times reasonable (2 – 4 minutes). These low dilution ratios were still large enough to keep sample temperatures at or below 52° C. Before each test, the Pallflex filter papers were placed in individual plastic petri dishes and allowed to condition for at least 8 – 56 hours as recommended by the EPA [50]. After the conditioning period, 4 PM samples were taken consecutively to have a large enough sample to average. After the filter papers were loaded, they were again allowed to sit for at least 24 hours in order to dry the paper and settle the particulates. All filter preparation, conditioning, and settling were done in an air-conditioned room where the temperature was between the EPA mandated

range of 68° – 86° and relative humidity of 30% – 70%. However, filter weight measurements were done in a relatively hot and humid room, where conditions were outside of the EPA mandates. However, it is believed that the low moisture uptake of the Pallflex filters minimizes the effects of humidity differences between storage and weighing. Even without stringently controlled conditions, the diluted PM emission levels were very close to the data provided by Cummins. See Section 7.2.3.

When running the scans with the SMPS system, dilution ratios from 50 – 70 were needed to lower the concentration of particles below the limit defined by the SMPS hardware. As such, running gravimetric samples and SMPS scans simultaneously were impossible, since the gravimetric sampling times would increase by an order of magnitude. Therefore, only SMPS scans were taken during the experimental setup and shake down period.

6.2.2 Raw Exhaust Sampling

In order to efficiently use the FT fuel supply on hand, the raw, undiluted exhaust was sampled and filtered through the Pallflex filters. Sampling times were reduced to 1 – 2 minutes per filter, depending upon the EGR rate; high EGR rates produce more PM (see Section 7.2.3). The same procedures for filter conditioning, storage, and weighing described for dilute exhaust samples was followed with the raw exhaust sampling method.

Since the dilute sampling method described above gave similar results to the data provided by Cummins, there is merit in sampling a raw exhaust since only the sample stream is changed and not the sampling hardware. The only modification to the hardware was the sample stream was kept as hot as possible by insulating and externally heating the sample lines to prevent water from condensing onto the filters, which would most likely skew the sample weight. As a result, the temperatures upstream of the filter paper ranged from 120°C to 190°C, much higher than the EPA mandate, but well below the maximum allowable temperature advised by the Pall Corporation. Since the raw exhaust is sampled hot and undiluted, the driving forces for nucleation and adsorption of condensable gas species is severely reduced. Therefore, the raw PM emission levels are much less than a comparable sampling run with a dilute sample for the same operating point. See Section 7.2.3 for the results of the PM sampling tests.

6.3 Engine Operation During Experiments

Before beginning each round of experiments, the CAI Model 300-HFID and TEI Model 42C-HL gas analyzers were calibrated with zero and span gases at least twice, with each instrument settling for about 10 – 15 minutes before switching between calibration samples. The instruments were continually left on so the internal electronics would stay at the appropriate operating temperatures, reducing drift and noise. With the engine key switch in the ignition position, all components on the engine would turn on.

The rope heater surrounding the raw exhaust sampling system would turn on and heat up the sampling lines. The National Instruments DAQ hardware was also continually left on to keep the components at the appropriate operating temperature.

After the instrumentation was properly calibrated, the engine would be started and allowed to idle for a few minutes as the National Instruments and CalTerm software programs were started and the dynamometer idle torque offset would settle. Before turning on the field current to the dynamometer through the push-button switch on the dynamometer controller, the torque offset was noted and recorded. After all the computers and gas analyzers were ready for use, the ECM settings were left in stock form while the voltage output from the Watlow controller was increased until the appropriate load condition was reached. While the engine continued to warm up, preliminary raw exhaust samples were taken in order to heat up all components in the gravimetric sampling system and purge the sampling lines of PM material. Since two filter holders were used, both were allowed to run for 3 – 5 minutes apiece to ensure a thorough flushing and heating of the system.

Once the engine reached a steady-state condition, a 30-second scan of all slow-speed engine data was taken. After this, a 15-second scan of the gas analyzers was run. Immediately after the first recording of emissions data, the bulkhead connector was switched to sample from the second sample point (either intake or exhaust, depending upon the initial emission scan). At this point, a 10-cycle high-speed scan of in-cylinder pressure, crankshaft sensor, and intake manifold pressure data was taken while the gas analyzers resettled. After another 1 – 2 minutes of settling time, the gas analyzers were rescanned. After this preliminary round of data, two PM samples were taken one right after another, using two filter holders. During each PM sample, a scan was run to record the sample flow rate and pre- and post-filter temperatures. After these two filter samples, another round of data scans was taken (low-speed, high-speed, and two emission scans) to have data in between sample runs. After the interim data scans, another two filter papers were loaded with the appropriate data recorded. Finally, after all PM samples were taken, a final scan of all data was taken, along with a 100-cylce high-speed scan that would be used for combustion analysis. The 100-cycle scan was taken at the end of all tests (about 20 minutes after the start of the first low-speed scan) since this ensured ample time for all operating parameters to reach a steady state.

The same procedure as states above was used in running the No. 2 diesel and FT diesel fuel tests. In order to transition to the FT diesel, one gallon was placed into the appropriate FT fuel tank. The bulkhead connections controlling the fuel supply, return and bypass were switched to the FT fuel tank and the fuel bypass setting. The fuel lift pump was continuously switched on and off since it runs through a 30-second prime procedure every time the key has been off for more than 30 seconds. The fuel lift pump was run until the diesel fuel coming out of the fuel bypass was FT fuel. FT fuel has a noticeably different

color and smell versus No. 2 diesel, so recognizing FT fuel is quite easy. At this point, the fuel filter was removed and switched with a brand new one, preventing the cross contamination of sulfur.

Although the engine system has been purged up to this point, the fuel flow meters and fuel heat exchanger system still contains No. 2 diesel fuel. Next, the return line to the FT fuel tank was disconnected and placed into a waste-fuel container. The fuel lift pump was again switched on and off until the fuel that drained into the bucket was FT fuel, and the return line was reconnected to the fuel return port on the fuel tank. As a final step, the flow computers on the fuel flow meters were recalibrated to work with the FT fuel.

6.4 Data Processing

Especially during the low-load tests (25% load), the slow-speed data had to be preprocessed before the fuel flow values were used since the fuel flows in the low-load tests were near the lower limit of the fuel flow meters. In order to get reasonable average fuel low readings, abnormally high and low fuel readings were removed so that the equivalence ratio matched a value close to the reported value in the ESC data provided by Cummins ($\phi_{low\text{-}load}$ = ~0.43, $\phi_{high\text{-}load}$ = ~0.57).

The emission data reported by Cummins is given on a wet basis. The values recorded by the Model 300-HFID are already on a wet basis, while the Model 42C-HL reports data on a dry basis due to the sample chiller used upstream. Therefore, to convert everything to a wet basis to compare to the ESC data, the water content of the intake and exhaust had to be estimated. The following equation was used to estimate the mole fraction of species in an intake mixture with EGR [2]. The unburned mixture per mole of O_2 is:

Equation 6.7
$$(1-x_b)\left[\frac{4}{M_f}(1+2\varepsilon)\phi(CH_y)_\alpha + O_2 + \psi N_2\right] + x_b(n_{CO_2} + n_{H_2O} + n_{CO} + n_{H_2} + n_{N_2})$$

where x_b is the burned gas fraction (equal to the EGR rate in the case of no residuals), M_f is the molecular weight of the fuel, y is the molar H/C ratio of the fuel, ε is 4/(4+y), ϕ is the fuel/air equivalence ratio, n_i is the mole fraction of species *i* per mole of O_2 reactant, α is the coefficient to multiply the molecular weight of the simplified chemical composition to equal M_f, and ψ is the molar N/O ratio (3.773 for air). The mole fractions of each species are obtained by dividing by the total number of moles of unburned mixture [2]:

Equation 6.8

$$n_u = (1 - x_b)\left[\frac{4(1+2\varepsilon)\phi}{M_f} + 1 + \psi\right] + x_b n_b$$

where n_b, the total number of moles of burned mixture is given by (for a lean mixture) [2]:

Equation 6.9

$$n_b = (1-\varepsilon)\phi + 1 + \psi$$

An assumption made in the above equations is the residual gas fraction is negligible since the engine is turbocharged. Therefore, x_b is initially equal to the EGR rate determined from the dry-basis NO_x ratio from scans in the intake and exhaust system. After finding the corrected water vapor mole fraction in the intake, and estimating the water vapor mole fraction from the ideal combustion of the above reactants, the dry-basis NO_x readings can be corrected to a wet basis, and the actual EGR rate can be determined. The above equations are iterated with the newly determined EGR until a steady-state value is found.

It should be mentioned that the NO_x data for FT fuel run on the stock EGR rates for both fuels had to be corrected. Initial tests showed NO_x reductions on the order of 50% – 60 %, drastically different than was expected or is reported in the literature. High load tests were rerun at a later date, showing the NO_x meter was out of calibration during the initial stock-EGR tests. It was found that tests run the previous day with the NO_x meter were run using an SI engine in the laboratory, the high water content in the SI engine clogging some of the capillaries in the NO_x meter. Nonetheless, the data from latter runs was compared to the erroneous data at high loads and the differences were averaged. This average difference was then used to rescale the data for both low- and high-load tests. This adjustment procedure produced similar trends to the increased-EGR tests at low- and high-loads where the NO_x meter was calibrated carefully before any tests were run, giving some validity to the stock-EGR runs with FT.

The PM sample flow rate data recorded from the Omega FVL-1611 volumetric flow meter was averaged during the PM sampling period. Any offsets during filter loading were recorded and appropriately applied to get a properly scaled and average sample flow rate across the filter.

The high-speed in-cylinder pressure data commonly had high-frequency oscillations after the start of combustion. Copies of the pressure traces were sent to AVL and Cummins engineers and both companies reported the oscillations were typical of diesel combustion behavior. Calculations were done to determine the speed of sound within the combustion chamber during the time periods when the oscillations occurred. Crude approximations showed that the speed of sound divided by twice the cylinder bore (total distance for a wave to travel) was about equal to the frequency of the oscillations. In

order to reduce this unwanted "noise," the high-speed pressure data was preprocessed using a MATLAB script (see Appendix D) incorporating an FFT filter to eliminate the unwanted high-frequency signals.

6.5 Heat Release Analysis

The heat release analysis used to process the pressure data applies the First Law of Thermodynamics assuming the closed system between intake valve closing (IVC) and exhaust valve opening (EVO) is a single-zone of uniform products. The gas properties are predicted using ideal-gas relationships, with a gas constant for air. The First Law expanded to include various heat sources (neglecting heat loss through crevice effects) is:

Equation 6.10

$$dU_{internal} = \delta Q_{chemical} - \delta Q_{HT} - \delta W$$

where $\delta Q_{chemical}$ is the calculated energy of the fuel, δQ_{HT} is the energy lost through heat transfer and δW is the work term. To apply the First Law to in-cylinder pressure data, the following form of the First Law is used:

Equation 6.11

$$\frac{\delta Q_{chemical}}{d\theta} = \frac{1}{\gamma - 1} V \frac{dP}{d\theta} + \frac{\gamma}{\gamma - 1} P \frac{dV}{d\theta} + \frac{\delta Q_{HT}}{d\theta}$$

where V is the cylinder volume, P is the cylinder pressure, and γ is the ratio of specific heats. The differential forms of some of the terms are written on a crank-angle basis, since pressure and volume data are normally recorded with a crank-angle encoder as an external clock to the DAQ system. The heat transfer term was determined from a Nusselt-Reynolds number correlation analogous to that used for steady turbulent pipe flow. See Assanis [53] for further information on the heat transfer model and Appendix D for its implementation in the heat-release analysis code.

Typical curves obtained from the heat release analysis code with the injection events denoted are found in Figure 6.5, Figure 6.6 and Figure 6.7.

6.5.1 Caveats of the Heat Release Analysis

The limitations of a single-zone combustion model became quite apparent when the heat release analysis was used to process the in-cylinder pressure data. The data failed consistency checks with actual fuel flow measurements unless one assumed zero heat transfer and a large gamma (γ). Making these non-physical assumptions could not account for the discrepancy in the integrated heat release alone. After some analytical checks, a recalibration of the cylinder pressure would most likely achieve a consistency

between the measured and integrated fuel energy values. This is based on the fact that the shape of the normalized cumulative heat release fraction curve determined from the total integrated heat released should not vary much, even though the magnitude of the integrated heat release is incorrect.

We can see how a rescaled pressure can reduce the overall integrated heat release by rearranging Equation 6.10 to place the fuel energy term on the left-hand side (LHS) and the other terms on the right-hand side (RHS) and expanding each term based on the ideal gas law:

Equation 6.12
$$\underset{1\to 2}{\Delta} Q_{chemical} = mc_V(T_2 - T_1) + \int_1^2 PdV + \sum_{1\to 2}^{i} h_i A_i (T_i - T_{w,i})$$

Equation 6.13
$$\underset{1\to 2}{\Delta} Q_{chemical} = \frac{(P_2V_2 - P_1V_1)}{\gamma - 1} + \int_1^2 PdV + \sum_{1\to 2}^{i} h_i A_i \left(\frac{P_iV_i}{mR} - T_{w,i} \right)$$

in the above equations, the unidentified terms include h_i, the heat transfer coefficient of various surfaces in the combustion chamber (piston heat, cylinder liner, cylinder walls); A_i, the heat transfer areas of various surfaces in the combustion chamber; $T_{w,i}$, the wall temperature of the aforementioned surfaces; m, the trapped mass in the combustion chamber between IVC and EVO; and R, the gas constant for air. If we scale all the pressures above by a factor α (and if an appropriate scaling for $T_{w,i}$ is used as well), we can see:

Equation 6.14
$$\underset{1\to 2}{\Delta} \alpha Q'_{chemical} = \frac{\alpha(P'_2V_2 - P'_1V_1)}{\gamma - 1} + \alpha\int_1^2 P'dV + \sum_{1\to 2}^{i} h_i \left(\frac{\alpha P'_iV_i}{mR} - \alpha T'_{w,i} \right)$$

Therefore, if the pressure was appropriately scaled, the total integrated heat release would scale accordingly. Thus, although there is uncertainty in the current model with the appropriate heat transfer and gamma correlations for varying volumes of unburned gas, burned gas, and compressed air, a proper scaling of the pressure data to reflect measured fuel flow figures would change the absolute values of the heat release rate, but it should not affect the normalized shape of the cumulative heat release fraction. Since most of the discussion of results deals with relative points of the cumulative heat release curves, the following discussion still has some technical merit.

Table 6.1 European Stationary Cycle (ESC) test modes [8].

Mode	Engine Speed	% Load	Weight Factor, %	Duration.
1	Low Idle	0	15	4 Minutes
2	A	100	8	2 Minutes
3	B	50	10	2 Minutes
4	B	75	10	2 Minutes
5	A	50	5	2 Minutes
6	A	75	5	2 Minutes
7	A	25	5	2 Minutes
8	B	100	9	2 Minutes
9	B	25	10	2 Minutes
10	C	100	8	2 Minutes
11	C	25	5	2 Minutes
12	C	75	5	2 Minutes
13	C	50	5	2 Minutes

Table 6.2 Definitions of operating conditions. Shortened label provides load, timing, and EGR information.

	Timing	Retard		Advance	
EGR	Stock	3°	7°	3°	7°
Stock	*1	*2	*3	*4	*5
-0.10	*6	*7	*8	*9	*10
+0.10	*11	*12	*13	*14	*15

Notes: * = Fuel type and load (L, H, FTL, FTH). L/H = No. 2 diesel, FTL/FTH = FT diesel
Timing in Cummins ECM given as °bTDC.
EGR rates are 10% of total charge flow from stock setting.

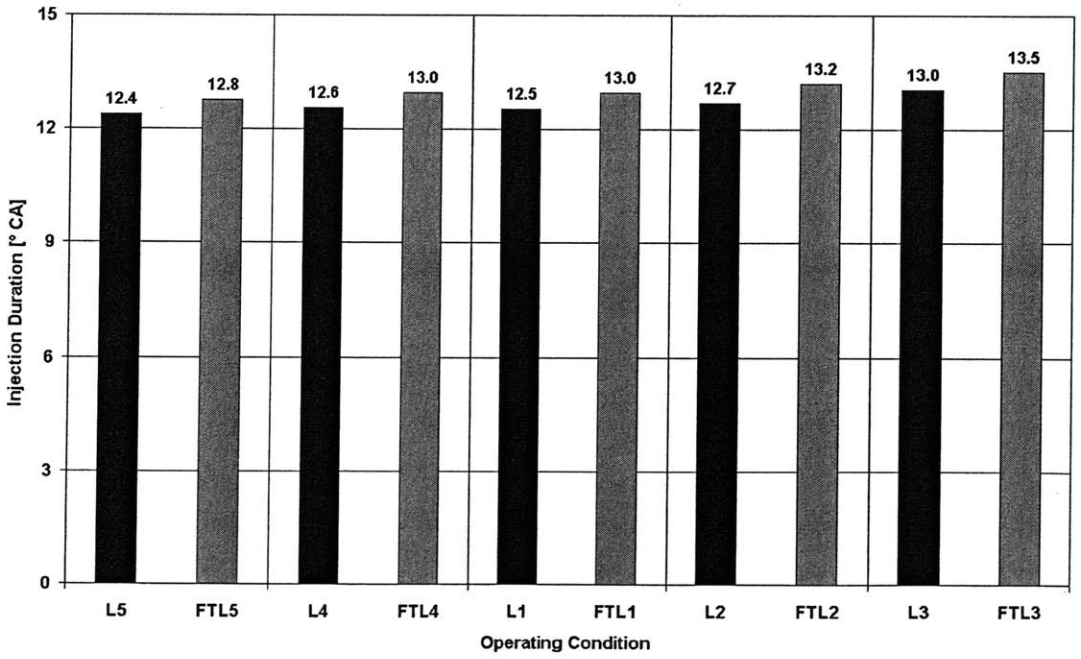

Figure 6.1 Injection duration using No.2 diesel fuel and Fischer-Tropsch fuel during timing sweep test with stock EGR rates in low-load tests. The operating conditions are normal diesel (L1 – L5) and Fischer-Tropsch (FTL1 – FTL5). Stock timing is in the center with the most advanced timing to the left and the most retarded timing to the right.

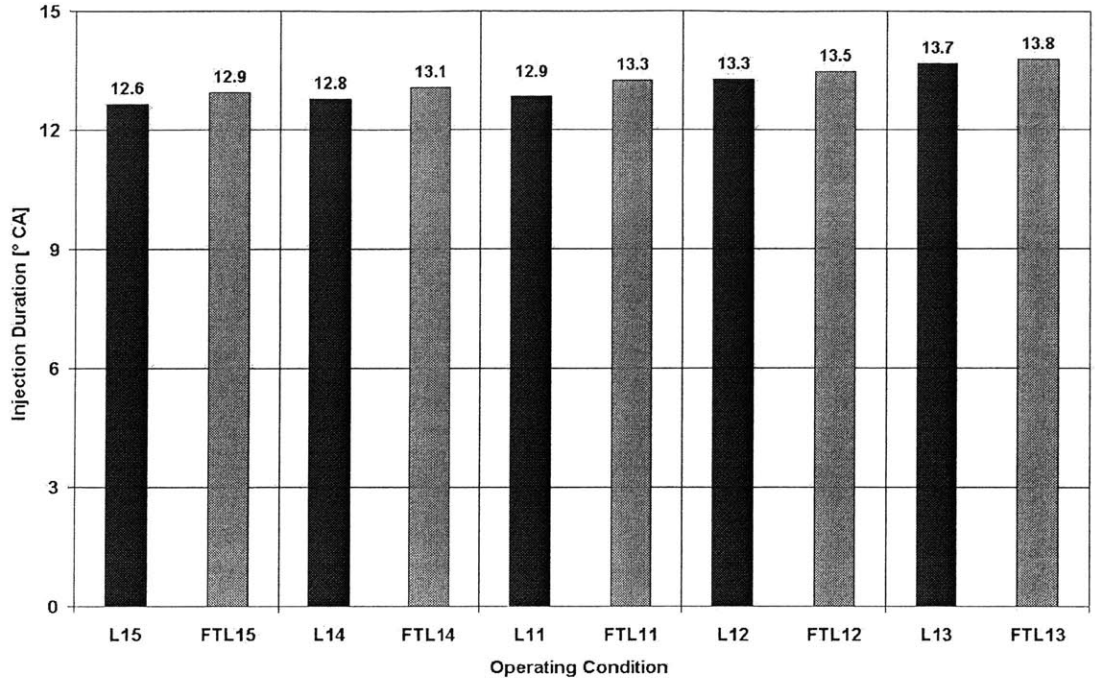

Figure 6.2 Injection duration using No.2 diesel fuel and Fischer-Tropsch fuel during timing sweep test with increased EGR rates in low-load tests. The operating conditions are normal diesel (L11 – L15) and Fischer-Tropsch (FTL11 – FTL15). Stock timing is in the center with the most advanced timing to the left and the most retarded timing to the right.

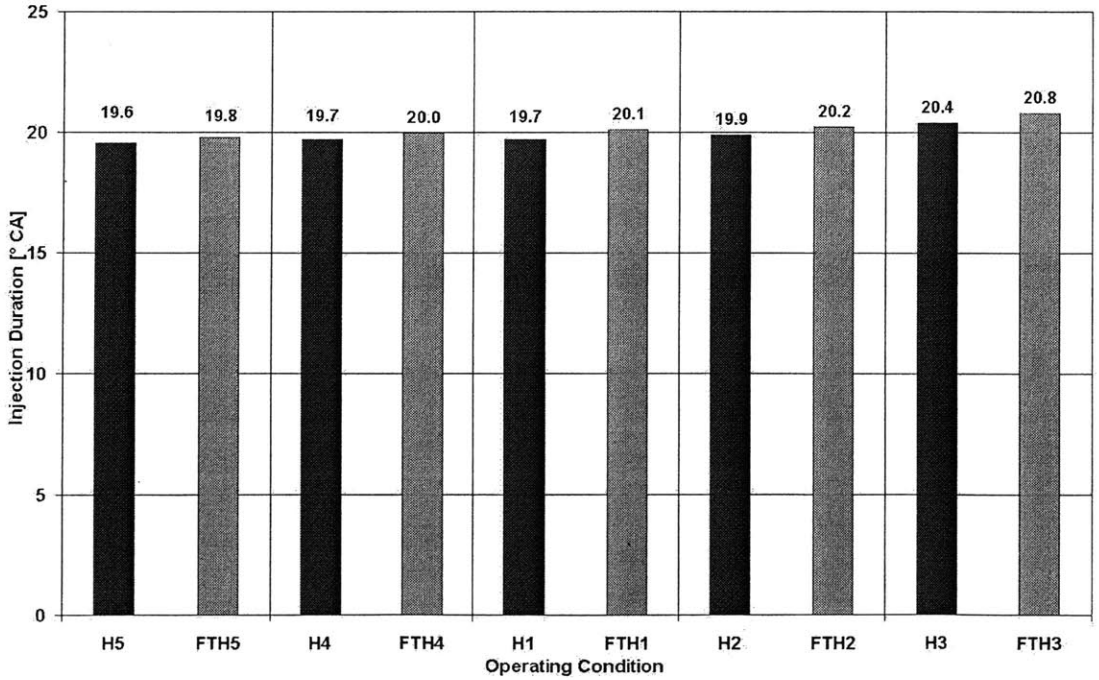

Figure 6.3 Injection duration using No.2 diesel fuel and Fischer-Tropsch fuel during timing sweep test with stock EGR rates in high-load tests. The operating conditions are normal diesel (H1 – H5) and Fischer-Tropsch (FTH1 – FTH5). Stock timing is in the center with the most advanced timing to the left and the most retarded timing to the right.

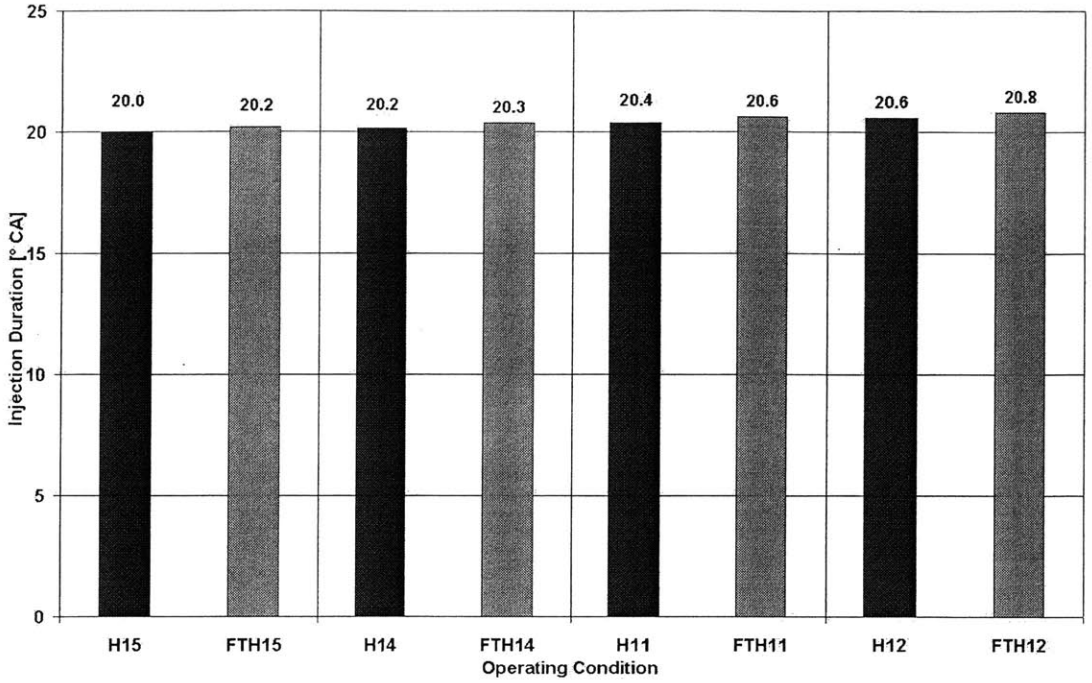

Figure 6.4 Injection duration using No.2 diesel fuel and Fischer-Tropsch fuel during timing sweep test with increase EGR rates in high-load tests. The operating conditions are normal diesel (H11 – H15) and Fischer-Tropsch (FTH11 – FTH15). Stock timing is in the center with the most advanced timing to the left and the most retarded timing to the right.

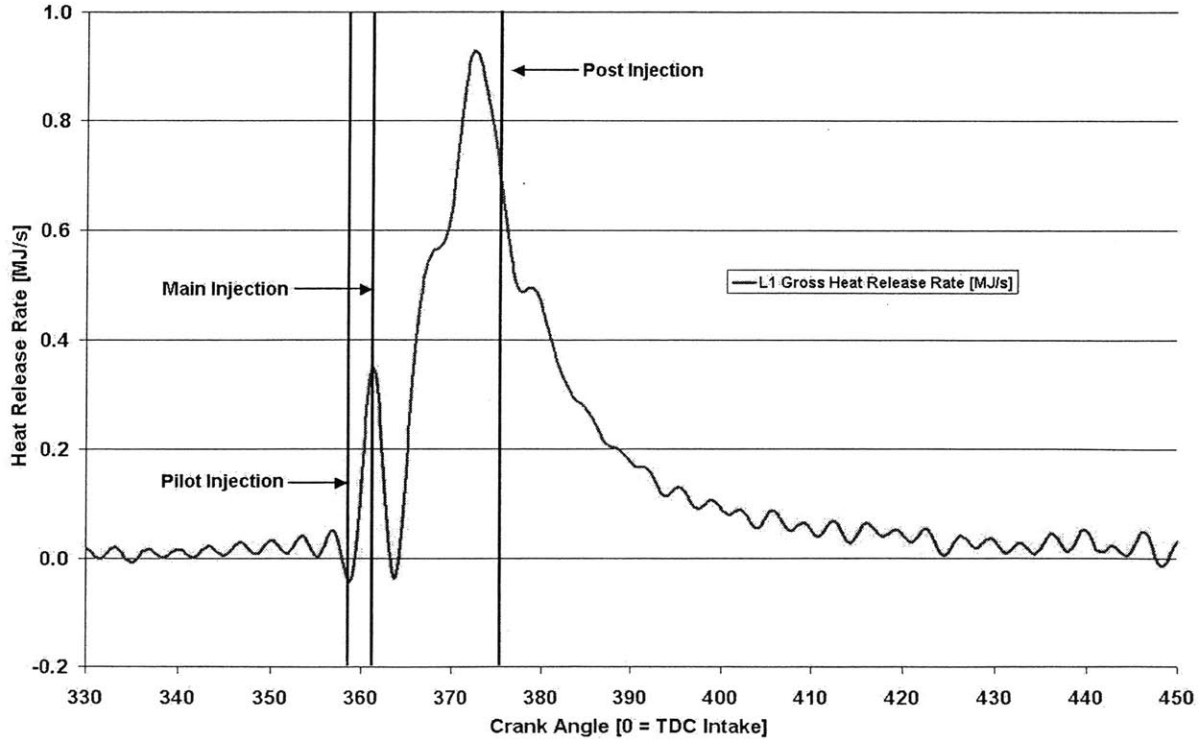

Figure 6.5 Event diagram for low-load (25%), stock timing and stock EGR rate.

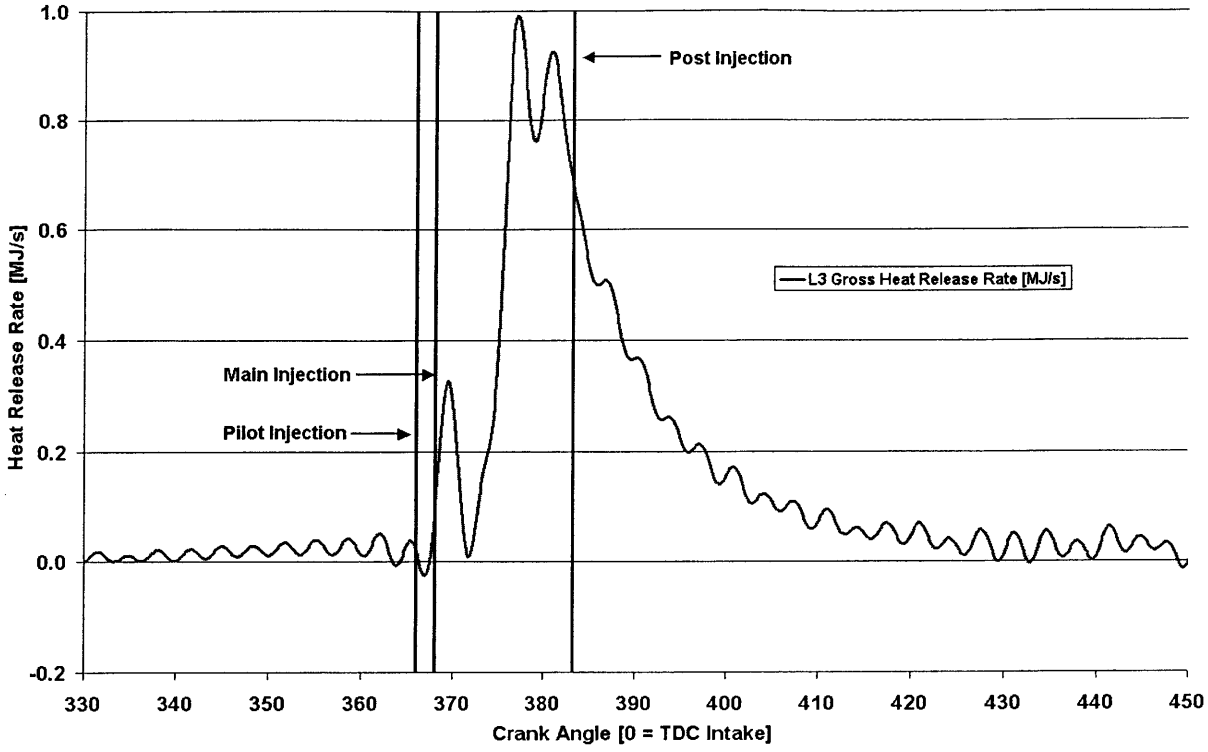

Figure 6.6 Event diagram for low-load (25%), injection 7° retarded from stock setting and stock EGR rate.

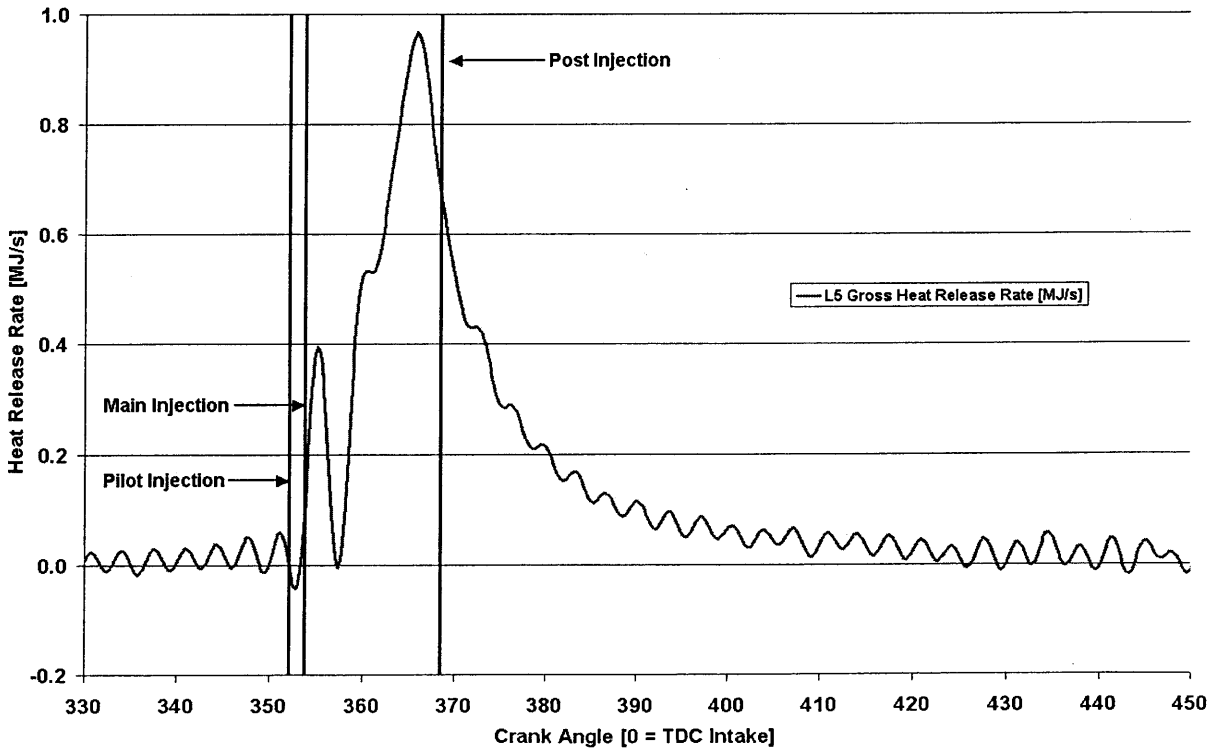

Figure 6.7 Event diagram for low-load (25%), injection 7° advanced from stock setting and stock EGR rate.

Chapter 7 Results and Discussion

7.1 Combustion Characteristics

The phenomenological diesel combustion model discussed in Section 2.1.2 detailed the major physical characteristics and processes of combustion such as the spatial and temporal development of the fuel-air plume, equivalence ratios of the standing premixed flame and surrounding diffusion flame, and spatial regions where emissions are most likely forming. Many other details about the combustion event are also important when trying to gain a fundamental understanding of the effects of fuel properties on engine performance and emissions. Additional analyses with the heat-release-rate curves give such details as how soon after injection the initial premixed burn fraction occurs, crank-angle locations of when certain percentages of the total energy is released, or when the end of combustion occurs. These and other parameters are helpful in determining why fuel properties affect an engine's overall operating characteristics.

7.1.1 Ignition Delay

The ignition delay in diesel combustion is defined as the time between the start of injection and the start of combustion. As described in Section 3.2, one of the main factors governing the ignition delay in diesel combustion is the cetane number (CN) of a fuel. Although the magnitude of ignition delay is usually only described chemically through a fuel's (CN), physical processes and conditions inside the combustion chamber are equally important in determining the ignition delay.

Experiments done in constant-volume bombs, steady-flow reactors, and in rapid-compression machines have been used to study the autoignition characteristics of fuel-air mixtures [2]. The ignition delay data from experiments carried out in these different combustion configurations can all be correlated by an Arrhenius-type equation of the following form [2]:

Equation 7.1

$$\tau_{id} = Ap^{-n} \exp\left(\frac{E_A}{\tilde{R}T}\right)$$

where τ_{id} is the ignition delay; A and n are constants that depend on the fuel, injection, and air-flow characteristics; p is the cylinder pressure; E_A is the apparent activation energy for a fuel to autoignite; $\tilde{R}$ is the universal gas constant; and T is the cylinder temperature. Based on Equation 7.1's Arrhenius form, temperature plays a significant role in determining the ignition delay. Additionally, in the above

equation, representative values of n can range from between 1 – 2 [2], clearly showing that cylinder pressure can have large effects on ignition delay.

Although a combustion chamber may have favorable pressures and temperature to promote autoignition, physical processes within the cylinder can either enhance or impair the actual ignition delay. Without proper fuel preparation such as liquid atomization, vaporization, and mixing, the fuel will take much longer to autoignite. Furthermore, processes that can affect large-scale mixing of fuel and air such as fuel injection pressure and piston motion can also play a role in the autoignition of a fuel. If physical processes occur on much longer time scales than the chemical processes governing autoignition, then equations such as Equation 7.1 that do not take into account physical mixing must be used with caution. A more appropriate empirical relation from actual engine experiments is [2]:

Equation 7.2
$$\tau_{id}(CA) = (0.36 + 0.22\bar{S}_p)\exp\left[E_A\left(\frac{1}{\tilde{R}T} - \frac{1}{17{,}190}\right) + \left(\frac{21.2}{p - 12.4}\right)^{0.63}\right]$$

where $\bar{S}_p$ [m/s] is the mean piston speed, T [Kelvin] and p [bars] are the charge temperature and pressure during the ignition delay (taken as TDC conditions), E_A [J/mol] is the apparent activation energy for autoignition, and $\tilde{R}$ is the universal gas constant. In Equation 7.2, the importance of a fuel's cetane number is correlated by [2]:

Equation 7.3
$$E_A = \frac{618{,}840}{CN + 25}$$

Thus, as expected, as a fuel's CN rating increases, the required activation energy required for autoignition drops, reducing the ignition delay for a given temperature and pressure. Furthermore, the exponential dependence of ignition delay on cylinder temperature is still evident in Equation 7.2. Unlike Equation 7.1 however, the ignition delay described by Equation 7.2 is exponentially dependent on pressure, although to a lesser extent compared to temperature. Regardless, Equation 7.2 shows that increasing temperature and pressure during injection will reduce ignition delay.

As described in Section 1.3, modern fuel-injection technology gives engine designers precise control of fuel delivery, allowing for injection rate shaping and multiple injections per cycle. The test engine used to run experiments is equipped with a Bosch common-rail system, allowing Cummins engineers to use a multiple-injection fueling strategy. According to Cummins engineers, pilot injection is used nowadays to reduce the typical diesel "knocking" sound for societal benefits. Pilot injection

accomplishes this by reducing the amount of fuel that autoignites in the initial premixed burn fraction, decreasing the sudden pressure rise that is associated with the diesel-engine sound. The small amount of fuel (1 mg/stroke in all experiments) injected a few degrees before the main injection event occurs starts the autoignition chemistry, helping to bring the prevailing cylinder conditions into a more favorable state once the main fuel is injected, reducing the overall ignition delay of the main fueling quantity.

Although SOI is quite easily measured by a Hall-effect sensor in a needle-lift indicator, or in modern engines, through the commanded settings of an ECU to the electronically controlled injector, SOC is much more difficult to determine precisely [2]. In the burn rate analysis program used to process the cylinder pressure traces, the SOC was defined as the point after the main start of injection when the heat release went through an inflection point (some conditions had two inflection points; the first was used in these cases), going from a decreasing rate in heat release to an increasing rate of heat release. The heat release drops after the start of the main injection due to the evaporative cooling effect of vaporizing fuel. Due to time constraints, the SOC was manually chosen by visually inspecting the heat-release rate curves. The behavior in the high-load, most advanced cases (H5, FTH5, H15, and FTH15) is suspect, since the SOC was difficult to pinpoint manually. Thus, the following discussions ignore these points when comparing trends.

7.1.1.1 Ignition Delay In Low-Load Tests

In order to reduce overall NO_x emissions, modern diesel engines use heavily retarded timing compared to older engines. Diesel engines from the 1970s and 1980s commonly had injection timings between 20° – 30° bTDC, whereas nowadays, fuel injection occurs around TDC. In the low-load experiments (~480 kPa BMEP), the stock injection timing is 1° aTDC. Since the piston is largely still near TDC, even with advanced and retarded timing, the cylinder temperatures and pressures vary little with injection timing. As compression temperatures and pressures around TDC are much higher versus conditions 20° – 30° before TDC, the ignition delays in engines with near-TDC timing should be shorter relative to older engines, and should not vary much with injection timing.

Examining Figure 7.1 (see end of chapter for figures), the average ignition delay under the stock-EGR operating conditions with No.2 diesel fuel is $\tau_d = 3.4° \pm 0.4°$. Repeating the same EGR rate tests with FT fuel resulted in an average ignition delay of $\tau_d = 2.3° \pm 0.3°$. Based on Equation 7.2, which was correlated using TDC conditions, the ignition delay should not change much with timing, although the CN (or CNI for FT, see Section 3.2.1 for definitions of CNI and CN) effect should make the ignition delay shorter with FT fuel. The small spread in ignition delay is attributed to the fact that the temperatures and pressures at SOI varied little, ranging from about $T_{SOI,L1\text{-}L5} = 710 – 760$ K and $P_{SOI,\ L1\text{-}L5} = 5.7 – 6.5$ MPa for No.2 diesel fuel and $T_{SOI,\ FTL1\text{-}FTL5} = 730 – 760$ K and $P_{SOI,\ FTL1\text{-}FTL5} = 6.0 – 6.7$ MPa.

Using the individual temperatures and pressures at the start of injection, shown in Figure 7.2 and Figure 7.3, Equation 7.2 predicts differences of about 1° – 2° between No. 2 diesel and FT diesel, which is seen in the data. Thus, since the CNI of the FT fuel is much larger than the equivalent CNI of No. 2 diesel fuel, the ignition delay reduction is an expected trend.

Likewise, in the increased-EGR operating conditions shown in Figure 7.4, the FT fuel had ignition delays (τ_d = 2.0° ± 0.3°) that were about 1.0° shorter than the equivalent operating conditions with No. 2 diesel fuel (τ_d = 3.2° ± 0.2°). Again, the higher relative CN (as CNI ≅ CN) rating of the FT fuel reduces the overall ignition delay. The low standard deviation among the recorded spread of ignition delays again shows that the ignition delay did not change with injection timing. The slight reduction in ignition delay compared to the stock EGR conditions is attributed to the fact that the intake charge temperature is increased due to the addition of hot-products through the recycled exhaust. Intake manifold temperatures jump from T_{IMT} = ~50°C at the stock EGR conditions to T_{IMT} = ~70°C, resulting in temperatures at SOI that range from about $T_{SOI\text{-}Increased\ EGR}$ = 750 – 825 K, about 20 – 70 K higher than the stock EGR tests (see Figure 7.5), depending on the injection timing. Pressures around SOI at this EGR rate range from $P_{SOI\text{-}Increased\ EGR}$ = 6.0 – 6.8 MPa (see Figure 7.6), slightly higher than the SOI-pressures at the stock EGR rate due to the increase in cylinder temperatures.

7.1.1.2 Ignition Delay in High-Load Tests

In general, ignition delay drops linearly with increasing load as gas temperatures and engine wall temperature increase [2]. Taking into account the ± 0.2-degree resolution of the experimental setup, Figure 7.7 shows that except for the most-advanced timing condition, the ignition delays for each fuel during the high-load (~1000 kPa BMEP) experiments running with the stock-EGR rates are essentially the same (τ_d = 2.4° ± 0.2°). Similarly, in the increased-EGR operating conditions, ignition delay values are essentially equal and equivalent to the stock-EGR conditions (τ_d = 2.4° ± 0.2°) as illustrated by Figure 7.10. The shorter ignition delay at the most-advanced timing condition may be physically occurring, since ignition delays are minimized when fuel is injected 10° – 15° bTDC [2]. However, the shorter delays may also be a function of the difficulty to determine the SOC in a diesel engine.

Interestingly, the ignition delays at high loads did not change much with the FT fuel. This may be due to the fact that SOI temperatures at high loads did not change much (compression of only properly-aftercooled air up to TDC in the test engine) compared to the low-load tests (see Figure 7.8 and Figure 7.11). With respect to No. 2 diesel, however, the ignition delays did drop at the higher loads. Equation 7.2 suggests that higher in-cylinder pressures (see Figure 7.9) should lead to smaller ignition delays, which explains the behavior of No. 2 diesel. The above trends are most likely a function of each fuel's CN/CNI rating. With respect to FT fuel, the CNI is high enough such that the ignition delay is

governed more by temperature in Equation 7.2 more than anything else, resulting in the constant ignition delays seen in the data. With No. 2 diesel fuel, the CN number is low, resulting in higher required activation energies, placing more importance on in-cylinder temperatures and pressures in the ignition delay relation of Equation 7.2.

In summary, at low-loads, incorporating pilot-injection strategies and near-TDC injection timings, cylinder temperatures in the test engine are high enough such that the ignition delay reaches a constant, minimum value, with the CN or CNI of the fuel in use describing the relative magnitude of this minimized ignition delay. As load increases, cylinder temperatures around TDC remain constant and are equivalent to TDC temperatures at low loads, again resulting in a constant, minimized ignition delay. With FT fuel, this delay was equivalent to the low load conditions since the elevated CNI rating gives the temperature term in Equation 7.2 much more importance versus the pressure term. With No. 2 diesel, the ignition delay was further reduced at high loads due to the substantially higher pressures. Since No. 2 diesel has a lower CN than FT fuel, it is more dependent upon pressure in Equation 7.2.

7.1.2 Combustion Duration

After the ignition delay period, autoignition establishes the standing premixed flame. Combustion proceeds until either the fuel is completely burned or the flame is quenched. The combustion duration gives a qualitative indication of the chemical reaction rates during the two-stage oxidation of diesel fuel; long durations imply low chemical reaction rates while short durations imply high chemical reaction rates. The combustion duration referred to in the following sections is derived from the heat-release analyses of cylinder pressure traces. Combustion duration was defined as the time between the SOC and the EOC, the EOC defined as the point of 90% of the integrated heat release. This definition of combustion duration resulted in combustion durations between about 40° – 50° at low loads and 50° – 70° at high loads (more fuel burned at high loads requires more time for combustion). Defining the EOC at locations greater than the 90% integrated heat release point resulted in abnormally long combustion durations, some points being greater than 100°. Heywood suggests that fuel conversion efficiencies are highest when the combustion duration is between 40° – 50° [2], suggesting that the EOC definition used in the heat-release analysis program is an appropriate, although arbitrary, definition of when combustion ends.

The first major trend in the combustion duration data illustrated in Figure 7.13 – Figure 7.16 show that at a constant BMEP and timing, the combustion duration increases as the EGR rate increases. The combustion duration increased from about 3° – 7° at low loads, depending upon timing, while changing from about 7° – 10° at high loads depending upon timing. This is expected since EGR acts as a diluent, and more importantly in diesel engines, as a displacement for oxygen in the intake. Since the

overall temperatures are lower and the amount of oxygen available for oxidation is reduced, the reaction rates in the diffusion flame are substantially reduced, leading to prolonged combustion durations. The combustion duration is affected more at high loads since the composition of the EGR contains exhaust-gas products from combustion that is closer to stoichiometric. The oxygen content in diesel exhaust steadily decreases, reaching zero when $\phi = 1$ (see Figure 7.65). Furthermore, the heat capacity of the exhaust-gas products increases as ϕ approaches 1, making EGR a better diluent at higher loads.

Another trend shown by the data is that at low loads, the combustion duration is approximately constant for No. 2 diesel for a given EGR rate, while for FT diesel fuel, the combustion durations are essentially constant at a given EGR rate until timing is phased past TDC. At high load, ignoring the most-advanced cases since the ignition delays are questionable, the combustion durations decrease as injection timing is retarded. What the data seem to demonstrate is that the rate of combustion must be increasing as injection timing is retarded. Although the low-load points do not show drastically reduced combustion durations, the rate of combustion must nonetheless be increasing since the BSFC rises as timing is retarded for all different loads and EGR rates (see Figure 7.17 and Figure 7.18). Increases in BSFC suggest that the combustion duration should increase since more fuel is injected that must be burned, to keep load constant as combustion is phased past TDC. Also, as timing is retarded from TDC, the prevailing cylinder temperatures are less conducive for high reactions rates (laminar burning velocity and thermal diffusivity decrease with decreasing temperature, see Section 2.1.3) further implying an increase in combustion duration. Therefore, the actual combustion duration trends seen in the experiments is unexpected, and attempts in explaining the combustion duration behavior using previously accepted diesel-combustion-model concepts results in contradictions like the BSFC behavior described above.

Since the cylinder conditions change drastically as timing is varied (keeping EGR rate and BMEP constant), the overall combustion duration does not reveal much about the actual processes that might be contributing to the changes in combustion duration. To get a better understanding of combustion development, the combustion duration is divided into three intervals describing the beginning, middle and end of combustion. In the heat release program, in addition to the 90% integrated heat release location that defined EOC, the 10% and 50% integrated heat release locations were calculated. From these points, the durations between SOC to the 10% integrated heat release point, 10% to 50% heat release points, and 50% to 90% heat release points were determined, giving further insight into the combustion duration trends.

As described in Section 2.1.2, new theories about diesel combustion and spray development have been formulated, some as recently in the past couple of years. Applying these new concepts, especially those describing fuel spray and flame establishment, to the heat-release analysis results help in explaining

the combustion duration trends. Therefore, before discussing the combustion duration intervals mentioned above, air entrainment concepts will be developed that will give better insight into the combustion process and its temporal development.

7.1.2.1 Air Entrainment Concepts Derived From Flame Lift-Off Theory

The section on flame lift-off in Chapter 2 describes how flame lift-off can change based on fuel injection and in-cylinder conditions. Researchers at Sandia National Laboratories [30] took the flame lift-off theory, combined it with previous work from their coworkers [31], and formulated a combined theory describing how flame lift-off can describe the amount of mixing occurring before autoignition in the standing premixed flame.

Changes in diffusion flame lift-off length based on gas temperature, gas density, and fuel-injection pressure (or velocity) stem from changes in the amount of air entrained into the spray and the relative mixing rates between the fuel vapor and the surrounding air. With respect to diesel combustion, the flame lift-off length thus describes the amount of fuel-air mixing that occurs before the standing, premixed flame. Consequently, changes in the lift-off length due to in-cylinder condition and injection parameter variations will change the equivalence ratio of the fuel-rich premixed flame in the phenomenological model proposed by Dec et al. [24] – [29]. Researchers at Sandia National Laboratories have characterized a parameter called the percent of stoichiometric air (ζ_{st}), defined as the amount of air entrained up to the lift-off length as a percentage of the total air required to burn the fuel being injected, and have correlated it to the flame lift-off length.

Siebers and Higgins [30] found that in a quiescent combustion bomb at constant ambient gas density, decreasing the ambient air temperature leads to an increase in the amount of air entrained upstream of the lift-off length. This occurs because the lift-off length increases due to the late temporal development of the standing, premixed flame as ignition delays are prolonged at lower in-cylinder gas temperatures. Again, the relationship between flame lift-off length and ambient gas temperature is given as $H \alpha T^{-3.74}$ [30], implying the change in lift-off length and amount of air entrainment is much greater with a given temperature difference between cooler gases (see Figure 2.8 and Figure 7.19). Also, at a constant cylinder temperature, although decreasing the cylinder gas density (and thus in-cylinder pressure) increases the lift-off length (see Figure 2.8) it does not affect the amount of air entrainment upstream of the lift-off point (see Figure 7.20). This occurs because an increase in the air entrainment rate (fluid dynamically, the larger velocity gradients lead to higher entrainment rates) due to lower density fluid is proportionately offset by the fact that the lower density air has less mass per volume. Furthermore, as stated in Section 2.1.3, as injection pressure is increased, the flame lift-off length increases, as the flame tries to keep a constant Damköhler number, also suggesting more air entrainment

before the standing, rich premixed flame. Thus, in quiescent chambers, the main factors controlling air entrainment rates are bulk gas temperature and fuel injection pressure.

Although the above observations were made in a quiescent reaction chamber, the physics behind the observations can be extended to diesel engines. Based on Figure 2.9, large changes in injection pressure (at least a 10-20 MPa pressure change for small-diameter nozzles) are required to substantially change the lift-off height. Nowadays, common-rail fuel injection systems have typical operating pressures of about 140 MPa and are able to keep such high pressures regardless of engine load or speed [44]. Thus, the only avenue of changing the injection-pressure difference is through in-cylinder pressure changes. However, the substantial changes in injection-pressure difference required to increase the amount of air entrainment are unlikely to occur by in-cylinder pressure changes alone. Therefore, the gas temperature of the surrounding air is the main parameter that controls the amount of air entrainment up to the lift-off length in modern diesel engines.

Since the lift-off length of the diffusion flame in a diesel engine is largely dependent on the temperature of the unburned gas, changes in the engine operating conditions that affect the unburned gas temperature during the injection event play the largest role in determining the characteristics of the ensuing combustion event. The most important parameter that affects the cylinder temperature during injection is the start of the main injection of fuel and its phasing with respect to TDC while turbocharger boost pressure and the amount of aftercooling after the compressor play less significant roles.

With fuel injection occurring advanced from TDC, fuel is injected into an environment that continually heats up as the piston moves towards TDC. This results in reduced ignition delays, leading to standing premixed flames with richer equivalence ratios. Furthermore, the diffusion flame that forms does so in a very hot environment. Initially having elevated reaction rates, the flame lift-off point quickly moves closer to the injector tip to keep a constant Damköhler number. With the hot diffusion flame now enveloping more of the rich vaporized fuel-air mixture, heat transfer from the diffusion flame also reduces the mixing time required before the unburned fuel-air mixture reaches an appropriate condition to burn in the rich, standing premixed flame. As a result, the equivalence ratio of the rich, premixed flame is made more rich, reducing the overall temperatures in the interior of the fuel plume, slowing down the reactions that prepare the fuel for the diffusion flame, and causing an overall reduction in the oxidation rate of the fuel. As such, the flame structure physically appears more like the schematic on the left of Figure 2.12.

With fuel injection timing retarded from TDC, fuel is injected into an environment that is continually cooling as the piston moves down, expanding the gases and extracting work. Thus, ignition delays will be prolonged as the driving forces for autoignition are reduced. Also, as temperatures drop during the entire injection event, the length of time required before the injected fuel heats up and mixes with enough air to an appropriate condition before going through the first oxidation stage is increased,

forcing the standing premixed flame to become less and less rich as combustion proceeds. Furthermore, as the equivalence ratio of a rich premixed flame is made less rich, the temperature of the combustion products increases substantially. For example, with a mixture of methane and air at a fuel-air equivalence ratio of $\phi = 4$ starting at standard ambient conditions, the adiabatic flame temperature predicted by equilibrium codes (UWEQUIL, [45]) is $T_f = \sim 930$ K, while the same mixture at a fuel-air equivalence ratio of $\phi = 2$ starting at the same ambient conditions results in an adiabatic flame temperature of $T_f = \sim 1565$ K. Thus, as the temperature in the interior of the diesel flame is substantially increased, the laminar burning velocity (see Equation 2.1) and thermal diffusivity of the mixture increase, leading to faster and faster burning rates in the surrounding diffusion flame, decreasing the time required to burn a given amount of fuel. In summary, as combustion is phased later in the combustion stroke, substantially more mixing between fuel and air can occur, increasing the likelihood the flame structure resemble the schematic on the right of Figure 2.12.

7.1.2.2 SOC-to-10% Heat Release Duration

According to the new phenomenological model for diesel combustion, the autoignition of the initial mass of fuel establishes the standing premixed flame very quickly, only a few degrees after the start of injection [26]. Therefore, the duration between the start of combustion and the location of the 10% heat release gives a relative indication of the amount of fuel that autoignites in the initial premixed burn fraction and continues to release energy through pyrolysis and oxidation reactions. At constant cylinder conditions, short SOC-to-10% heat release durations are associated with larger amounts of fuel going through autoignition and subsequent pyrolysis and partial oxidation in the rich premixed flame, versus prolonged SOC-to-10% heat release durations. Although the SOC-to-10% duration is coupled to the ignition delay time as it describes the amount of mixing before autoignition (see Section 7.1.2.1) and thus the equivalence ratio of the standing premixed flame, other engine operating conditions can affect the initial heat release in diesel combustion.

In order to reduce both particulate matter and NO_x output, the test engine is equipped with a common rail fuel injection system, injects fuel around TDC, and uses multiple-injection fueling strategies. As a result of these emission-reducing technologies, the test engine has shorter ignition delays compared to older engines (on a time basis, 0.2 to 0.3 ms for the test engine vs. 0.4 to 1.5 ms for high-compression ratio and turbocharged engines [2]) along with combustion that occurs predominantly in the expansion stroke. This late phasing of combustion leads to trends not seen in older engines.

Based on Figure 7.21 and Figure 7.22, the 10% heat release location occurs at least 2° after SOC and at least about 6° after SOI in the low-load tests, suggesting the fuel-rich premixed zone is established

and growing[4] [26] (see Section 2.1.2 as well). As show in Figure 7.23, at stock EGR rates, the duration between the start of combustion to the point of 10% heat released essentially increases as timing is retarded from the most-advanced injection timing point. Also, comparing No. 2 diesel and FT diesel, the SOC-to-10% heat release duration is longer for every operating condition with FT diesel. This trend is a function of a fuel's associated ignition delay and the phasing of combustion with respect to TDC. Similar trends with respect to timing (No. 2 diesel shows an insensitivity to timing until the most-retarded injection condition) and fuel type are seen with the increased-EGR operating points (see Figure 7.24).

With ignition delays for each operating condition essentially the same, depending only on the fuel's CN or CNI, the SOC-to-10% durations should be relatively constant. Since the differences between the smallest and largest duration shown in the above figures are greater than the resolution of the data acquisition system, the prevailing physical conditions in the engine must then be playing a role in the initial heat release rate. Based on air entrainment concepts developed in Section 7.1.2.1, the similar temperatures shown in Figure 7.2 and Figure 7.5 during the start of injection along with the narrow spread ignition delay implies the amount of fuel and air mixing before the initial-premixed burn occurs must be similar [31], regardless of injection timing. Thus, the reaction rates governing autoignition and the subsequent diffusion flame should be similar. However, ensuing cylinder conditions change drastically as the SOI is retarded from the most-advanced point.

With the advanced injection timings occurring 6° and 2° bTDC, fuel injected up to TDC is sprayed into a cylinder that is continually heating up due to the compression process. This promotes a much more rapid heat release as the ensuing fuel vaporizes more rapidly and autoignites before TDC compared to the most retarded fuel injection timings. Also, at elevated ambient gas temperatures, the rate of oxidation and pyrolysis throughout the fuel-rich premixed zone is increased, releasing energy at greater rates, decreasing the SOC-to-10% heat release duration in the most-advanced timing condition. Thus, with the slightly advanced timing conditions, cylinder temperatures are suitably high to begin with, allowing for the relatively rapid evaporation and oxidation of the initial fuel. As injection timing is phased slightly after it TDC, all the fuel is injected while the piston is moving down. Therefore, the SOC is phased toward the expansion stroke, occurring at pressures and temperatures lower than those found at SOI. With combustion initiating in conditions with lower and lower unburned gas temperatures, the

[4] Although TDC conditions between the engine at MIT and the engine used in Sandia National Laboratories to produce the temporal development of the fuel spray in Figure 2.7 are drastically different, the point of autoignition in both cases occurs around the same point on a crank-angle basis (autoignition about 2° – 3° after SOI). This gives some validity in comparing combustion characteristics from the MIT test engine to the pictorials in Figure 2.7. The reason that the ignition delays are similar is attributed to the increased mixing of fuel and air from higher injection pressures with the common-rail injection system.

initial oxidation and pyrolysis rates steadily decrease, prolonging the SOC-to-10% heat release duration in the timing conditions occurring after TDC.

The temporal dependence of air entrainment suggest the SOC-to-10% heat-release duration should have an inverse relationship with ignition delay; shorter ignition delays lead to longer SOC-to-10% heat release durations. This is shown by the magnitude of the SOC-to-10% heat release durations with FT fuel. With similar trends based on phasing, FT fuel shows prolonged SOC-to-10% heat release durations compared to Number 2 diesel fuel at the same operating condition. This occurs due to FT fuel's higher CNI rating versus Number 2 diesel fuel, which implies less air entrainment and lower initial reaction rates when using FT fuel. Therefore, with near-TDC timing, the time of injection and not the fuel's CN control the SOC-to-10% heat release duration, a fuel's CN only describing the relative magnitude of the SOC-to-10% duration.

The physical phenomenon occurring in the SOC-to-10% burn durations at low loads is not evident at high loads. As Figure 7.25 and Figure 7.26 show, with the 10% heat release location at least 6° after SOI, the two-stage oxidation model of diesel combustion again suggests that the rich, standing premixed flame is established and growing spatially [26]. Unlike the low-load tests, Figure 7.27 and Figure 7.28 show the SOC-to-10% burn duration is constant for a specific fuel (No. 2 = 4.6° and FT = 5.0°) during all timing conditions at stock EGR rates. In the increased-EGR tests, both fuels have essentially the same SOC-to-10% durations of about 5.0°. The constancy of the SOC-to-10% burn duration is most likely attributed to the fact that fuel-air mixing is enhanced as injection pressures increased by about 13 –14 MPa while in-cylinder pressures increased by only about 3 – 4 MPa (see Figure 7.29 – Figure 7.32 for accumulator pressure data). Since cylinder temperatures were constant near injection leading to equivalent ignition delays, the initial premixed burn fraction, and thus the SOC-to-10% burn duration, is consistent due to the enhancement in bulk mixing of fuel and air in all timing conditions.

Compared to the low-load tests, the SOC-to-10% durations were longer in the high-load conditions. Since the overall integrated heat release scales with load, more time is required to reach the 10% point at high loads since the amount of fuel burned initially is not drastically different to the low-load cases, based on the similar ignition delays between the two load conditions.

7.1.2.3 10%-to-50 Heat Release Duration

The two-stage oxidation model of diesel combustion proposes the diffusion flame envelops the dispersing fuel-vapor jet only a few degrees the establishment of the standing, premixed flame [26]. Therefore, the 10%-to-50% heat release provides a relative indication of the initial inception of the diffusion flame that surrounds the continually oxidizing fuel-air jet.

Compared to heat release rate curves common to older engine technology (see Figure 7.33 and Figure 7.34), the heat release rates of the modern engine used in this study are drastically different (Appendix B). At low-loads, Figure 7.33 shows that the longer ignition delays in older engines result in a large initial peak, meaning a considerable amount of fuel underwent autoignition in the initial premixed burn. At higher loads, Figure 7.34 shows that the initial premixed burn is still dominant in older engines, although the magnitude is lessened due to decreased ignition delays. These curves suggest that the majority of the initial heat release is controlled by the autoignition event in older engines. Heat release curves (see Figure 7.35 and Figure 7.36) from the model year 2002 (MY 02) engine at MIT show that at low and high loads, the initial peak common in older engines is virtually non-existent, the only evidence that autoignition occurs is the change in slope as the curve rises to a single peak. Therefore, the diffusion flame dominates the initial heat release in a modern diesel engine.

Since the diffusion flame in a diesel engine burns stoichiometrically, or very close to stoichiometric, its adiabatic flame temperature is very high, ranging from 2300 K – 2700 K [29] depending upon initial conditions. As stated in Section 7.1.2.1, the adiabatic flame temperature of a rich premixed flame composed of methane and air can be quite low, and researchers suggest that the rich fuel-air mixture in a diesel fuel jet can range from 825K – 1600 K [29]. Therefore, once the diffusion flame establishes, the rate of heat release will completely dominate over the premixed flame.

Since the flame lift-off point delineates where the Damköhler number is of order magnitude one, the initial rate of reaction in the diffusion flame will be controlled by the amount of fuel-air mixing, dictated by the pressure difference across the nozzle during injection. Since the injection pressure in modern diesel engines is substantially higher than the peak pressures seen during combustion, the initial rate of heat release following the establishment of the diffusion flame will be mostly dependent upon the injection pressure. Therefore, the near-constant 10%-50% heat release durations shown in Figure 7.37 and Figure 7.38, for low-load experiments depending on EGR rates with both normal (8.8° ± 0.4° and 9.5° ± 0.2°) and synthetic fuel (8.4° ± 0.2° and 9.1° ± 0.4°) is expected. At high loads, Figure 7.39 and Figure 7.40 show a slightly longer duration, about ~1°, as timing is retarded from the most-advanced to the most-retarded timing cases with both EGR rates. This is most likely to due to the fact that the cylinder gases are cooling faster as combustion is phased past TDC (higher temperature gradients and surface areas), slowing down the chemical reaction rate in the diffusion flame.

7.1.2.4 50%-to-90% Heat Release Duration

Based on heat release analyses done on the low-load pressure traces, the EOI occurred from 2° – 4° before the location of 50% heat release, while analyses of the high-load pressure traces showed the EOI occurred very near EOI and up to 2° after the point of 50% heat release. Therefore, the 50%-to-90% heat

release duration describes the tail end of the quasi-steady portion of the two-stage oxidation process in diesel combustion. Up to this point, for a specific fuel, differences in the SOC-to-50% heat release durations have been no larger than 2.0° between the most-advanced and most-retarded injection timing for both high- and low-load tests. However, differences in the 50%-to-90% heat release as injection timing is swept over the chosen range clearly show the difference in overall combustion duration is due to the latter part of combustion.

Based on the 50%-to-90% heat release duration data shown in Figure 7.41, Figure 7.42, Figure 7.43 and Figure 7.44 (again, the H5, H15, FTH5, and FTH15 points are in question) the overall rates governing the combustion process are steadily increasing as the injection timing is retarded from the most-advanced injection timing. Even though the thermodynamic cycle efficiency is decreasing (notice increases in BSFC as injection timing is retarded in Figure 7.17 and Figure 7.18) as work is extracted from cooler gases, the combustion efficiency does not decrease, as the bsHC output remains constant, regardless of injection timing, shown in Figure 7.45 and Figure 7.46 (the changes in bsHC are due to changes of about 4 –5 PPM of C_3H_8 measured by the HFID). Chemical reaction rates must therefore be increasing since the amount of fuel injected into the cylinder to keep the BMEP constant increases as combustion is phased later in the expansion stroke. To increase the chemical reaction rates in diffusion flames, the diffusion-flame-rate characteristics must be improved (laminar burning velocity and/or thermal diffusivity) through changes in ambient conditions, reactant mixture state (equivalence ratio, temperature and pressure), and/or the extent of bulk motion mixing the fuel and oxidizer. For combustion phased towards the expansion stroke, the prevailing cylinder conditions diminish the burning velocity (the effect of the drop in temperature supersedes the effect of the drop in pressure, see Equation 2.1). Thus, either the mixing of fuel and oxidizer is improving or the unburned mixture is reaching a more reactive state as the piston moves away from TDC.

Two bulk-fluid-mixing phenomena governed by the piston were investigated as to the cause for the increase in mixing rate. Firstly, with a bowl-in-piston combustion chamber design, the reverse-squish velocity was investigated, as it is known to increase dramatically between motoring and firing conditions [46]. However, calculations using squish velocity relations [2] showed that the reverse-squish velocities at EOI were very similar, ranging from υ_{sq} = 0.70 m/s – 1.20 m/s regardless of load, between the extremes in injection timing. Thus, reverse-squish is most likely not playing a role in increasing the mixing rate of fuel and oxidizer. Secondly, flows induced by piston-cylinder wall interactions were compared. Comparing the Reynolds number at the wall at EOI, the flow grew from being turbulent to very turbulent sweeping from the most-advanced to the most-retarded injection timing (Re_w = ~$1.4x10^5$ to ~ $3.3x10^5$ at low loads, stock EGR; Re_w = ~$1.4x10^5$ to ~ $3.1x10^5$ at low loads, increased EGR; Re_w = ~ $3.7x10^5$ to ~$4.9x10^5$ at high loads, stock EGR; and Re_w = ~ $2.8x10^5$ to ~$4.0x10^5$ at high loads, increased EGR). The

Reynolds number where flow transitions between laminar and turbulent regimes (although only defined for pistons moving towards TDC) is around $Re_w = 1x10^4 - 2x10^4$ [2]. As there is a diminishing return in mixing once Reynolds numbers are very large, the piston-cylinder wall interaction is most likely not contributing to the large reduction in combustion duration. One last fluid-mixing phenomenon exists that is enhanced as the piston moves away from TDC, that being the increase in air entrainment into the interior of the diesel-fuel jet, unlike bulk mixing through the periphery of the diffusion flame as the two aforementioned piston-driven mixing phenomena act.

Air entrainment concepts derived earlier give another possibility to support the increase in chemical reaction rates as combustion occurs later in the expansion stroke. Since ambient gas density, and hence pressure do not play a role in the percent of stoichiometric air entrained, especially with common-rail fuel injection systems, the main driving force governing the amount of air entrainment is the ambient unburned gas temperature at EOI. To compare the differences in air entrainment, the temperature in the unburned gas at EOI was modeled by taking the bulk temperature of the cylinder at SOC (since it is mostly air, with some fuel) and compressing it adiabatically to the prevailing cylinder pressure at EOI. The ratio of specific heats used in the polytropic equation was taken from fully warmed, motored-engine tests when the data acquisition system was shaken down (see Section 5.4.1.1). As shown in Figure 7.47, Figure 7.48, Figure 7.49 and Figure 7.50, large differences in the unburned gas temperatures at EOI are evident between the injection-timing extremes; the differences accounting for the trend in combustion duration.

In the low-load tests, the temperature differences between the most-advanced timing conditions (Modes L5, FTL5, L15 and FTL15), and the most-retarded conditions (Modes L3, FTL3, L13 and FTL13), range from 90 K – 110 K. Using Figure 7.19 as a basis of comparison and noting that the diameter of the nozzles in the injectors in the test engine are 158 μm, moving from an ambient gas temperature of $T_{EOI\text{-}Adiabatic}$ = ~815 K (Modes L5 and FTL5) to $T_{EOI\text{-}Adiabatic}$ = ~715 K (Modes L3 and FTL3), changes the amount of stoichiometric air entrained into the fuel jet substantially (no data is available below 800 K in Figure 7.19, although the curve may be extrapolated). As the equivalence ratio of the standing premixed flame becomes less and less rich, the adiabatic flame temperatures increase, driving the overall gas temperatures up, enhancing the rate of burning in the diffusion flame. Similarly, at increased EGR rates, temperatures drop from about $T_{EOI\text{-}Adiabatic}$ = ~855 K (Modes L15 and FTL15) to $T_{EOI\text{-}Adiabatic}$ = ~755 K (Modes L13 and FTL13) again predicting a significant increase in air entrainment as injection timing is retarded. Again, bulk gas temperatures rise with increased EGR due to the recycling of hot combustion products.

Examining the behavior at high loads, although boost pressure increases, appropriate charge-air-cooling kept the intake temperatures essentially the same compared to low loads. Therefore, in-cylinder

temperatures during injection are similar regardless of load. Ambient gas temperatures drop from $T_{EOI\text{-}Adiabatic}$ = ~800 (Modes H5 and FTH5) to $T_{EOI\text{-}Adiabatic}$ = ~710 K (Modes H3 and FTH3) using stock EGR rates, while temperatures go from $T_{EOI\text{-}Adiabatic}$ = ~890 K (Modes H15 and FTH15) to $T_{EOI\text{-}Adiabatic}$ = ~810 K (Modes H13 and FTH13) at the increased EGR rates. The similar 50%-to-90% burn duration difference between injection timing extremes at high loads and low loads (~ Δ 3° – 4°) is attributed to the comparable cylinder conditions at EOI.

7.1.2.5 Combustion Duration Behavior and Fuel Properties

The figures at the end of the chapter showing the combustion duration for each operating mode also show a trend between the two fuels at low loads. The figures show that the combustion duration is shorter, in favor of FT fuel. Section 7.1.2.3 showed that the 10%-to-50% burn duration was essentially constant for a given fuel and differences between fuels were slight due to physical mixing dominating the combustion rate in the initial inception of the diffusion flame. Therefore, based on the preceding sections, CN/CNI ratings are only important in dictating the duration of the start and end of combustion in the test engine.

As explained in Section 7.1.2.2, the SOC-to-10% burn duration takes longer with FT fuel due to its increase CN number rating. Therefore, the decrease in overall burn duration due to fuel properties must be related to behavior at the end of combustion. In general, as combustion is phased later in the expansion stroke, the temperature of the ambient unburned gas decreases. As fuel is still being injected into the cylinder up until around the point of 50% heat release in both low- and high-load tests, the drop in cylinder temperature affects the autoignition chemistry of fuel at the end of injection. As CN increases, the sensitivity on ambient temperature before autoignition occurs is lessened. Therefore, especially with combustion phased in the expansion stroke, late-injected fuel of high CN, competing against the motion of the piston that is extracting work and cooling the gases, can still autoignite relatively quickly to keep the bulk cylinder temperatures warmer and reaction rates higher. This is clearly evident in Figure 7.41 and Figure 7.42, which show that the 3°- and 7°-retard conditions show the largest differences in 50%-to-90% heat release durations, versus timing near TDC.

Comparing the two fuels at high loads, except for the advanced-timing, high-EGR point, the combustion durations were essentially the same, or varied only slightly. The insensitivity of the burn duration to fuel type at a specific condition at high loads is attributed to the increase of the overall cylinder temperature and injection pressure that promote mixing and reduce the time before autoignition.

7.1.3 General Heat Release Trends Between Number 2 Diesel and FT Fuel

In order to meet current EPA emission requirements, the test engine uses a high-pressure common-rail fuel injection system, retarded fuel-injection strategies, a cooled EGR system, and a VGT turbocharger. The implementation of the first two aforementioned emission-reducing methods results in heat release characteristics in modern engines that differ substantially from older engines. In general, compared with Figure 7.33 and Figure 7.34, the heat release graphs found in Appendix B do not exhibit the usual dual-peak heat release characteristic. The small spike before the large heat release portion in the graphs is due to the pilot injection of the overall fueling strategy. It does not correspond to the initial premixed burn fraction as only about 3% or less of the fuel is injected during the pilot injection. The lack of an initial, premixed burn peak is a function of the small ignition delays and increased injection pressures that reduce the size of the initial fuel-rich mixture that autoignites. Thus, as the majority of the fuel is burned in a diffusion flame, usually one peak persists, although premixed burn peaks are sometimes present depending the degree of injection retard, as evinced by the aforementioned figures.

At low loads and stock EGR rates, summarized in Figure 7.51, FT fuel has higher maximum heat release rates, by about 0.040 MJ/s (note, absolute numbers are not necessarily correct), versus No. 2 diesel fuel. According to Figure 7.52, the location of maximum heat release is similar for both fuels, occurring slightly before the point of 50% heat release. The combination of the two figures supports the previous discussion that FT's higher CN allows for a more rapid autoignition of late-injected fuel at the tail end of combustion, where the unburned gases are cooling from the downward motion of the piston.

At low loads with increased EGR rates, the difference in maximum heat release rates is suppressed at timing conditions before TDC, as shown in Figure 7.53. The overall-higher gas temperatures reduce the effect of FT fuel's CNI advantage, closing the gap between the maximum heat release rates. The retarded injection timings show increasingly larger differences between the two fuels, again based on the fact the higher CNI rating of FT diesel fuel allows for faster oxidation even as the cylinder contents have cooled due to the late SOC. The slight reduction in the maximum rate of heat release in some timing conditions as EGR is increased is due to the rise in the burned gas fraction that is know to decrease the laminar burning velocity [2]. Since the composition of EGR at low loads still contains a considerable amount of excess air, the oxygen concentration does not drop by much when EGR is increased, only slightly affecting the rate of reactions in the diffusion flame.

In general, the heat release curves for FT diesel show that the heat release rate races to a peak sooner than No. 2 diesel, due to the reduced ignition delay times with FT fuel at low loads. Also, although the maximum heat release rates for FT fuel are different from No. 2 diesel at the low load conditions discussed above, the general shape and characteristics of the heat release curves for each operating condition are essentially the same. These suggest that the oxidation pathways for each fuel are

not drastically different [47], although the oxidation rates are different, based on each fuel's CN rating. Of note however, are the most-retarded injection timings at stock and increased EGR rates (Modes L3, FTL3, L13, and FTL13). As combustion in these conditions is phased furthest away from TDC, fuel is injected into increasingly cooler conditions, making autoignition chemistry more important. The two No. 2 diesel curves approach the behavior of the classical heat release shape, as two peaks are clearly evident, supporting the fact that the initial and standing premixed flame are increasingly important due to the low CN number rating of the fuel. Under the same engine conditions with FT fuel, the peak due to the premixed flame is heavily reduced in magnitude, again a function of FT fuel's higher CNI rating.

At high loads, except for the values of the maximum heat release rate in some conditions, the shapes, features, and magnitudes of the heat release curves for both fuels are very similar, as summarized in Figure 7.55, Figure 7.56, Figure 7.57 and Figure 7.58. Since the ignition delays between the two fuels are similar, both fuels show the rise to the maximum heat release point occurring around the same time after injection. Thus, as stated before, the oxidation pathways for both fuels are similar, the only differences between the two fuels being the rates of the elementary reactions. With elevated temperatures to drive the reactions forward, both fuels burn with similar characteristics.

7.2 Emissions Characteristics

The heterogeneous, two-stage oxidation characteristics of diesel combustion establish oxides of nitrogen (NO_x) and particulate matter (PM), defined as a conglomeration of soot, sulfates, and volatile species as the dominant pollutants in a diesel engine (see Section 2.1.2). Due to the overall-lean operation of diesel engines, carbon monoxide (CO) levels are negligible, while the compression of only air during the compression stroke prevents fuel from entering the crevices, leading to minor levels of unburned hydrocarbons (UHC). As such, the following discussion focuses only on the NO_x and PM behavior in the experiments.

7.2.1 NO_x Emission Trends with Engine Operating Characteristics

As shown in Figure 7.59 and Figure 7.60, NO_x output is a strong function of injection timing. This well-known trend is a function of the peak gas temperatures during combustion. As shown in the pressure traces for each load condition and fuel, (see Appendix A for graphs) phasing of combustion affects the peak cylinder pressures, and hence, peak cylinder temperatures. Using the single-zone heat release model, the bulk cylinder temperature at the maximum pressure after SOC increases appreciably as injection timing is advanced from the stock timing point while noticeable temperature reductions occur as timing is retarded from stock (see Figure 7.61, Figure 7.62, Figure 7.63 and Figure 7.64). Since the predominant NO_x-formation mechanism in diesel engines is thermally driven, NO_x emissions should scale

with peak cylinder temperatures. Interestingly, the gas temperatures in the exhaust manifold show the opposite trend with timing, lower temperatures in advanced timing with higher temperatures in retarded timing, contradicting the measured trends. However, the increase in exhaust gas temperature is a function of the reduced cycle efficiency and phasing of combustion, supported by increases in BSFC with timing retard. As combustion occurs later in the expansion stroke, less work is extracted per crank angle due to the thermodynamic reduction in efficiency with cooler working fluids, resulting in elevated exhaust gas temperatures.

Figure 7.59 and Figure 7.60 also show that NO_x output is also strongly dependent upon EGR rates. Increasing EGR was effective in decreasing $bsNO_x$ for both fuels at every operating condition. At low loads, NO_x outputs dropped from 10% – 16% when moving from reduced EGR rates to stock EGR rates. Moving from stock EGR rates to increased EGR rates, NO_x reductions ranged from 20% – 30%. At high loads, NO_x outputs dropped from 22% – 32% when increasing EGR rates from the reduced- to stock-EGR set points. Increasing EGR from the stock setting, NO_x outputs dropped from 38% – 46% at high loads.

Comparing the results between engine outputs, the effects of EGR are more pronounced at high loads. This stems from the composition of EGR at high loads. As stated in Section 1.3, EGR effectively reduces NO_x in two distinct ways. Similarly to SI engines, EGR acts as a diluent with added heat capacity, helping reduce peak gas temperatures. More importantly for diesel engines, especially at high loads, EGR reduces the amount of oxygen available. As the fuel-air equivalence ratio increases towards the stoichiometric value, the mole fraction of oxygen steadily decreases while the mole fractions of both carbon dioxide (CO_2) and water vapor (H_2O) steadily increase in the exhaust-gas composition (see Figure 7.65). Furthermore, as the exhaust gas is composed of more polyatomic species, the heat capacity increases (based on the Kinetic Theory of Gases), shown by a related decrease in $\gamma_{exhaust}$ as the fuel-air equivalence ratio increases towards $\phi = 1$ (see Figure 7.66).

7.2.2 NO_x Emission Trends with Fuel Properties

Data on the adiabatic flame temperature of the Syntroleum Fischer-Tropsch fuel is not available, so a flame temperature correlation based on fuel composition [48] was used to predict the adiabatic flame temperature. The flame temperature correlation was used for No. 2 diesel as well, as most adiabatic flame temperature data in the literature is that of primary reference fuels and not practical fuels. Syntroleum states their FT fuel has the simplified chemical composition of $CH_{2.12}$, while No. 2 diesel fuel can be taken as $CH_{1.80}$ [2]. Based on these ratios, the equation predicts adiabatic flame temperatures of stoichiometric mixtures of about ~2270 K and ~2280 K for FT and No. 2 diesel fuel respectively starting from standard temperature and pressure. Although the expected trend of higher H/C fuels having lower

flame temperatures is correctly predicted, the flame temperature equation does not apply to fuels with olefin concentrations greater than 10% by volume. Since No. 2 diesel can have anywhere from 20% – 30% total aromatic content, another check was done to compare the adiabatic flame temperatures of the two test fuels.

The adiabatic flame temperature based on the first law of thermodynamics are: ~2480 K and ~2482 K respectively for No. 2 diesel and FT diesel fuel. The large difference between the flame-temperature correlation and the first-law approach is the fact that the correlation accounts for full equilibrium and dissociation while the first-law approach assumes ideal combustion. By comparing lower heating values, the reason for similar flame temperatures between the two fuels is evident. The Syntroleum Corporation has available on their website a brochure about their S-2 fuel [54]. Syntroleum reports a lower heating value, measured using the ASTM D-240 method, of 121,500 Btu/gal and compares it to the EPA No. 2 Diesel requirement of 129,400 Btu/gal. As the No. 2 diesel fuel meets EPA requirements for No. 2 classification, the value reported by Syntroleum was used in further comparisons. Calculating the heating value of the fuel on a mass basis, the No. 2 diesel fuel has a lower heating value of 42.9 MJ/kg while the Syntroleum Fischer-Tropsch fuel has a lower heating value of 43.7 MJ/kg. Although the volumetric energy content of most FT fuels is lower than normal diesel, FT fuel's lower density can actually make it more energy dense on a mass basis, depending on the actual properties of a given FT fuel. Yet, although the lower heating value of FT fuel is about 1.8% higher than No. 2 diesel's heating value, suggesting higher adiabatic flame temperatures, the increased air/fuel ratio to burn FT (about 3.1% more air required) offsets the increased lower heating value.

The empirical formulation and thermodynamic data predict almost equivalent flame temperatures with the two test fuels, suggesting the thermally driven extended Zeldovich mechanism, highly activated at temperatures above 1700 K [5], should produce similar NO_x emissions between the two fuels. Additionally, the similarities in bulk cylinder temperature shown in Figure 7.61, Figure 7.62, Figure 7.63 and Figure 7.64 show that NO_x emissions should be almost constant, irrespective of fuel properties.

However, Figure 7.59 and Figure 7.60 show this is not necessarily true as no clear trend is seen based on the argument above. At low loads, the NO_x data seem to be very similar, although FT seems to produces more NO_x as timing is advanced and less NO_x with timing retard while at high-loads, FT fuel shows reductions in NO_x emissions at all timing points. Taking into account the NO_x values reported for the stock-EGR tests at low load may be slightly off (see Section 6.4), comparing it to the behavior at the increased EGR rates shows that from the stock injection timing to the most-retarded timing condition, the NO_x values are almost constant, while both curves show NO_x increases as timing in advanced. No clear theory describes this trend, except for the thermodynamically derived adiabatic flame temperature, showing FT burns hotter than No. 2 diesel. As timing is advanced, peak cylinder temperatures rise.

Since the extended Zeldovich mechanism is exponentially dependent on temperature, the slight increase in adiabatic flame temperature predicted for FT from the lower heating value may increase the NO_x emissions accordingly.

At high loads, FT fuel consistently reduces NO_x emissions (again note stock-EGR curve was corrected although it shows behavior like the increased-EGR case) even though the similar bulk cylinder temperatures when using either fuel suggests the kinetic rates driving NO_x should be similar. An explanation of this behavior is suggested by Lee et. al. [35]. Lee et. al. believe the H/C ratio of a fuel can also impact NO_x emissions by influencing another aspect of the kinetic pathway through reductions of the concentration of species required by the rate-limiting step in the extended Zeldovich mechanism. As shown in Figure 7.65, the mole fraction of water in the exhaust gas of FT fuel is slightly higher than No. 2 diesel fuel due to its higher H/C ratio. Lee et. al. go further and propose that since water has a lower tendency to dissociate at high temperatures compared to carbon dioxide, fuels with higher H/C ratios will have lower concentrations of $\dot{O}$ radicals (see also Equation 2.9), reducing the kinetic production of NO_x as it relies on radical-oxygen concentration as shown in Equation 2.8. Furthermore, Figure 7.65 shows that the concentration of nitrogen is lower for the high-H/C ratio FT fuel. Again, based on Equation 2.8, a reduction in nitrogen concentration should reduce the production rate of NO_x. Although the above arguments should also apply to the low-load tests, the difference in H_2O and N_2 mole fractions between FT fuel and No. 2 diesel fuel decreases as the overall fuel-air equivalence ratio decreases, while the mole fraction of oxygen rises substantially as conditions become more lean. As such, the importance of H_2O dissociation decreases as the radical-oxygen contribution from molecular oxygen takes precedence.

7.2.3 Particulate Matter Emission Trends with Engine Operating Characteristics

The low-load brake-specific particulate matter (bsPM) output trends shown in Figure 7.67 show a peculiar behavior. Normally, particulate-matter levels reach a minimum as timing is optimized for a specific load, speed, and EGR rate. However, the low-load trends show that the PM output of the test engine actually had locally-maximized PM outputs at the factory injection timing settings and at timings close to TDC (Modes L4 and FTL4) while PM levels drop as injection timing is moved away from TDC. In addition, for a well-optimize direct-injection (DI) diesel engine, the well-established tradeoff between particulate matter and NO_x is usually independent of engine speed, injection rate, injection timing, and EGR [2]. Therefore, based on Figure 7.59, one would expect PM output to drop as timing is advanced (increasing NO_x as shown) and increase as timing is retarded (decreasing NO_x as shown).

The final output of PM is based on two competing processes, the extent of both PM formation and oxidation. Many models for soot formation and oxidation exist [55] ranging in scope from empirical,

semi-empirical, and detailed-chemistry formulations. Empirical models are relatively crude, as they do not separate formation and oxidation in their prediction of soot while detailed-chemistry models came become overly complex. A commonly used semi-empirical model in diesel engines is that of Hiroyasu [57] that considers the overall soot mass formation rate, $\frac{dM_s}{dt}$, as function of the formation rate, $\frac{dM_{sf}}{dt}$, and oxidation rate, $\frac{dM_{so}}{dt}$, considered separately from one another:

Equation 7.4
$$\frac{dM_s}{dt} = \frac{dM_{sf}}{dt} - \frac{dM_{so}}{dt}$$

Equation 7.5
$$\frac{dM_{sf}}{dt} = A_f M_{fv} p^{0.5} \exp\left(\frac{-E_f}{\tilde{R}T}\right)$$

Equation 7.6
$$\frac{dM_{so}}{dt} = A_o M_s x_O p^{1.8} \exp\left(\frac{-E_o}{\tilde{R}T}\right)$$

In Equation 7.5, A_f is the pre-exponential factor for soot formation, M_{fv} is the mass of fuel vapor, and E_f is the activation energy for soot formation. In Equation 7.6, A_o is the pre-exponential factor for oxidation, M_s is the mass of soot, and x_O is the mole fraction of molecular oxygen. Common to both rate equations are the pressure and temperature of the cylinder, p and T, along with the universal gas constant. The formation and oxidation rate equations proposed by Hiroyasu are both Arrhenius-type rate equations with activation energies of $E_f = 8 \times 10^4$ kJ/mol for formation and $E_o = 12 \times 10^4$ for oxidation. The magnitudes of each make sense since formation occurs at lower temperatures than oxidation, so its activation energy should be lower.

Based on the fact that higher peak cylinder pressures and temperatures lead to increasing NO_x as injection timing is advanced, the overall PM output is most likely a difference of two large numbers as formation and oxidation rates are likely elevated. Since PM drops as the cylinder gets hotter, the oxidation rate is most likely dominating as injection timing advances, leading to the drop in PM shown in the data. Combine this with the fact that the combustion duration grows with injection timing advance, and the time for PM oxidation increases helping to lower the overall engine-out PM level.

As combustion is phased after TDC, the overall cylinder conditions become cooler as the piston expands the cylinder contents. With the drop in temperatures during fuel injection after TDC, the rate of formation of soot is most likely decreasing. Furthermore, the amount of air entrainment before the

standing premixed flame seems play a role in the overall soot formation process. Flynn et al. showed [29] that as more oxygen is mixed with the fuel-rich vapor feeding the premixed flame, less carbon went into soot precursor formation and more went into forming carbon monoxide. As suggested using flame lift-off theory in Section 7.1.2.4, air entrainment increases as the unburned gases in the cylinder cool. Therefore, as timing is retarded away from TDC, the PM levels should drop as the data show since less soot is initially formed.

The behavior at high loads is somewhat muddled, although the above theory still applies. In general, peak in-cylinder pressures and temperatures rise as load increases. With stock and reduced EGR rates, the oxidation mechanism seems to be dominant as timing is advanced due to the elevated bulk cylinder temperatures while reductions in soot oxidation as timing is retarded is accompanied by similar reductions in soot formation helping keep the overall PM output low. In the increased-EGR conditions, the rate of soot oxidation seems to be lower than its formation rate. The relatively smaller amount of fuel-air mixing may be contributing to this trend. As timing is retarded and air entrainment increases, the PM output level drops, suggesting the increased mixing reduces the soot formation rate.

Another trend common to both fuels shown in the aforementioned bsPM graphs is the increase of PM as EGR rates increase. In general, EGR reduces the overall flame temperature through the increase in heat capacity of the recycled exhaust gases and reduces the oxygen concentration of the fresh air by diluting it with burned-gas products. The combination of the reduced temperature and oxygen concentration lowers the soot oxidation rate seen in Equation 7.6. A scanning-mobility particle size (SMPS) scan (see Figure 7.71) corroborates this by showing the size distribution moves towards more and larger particles. Since oxidation is less important, the soot formed initially can grow into larger carbonaceous agglomerates as combustion progresses.

7.2.4 Particulate Matter Emission Trends with Fuel Properties

Before any conclusions were made on the effectiveness of fuel properties in reducing PM outputs, the sampling system (sampling either raw or diluted exhaust) used to take the presented particulate data was investigated. Prior to running any tests on FT fuel, extensive tests were done with No. 2 diesel to characterize the dilution system and sampling system. For the final dilute-sample numbers with No. 2 diesel, twelve filter paper samples were taken at the low-load condition with stock fuel injection timing and EGR rates with dilution ratios from 6 – 7 (to reduce sampling time). The diluted sampling resulted in PM outputs very close to data provided by Cummins. Cummins reports a PM output of 0.167 g/kW-h at this load point while measurements at MIT were 0.169 ± 0.011 g/kW-h. This gave confidence in sampling with a dilute exhaust. Replicating the engine conditions while sampling the hot, raw exhaust gave a PM output of 0.0981 ± 0.004 g/kW-h, a reduction of about 0.071 g/kW-h in total PM. With FT

fuel, a diluted sample was taken at the same conditions as stated above, resulting in a PM output of about 0.106 ± 0.005 g/kW-h, while a raw sample gave a PM output of 0.028 ± 0.005 g/kW-h, a reduction of about 0.078 g/kW-h.

Although the reduction in both cases is similar, the percentage reduced is drastically different for the two fuels. Based on the above numbers, the PM output drops by about 42% with No. 2 diesel fuel and about 74% with FT diesel fuel. This phenomenon is attributed to particle dynamics and transformations that occur in the exhaust pipe, including coagulation, nucleation, adsorption and condensation. The surface area available for mass transfer affects all these physical processes, making some dominant over others. For example, if the number of carbonaceous agglomerates is low, as in FT fuels that have low aromatic contents, saturation ratios[5] will rise, triggering the homogenous condensation of volatile species. However, if large numbers of carbonaceous agglomerates survive the in-cylinder combustion process, such is the case with No. 2 diesel, condensable gas-phase species will preferentially adsorb onto the agglomerates, preventing saturation ratios from becoming too large, ending any chance for the homogenous nucleation of gaseous species to occur. As such, it is common for modern engines that are designed to reduce the amount of carbonaceous agglomerates to have PM that is composed more of soluble organic fraction (SOF) and sulfate compounds than older engines that produce more carbonaceous agglomerates [56]. In the test engine, switching fuels from No. 2 diesel to FT diesel reduced the amount of carbonaceous agglomerates (see later discussion in this section), resulting in a larger portion of the PM in the diluted FT exhaust originating from SOF-based compounds.

As the elevated temperatures during the raw sampling method reduce the driving force for gaseous particles to condense (vapor pressure increases with temperature) onto carbonaceous agglomerates, the overall PM output drops. According to Kittelson et al. [56], typical diesel exhaust (without any after-treatment devices) has sulfuric acid concentrations ranging from 5 – 20 PPM when using fuel with a sulfur content of 0.04% by mass. The No. 2 diesel used in the experiments has exactly this sulfur content, so estimations were made as to the sulfate contribution to PM for this fuel. Using this sulfate-exhaust concentration, the exhaust of the test engine should have sulfate levels between 0.015 – 0.060 g/kW-hr at the stock timing, stock EGR, low load condition. Thus, the drop in PM for No. 2 diesel when sampling raw is attributed to the reduction of the sulfate contribution to PM. The FT fuel used in the tests is essentially sulfur-free, so the PM of FT diesel fuel is composed primarily of SOF. Based on the above discussion, the large drop in PM due to the raw-sampling method is not unlikely, as the gaseous species do not have many sites to condense and condensation is difficult at high temperatures. Therefore,

---

[5] The saturation ratio (S) is the ratio of the partial pressure of a condensable species to its local vapor pressure. For intermediate values of S, adsorption onto carbonaceous agglomerates is more likely to occur. As S approaches one, the homogenous nucleation (condensation) of the gaseous species will occur.

comparisons of the PM output between No. 2 diesel and FT fuel focus are still valid with the raw-sampling method, with the focus on carbonaceous agglomerate formation and destruction.

Neglecting the increased-EGR runs done only with No. 2 diesel, FT shows PM reductions in all operating conditions, consistent with many other results from the literature. The reductions ranged from about 53% – 56% at low loads and about 72% – 89% at high loads. Based on the raw sampling method, the PM collected in the experiments is most likely carbonaceous agglomerates. Therefore, the PM reductions must be related to the soot particles themselves, and not to the species that usually contribute to surface growth such as volatile species and sulfates. The reason for the reduction in soot particles due to fuel properties is most likely the chemical structure of the fuels themselves. According to Flynn et al., when the atomic oxygen to carbon (O/C) ratio decreases to values in the range of 1.3 to 1.6 in the standing premixed flame, soot precursors are no longer formed. The O/C ratio of No. 2 diesel fuel and FT fuel are $2.93\phi^{-1}$ and $3.06\phi^{-1}$ respectively, based on the ideal combustion of both fuels. Since these are very close, the O/C ratio at the premixed flame should be similar for each fuel, although possibly higher for No. 2 since during the transient portion of fuel injection and near the end of injection its longer ignition delays allow for better mixing of fuel and air compared to FT fuel. Based on this fact, PM output of No. 2 diesel should be as low as, or even better than, FT fuel. This is not the case as the data shows, however.

As described in Section 2.2.2, soot is primarily composed of polycyclic aromatic molecules. An important precursor species to the formation of aromatic rings is acetylene (C_2H_2). As fuel molecules are known to break into smaller, lighter species as reactions begin to occur [1], the chemical composition of a fuel does not dictate the concentration of lighter species; paraffinic fuels will not make less multiple-bond species just because they are predominantly made of single-bond carbons. Thus, the presence and/or absence of acetylene as a soot nucleation precursor is not a factor driving the PM differences between the two fuels. Frenklach and Wang [58] and Richter et al. [59] suggest that the initial inception of the smaller polycyclic aromatic hydrocarbons (PAHs) that eventually combine to form soot is dependent upon the availability of aromatic molecules after the initial breakdown of the fuel molecules. If aromatic molecules are present, the hydrogen-abstraction carbon-addition (HACA) mechanism can proceed directly on a simple aromatic to form the second aromatic rings. The process generally occurs as such: 1) a free hydrogen atom can abstract an existing hydrogen atom from an aromatic molecule such as benzene, forming an aromatic radical, 2) an acetylene radical reacts with this active site, 3) the HACA process continue on an adjoining carbon in the benzene ring, with the end result being two acetylene radicals attached to two neighboring carbon atoms in the benzene ring, 4) cyclization of the two acetylene radicals leads to an aromatic with two rings [1]. The above process continues to form larger and larger PAHs. If, however, no aromatic molecules are present, acetylene must react to form the first ring, such that the

above HACA mechanism can act upon this first ring to grow larger and larger particles. To form an aromatic ring, acetylene 1) forms a propargyl radical (C_3H_3) by pyrolysis, and 2) two propargyl radicals then recombine to form a benzene ring. After this benzene ring is formed, the HACA mechanism can proceed to grow the 1st aromatic ring to larger PAHs. Therefore, based on the fact that the FT fuel from the Syntroleum Corporation has less than 0.001% by weight aromatics (see fuel specifications), more time is spent forming the first rings than growing larger PAHs, leading to a reduction in PM when using FT fuel.

Comparing the dilute-sampling and raw-sampling case for the stock timing, stock EGR, low load condition, a reduction of about 37% in PM occurs when FT diesel fuel is used. Considering only the sulfate contribution estimated earlier in this section (0.015 – 0.060 g/kW-hr), removing fuel sulfur can account for PM reductions from 9% – 36%. Based on these estimations, the observed PM reductions with FT fuel under diluted sampling conditions may be primarily from the reduction of the sulfate contribution to PM.

7.3 Performance Trends and Tradeoffs

Inspecting the bsPM-bsNO_x tradeoff curves for each load condition show atypical behavior compared to the well-established bsPM-bsNO_x tradeoff in performance for diesel engines. Based on discussions above, in the low-load experiments, air entrainment as combustion is phased later in the expansion stroke seems to explain the drop in PM where an increase is expected. In the high-load tests, a slight bsPM-bsNO_x tradeoff with injection timing seems to be shown for the stock- and reduced-EGR test. At high EGR rates, better air entrainment as timing is retarded helps lower the PM output.

The BSFC-bsNO_x tradeoff curves shown in Figure 7.72 and Figure 7.73 seem to follow more closely to the well-established BSFC-bsNO_x tradeoff curves, especially with FT fuel. A few unexpected points occur at high loads, possibly due to unknown optimizations in the engine's ECM. In general, as injection timing is retarded, cylinder temperatures drop, reducing NO_x output, but also cycle efficiency. Thus, fuel consumption must increase to compensate for the reduction in fuel conversion efficiency. FT fuel consumption is shown to be more sensitive to injection timing even though the injection duration is the same, most likely due to the fact that FT fuel has a lower energy density by volume compared to No. 2 diesel fuel. An analysis of fuel density shows the lower density of the FT fuel used results in a ~4% lower volumetric flow rate through the fuel injector for a given pressure differential. Thus, since less energy is injected per unit time, less work can be extracted per unit time. Therefore, more fuel needs to be injected when running on FT fuel, especially as cylinder conditions cool when timing is retarded.

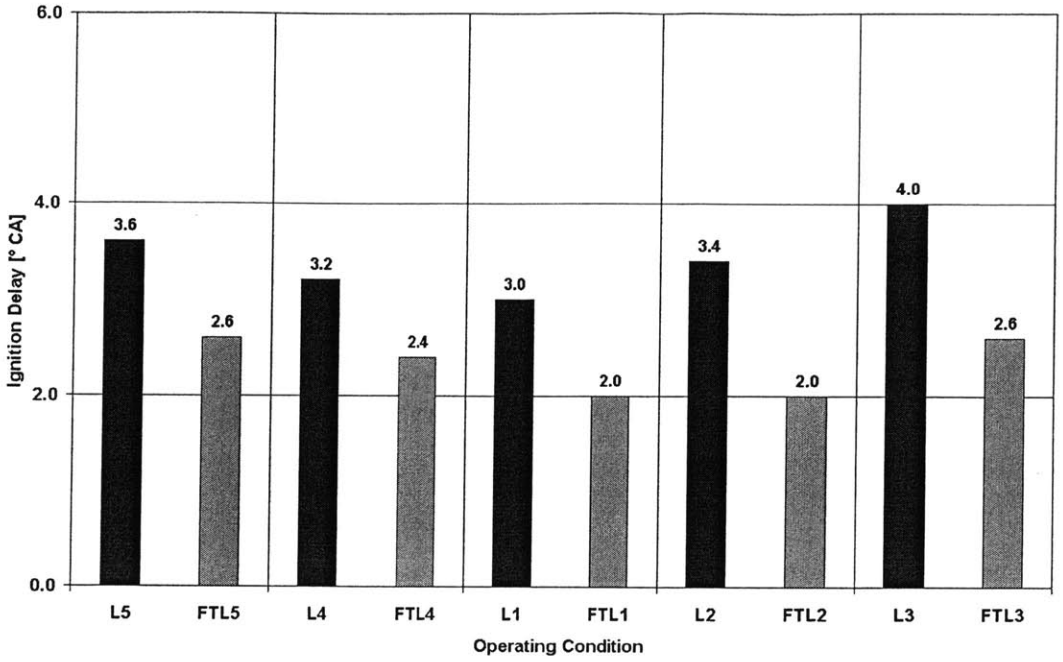

Figure 7.1 Ignition delay comparison between No. 2 diesel fuel and Fischer-Tropsch fuel during timing-sweep tests with stock EGR rates in low-load tests. The operating conditions are normal diesel (L1 – L5) and Fischer-Tropsch (FTL1 – FTL5). Stock timing is in the center with the most advanced timing to the left and the most retarded timing to the right.

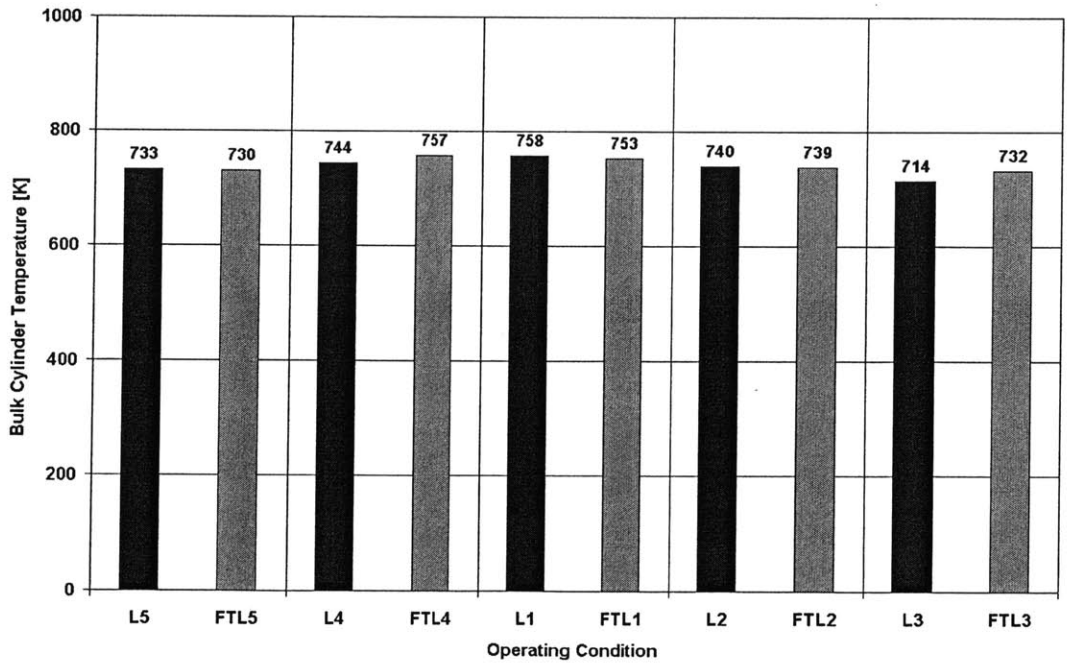

Figure 7.2 Bulk cylinder temperature at the start of injection using No. 2 diesel fuel and Fischer-Tropsch fuel during timing-sweep tests with stock EGR rates in low-load tests. The operating conditions are normal diesel (L1 – L5) and Fischer-Tropsch (FTL1 – FTL5). Stock timing is in the center with the most advanced timing to the left and the most retarded timing to the right.

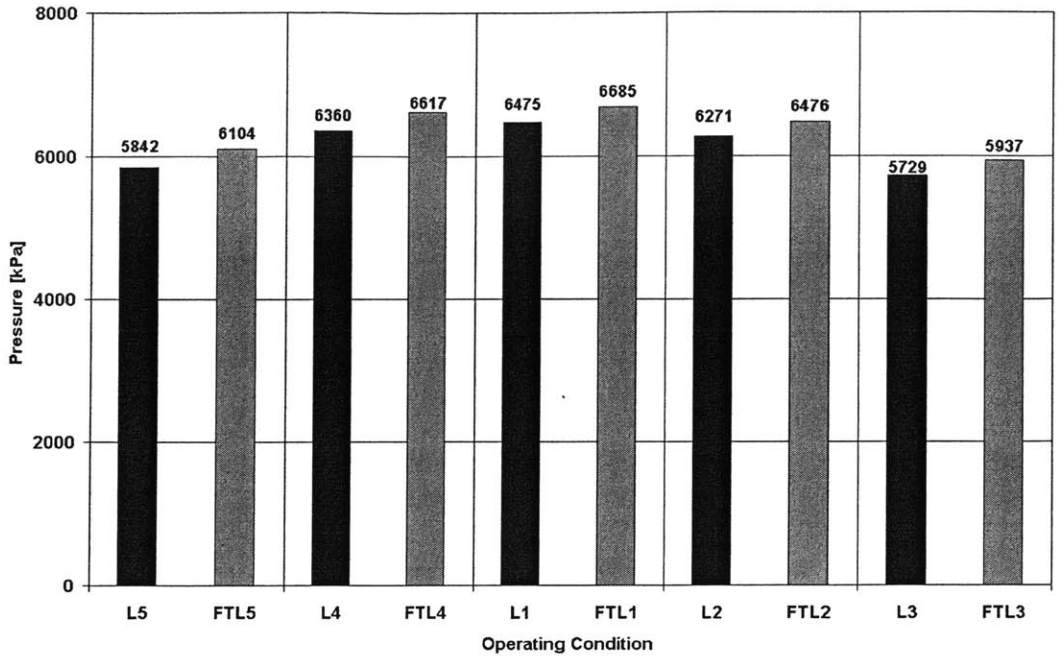

Figure 7.3 Cylinder pressure at the start of injection using No. 2 diesel fuel and Fischer-Tropsch fuel during timing-sweep tests with stock EGR rates in low-load tests. The operating conditions are normal diesel (L1 – L5) and Fischer-Tropsch (FTL1 – FTL5). Stock timing is in the center with the most advanced timing to the left and the most retarded timing to the right.

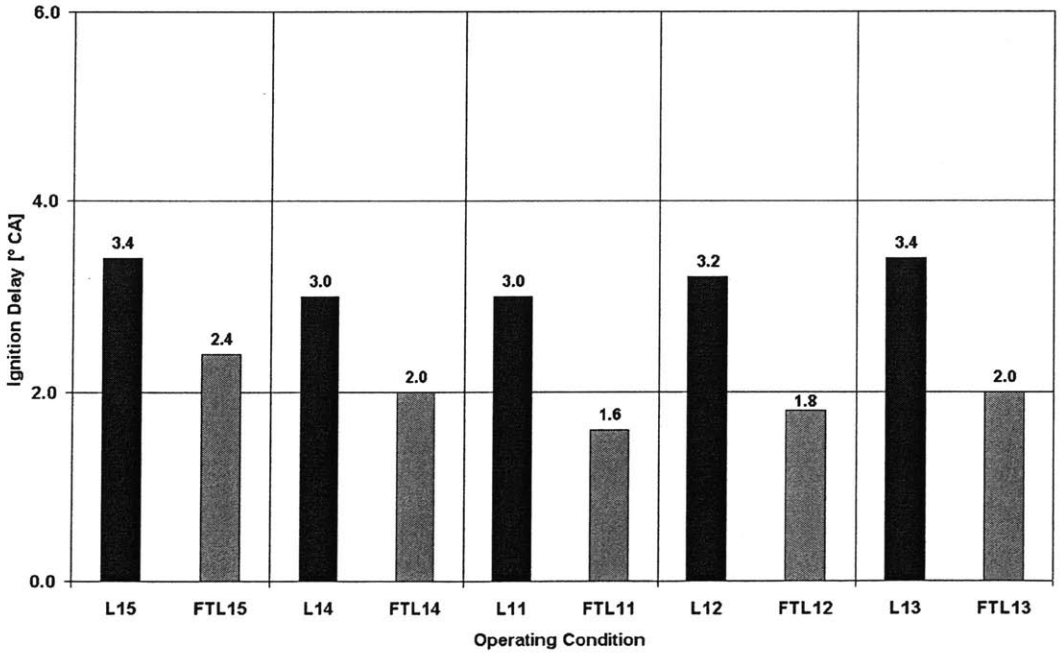

Figure 7.4 Ignition delay comparison between No. 2 diesel fuel and Fischer-Tropsch fuel during timing-sweep tests with increased EGR rates in low-load tests. The operating conditions are normal diesel (L11 – L15) and Fischer-Tropsch (FTL11 – FTL15). Stock timing is in the center with the most advanced timing to the left and the most retarded timing to the right.

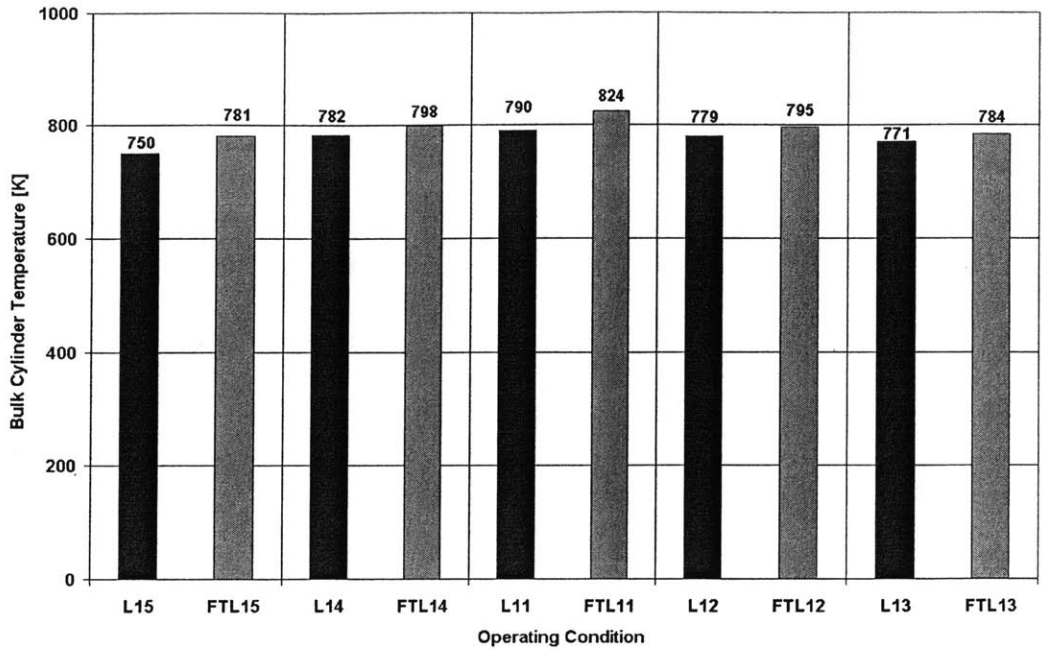

Figure 7.5 Bulk cylinder temperature at the start of injection using No. 2 diesel fuel and Fischer-Tropsch fuel during timing-sweep tests with increased EGR rates in low-load tests. The operating conditions are normal diesel (L11 – L15) and Fischer-Tropsch (FTL11 – FTL15). Stock timing is in the center with the most advanced timing to the left and the most retarded timing to the right.

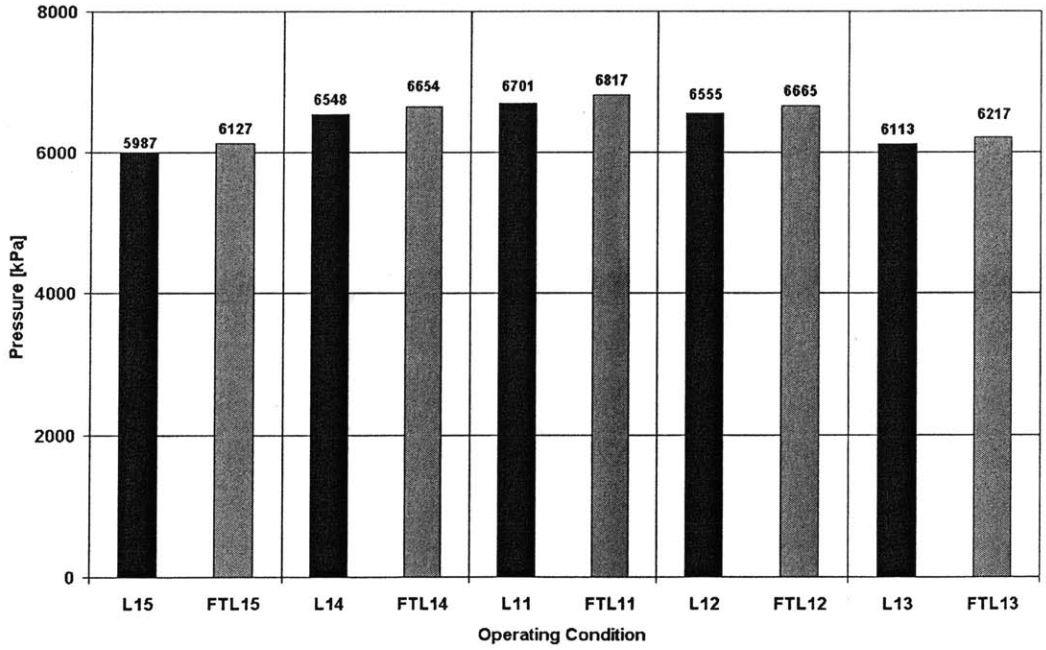

Figure 7.6 Cylinder pressure at the start of injection using No. 2 diesel fuel and Fischer-Tropsch fuel during timing-sweep tests with increased EGR rates in low-load tests. The operating conditions are normal diesel (L11 – L15) and Fischer-Tropsch (FTL11 – FTL15). Stock timing is in the center with the most advanced timing to the left and the most retarded timing to the right.

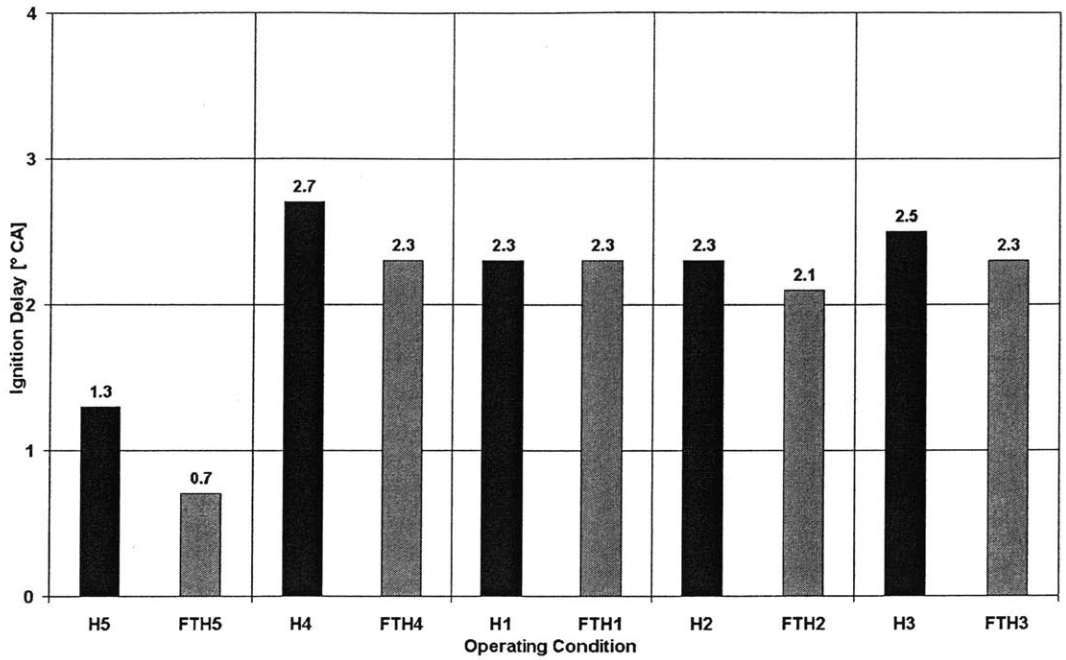

Figure 7.7 Ignition delay comparison between No. 2 diesel fuel and Fischer-Tropsch fuel during timing-sweep tests with stock EGR rates in high-load tests. The operating conditions are normal diesel (H1 – H5) and Fischer-Tropsch (FTH1 – FTH5). Stock timing is in the center with the most advanced timing to the left and the most retarded timing to the right. The leftmost point (H5 and FTH5) is suspect.

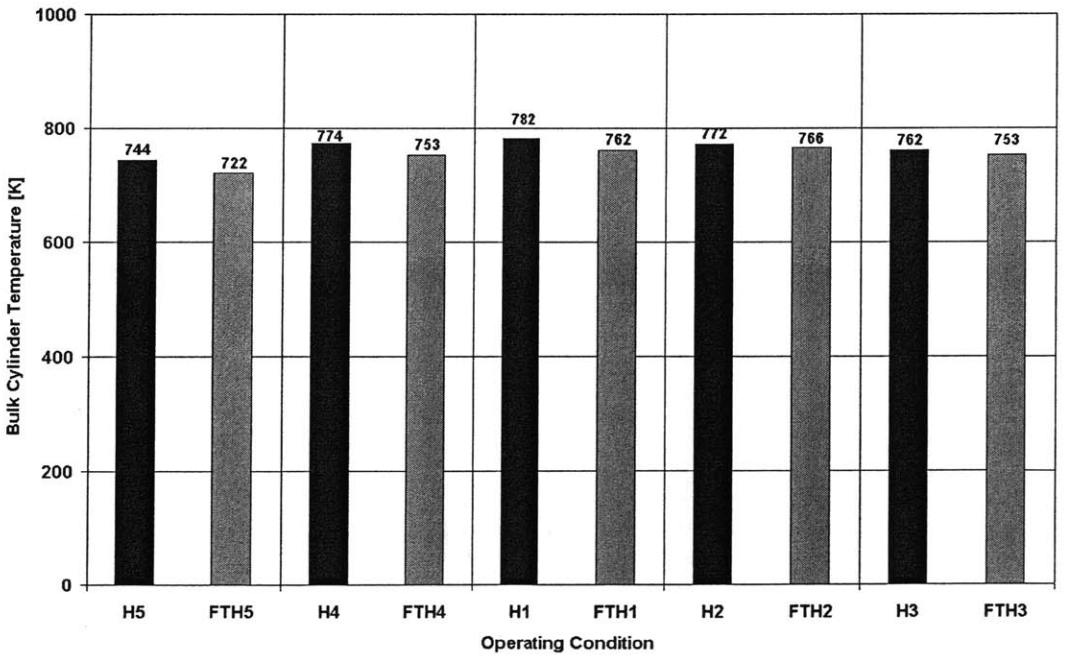

Figure 7.8 Bulk cylinder temperature at the start of injection using No. 2 diesel fuel and Fischer-Tropsch fuel during timing-sweep tests with stock EGR rates in high-load tests. The operating conditions are normal diesel (H1 – H5) and Fischer-Tropsch (FTH1 – FTH5). Stock timing is in the center with the most advanced timing to the left and the most retarded timing to the right.

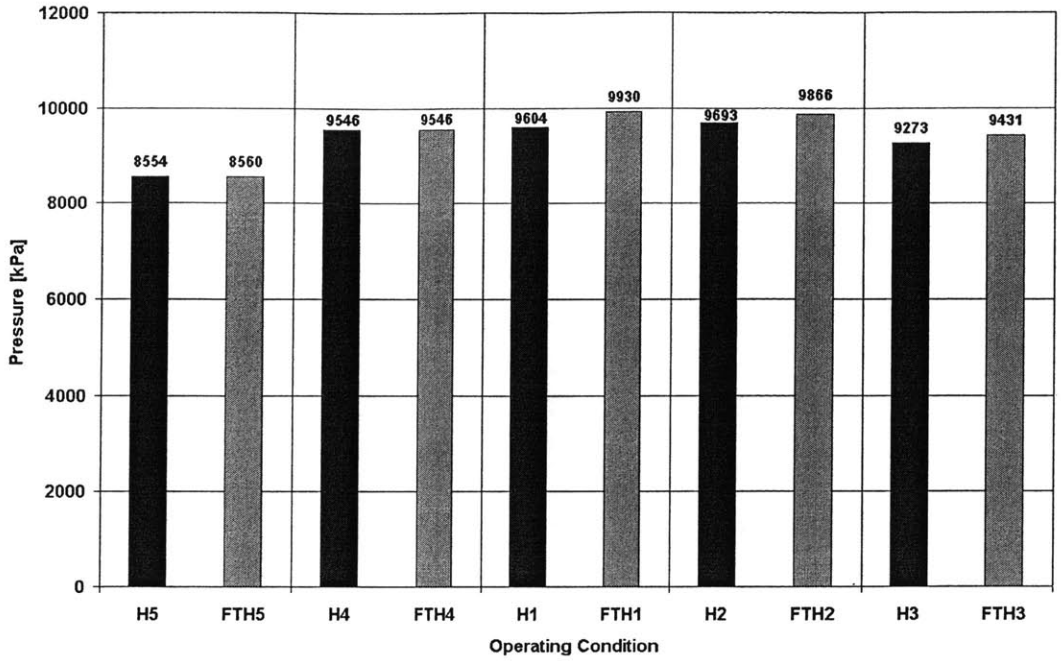

Figure 7.9 Cylinder pressure at the start of injection using No. 2 diesel fuel and Fischer-Tropsch fuel during timing-sweep tests with stock EGR rates in high-load tests. The operating conditions are normal diesel (H1 – H5) and Fischer-Tropsch (FTH1 – FTH5). Stock timing is in the center with the most advanced timing to the left and the most retarded timing to the right.

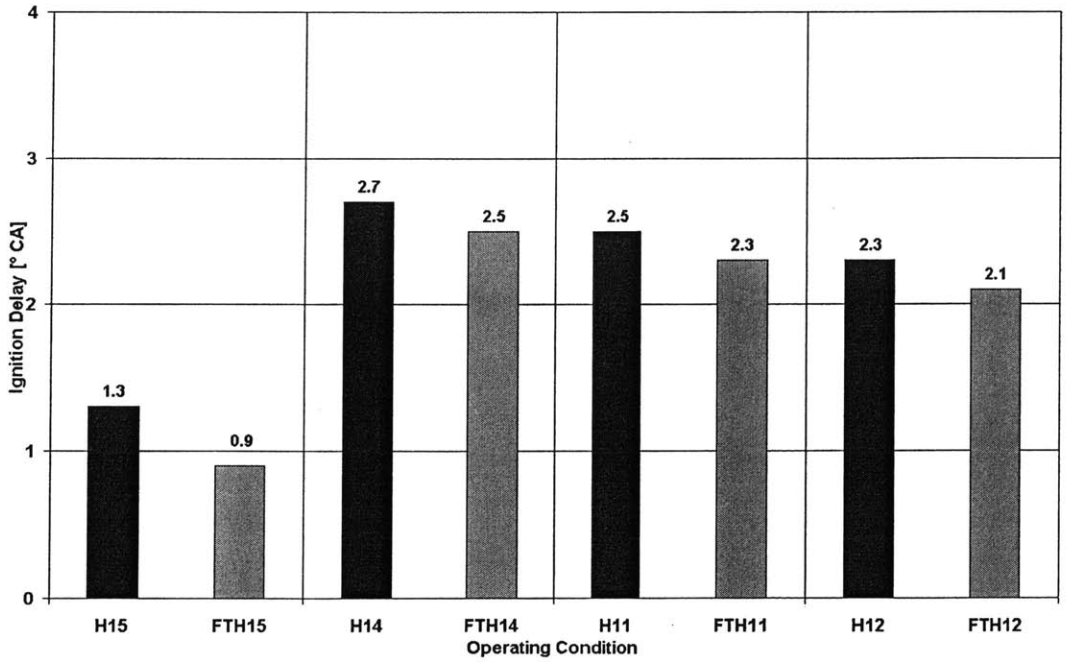

Figure 7.10 Ignition delay comparison between No. 2 diesel fuel and Fischer-Tropsch fuel during timing-sweep tests with increased EGR rates in high-load tests. The operating conditions are normal diesel (H11 – H15) and Fischer-Tropsch (FTH11 – FTH15). Stock timing is in the center with the most advanced timing to the left and the most retarded timing to the right. The leftmost point (H15 and FTH15) is suspect.

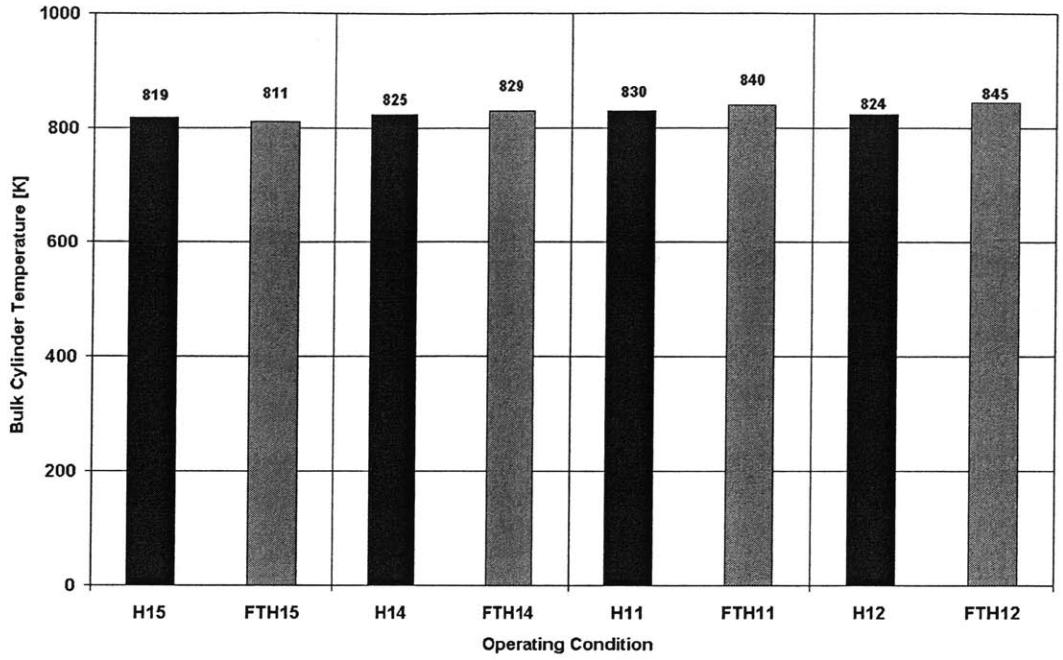

Figure 7.11 Bulk cylinder temperature at the start of injection using No. 2 diesel fuel and Fischer-Tropsch fuel during timing-sweep tests with increased EGR rates in high-load tests. The operating conditions are normal diesel (H11 – H5) and Fischer-Tropsch (FTL1 – FTL5). Stock timing is in the center with the most advanced timing to the left and the most retarded timing to the right.

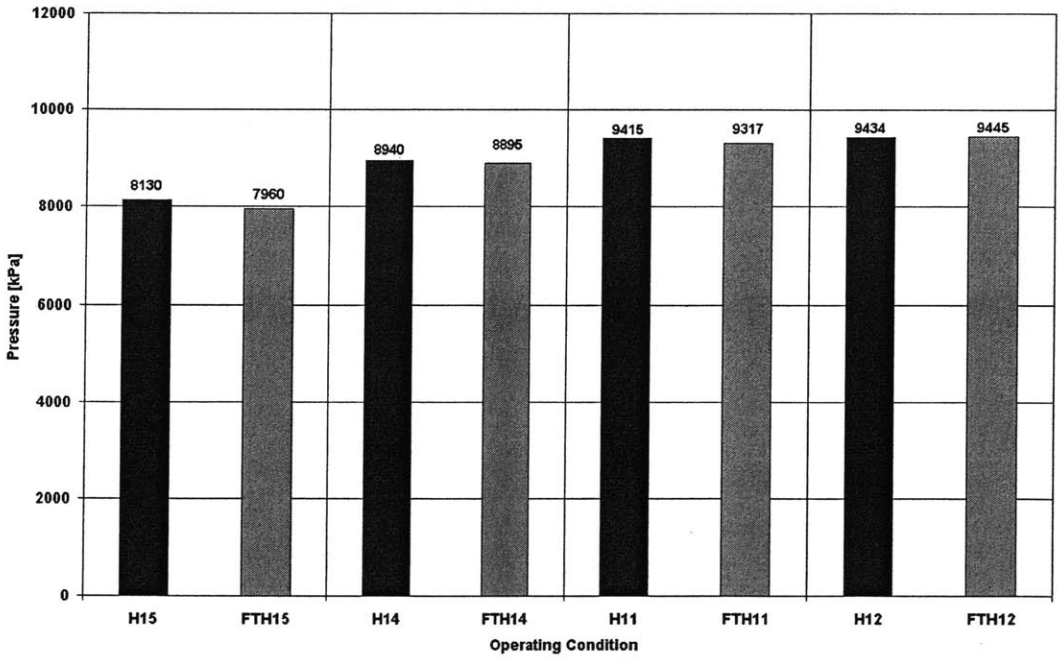

Figure 7.12 Cylinder pressure at the start of injection using No. 2 diesel fuel and Fischer-Tropsch fuel during timing-sweep tests with increased EGR rates in high-load tests. The operating conditions are normal diesel (H11 – H15) and Fischer-Tropsch (FTH11 – FTH15). Stock timing is in the center with the most advanced timing to the left and the most retarded timing to the right.

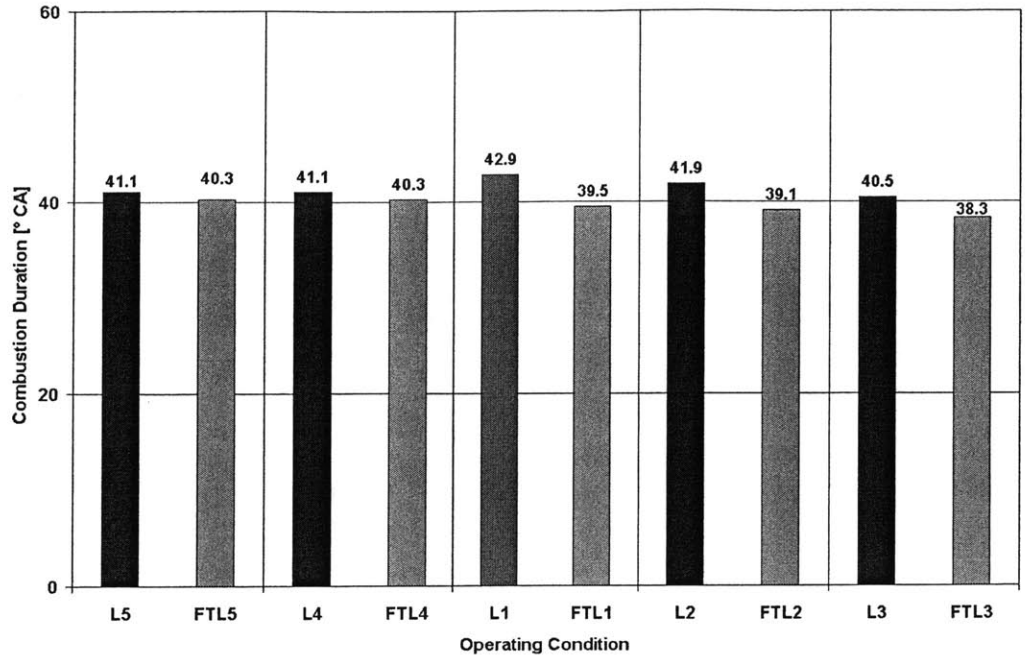

Figure 7.13 Combustion duration using No.2 diesel fuel and Fischer-Tropsch fuel during timing sweep test with stock EGR rates in low-load tests. The operating conditions are normal diesel (L1 – L5) and Fischer-Tropsch (FTL1 – FTL5). Stock timing is in the center with the most advanced timing to the left and the most retarded timing to the right.

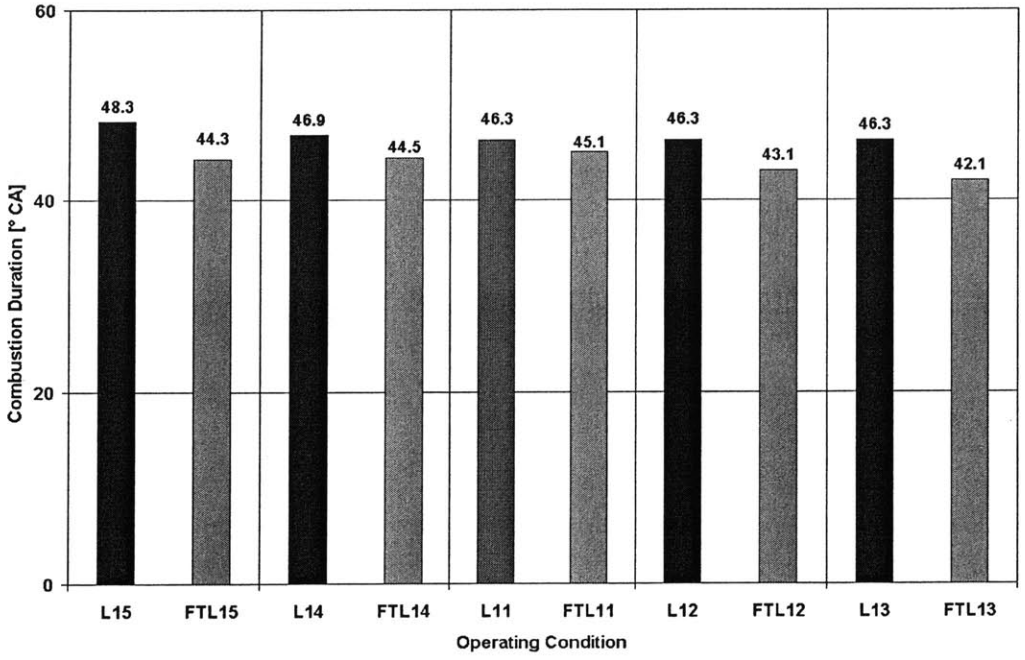

Figure 7.14 Combustion duration using No.2 diesel fuel and Fischer-Tropsch fuel during timing sweep test with increased EGR rates in low-load tests. The operating conditions are normal diesel (L11 – L15) and Fischer-Tropsch (FTL11 – FTL15). Stock timing is in the center with the most advanced timing to the left and the most retarded timing to the right.

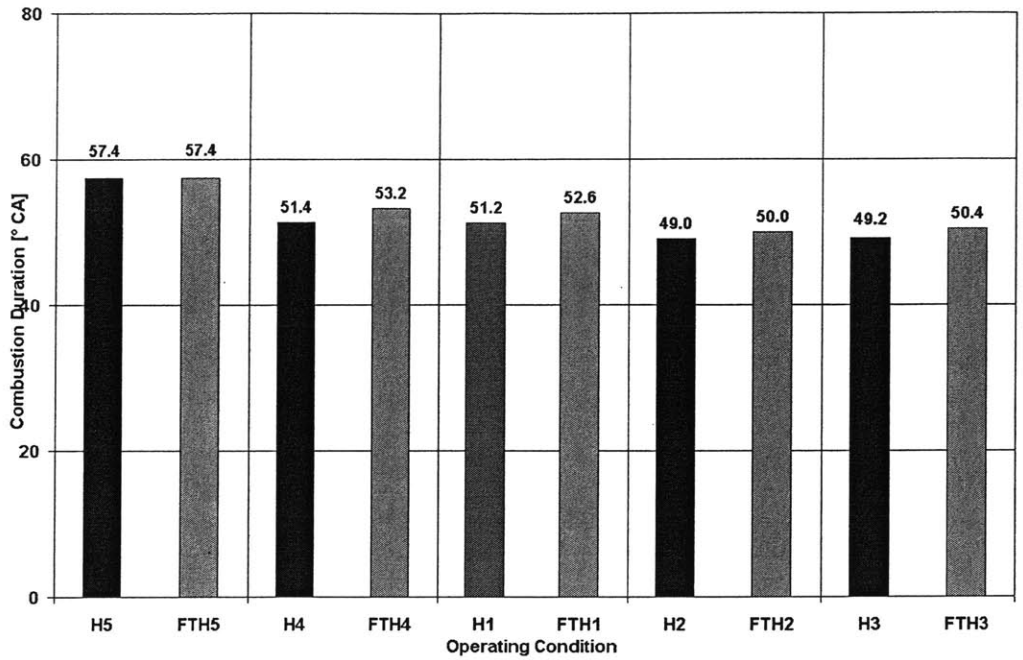

Figure 7.15 Combustion duration using No.2 diesel fuel and Fischer-Tropsch fuel during timing sweep test with stock EGR rates in high-load tests. The operating conditions are normal diesel (H1 – H5) and Fischer-Tropsch (FTH1 – FTH5). Stock timing is in the center with the most advanced timing to the left and the most retarded timing to the right.

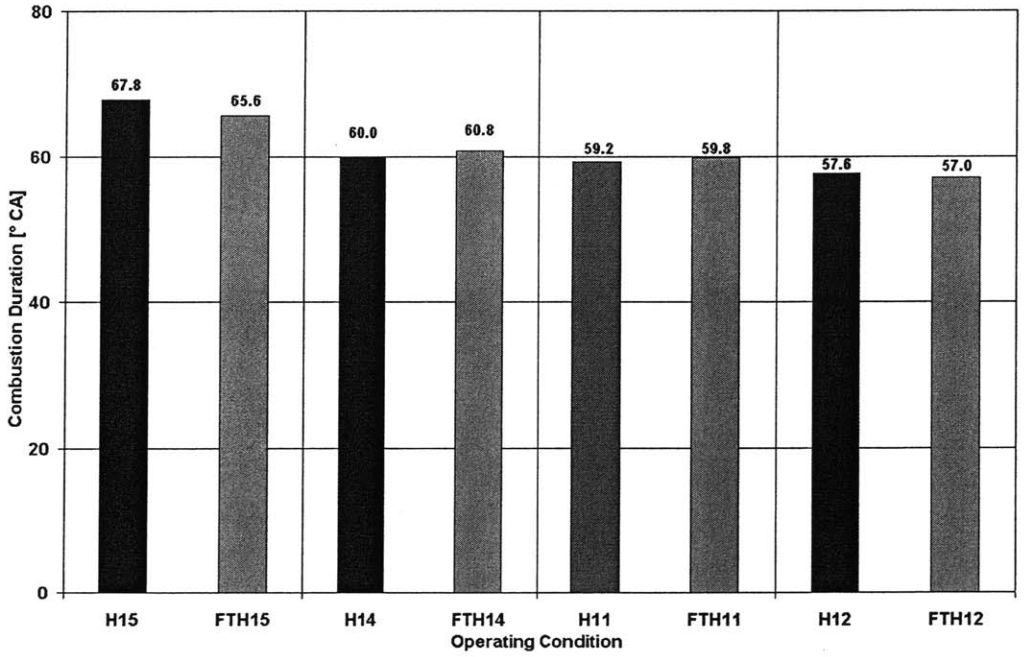

Figure 7.16 Combustion duration using No.2 diesel fuel and Fischer-Tropsch fuel during timing sweep test with increased EGR rates in high-load tests. The operating conditions are normal diesel (H11 – H15) and Fischer-Tropsch (FTH11 – FTH15). Stock timing is in the center with the most advanced timing to the left and the most retarded timing to the right.

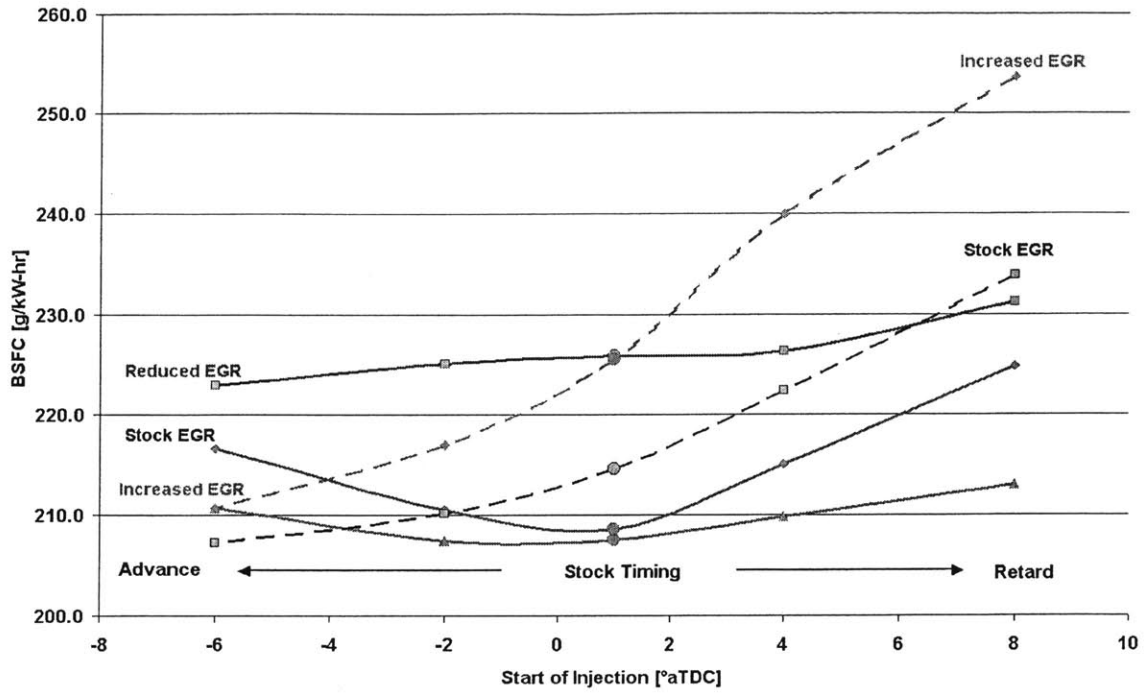

Figure 7.17 BSFC versus start of injection timing for No.2 diesel fuel (solid lines) and Fischer-Tropsch fuel (dashed lines) at reduced (No. 2 only), stock, and increased EGR rates in low-load tests. Enlarged circular data point designates stock timing point.

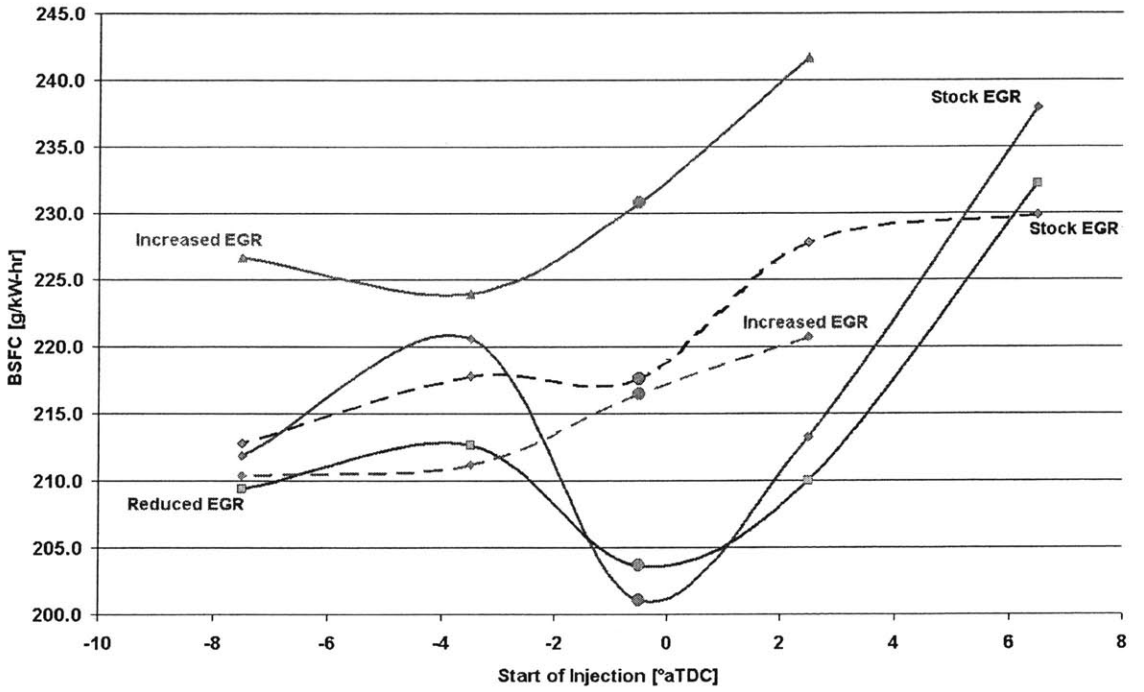

Figure 7.18 BSFC versus start of injection timing for No.2 diesel fuel (solid lines) and Fischer-Tropsch fuel (dashed lines) at reduced (No. 2 only), stock, and increased EGR rates in low-load tests. Enlarged circular data point designates stock timing point.

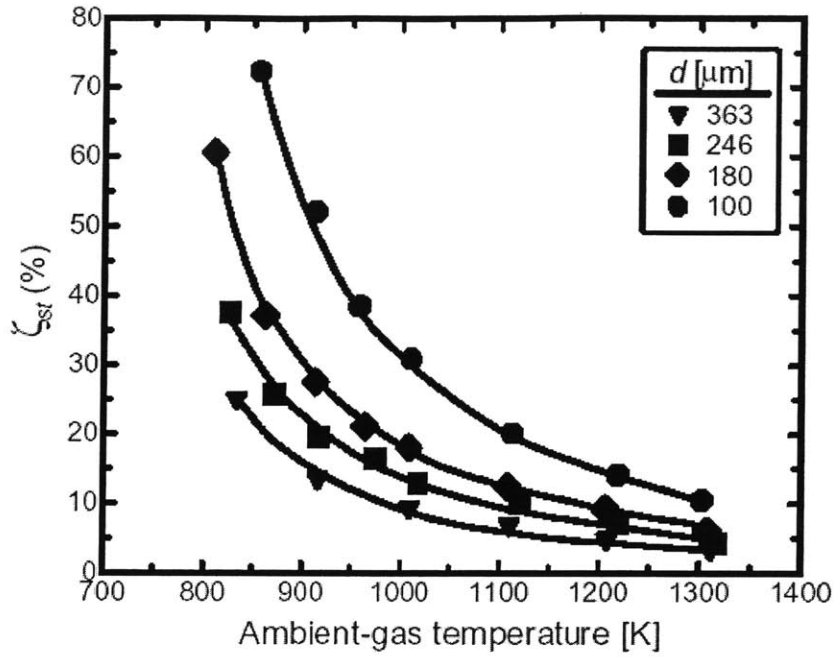

Figure 7.19 The percent of stoichiometric air entrained upstream up to the lift-off length versus the ambient gas temperature. The ambient gas density and pressure-drop across the injector orifice were 14.8 kg/m^3 and 138 MPa respectively. The curves through the data represent trends for a specific nozzle diameter [30].

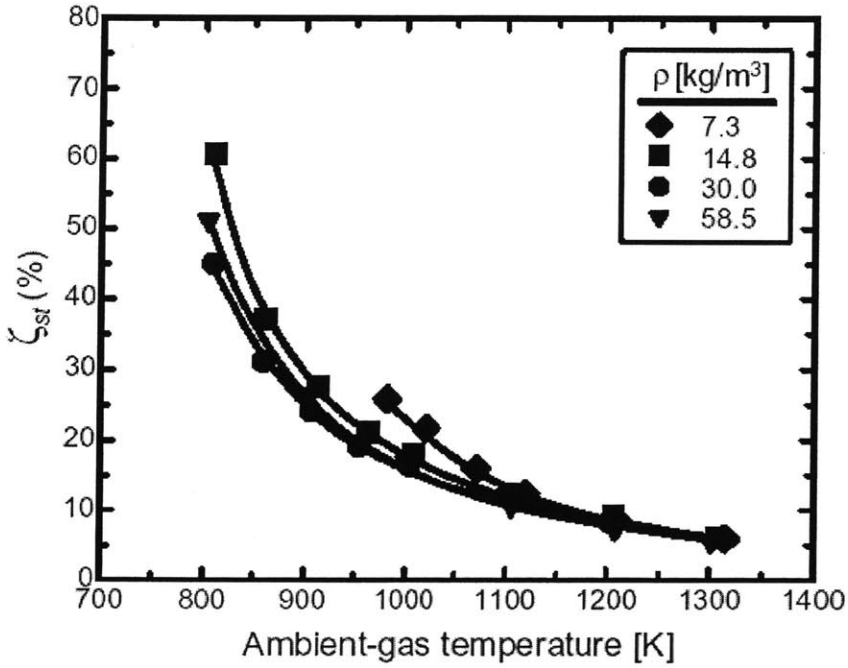

Figure 7.20 The percent of stoichiometric air entrained upstream up to the lift-off length versus the ambient gas temperature for a range of gas densities. The pressure-drop across the injector orifice and nozzle diameter were 138 MPa and 180 μm respectively. The curves through the data represent trends for a constant gas density [30].

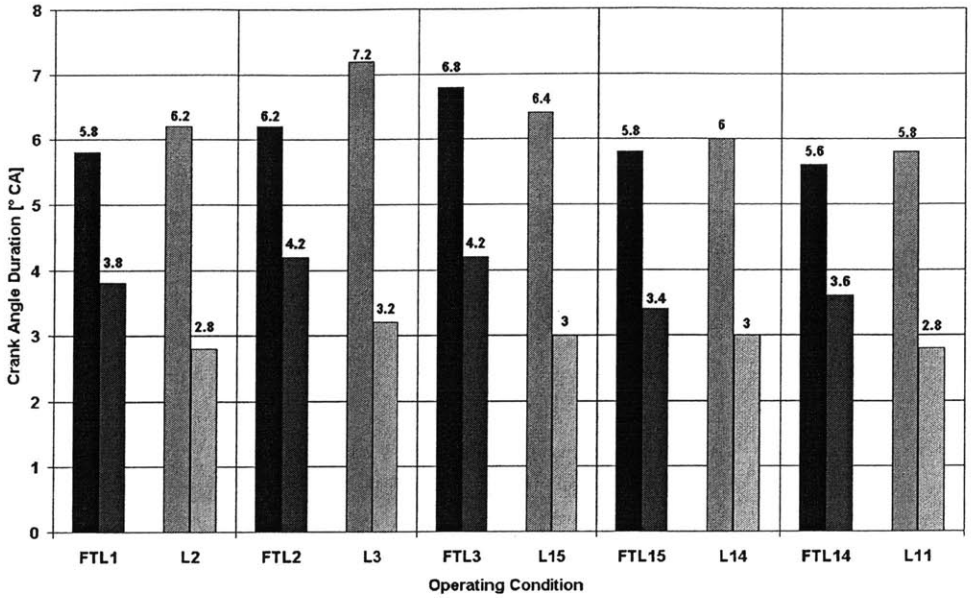

Figure 7.21 Comparison of durations between SOI-to-10% and SOC-to-10% durations using No.2 diesel fuel and Fischer-Tropsch fuel during timing sweep test with stock EGR rates in low-load tests. The operating conditions are normal diesel (L1 – L5) and Fischer-Tropsch (FTL1 – FTL5). Stock timing is in the center with the most advanced timing to the left and the most retarded timing to the right. The left-hand bar for each condition is the SOI-to-10% duration; the right-hand bar is the SOC-to-10%.

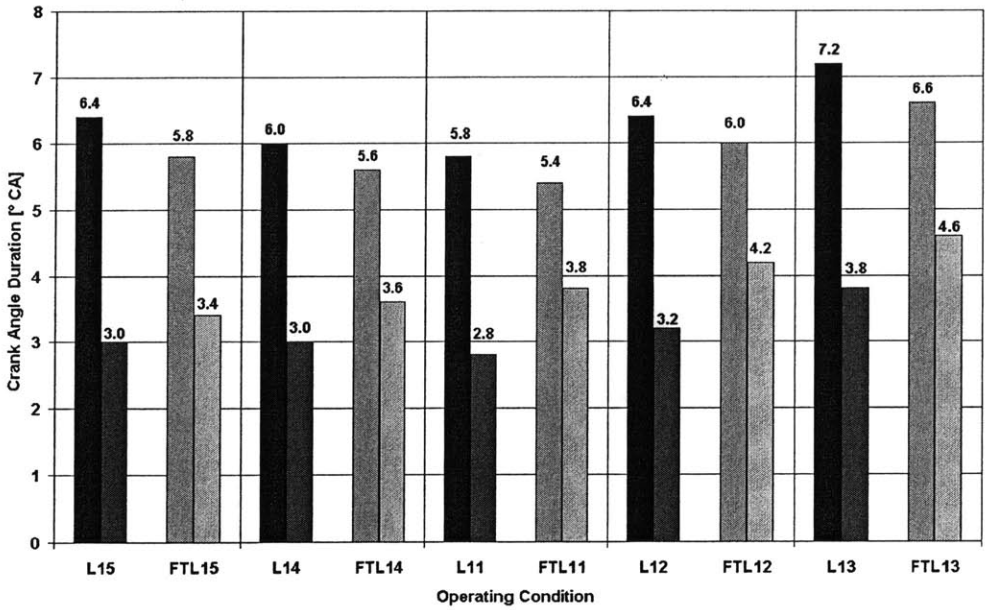

Figure 7.22 Comparison of durations between SOI-to-10% and SOC-to-10% durations using No.2 diesel fuel and Fischer-Tropsch fuel during timing sweep test with increased EGR rates in low-load tests. The operating conditions are normal diesel (L11 – L15) and Fischer-Tropsch (FTL11 – FTL15). Stock timing is in the center with the most advanced timing to the left and the most retarded timing to the right. . The left-hand bar for each condition is the SOI-to-10% duration; the right-hand bar is the SOC-to-10%.

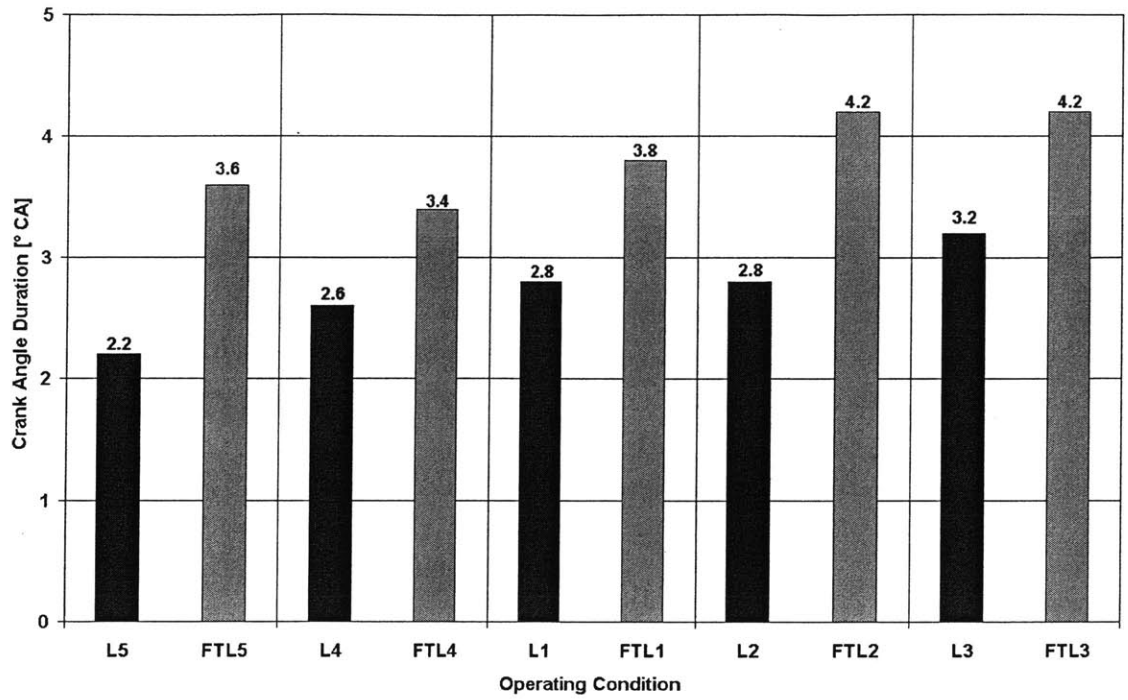

Figure 7.23 SOC-to-10% duration in Modes L1 – L5 and FTL1 – FTL5.

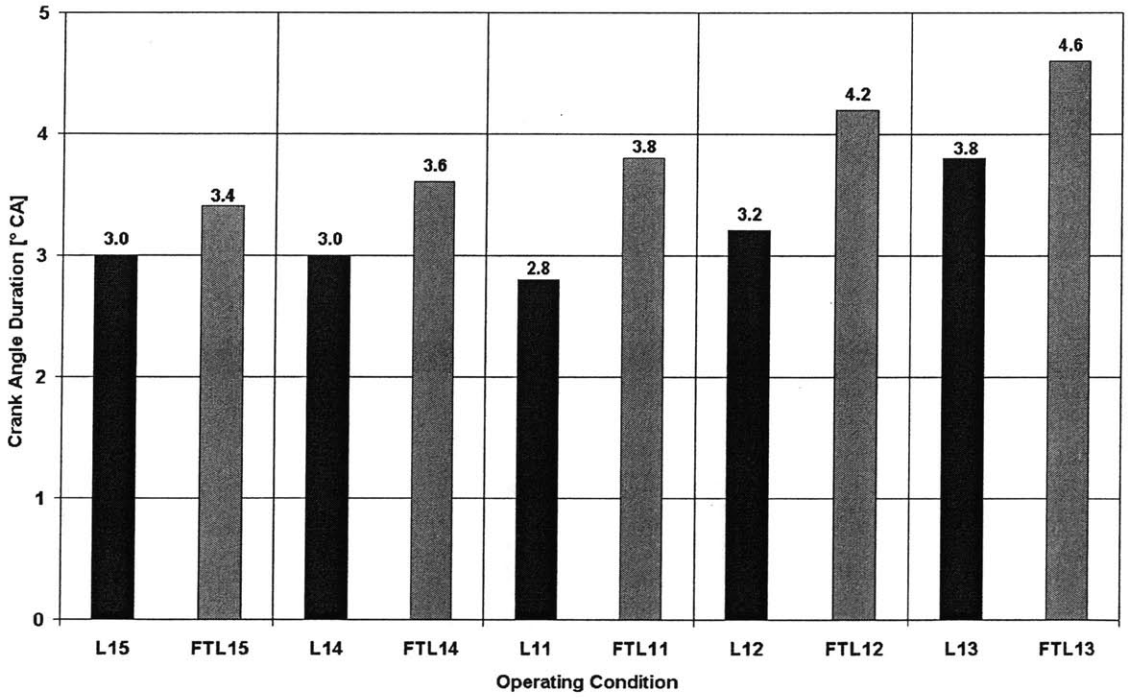

Figure 7.24 SOC-to-10% duration in Modes L11 – L15 and FTL11 – FTL15.

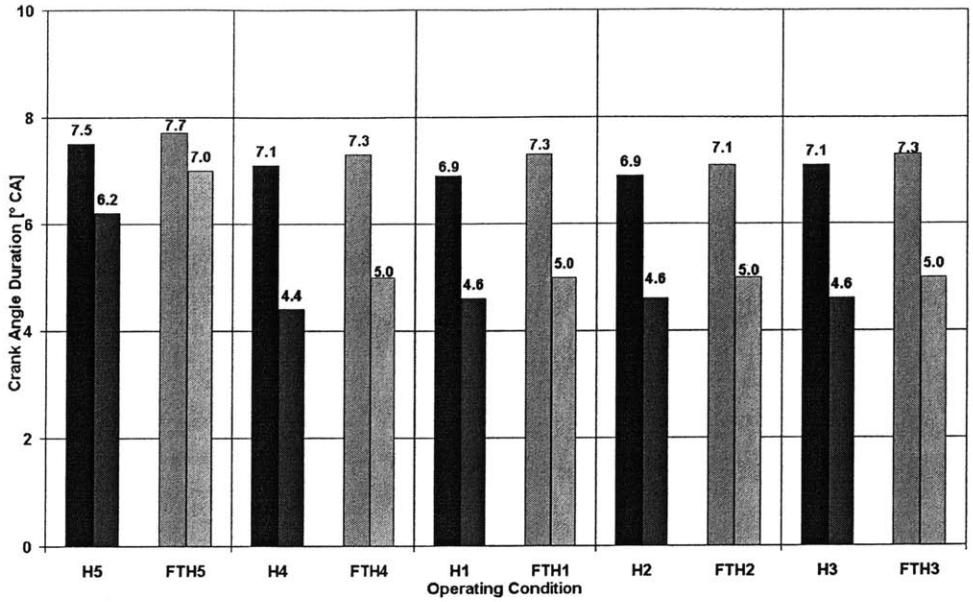

Figure 7.25 Comparison of crank angle durations between SOI-to-10% and SOC-to-10% durations using No.2 diesel fuel and Fischer-Tropsch fuel during timing sweep test with stock EGR rates in high-load tests. The operating conditions are normal diesel (H1 – H5) and Fischer-Tropsch (FTH1 – FTH5). Stock timing is in the center with the most advanced timing to the left and the most retarded timing to the right. The left-hand bar for each condition is the SOI-to-10% duration; the right-hand bar is the SOC-to-10%.

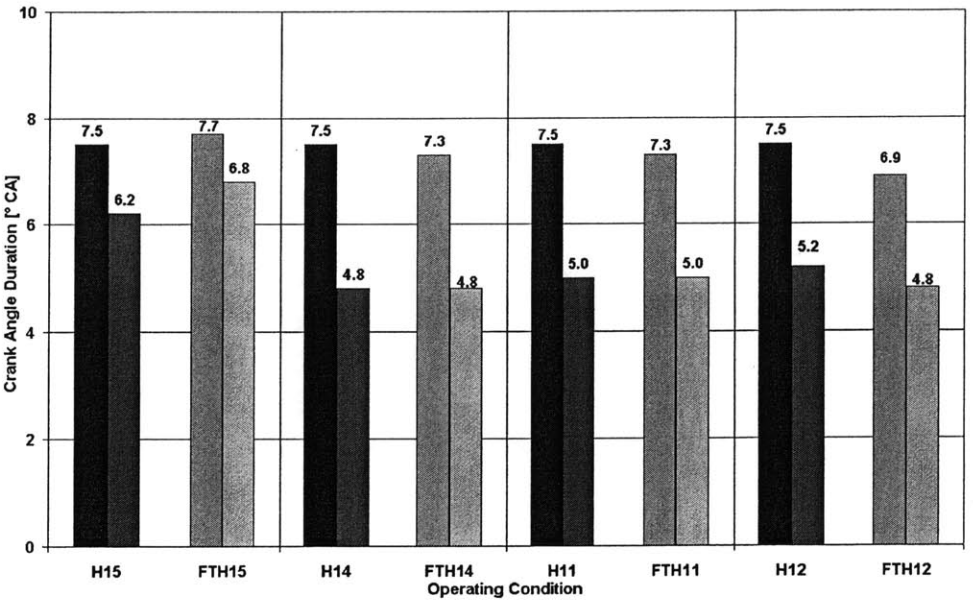

Figure 7.26 Comparison of crank angle durations between SOI-to-10% and SOC-to-10% durations using No.2 diesel fuel and Fischer-Tropsch fuel during timing sweep test with increased EGR rates in high-load tests. The operating conditions are normal diesel (H11 – H15) and Fischer-Tropsch (FTH11 – FTH15). Stock timing is in the center with the most advanced timing to the left and the most retarded timing to the right. The left-hand bar for each condition is the SOI-to-10% duration; the right-hand bar is the SOC-to-10%.

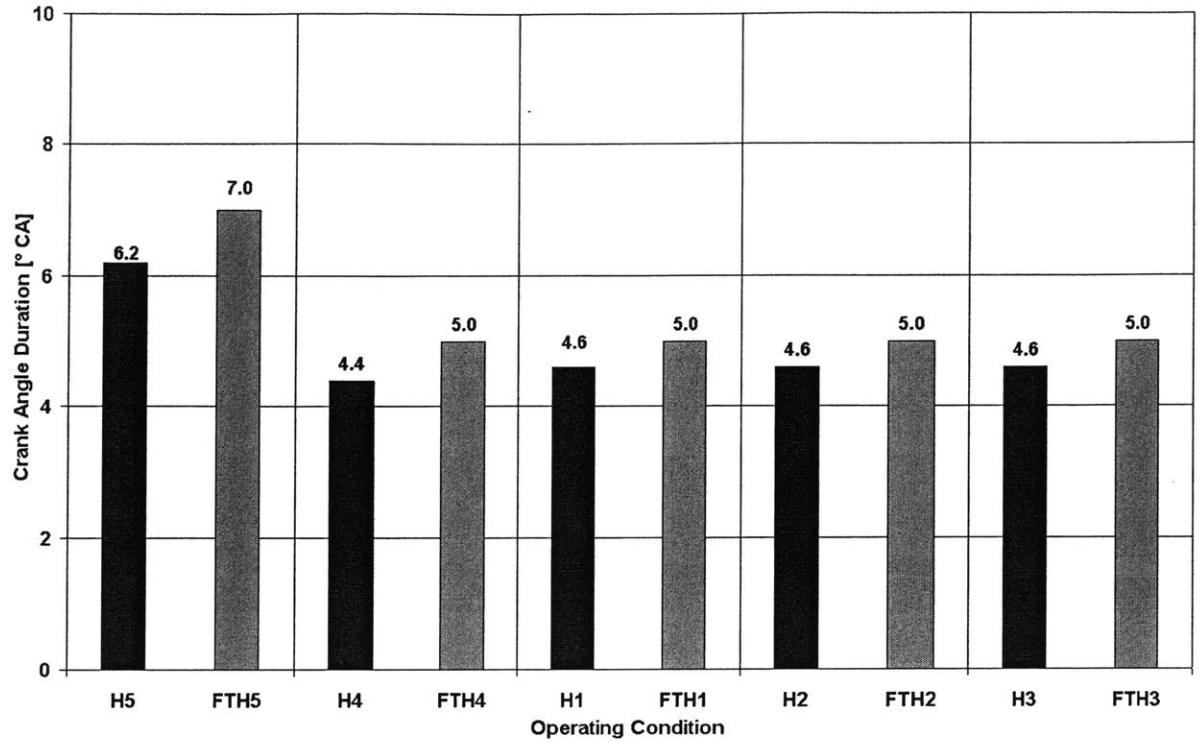

Figure 7.27 SOC-to-10% duration in Modes H1 – H5 and FTH1 – FTH5.

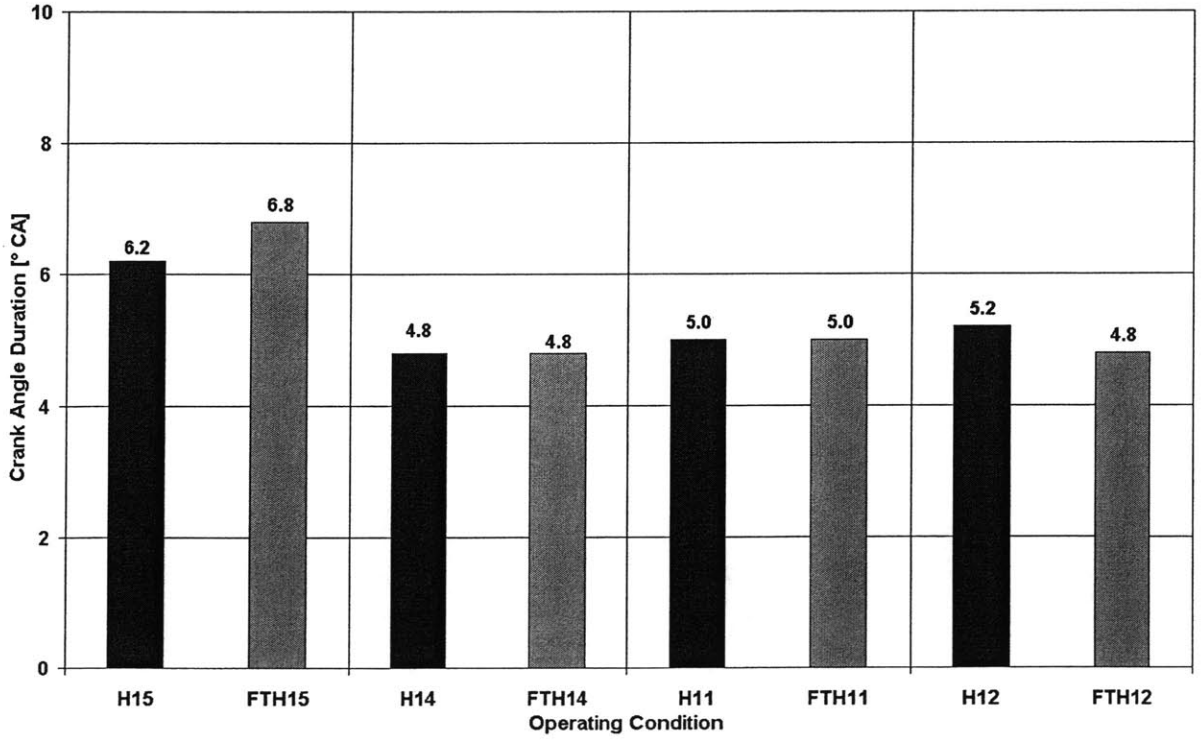

Figure 7.28 SOC-to-10% duration in Modes H11 – H15 and FTH11 – FTH15.

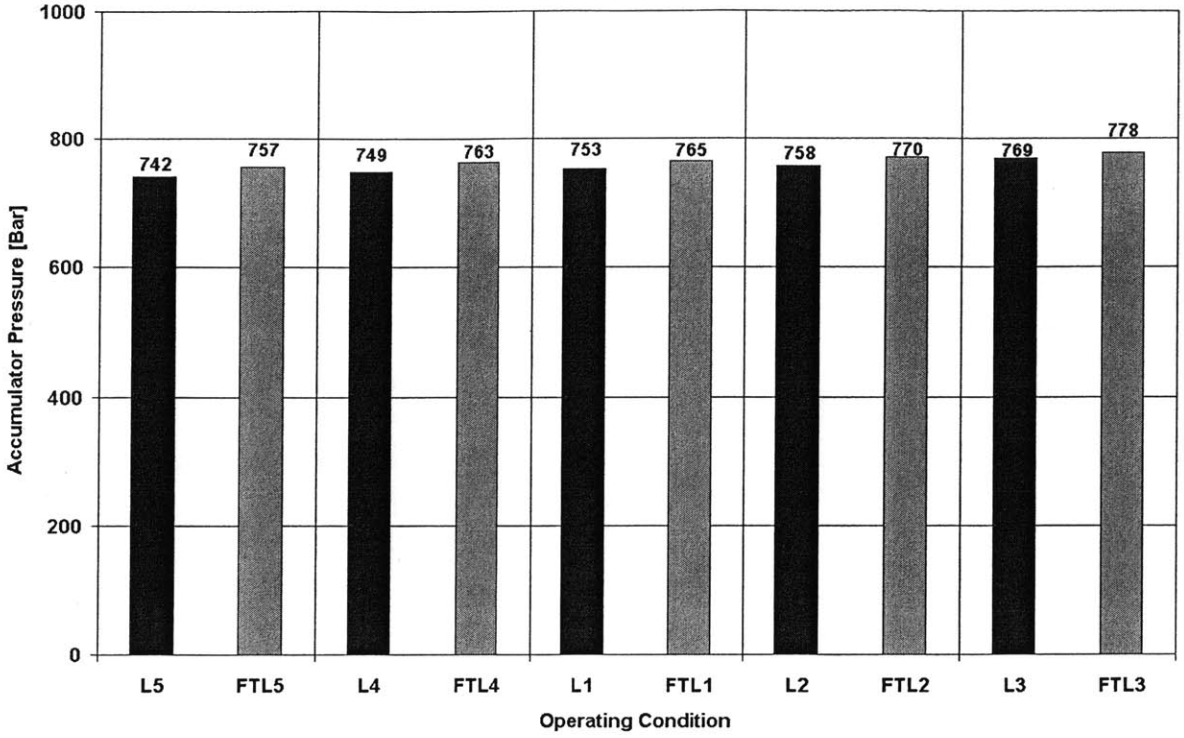

Figure 7.29 Accumulator pressures for low-load conditions L1 – L5 and FTL1 – FTL5

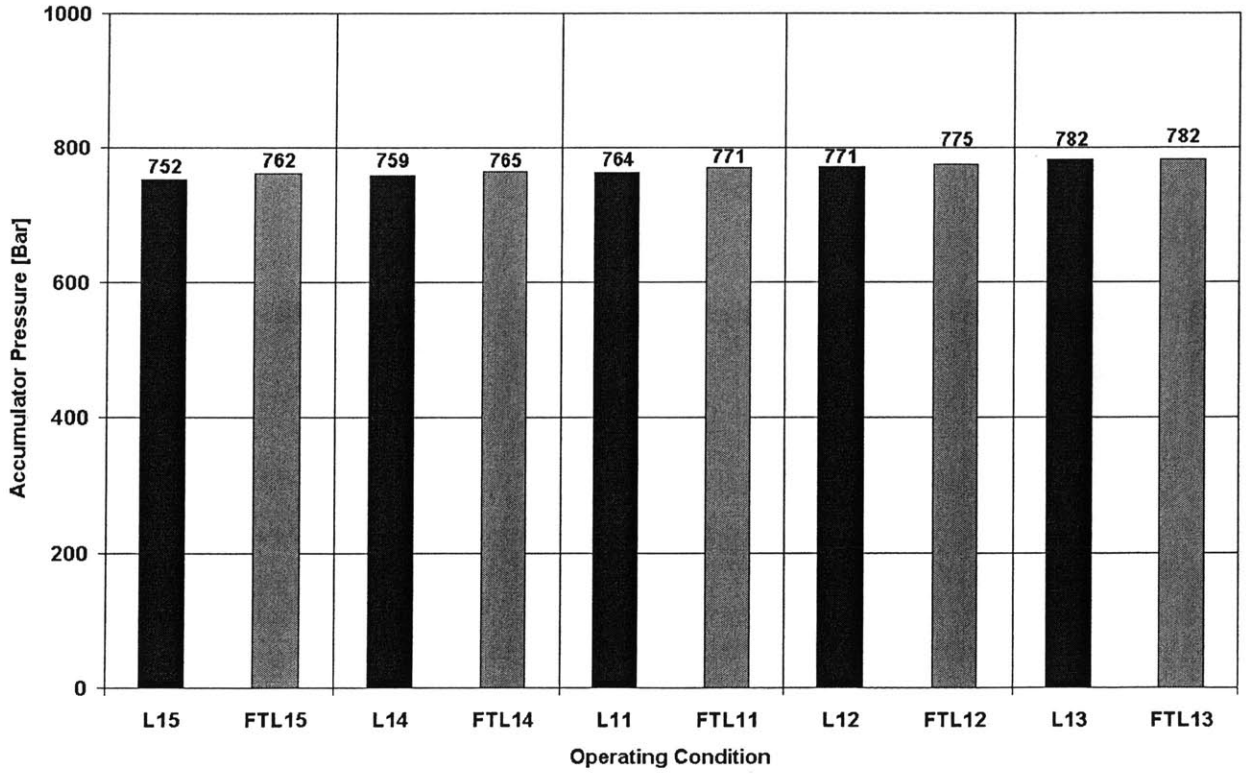

Figure 7.30 Accumulator pressures for low-load conditions L11 – L15 and FTL11 – FTL15

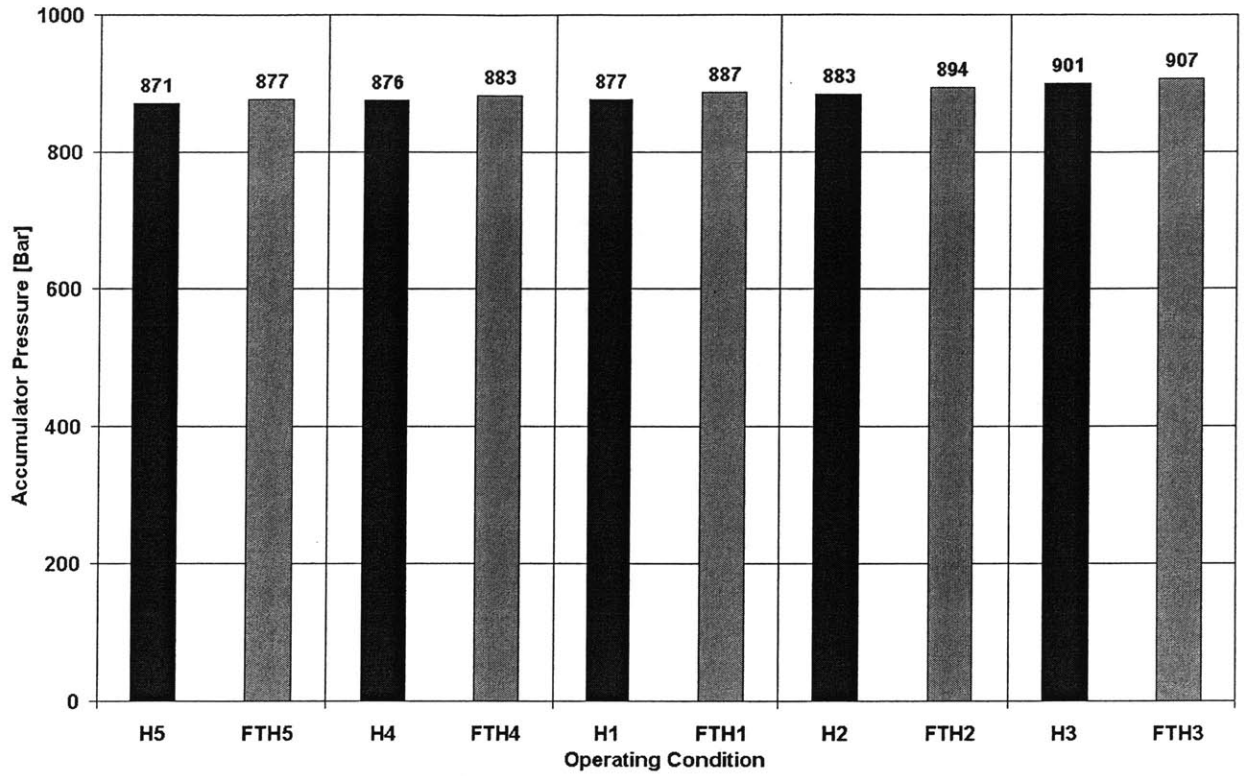

Figure 7.31 Accumulator pressures for low-load conditions H1 – H5 and FTH1 – FTH5

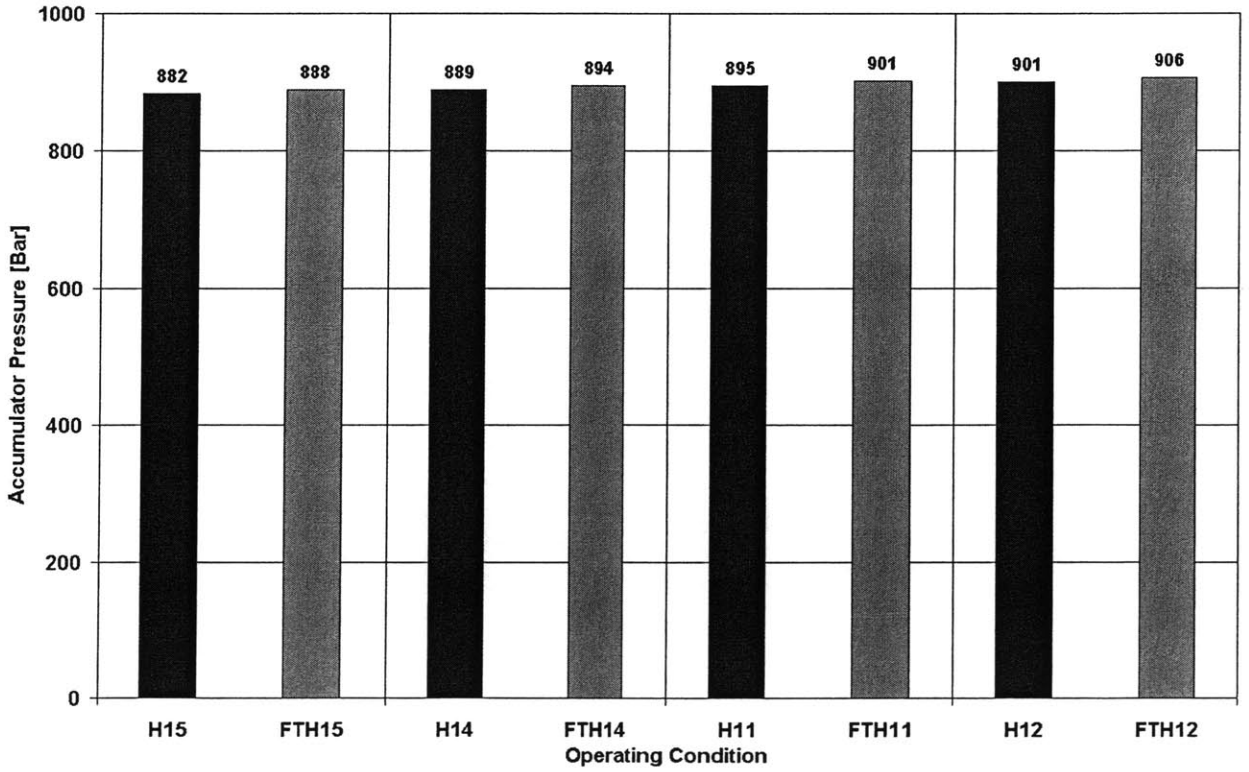

Figure 7.32 Accumulator pressures for low-load conditions H11 – H15 and FTH11 – FTH15

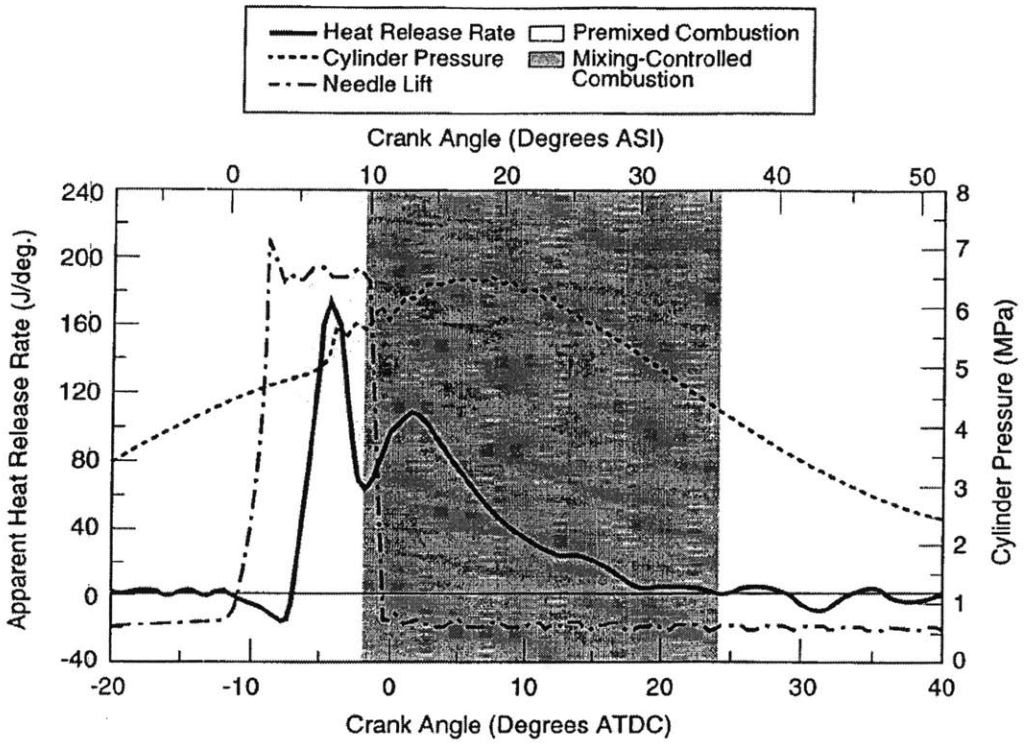

Figure 7.33 Heat release typical of older diesel engine technology. Low-loads. Figure 8a in [26].

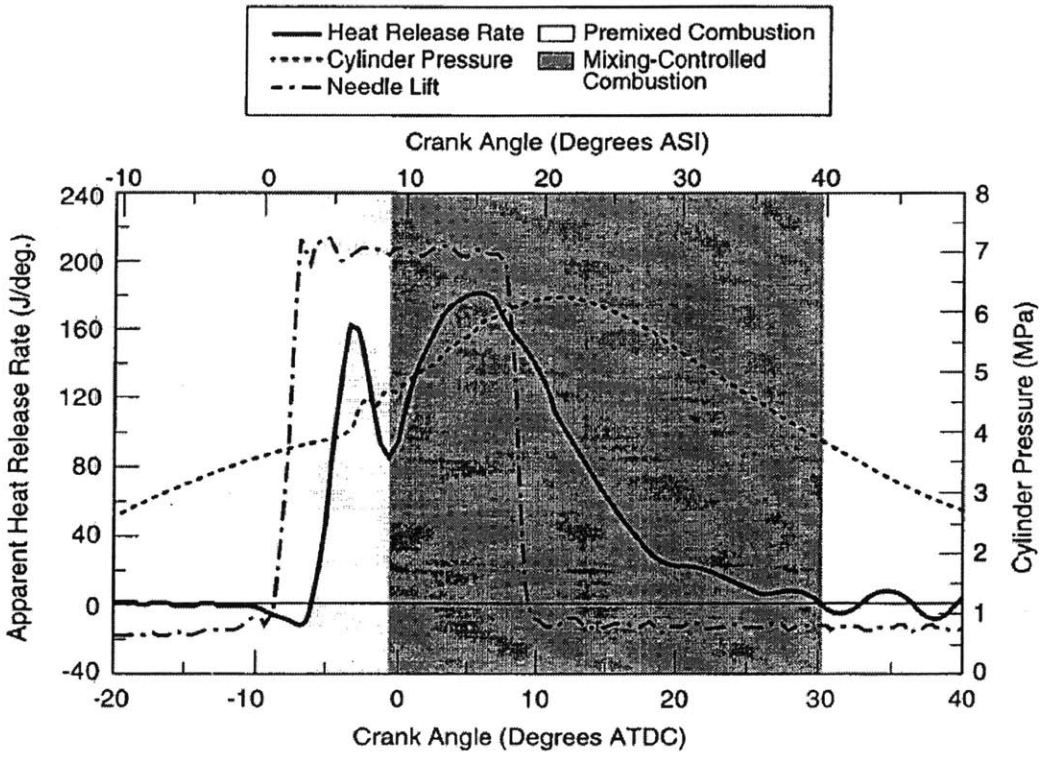

Figure 7.34 Heat release typical of older diesel engine technology. High-loads. Figure 8b [26].

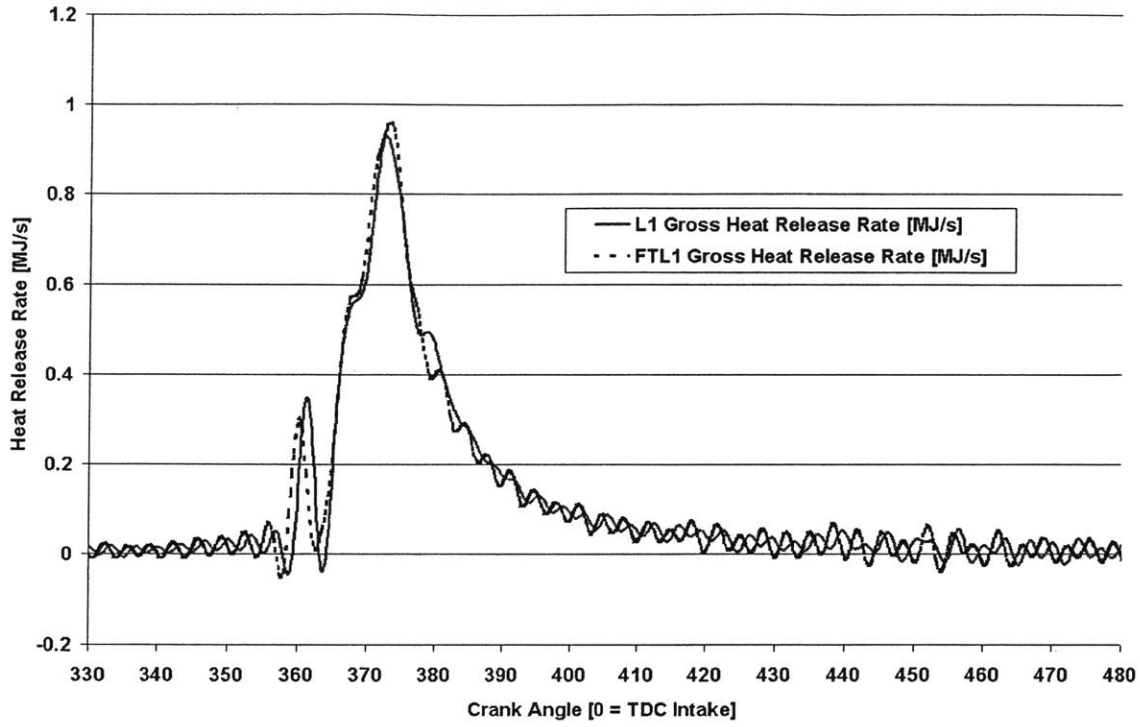

Figure 7.35 Heat release of Clean Diesel engine at MIT at low load with stock timing and EGR rate. Solid line applies to operation with No. 2 diesel, dotted line is for FT fuel.

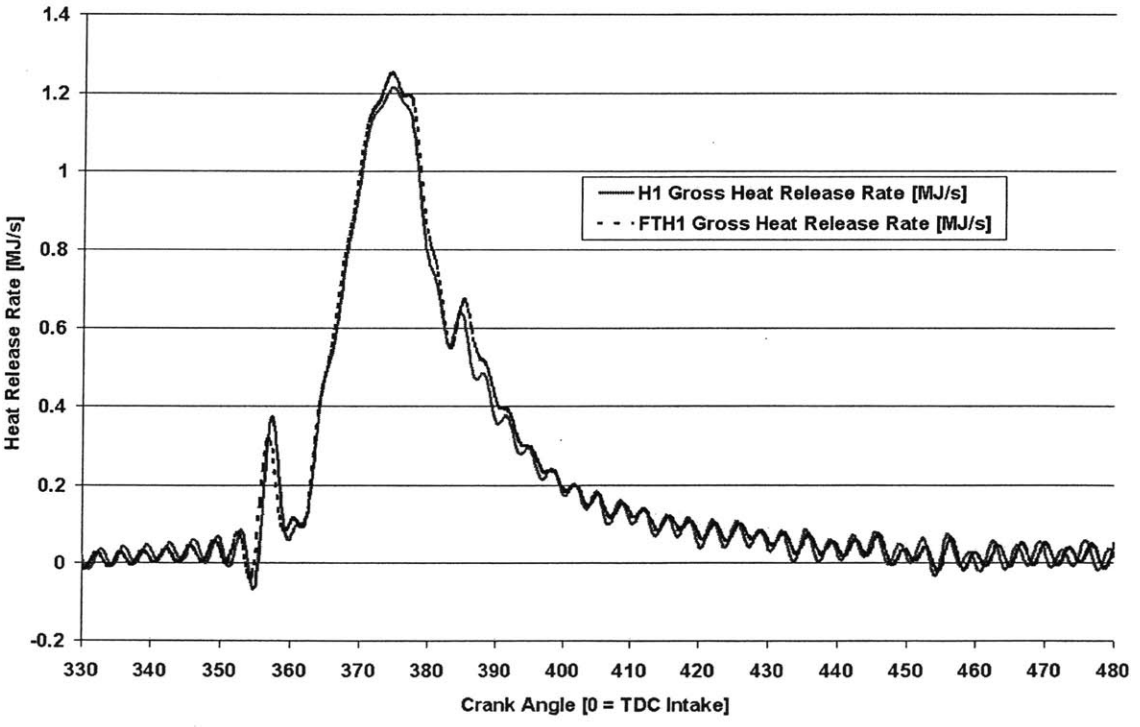

Figure 7.36 Heat release of Clean Diesel engine at MIT at high load with stock timing and EGR rate. Solid line applies to operation with No. 2 diesel, dotted line is for FT fuel.

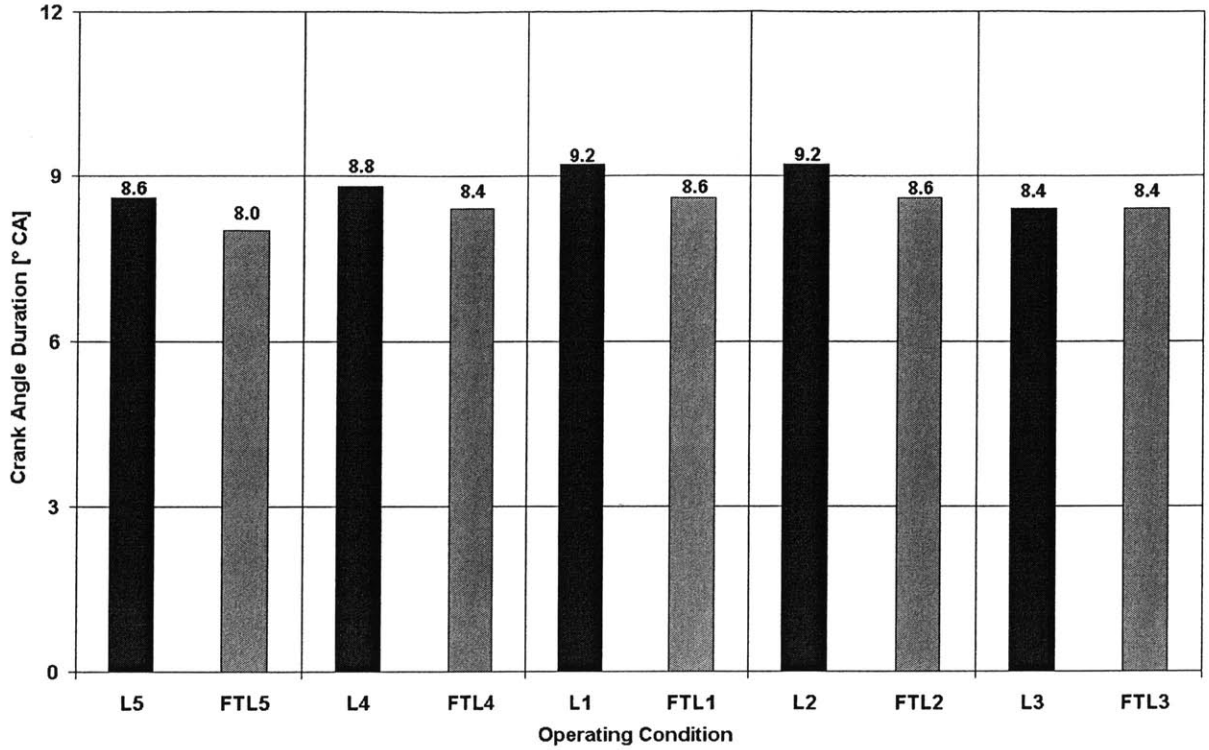

Figure 7.37 10%-to-50% heat release duration in Modes L1 – L5 and FTL1 – FTL5.

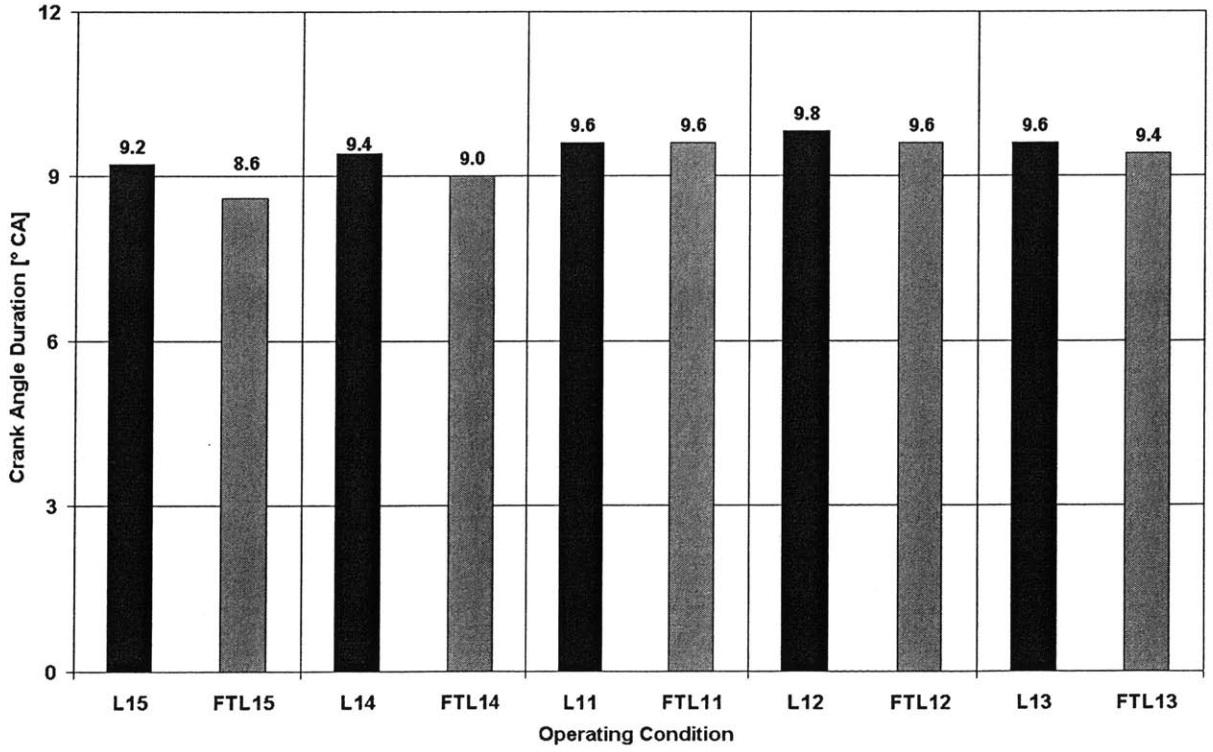

Figure 7.38 10%-to-50% heat release duration in Modes L11 – L15 and FTL11 – FTL15.

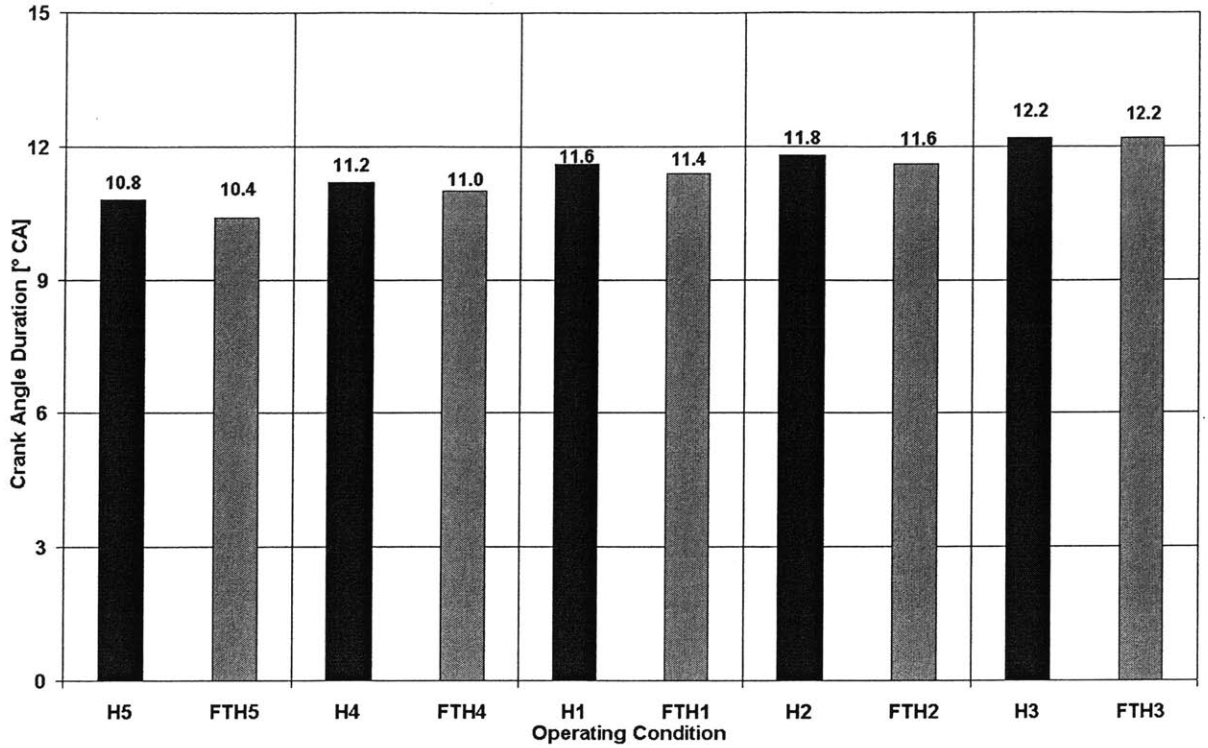

Figure 7.39 10%-to-50% heat release duration in Modes H1 – H5 and FTH1 – FTH5.

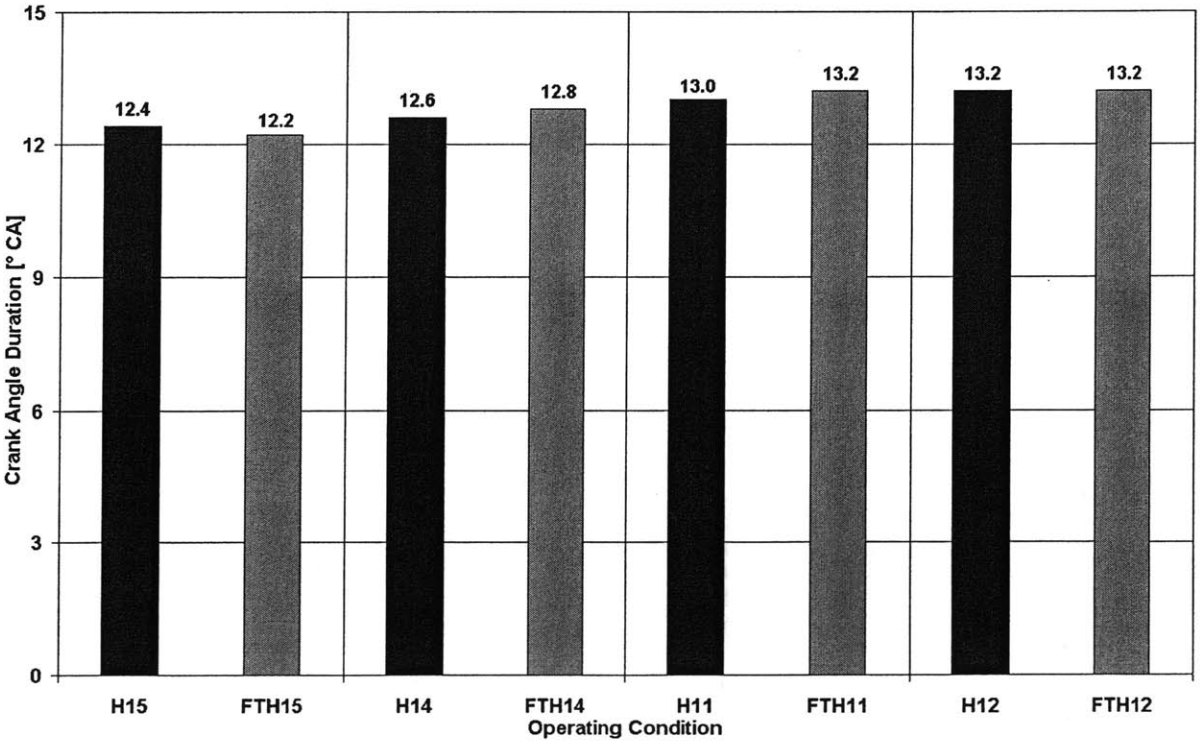

Figure 7.40 10%-to-50% heat release duration in Modes H11 – L15 and FTL11 – FTL15.

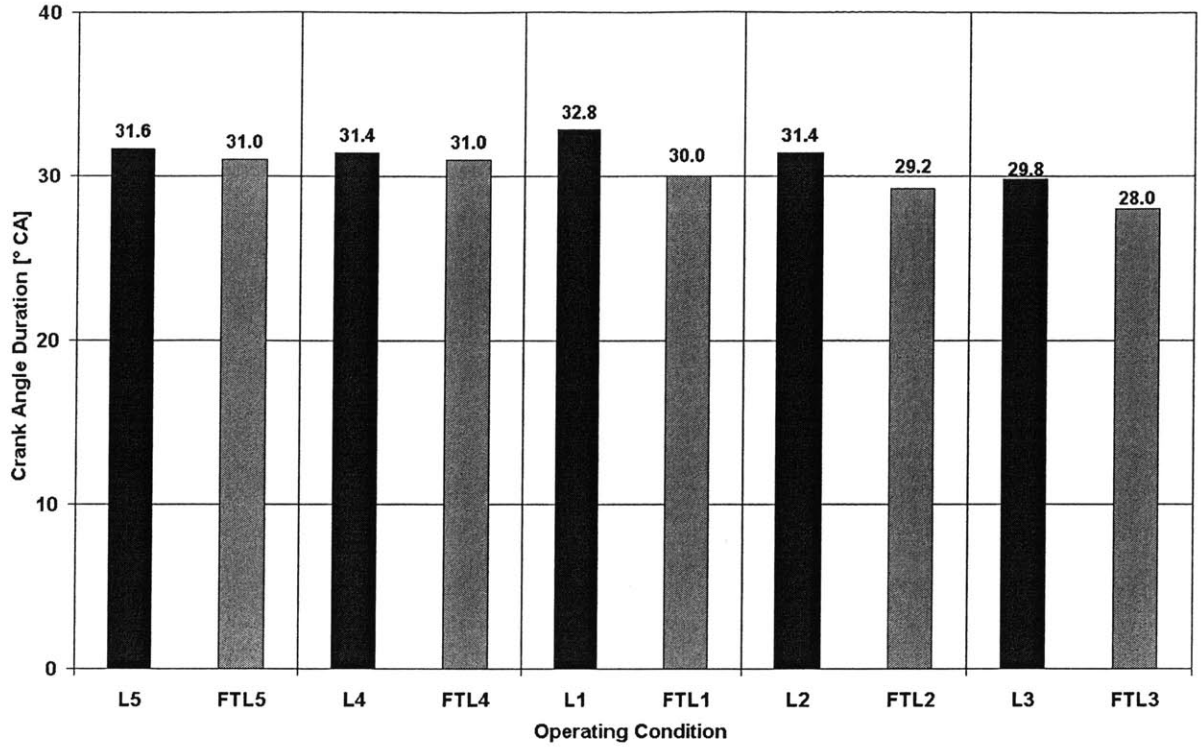

Figure 7.41 50%-to-90% heat release duration in Modes L1 – L5 and FTL1 – FTL5.

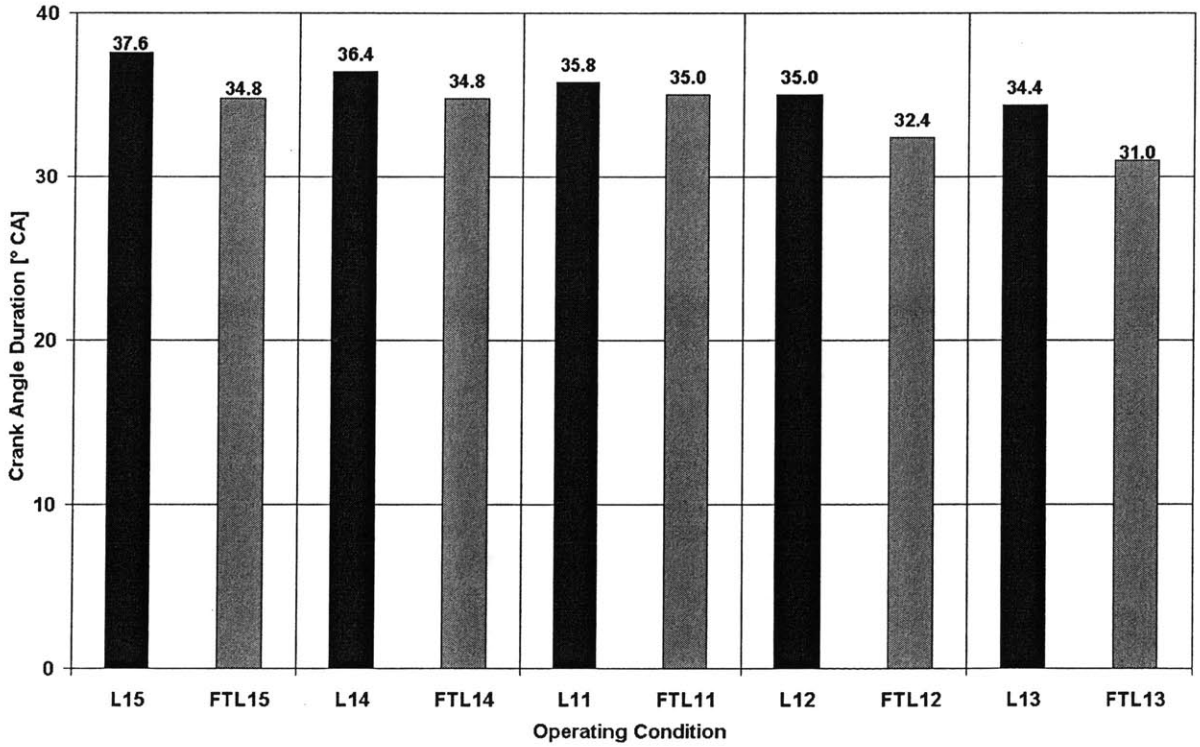

Figure 7.42 50%-to-90% heat release duration in Modes L11 – L15 and FTL11 – FTL15.

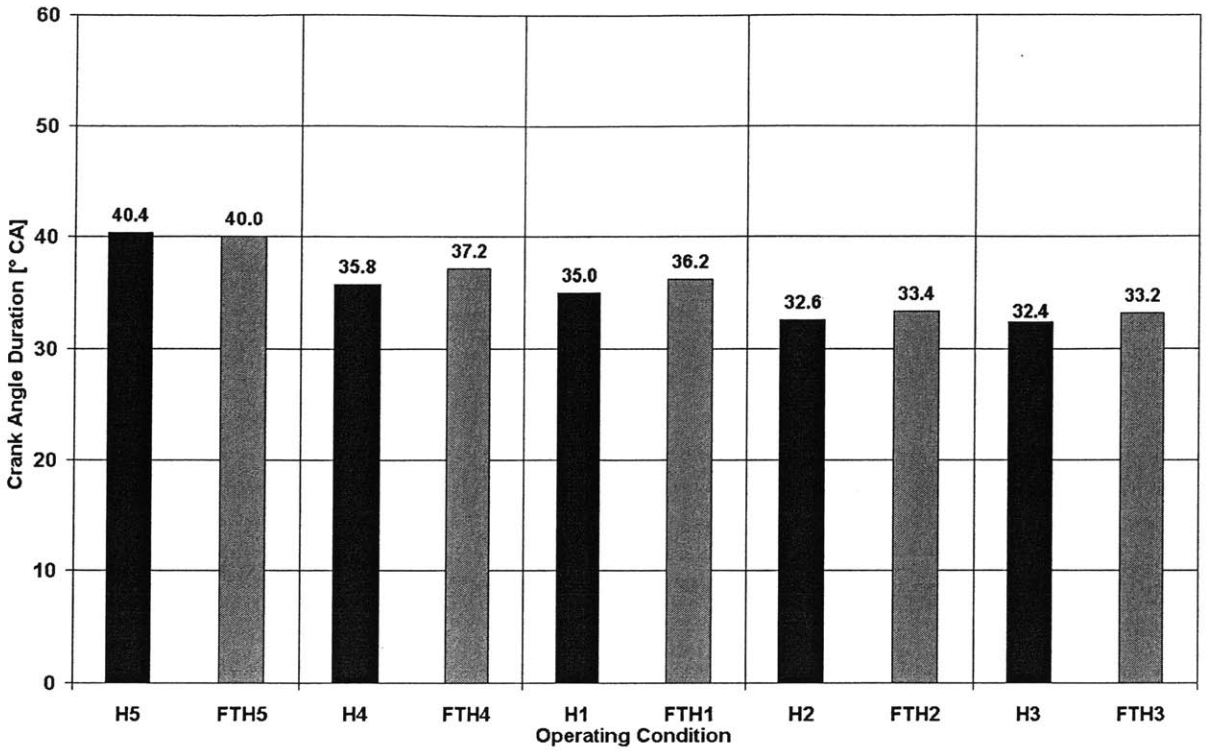

Figure 7.43 50%-to-90% heat release duration in Modes H1 – H5 and FTH1 – FTH5.

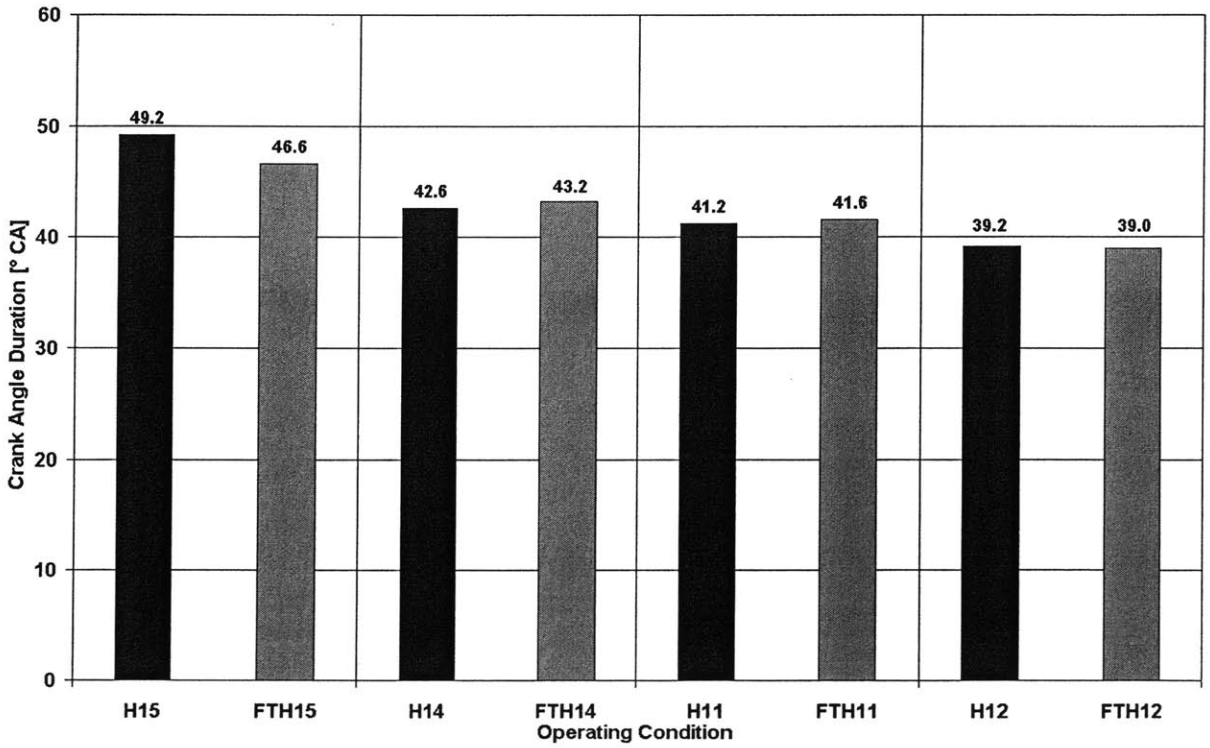

Figure 7.44 50%-to-90% heat release duration in Modes H11 – L15 and FTL11 – FTL15.

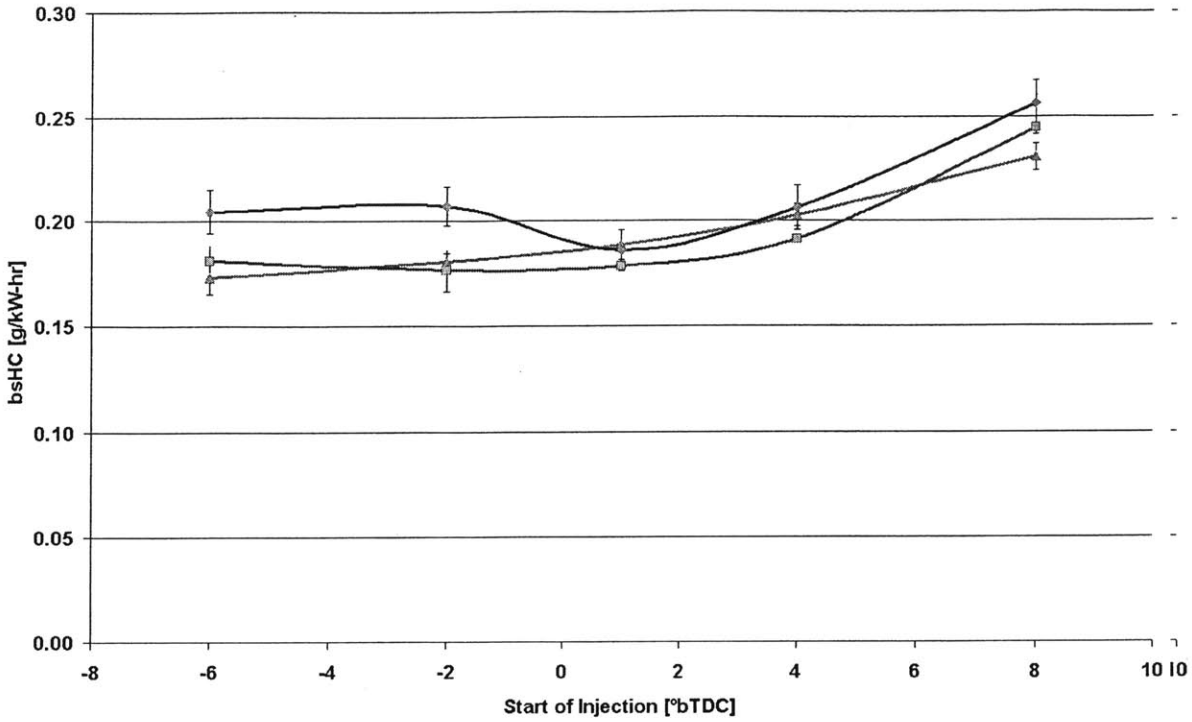

Figure 7.45 bsHC versus start of injection timing for No.2 diesel fuel (solid lines) at reduced, stock, and increased EGR rates in low-load tests. bsHC data not taken with Fischer-Tropsch fuel.

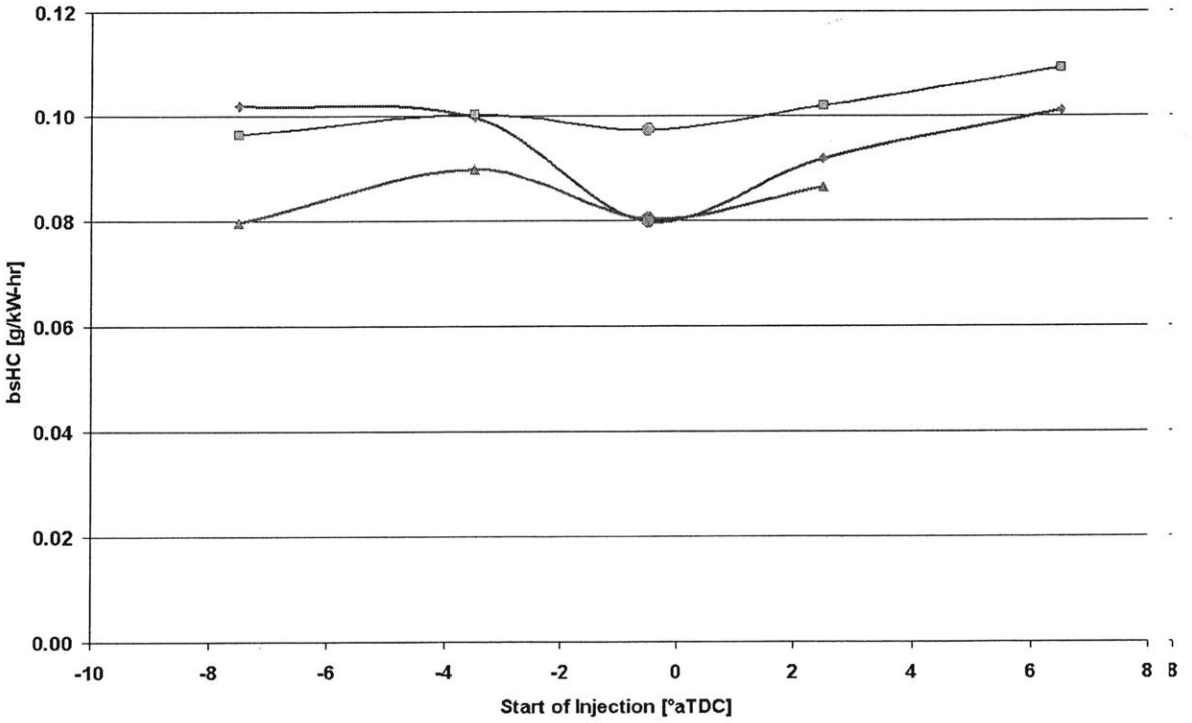

Figure 7.46 bsHC versus start of injection timing for No.2 diesel fuel (solid lines) at reduced, stock, and increased EGR rates in high-load tests. bsHC data not taken with Fischer-Tropsch fuel.

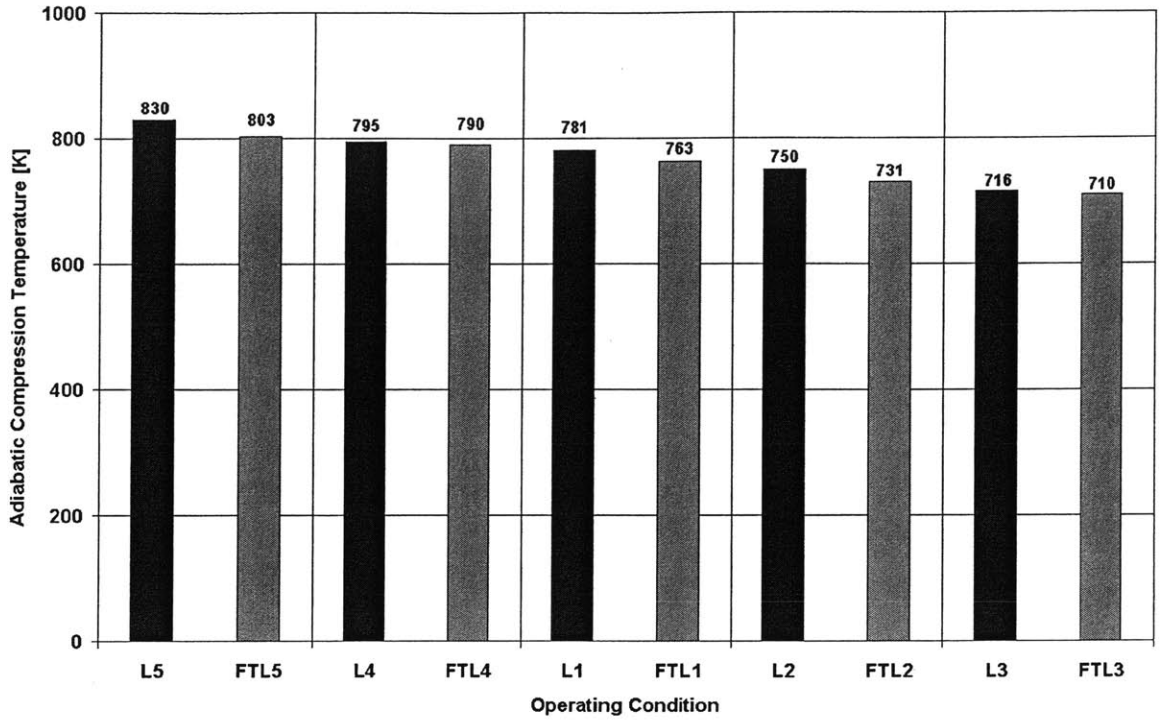

Figure 7.47 Adiabatic compression temperature of unburned gas at the end of injection (EOI) in Modes L1 – L5 and FTL1 – FTL5.

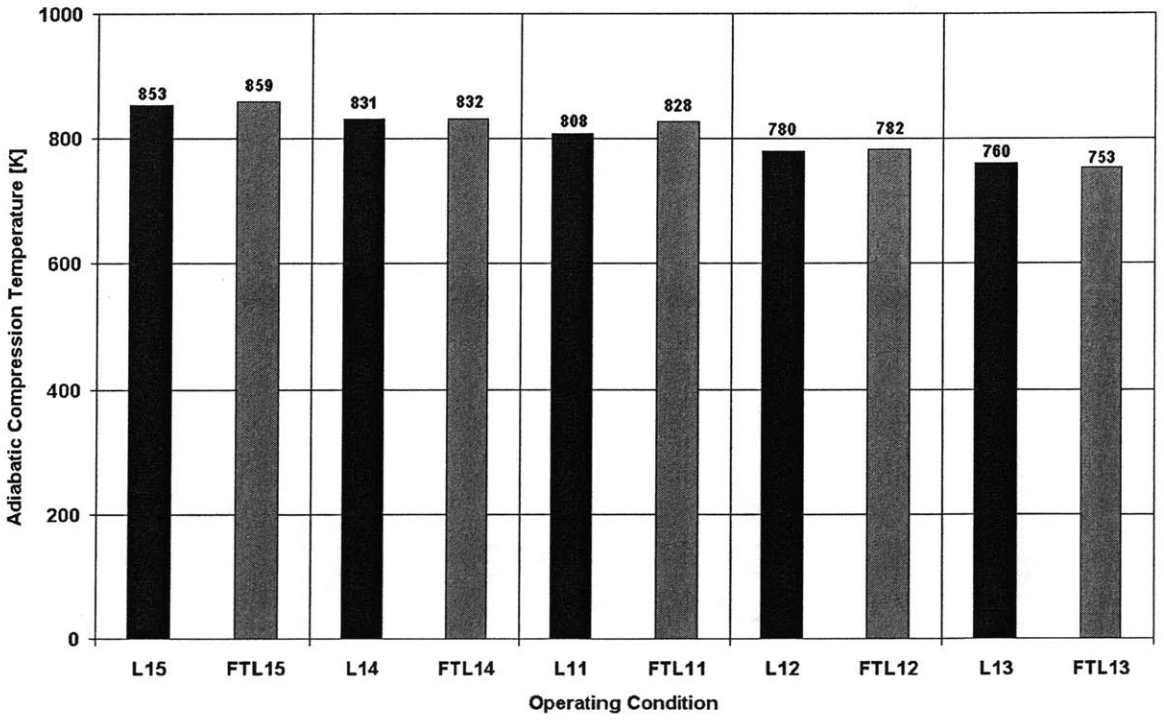

Figure 7.48 Adiabatic compression temperature of unburned gas at the end of injection (EOI) in Modes L11 – L15 and FTL11 – FTL15.

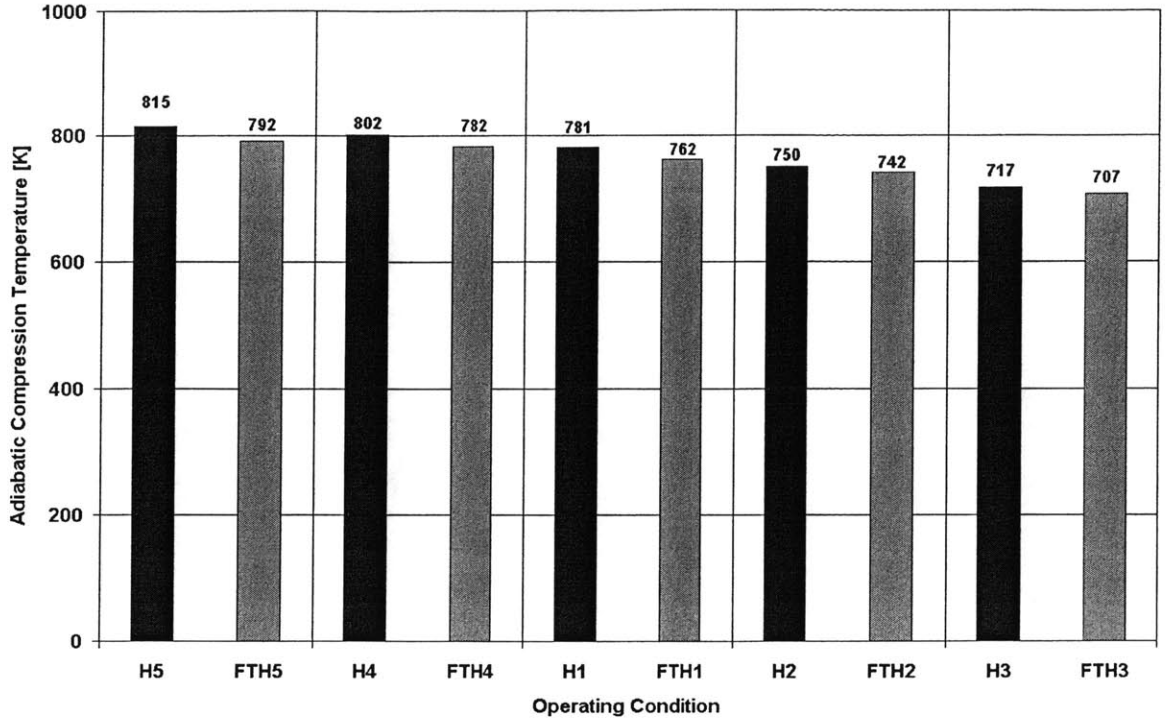

Figure 7.49 Adiabatic compression temperature of unburned gas at the end of injection (EOI) in Modes H1 – H5 and FTH1 – FTH5.

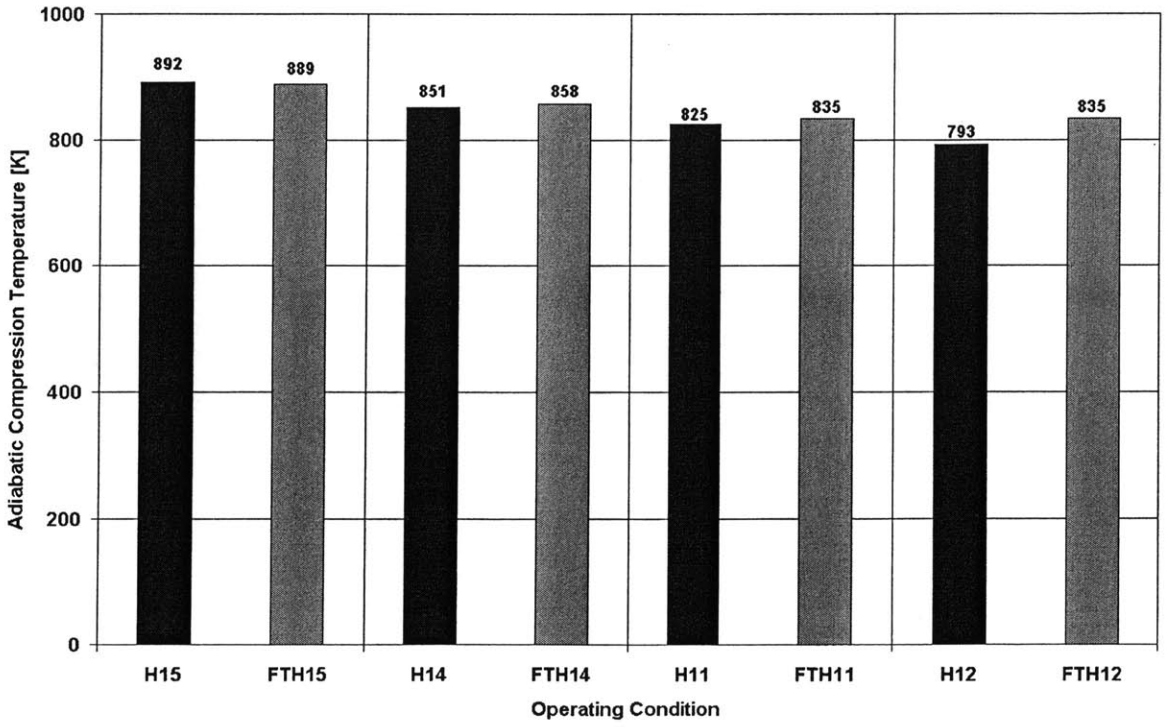

Figure 7.50 Adiabatic compression temperature of unburned gas at the end of injection (EOI) in Modes H11 – H15 and FTH11 – FTH15.

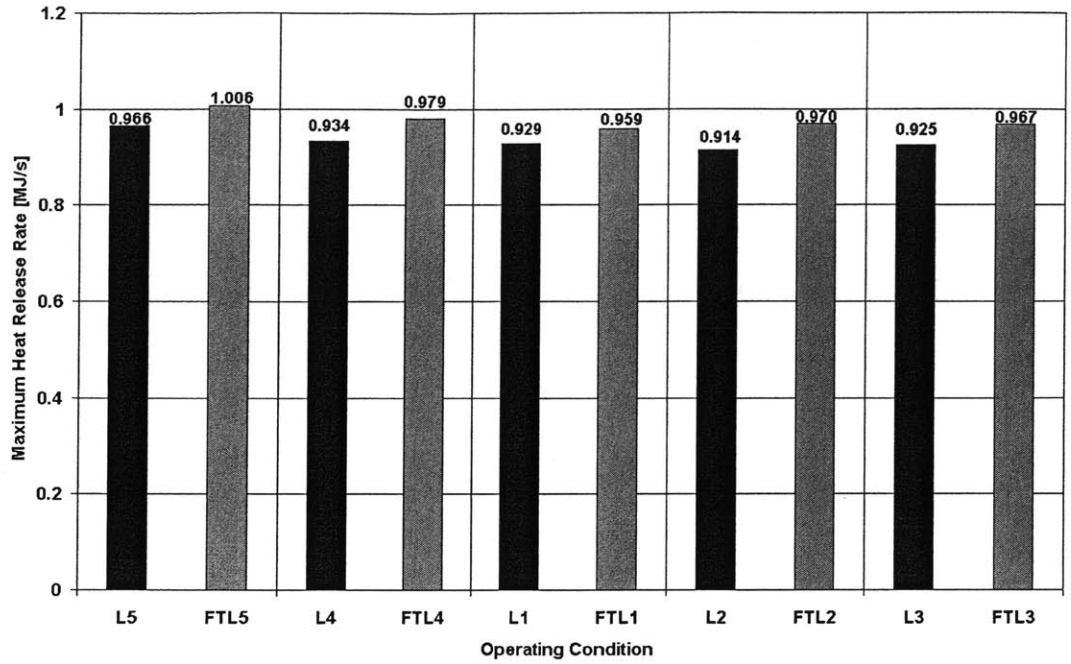

Figure 7.51 Maximum heat release rate using No.2 diesel fuel and Fischer-Tropsch fuel during timing sweep test with stock EGR rates at low loads. The operating conditions are normal diesel (L1 – L5) and Fischer-Tropsch (FTL1 – FTL5). Stock timing is in the center with the most advanced timing to the left and the most retarded timing to the right.

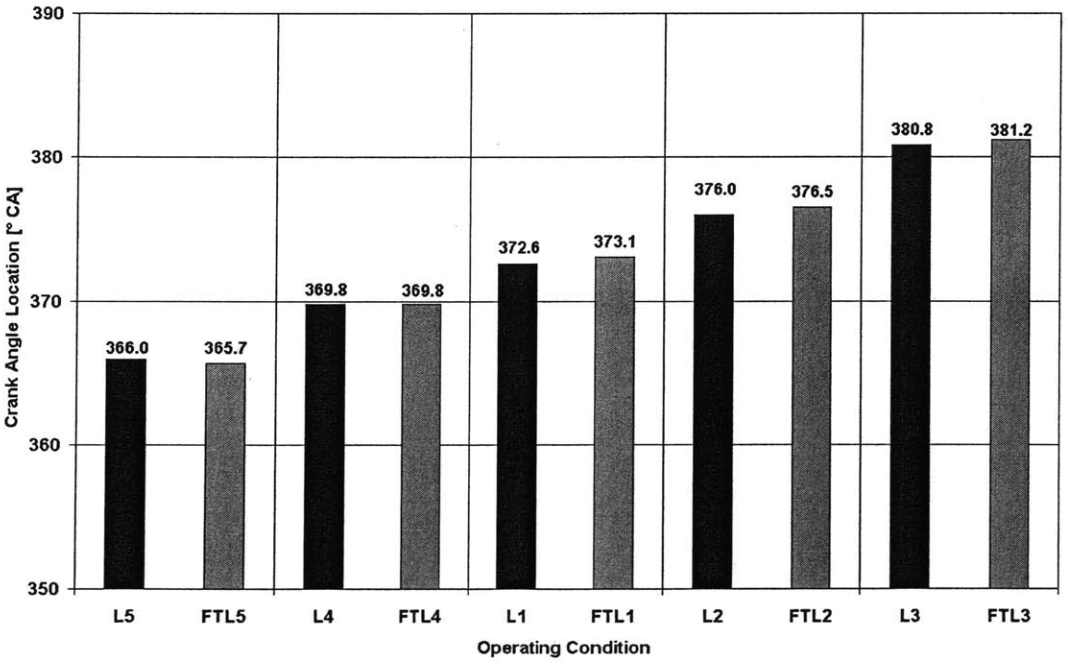

Figure 7.52 Location of maximum heat release rate using No.2 diesel fuel and Fischer-Tropsch fuel during timing sweep test with stock EGR rates at low loads. The operating conditions are normal diesel (L1 – L5) and Fischer-Tropsch (FTL1 – FTL5). Stock timing is in the center with the most advanced timing to the left and the most retarded timing to the right.

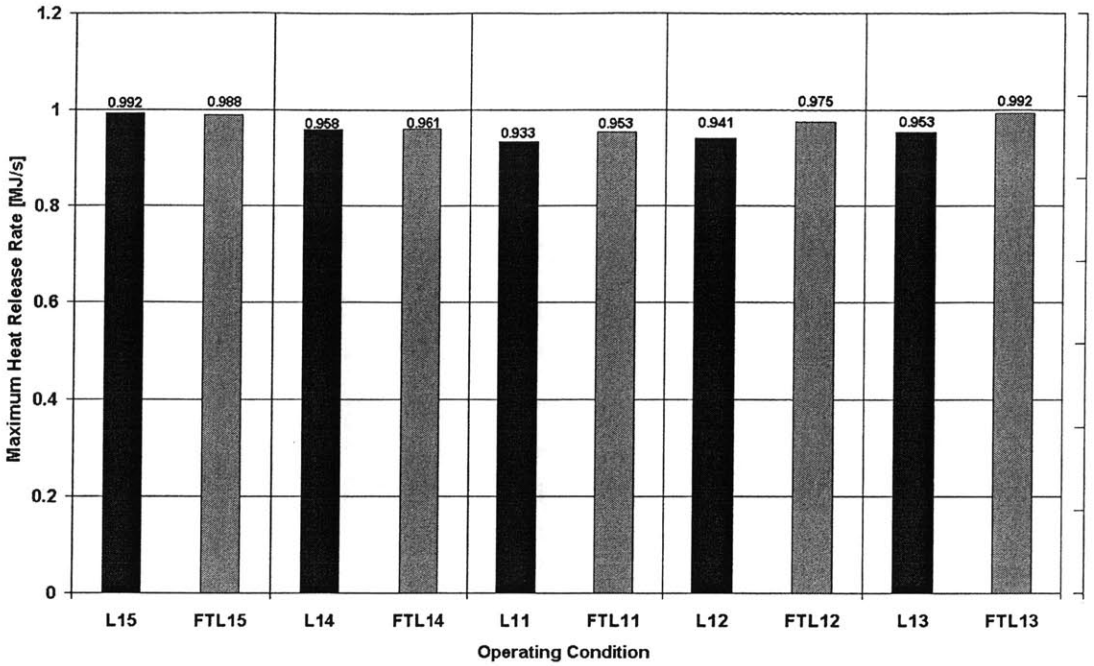

Figure 7.53 Maximum heat release rate using No.2 diesel fuel and Fischer-Tropsch fuel during timing sweep test with increased EGR rates at low loads. The operating conditions are normal diesel (L11 – L15) and Fischer-Tropsch (FTL11 – FTL15). Stock timing is in the center with the most advanced timing to the left and the most retarded timing to the right.

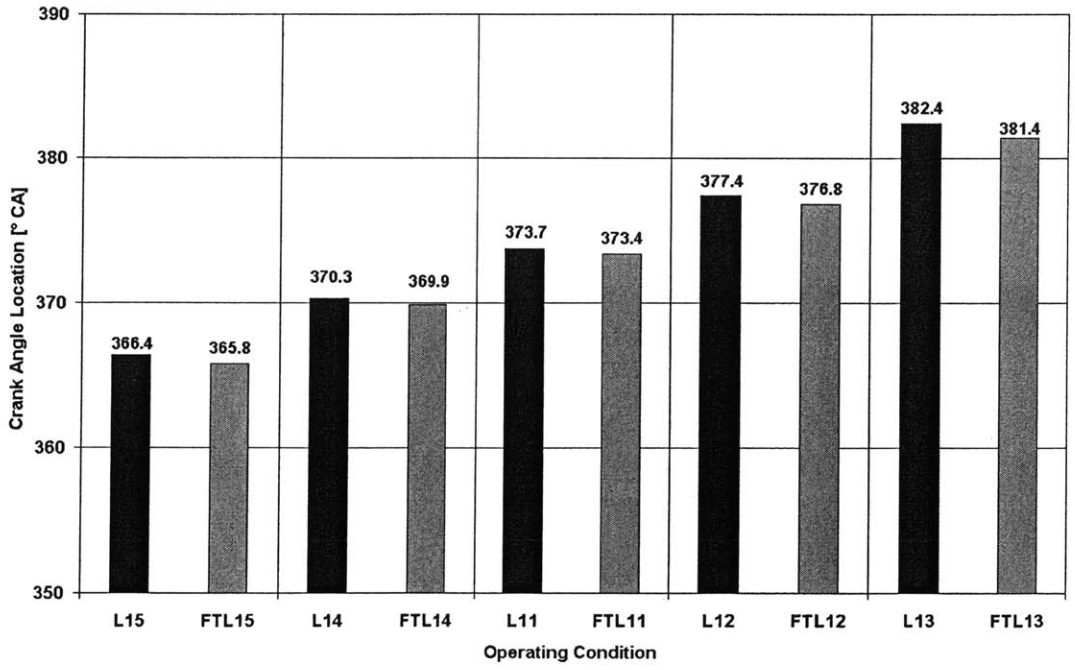

Figure 7.54 Location of maximum heat release rate using No.2 diesel fuel and Fischer-Tropsch fuel during timing sweep test with increased EGR rates at low loads. The operating conditions are normal diesel (L11 – L15) and Fischer-Tropsch (FTL11 – FTL15). Stock timing is in the center with the most advanced timing to the left and the most retarded timing to the right.

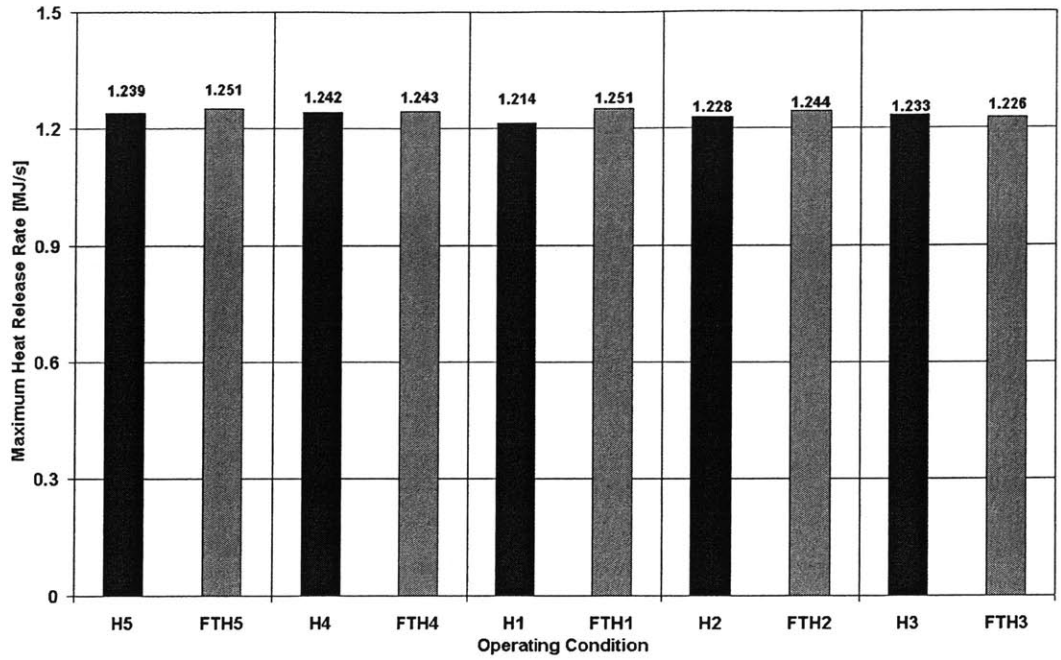

Figure 7.55 Maximum heat release rate using No.2 diesel fuel and Fischer-Tropsch fuel during timing sweep test with stock EGR rates at high loads. The operating conditions are normal diesel (H1 – H5) and Fischer-Tropsch (FTH1 – FTH5). Stock timing is in the center with the most advanced timing to the left and the most retarded timing to the right.

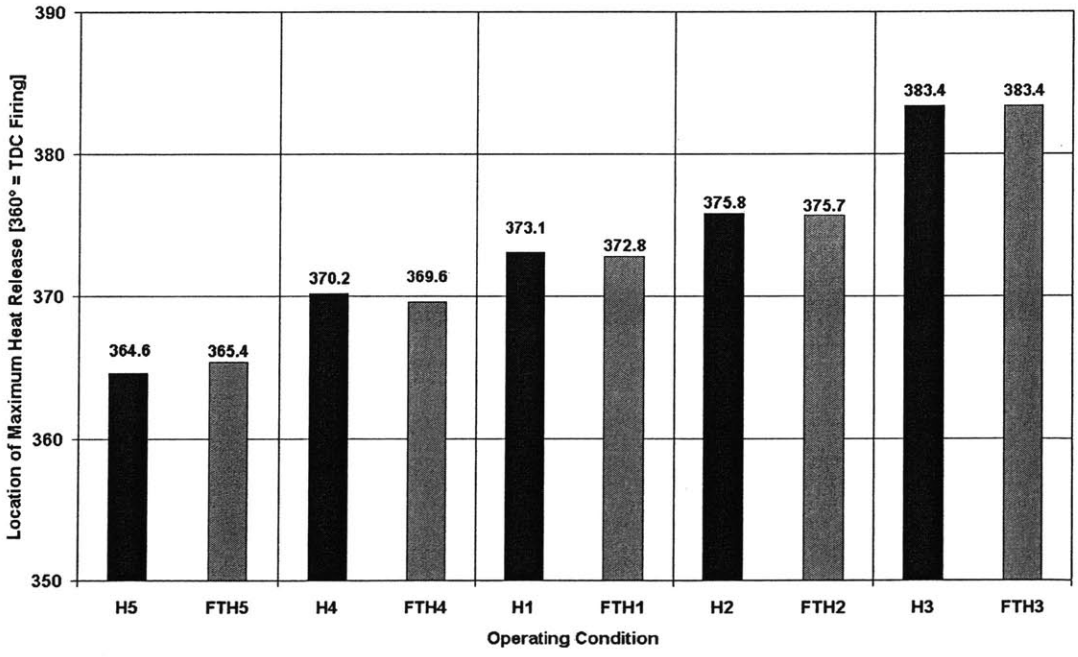

Figure 7.56 Location of maximum heat release rate using No.2 diesel fuel and Fischer-Tropsch fuel during timing sweep test with stock EGR rates at high loads. The operating conditions are normal diesel (H1 – H5) and Fischer-Tropsch (FTH1 – FTH5). Stock timing is in the center with the most advanced timing to the left and the most retarded timing to the right.

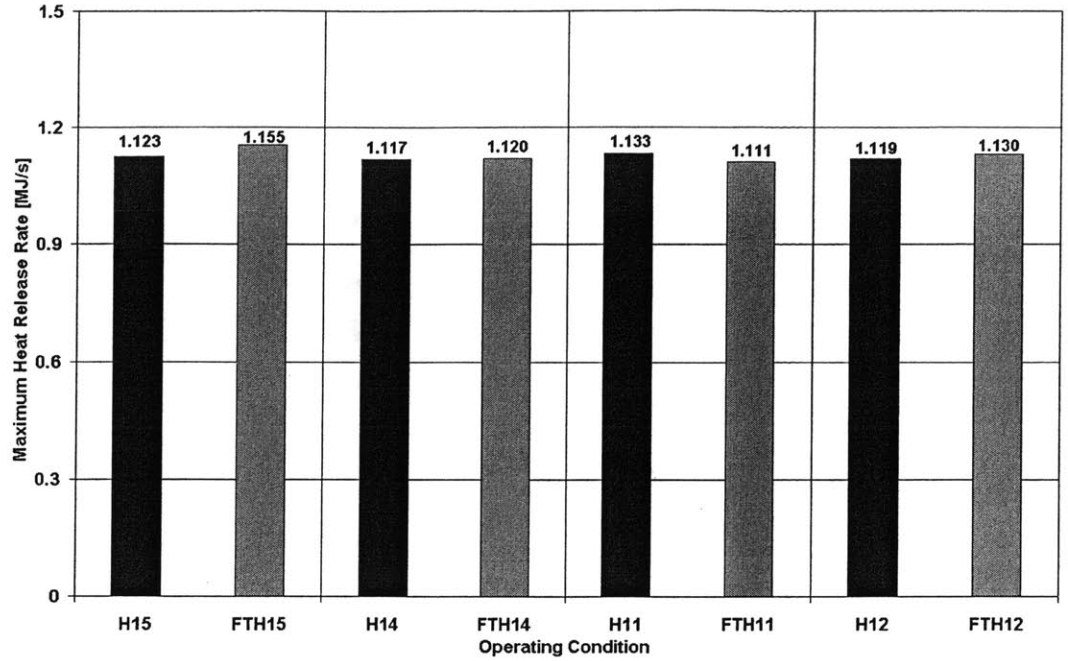

Figure 7.57 Maximum heat release rate using No.2 diesel fuel and Fischer-Tropsch fuel during timing sweep test with increased EGR rates at high loads. The operating conditions are normal diesel (H1 – H5) and Fischer-Tropsch (FTH1 – FTH5). Stock timing is in the center with the most advanced timing to the left and the most retarded timing to the right.

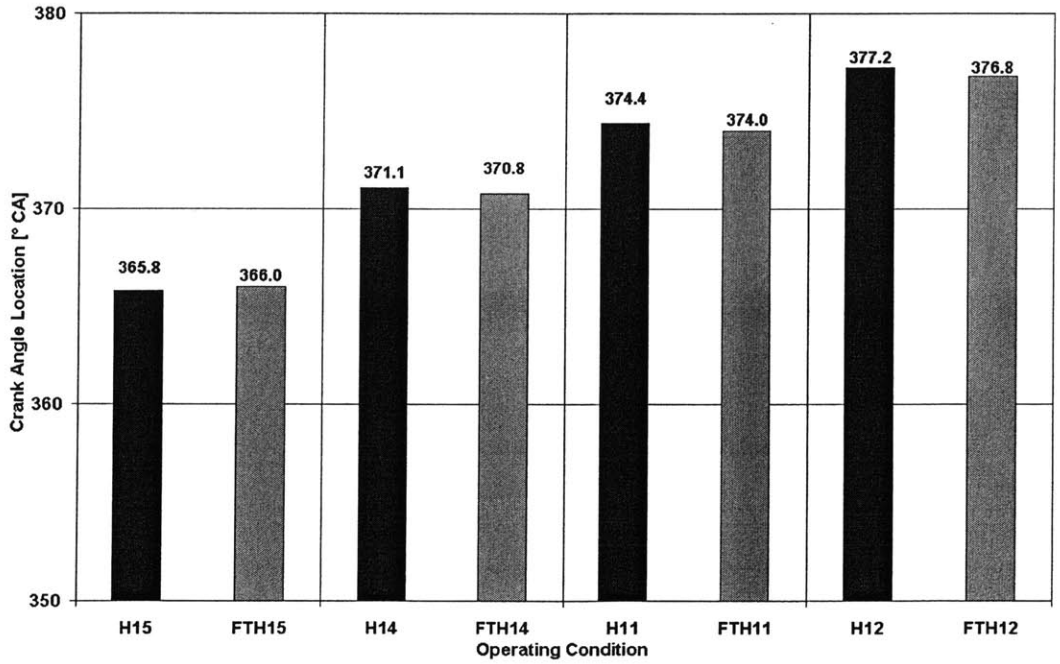

Figure 7.58 Location of maximum heat release rate using No.2 diesel fuel and Fischer-Tropsch fuel during timing sweep test with increased EGR rates at high loads. The operating conditions are normal diesel (H1 – H5) and Fischer-Tropsch (FTH1 – FTH5). Stock timing is in the center with the most advanced timing to the left and the most retarded timing to the right.

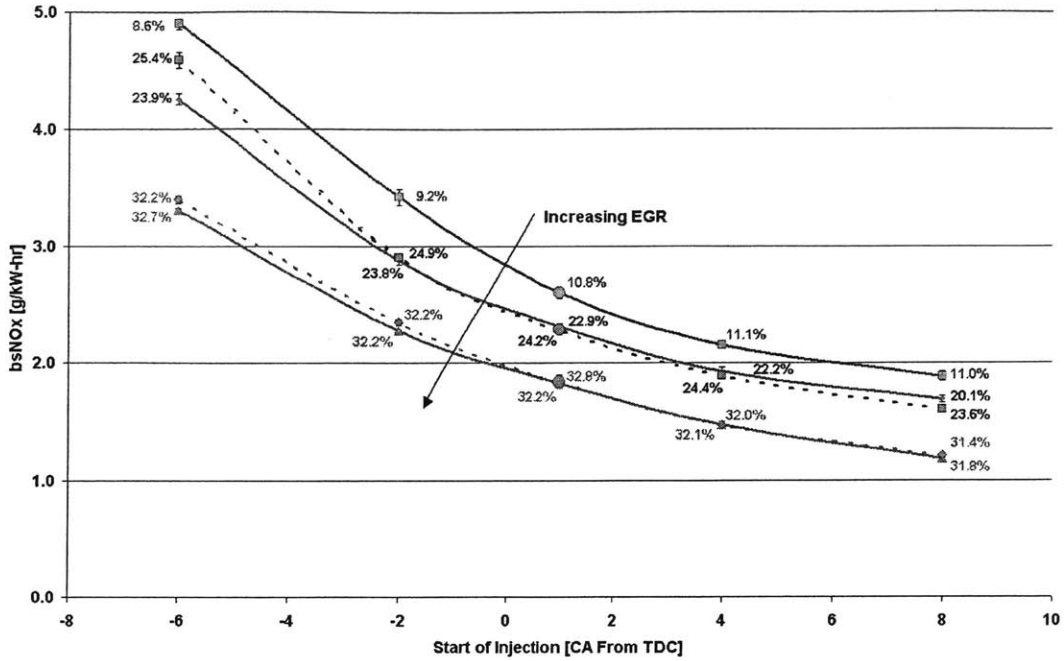

Figure 7.59 Brake-specific NO_x ($bsNO_x$) emissions versus the start of main injection timing for all experimental conditions at low loads. Solid lines apply to No. 2 diesel fuel and dashed lines apply to FT fuel. The individual data labels report the EGR rates for each condition while the error bars show the error for ± 1 S.D. Stock timing points are denoted with enlarged data points.

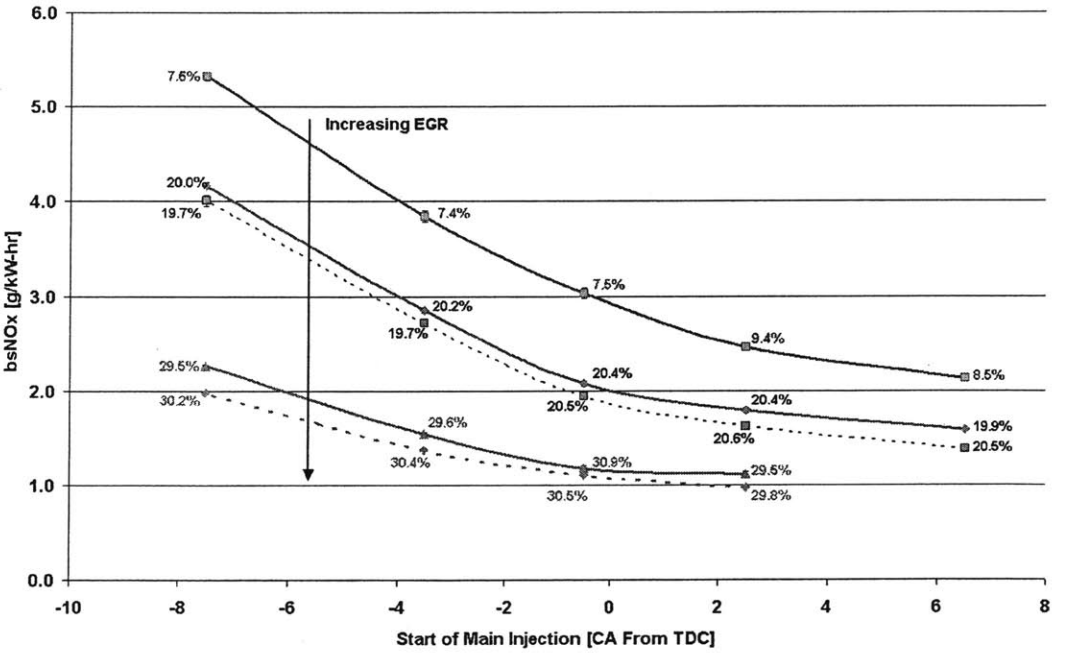

Figure 7.60 Brake-specific NO_x ($bsNO_x$) emissions versus the start of main injection timing for all experimental conditions at high loads. Solid lines apply to No. 2 diesel fuel and dashed lines apply to FT fuel. The individual data labels report the EGR rates for each condition while the error bars show the error for ± 1 S.D. Stock timing points are denoted with enlarged data points.

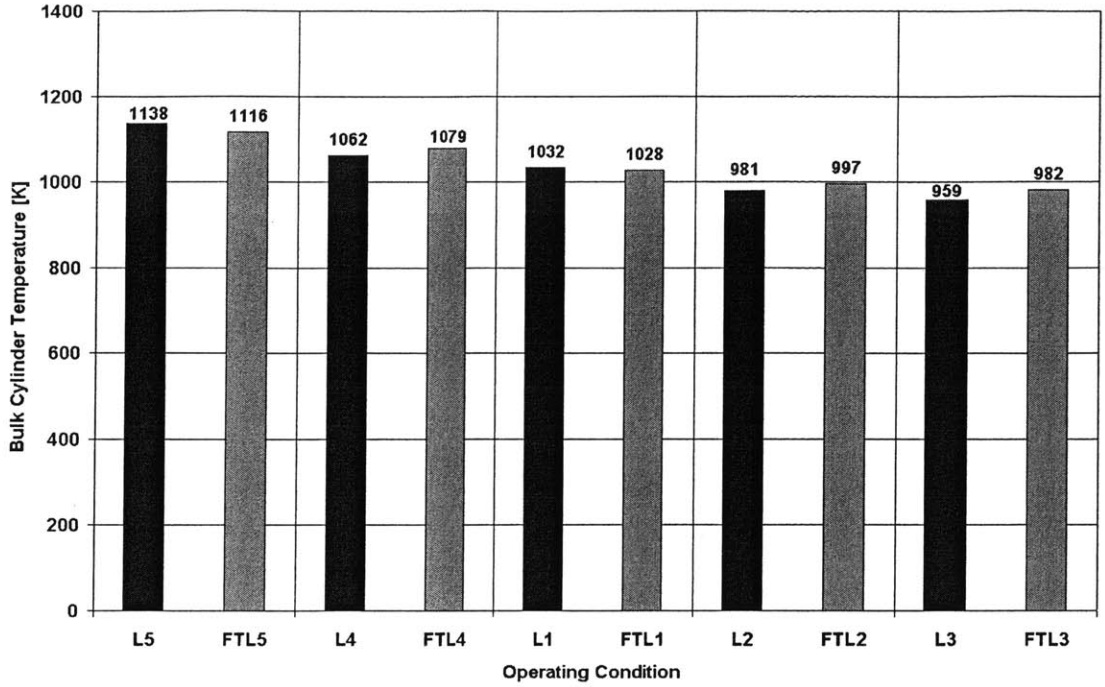

Figure 7.61 Bulk cylinder temperatures at maximum pressure after SOC, predicted by the single-zone heat release model using No.2 diesel fuel and Fischer-Tropsch fuel, during timing sweep test with stock EGR rates at low loads.

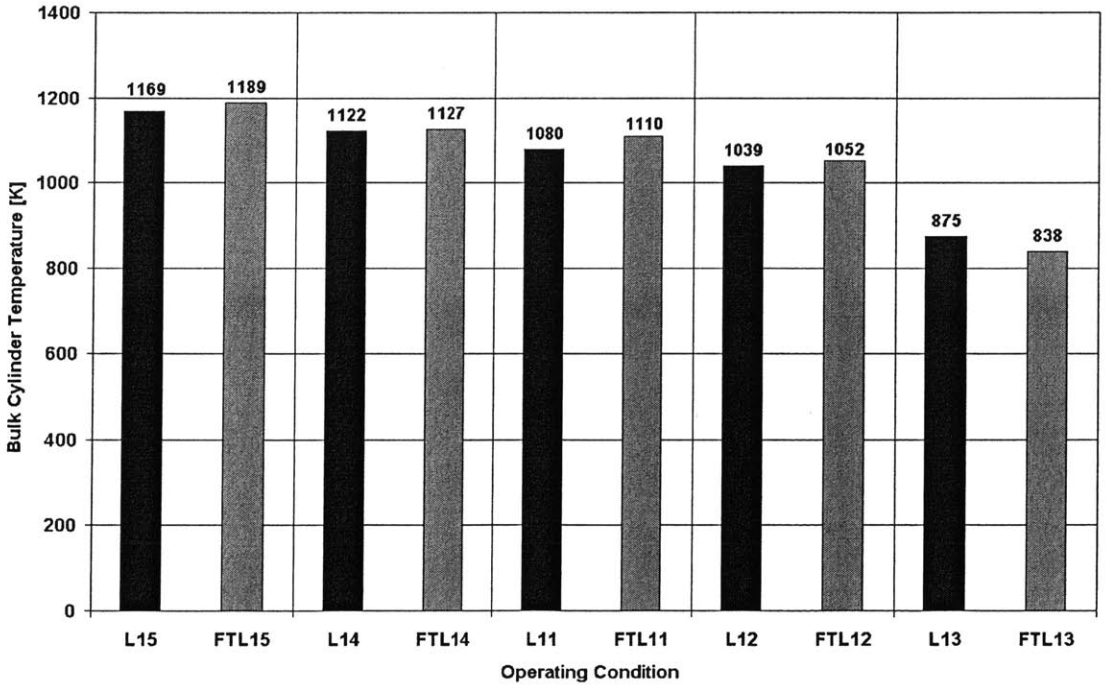

Figure 7.62 Bulk cylinder temperatures at maximum pressure after SOC, predicted by the single-zone heat release model using No.2 diesel fuel and Fischer-Tropsch fuel, during timing sweep test with increased EGR rates at low loads.

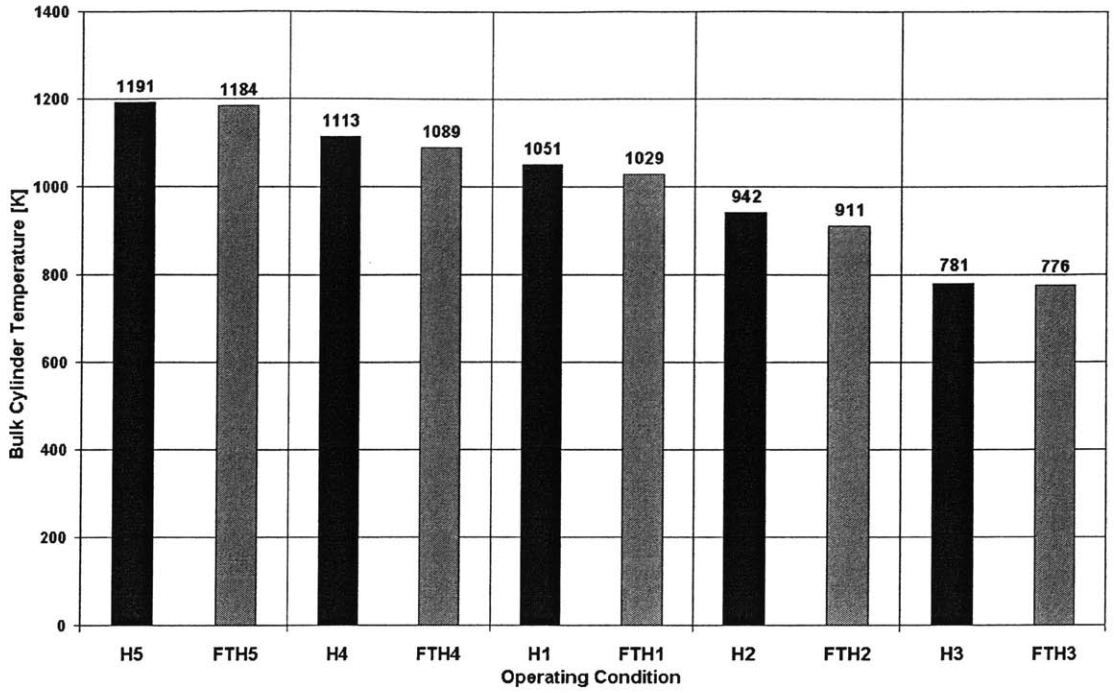

Figure 7.63 Bulk cylinder temperatures at maximum pressure after SOC, predicted by the single-zone heat release model using No.2 diesel fuel and Fischer-Tropsch fuel, during timing sweep test with stock EGR rates at high loads.

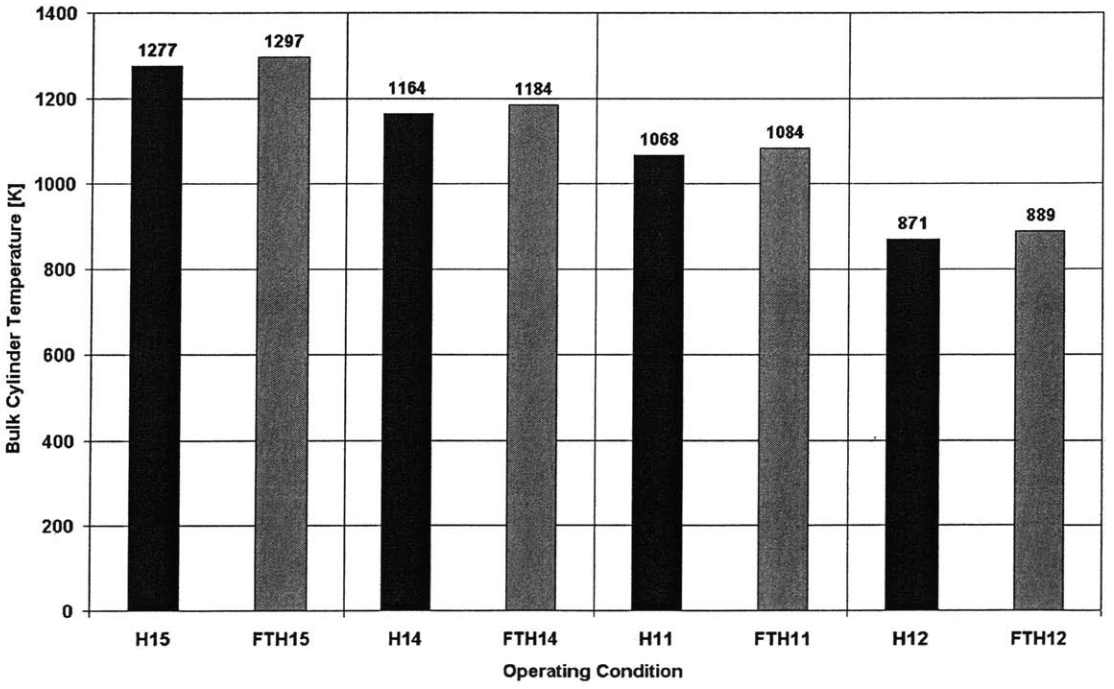

Figure 7.64 Bulk cylinder temperatures at maximum pressure after SOC, predicted by the single-zone heat release model using No.2 diesel fuel and Fischer-Tropsch fuel, during timing sweep test with increased EGR rates at high loads.

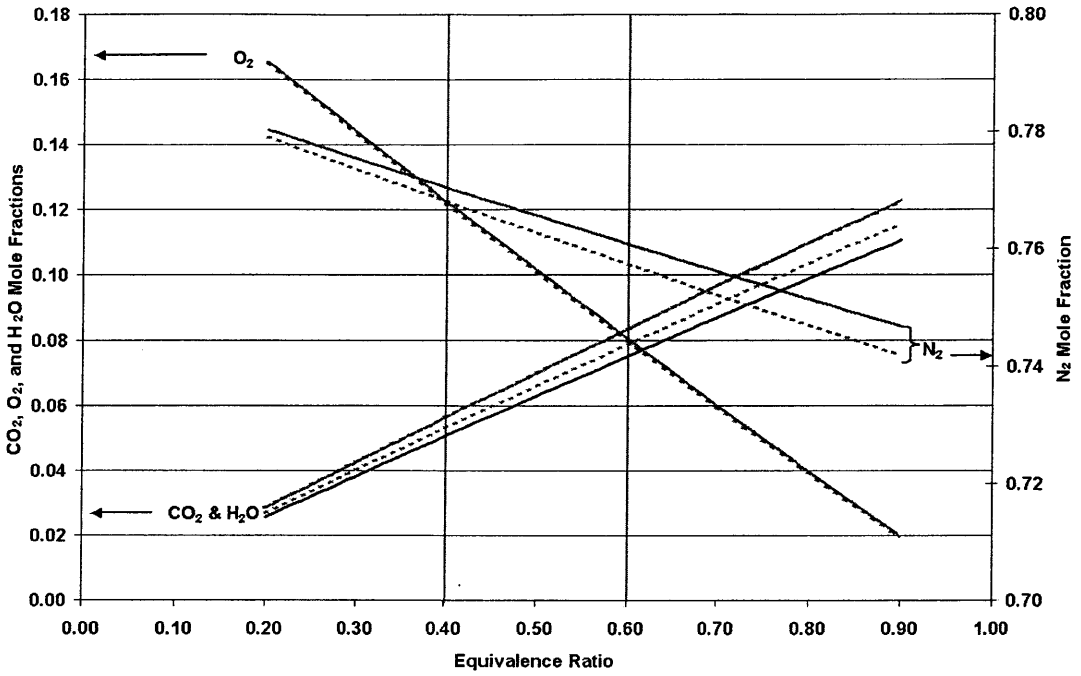

Figure 7.65 Exhaust gas composition versus fuel-air equivalence ratio for No. 2 diesel fuel and FT fuel. Mole fractions are based on No. 2 diesel fuel composition of ($CH_{1.80}$) and FT fuel composition of ($CH_{2.12}$). Solid lines pertain to No. 2 diesel fuel while dotted lines are for FT fuel. For CO_2 and H_2O lines, lower solid line is H_2O mole fraction for No. 2 diesel, while lower dashed line is CO_2 mole fraction for FT.

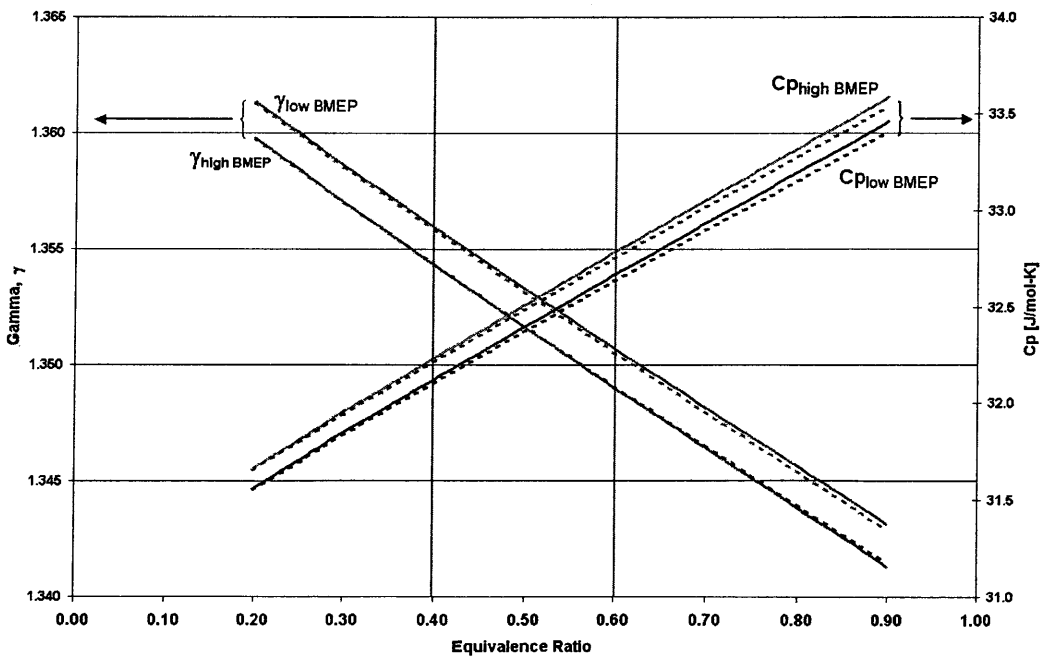

Figure 7.66 Ratio of specific heats of exhaust gas ($\gamma_{exhaust}$) versus fuel-air equivalence ratio of reactants. Mole fractions are based on No. 2 diesel fuel ($CH_{1.80}$). and FT fuel composition of ($CH_{2.12}$). Solid lines pertain to No. 2 diesel fuel while dotted lines are for FT fuel.

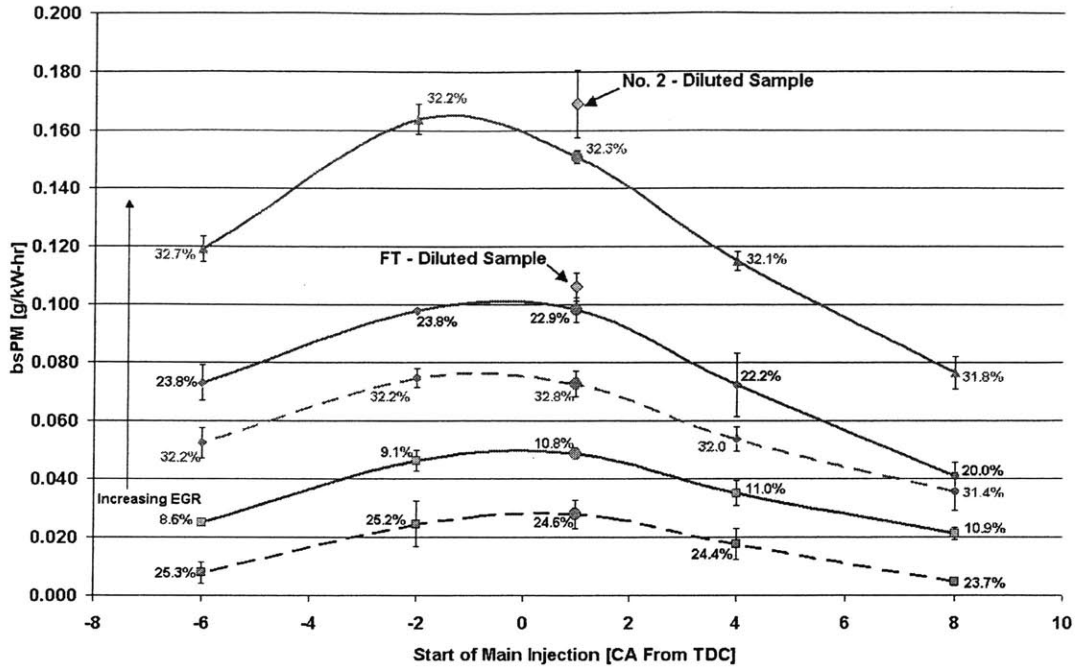

Figure 7.67 Brake-specific particulate matter (bsPM) emissions versus the start of main injection timing for all experimental conditions at low loads. Solid lines apply to No. 2 diesel fuel and dashed lines apply to FT fuel. The individual data labels report the EGR rates for each condition. Enlarged data points represent stock timing condition.

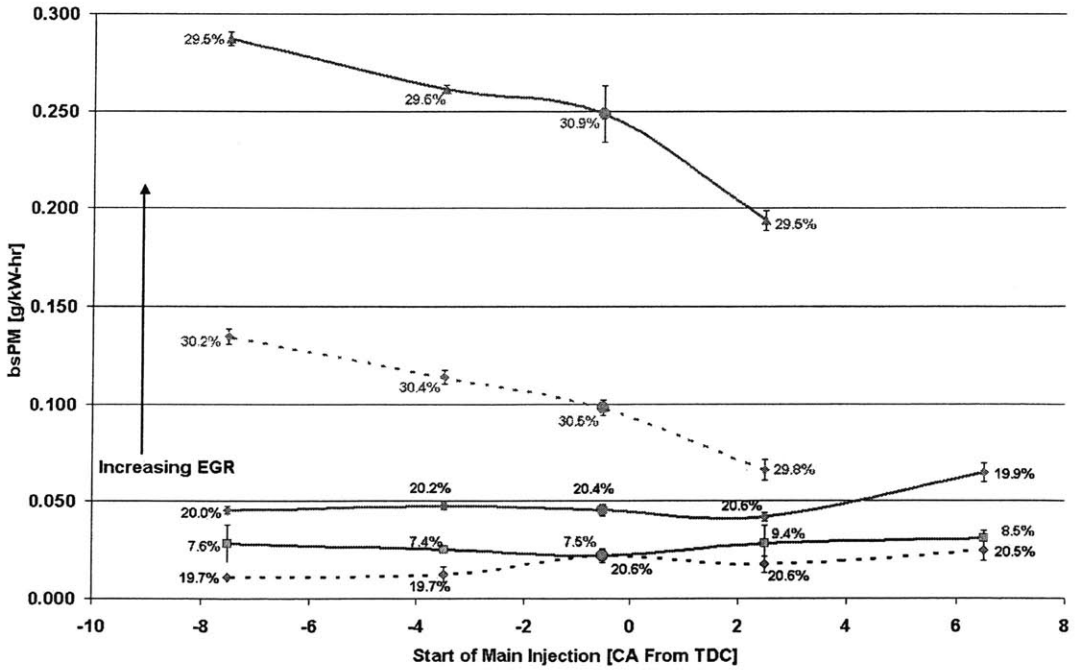

Figure 7.68 Brake-specific particulate matter (bsPM) emissions versus the start of main injection timing for all experimental conditions at high loads. Solid lines apply to No. 2 diesel fuel and dashed lines apply to FT fuel. The individual data labels report the EGR rates for each condition. Enlarged data points represent stock timing condition.

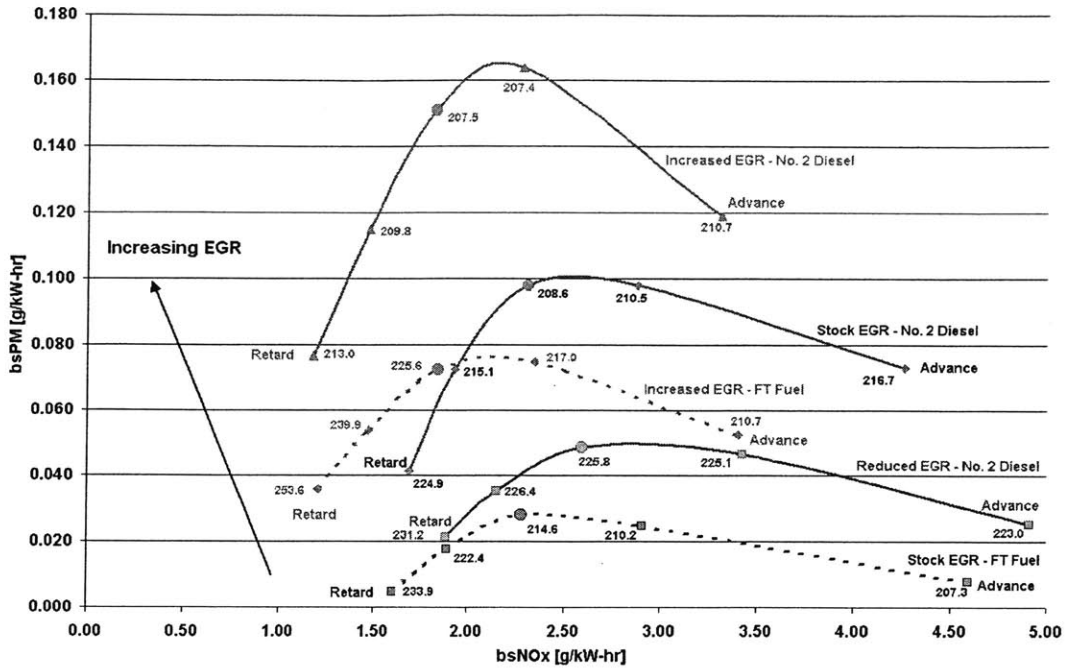

Figure 7.69 bsPM versus bsNO$_x$ for all experimental conditions at low loads. Solid lines apply to No. 2 diesel fuel and dashed lines apply to FT fuel. The individual data labels report the EGR rates for each condition. Enlarged data points represent stock timing condition. Data labels report BSFC [g/kW-h].

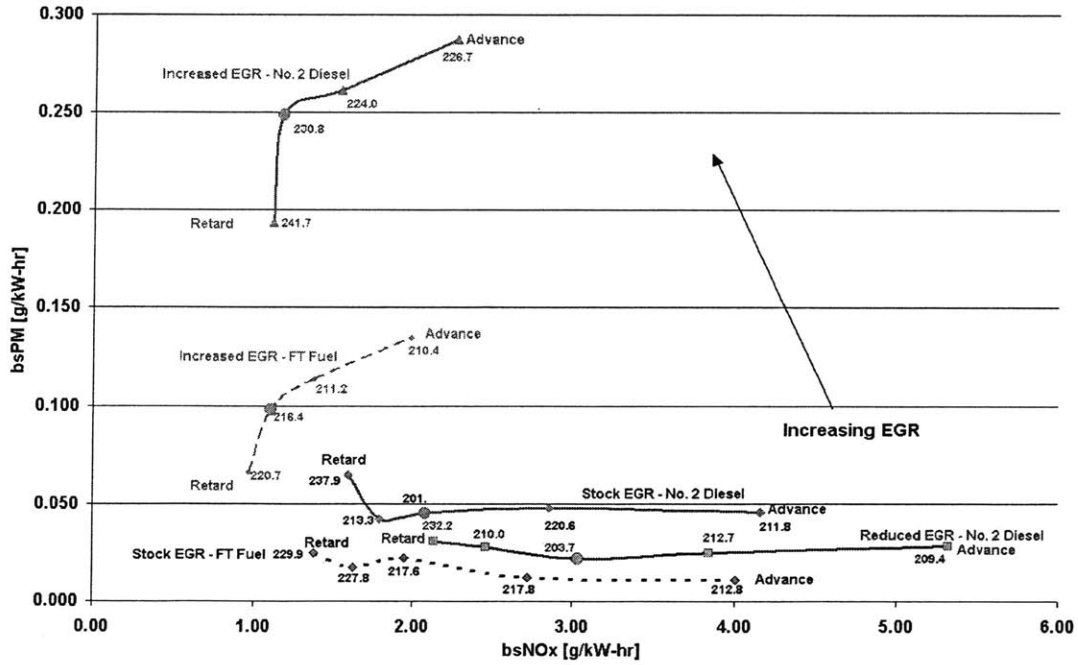

Figure 7.70 bsPM versus bsNO$_x$ for all experimental conditions at high loads. Solid lines apply to No. 2 diesel fuel and dashed lines apply to FT fuel. The individual data labels report the EGR rates for each condition. Enlarged data points represent stock timing condition. Data labels report BSFC [g/kW-h].

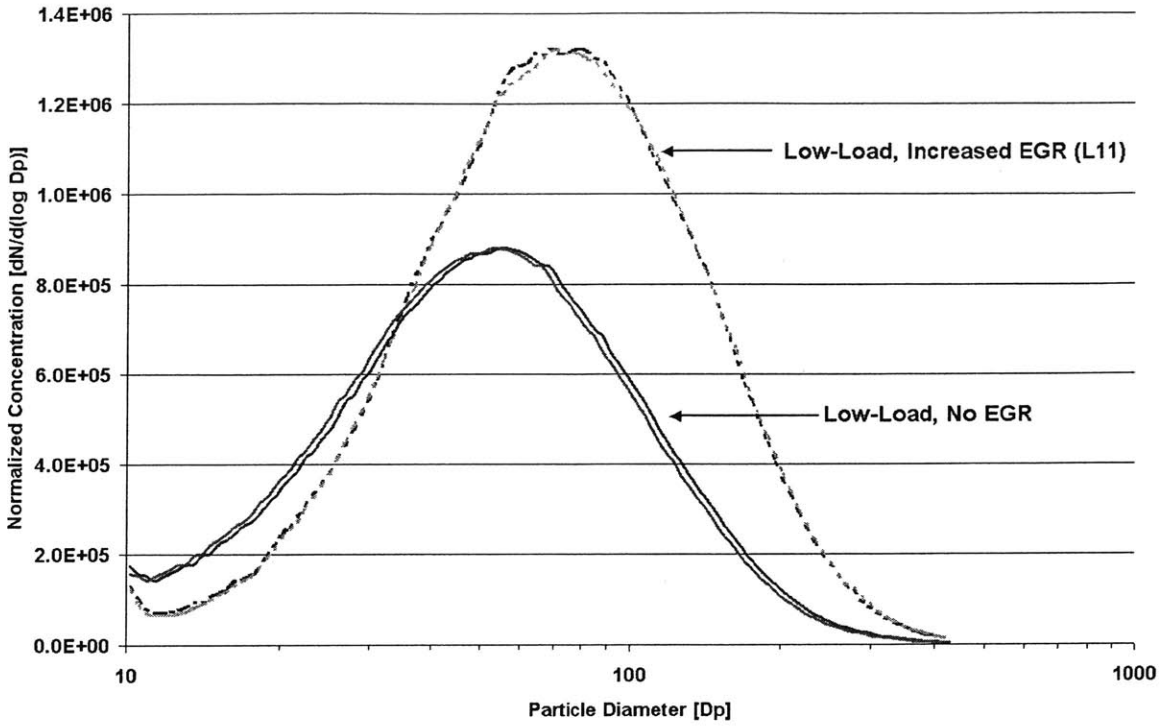

Figure 7.71 SMPS scans at low-load conditions with no EGR and increased-EGR settings (L11).

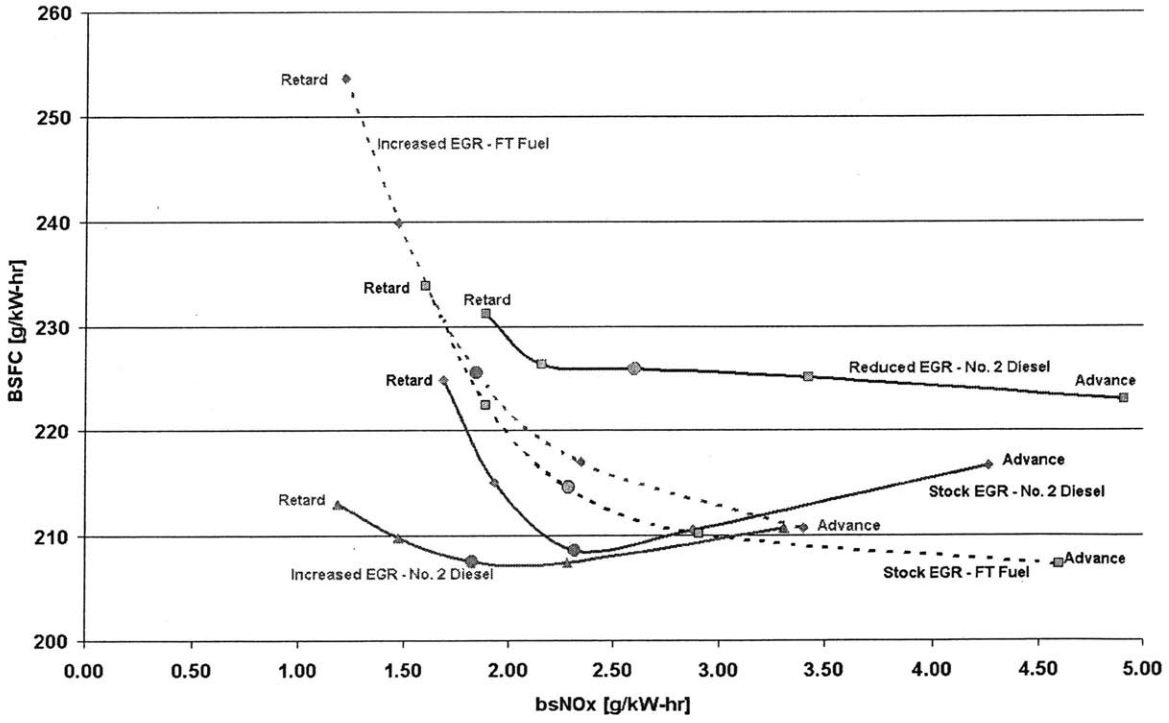

Figure 7.72 BSFC versus bsNO$_x$ tradeoff for all experimental conditions at low loads. Solid lines apply to No. 2 diesel fuel and dashed lines apply to FT fuel. Enlarged data points represent stock timing condition.

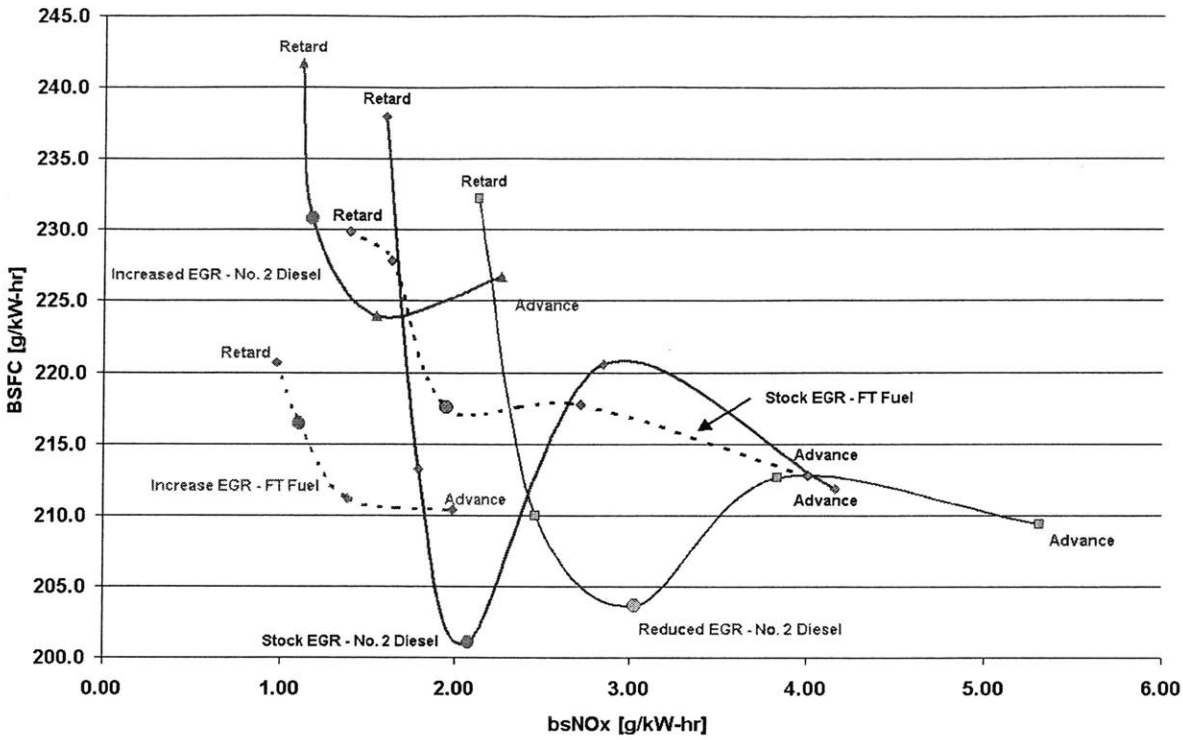

Figure 7.73 BSFC versus bsNO$_x$ tradeoff for all experimental conditions at high loads. Solid lines apply to No. 2 diesel fuel and dashed lines apply to FT fuel. Enlarged data points represent stock timing condition.

Chapter 8 Summary and Conclusions

8.1 Engine Operation and Technology

The experiments conducted during this project show FT diesel fuel can easily be used in diesel engines with little to no modifications. Additionally, based on the discussions presented in the previous chapter, further improvements in performance and emissions can be realized by configuring the engine to take advantage of FT diesel fuel's properties. The following conclusions about engine operation and technology with FT fuel can be made from the data presented earlier:

- FT fuel removes the sensitive dependence of PM production on EGR rate, allowing significant NO_x reductions through the use of higher EGR rates before PM levels become substantially large.
- Increases in PM output from increased EGR rates can be controlled by aftertreatment systems without concern of system performance deterioration from fuel sulfur, as FT diesel fuel is virtually sulfur free.
- Injection timing has no added effects on emissions with FT fuel. FT diesel fuel follows the same trends as the petroleum-based No. 2 diesel fuel used in the experiments. As timing is advanced, both fuels show increases in NO_x while timing retard results in NO_x reductions, showing both fuels have the same NO_x production mechanisms. With PM, both fuels show reductions in emissions as timing is changed from the stock timing point.
- FT fuel showed benefits in timing changes. Engine operation with FT fuel resulted in a standard BSFC-NO_x tradeoff, unlike the behavior seen with No. 2 diesel. It is believed No. 2 diesel was less sensitive to timing changes due to engine manufacturer optimizations in EGR, boost and timing retard. Therefore, timing advance to reduce BSFC using FT diesel fuel can be explored with higher EGR rates controlling NO_x output.

Summarily, FT fuel gives greater freedom to engine designers when trying to optimize engine parameters in modern engines since the performance-emission sensitivity in normal tradeoff curves is reduced.

Lastly, interesting combustion characteristics surfaced as combustion was phased to occur after TDC. Since timing in the test engine occurred at or very close to TDC, the general theories that apply to injection retard in engines that normally inject fuel 15° – 20° did not properly explain the measured

emission behavior. Concepts such as flame lift-off and its effects on air entrainment were used to try and explain the trends, although no direct measurements of these effects were made.

8.2 Fuel Properties

The CN of a fuel is commonly believed to control NO_x output by dictating the amount of fuel that autoignites in the initial premixed burn fraction. However, in engines designed to have small premixed burn fractions, such as those with high injection pressures and swirl to promote good mixing along with injection in hot cylinder conditions around TDC, NO_x emissions are less sensitive to the value of a fuel's CN. This occurs because the increased mixing of fuel and hot air reduce the overall ignition delay and resulting pressure/temperature rise after autoignition. However, the above description of the CN/CNI-NO_x relationship does not completely describe the behavior seen in the conducted experiments.

In the low load tests where the ignition delays with No. 2 diesel were slightly longer than FT diesel's, the NO_x outputs were comparable. However, at high loads, when the ignition delays between the two different fuels were almost equivalent, regardless of the respective CN/CNI rating of the fuel, FT showed consistent reductions. This suggests that the CN alone is the reason for the NO_x reduction seen with FT fuels; other properties may also be playing a role.

Using a raw exhaust sampling technique, FT diesel fuel reduced PM emissions in all operating conditions tested. Further investigations using a diluted exhaust sampling technique gave a better understanding of the general makeup of the sampled PM. No conclusions can be made about the effects of the increased cetane number rating of the FT fuel on PM emissions since this property was not properly decoupled in the experiments. Based on these broad observations, one can make the following conclusions:

- FT diesel fuel has the ability to reduce NO_x emissions, the reduction and its magnitude dependent upon engine operating conditions. At low loads, there is little difference in NO_x emissions between No. 2 diesel fuel and FT diesel fuel. At higher loads, FT diesel fuel shows consistent NO_x reductions versus No. 2 diesel fuel.
- Removing the driving force for nucleation and condensation of volatiles species using a raw sampling technique, FT diesel fuel produces less solid carbon.
- Promoting the condensation and nucleation of SOFs and VOFs using a dilute sampling technique, the difference between PM emissions with FT diesel fuel and No. 2 diesel fuel can be partly attributed to the near-zero sulfur content. The reduction in fuel sulfur helps reduce PM output when using FT fuels by decreasing the amount of sulfates.

- Although cetane ratings can help reduce NO_x emissions by decreasing the premixed burn fraction, FT diesel fuel's chemical composition (higher H/C ratio) can produce products of combustion that may make it more difficult to produce NO_x. Thus, a fuel's chemical composition must also be accounted for when trying to understand NO_x reduction mechanisms.
- Although the zero or near-zero aromatic content can reduce the number of soot precursors formed, the increased saturation ratios of exhaust gas with low concentrations of carbonaceous agglomerates may help nucleate and condense gaseous species. Thus, PM in FT exhaust contains a larger fraction of SOF/VOFs compared to No. 2 diesel, based on the larger drop in PM between dilute and raw sampling techniques for FT fuel than for No. 2 diesel fuel.

8.3 Recommendations

From the summary presented above, future work on the Clean Diesel Project should include a better understanding of the limits of FT diesel fuel on PM suppression under very high EGR rates. With NO_x effectively controlled, PM aftertreatment systems such as oxidation catalysts or diesel particulate filters with regeneration can be used extensively since their performance will not deteriorate due to sulfur poisoning and they need less user upkeep compared to NO_x treatment systems that require a separate tank to hold a reductant.

The mechanisms for NO_x formation and PM formation/destruction should be studied further by running more experiments that test the above conclusions. Higher load tests that result in different burned-gas compositions can provide more insight into the NO_x reductions seen as load increases

Furthermore, the burn rate analysis program should be properly calibrated or a better First Law treatment of combustion (multiple zones) should be incorporated in order to extract much more useful information from the high-speed, crank-angle resolved in-cylinder pressure traces. The development of the fuel-air vapor composition within the spray must be properly taken into account as well, since the earlier discussion shows that flame lift-off theories including air-entrainment concepts may become important as combustion is phased to occur after TDC. In addition to including these new entrainment concepts, better understandings of their behavior in an actual engine with swirl and squish need to be investigated.

(This page left intentionally blank.)

References

[1] Borman, G. L. and Ragland, K. W., Combustion Engineering, McGraw-Hill, Inc., Boston, 1998

[2] Heywood, J. B., Internal Combustion Engine Fundamentals, McGraw-Hill, Inc., New York, 1988

[3] Stone, R., Introduction to Internal Combustion Engines, 3rd Edition, SAE Publications, 1999

[4] Cheng, W. K., Hamrin, D., Heywood, J. B., Hochgreb, S., Min, K. and Norris M., "An Overview of Hydrocarbon Emissions Mechanisms in Spark-Ignition Engines," SAE Paper 932708, 1993

[5] Warnatz, J., Mass, U., Dibble, R. W., Combustion: Physical and Chemical Fundamentals, Modeling and Simulation, Experiments, Pollutant Formation, 2nd Edition, Springer-Verlag, Berlin, 1999

[6] United States Environmental Protection Agency (EPA) Report, "Health Assessment Document for Diesel Engine Exhaust," Report Number EPA/600/8-90/057F, May 2002

[7] Health Effects Institute, "Diesel Exhaust: A Critical Analysis of Emissions, Exposure, and Health Effects," April 1995

[8] DieselNet Website, http://www.dieselnet.com/

[9] World-Wide Fuel Charter, AutoAlliance Webstite, http://www.autoalliance.org/fuel_charter.htm

[10] Fischer-Tropsch Website, http://www.fischer-tropsch.org/

[11] Springer, P. S., Hugman, R. H., Costiness, M. J., Vidas, E. H., "Chemical Composition of Discovered and Undiscovered Natural Gas in the Continental United States – 1998 Update. Project Summary," Gas Research Institute, 1998

[12] Schaberg, P. W., Myburgh, I. S., Botha, J. J., Roets, P. N., Viljoen, C. L., Dancuart, L. P., and Starr M.E., "Diesel Exhaust Emissions Using Sasol Slurry Phase Distillate Process Fuels," SAE Paper 972898, 1998

[13] McMillian, M. H. and Gautam, M., "Consideration for Fischer-Tropsch Derived Liquid Fuels as a Fuel Injection Emission Control Parameter," SAE Paper 982489, 1998

[14] Norton, P., Vertin, K., Bailey, B., Clark, N. N., Lyons, D. W., Goguen, S., and Eberhardt, J., "Emissions from Trucks using Fischer-Tropsch Diesel Fuel," SAE Paper 982526, 1998

[15] World Crude Oil and Natural Gas Reserves, January 1, 2002, Department of Energy (DOE), http://www.eia.doe.gov/emeu/iea/table81.html

[16] Alleman, T. L. and McCormick, R. L., "Fischer-Tropsch Diesel Fuels – Properties and Exhaust Emissions: A Literature Review," SAE Paper 2003-01-0763, 2003

[17] Clark, N. N., Atkinson, C. M., Thompson, G. J. and Nine, R. D., "Transient Emissions Comparisons of Alternative Compression Ignition Fuels," SAE Paper 1999-01-1117, 1999

[18] Atkinson, C. M., Thompson, G. J., Traver, M. L., and Clark, N. N., "In-Cylinder Combustion Pressure Characteristics of Fischer-Tropsch and Conventional Diesel Fuels in a Heavy Duty CI Engine," SAE Paper 1999-01-1472, 1999

[19] Cheng, A. S. and Dibble, R. W., "Emissions Performance of Oxygenate-in-Diesel Blends and Fischer-Tropsch Diesel in a Compression Ignition Engine," SAE Paper 1999-01-3606, 1999

[20] Schaberg, P. W., Myburgh, I. S., Botha, J. J. and Khalek, I. A., "Comparitive Emissions Performance of Sasol Fischer-Tropsch Diesel Fuel in Current and Older Technology Heavy-Duty Engines," SAE Paper 2000-01-1912, 2000

[21] May, M. P., Vertin, K., Ren, S., Gui, X., Myburgh, I. And Schaberg, P., "Development of Truck Engine Technologies for Use with Fischer-Tropsch Fuels," SAE Paper 2001-01-3520, 2000

[22] Nord, K. and Haupt, D., "Evaluating a Fischer-Tropsch Fuel, Eco-Par™, in a Valmet Diesel Engine," SAE Paper 2002-01-2726, 2002

[23] Luders, H., Strommel, P., and Geckler, S., "Diesel Exhaust Treatment – New Approaches to Ultra Low Emission Diesel Vehicles," SAE Paper 1999-01-0108, 1998

[24] Dec, J. E., Espey, C., "Ignition and Early Soot Formation in a DI Diesel Engine Using Multiple 2-D Imaging Diagnostics," SAE Paper 950456, 1995

[25] Dec, J. E., Coy, E. B., "OH Radical Imaging in a DI Diesel Engine and the Structure of the Early Diffusion Flame," SAE Paper 960831, 1996

[26] Dec, J. E., "A Conceptual Model of DI Diesel Combustion Based on Laser-Sheet Imaging," SAE Paper 970873, 1997

[27] Dec, J. E., Canaan, R. E., "PLIF Imaging of NO Formation in a DI Diesel Engine," SAE Paper 980147, 1998

[28] Dec, J. E., Espey, C., "Chemiluminescence Imaging of Autoignition in a DI Diesel Engine," SAE Paper 982685, 1998

[29] Flynn, P. F., Durrett, R. P., Hunter, G. L., zur Loye, A. O., Akinyemi, O. C., Dec, J. E., and Westbrook, C. K., "Diesel Combustion: An Integrated View Combining Laser Diagnostics, Chemical Kinetics, And Empirical Validation," SAE Paper 1999-01-0509, 1999

[30] Siebers, D. and Higgins, B., "Flame Lift-Off on Direct-Injection Diesel Sprays Under Quiescent Conditions," SAE Paper 2001-01-0530, 2001

[31] Naber, J. D. and Siebers, D., "Effects of Gas Density and Vaporization on Penetration and Dispersion of Diesel Sprays," SAE Paper 960034, 1996

[32] Ryan, T. W. III, Erwin, J., Mason, R. L., and Moulton, D. S., "Relationships Between Fuel Propeties and Composition and Diesel Engine Combustion Performance and Emissions," SAE Paper 941018, 1994

[33] United State Environmental Protection Agency (EPA) Report, "The Effect of Cetane Number Increase Due to Additives on NO_x Emissions From Heavy-Duty Highway Engines: Final Technical Report," Report Number EPA420-R-03-002, February 2003

[34] Kwon, Y., Mann, N., Rickeard, D. J., Haugland, R., Ulvund, K. A., Kvinge, F., and Wilson, G., "Fuel Effects on Diesel Emissions – A New Understanding," SAE Paper 2001-01-3522, 2001

[35] Lee, R., Pedley, J., Hobbs, C., "Fuel Quality Impact on Heavy Duty Diesel Emissions: - A Literature Review," SAE Paper 982649, 1998

[36] Neill, W. S., Chippior, W. L., and Gülder, Ö. L., "Influence of Aromatic Type on Diesel Emissions Investigated by Blending Narrow-Cut Components and Pure Hydrocarbons into a Base Fuel," Paper No. 2001-ICE-420, ICE-Vol. 37-2, 2001 Fall Technical Conference, ASME 2001

[37] American Society for Testing and Materials (ASTM) International, www.astm.org

[38] Patel, V., Cetane Number of New Zealand: A Report by Vallabh Patel, Office of Chief Gas Engineer, Wellington, April 1999 (ISBN 0-47823422-8)

[39] Takahashi, S., Wakimoto, K., Lida, N., and Nikolic, D., "Effects of Aromatics Content and 90% Distillation Temperature of Diesel Fuels on Flame Temperature and Soot Formation," SAE Paper 2001-01-1940, 2001

[40] Daniels, T. L., McCormick, R. L., Graboski, M. S., Carlson, P. N., Rao, V, and Rice, G. W., "The Effect of Diesel Sulfur Content and Oxidation Catalysts on Transient Emissions at High Altitude from a 1995 Detroit Diesel Series 50 Urban Bus Engine," SAE Paper 961974, 1996

[41] Nagaki, H. and Korematsu, K., "Effect of Sulfur Dioxide Added to Induction Air On Wear of Diesel Engine," SAE Paper 930994, 1993

[42] Lüders, H., Krüger, M., Strommel, P., and Lüers, B., "The Role of Sampling Conditions in Particle Size Distribution Measurements," SAE Paper 981374, 1998

[43] Schmidt, D., Wong, V. W., Green, W. H., Weiss, M. A., and Heywood J. B., "Review and Assessment of Fuel Effects and Research Needs in Clean Diesel Technology", Proceeding of the ASME Internal Combustion Engine Division, 2001 Spring Technical Conference, ICE-Volume 36, Philadelphia, 2001

[44] Bauer, H., Editor-in-Chief, Bosch Automotive Handbook, 5th Edition, Robert Bosch Gmbh, Stuttgart, 2000

[45] UWEQL, University Of Washington Equilibrium, Code written by David T. Pratt, Professor Emeritus Of Mechanical Engineering of the University Of Washington, 1998

[46] Asanuma, T. and Obokata, T., "Gas Velocity Measurements of a Motored and Firing Engine by Laser Anemometry," SAE Paper 790096, 1979

[47] Atkinson, C. M., Thompson, G. J., Traver M. L., and Clark N. N., "In-Cylinder Combustion Pressure Characterisitcs of Fischer-Tropsch and Conventional Diesel Fuels in a Heavy Duty CI Engine," SAE Paper 1999-01-1472, 1999

[48] Gülder, Ö. L., "Flame Temperature Estimation of Conventional and Future Jet Fuels," ASME Journal of Engineering for Gas Turbines and Power, Vol. 108, Transactions of the ASME, 1986

[49] EPA Test Procedure TP 713D, "Sample Collection, Continuous Hydrocarbon Analysis and Particulate Collection of the Light Duty Diesel Test Procedure"

[50] EPA Test Procedure TP 714C, "Diesel Particulate Filter Handling and Weighing Procedure"

[51] Hallgren, B. E., "Effects of Oxygenated Fuels on DI Diesel Combustion and Emission," M.S. Thesis, MIT, 20002

[52] Payri, F., Arrègle, J., Fenollosa, C., Belot. G., Delage, A., Schaberg, P., Mybrugh, I., and Botha, J., "Characterization of the Injection-Combustion Process in a Common Rail D.I. Diesel Engine Running with Sasol Fischer-Tropsch Fuel," SAE Paper 2000-01-1803, 2001

[53] Assanis, D. N., "A Computer Simulation of the Turbocharged Turbocompounded Diesel Engine System for Studies of Low Heat Rejection Engine Performance," Ph.D. Thesis, MIT, 1985

[54] "Syntroleum S-2 Synthetic Diesel: Driving Clean-Fuel Innovation," http://www.syntroleum.com/media/syntroleum_s2.pdf, Syntroleum Corporation, 2002

[55] Kennedy, I. M., "Models of Soot Formation and Oxidation," Progress in Energy and Combustion Science, Vol. 23, Elsevier Science, 1997

[56] Kittelson, D. B., Arnold, M. and Watts, and W. F. Jr., "Review of Diesel Particulate Matter Sampling Methods: Final Report," University Of Minnesota, 1999

[57] Costa, M., Merola, S. S., and Vaglieco, B. M., "Mulitdimensional Modeling and Spectroscopic Analysis of the Soot Formation Process in a Diesel Engine," SAE Paper 2002-01-2161, 2001

[58] Frenklach, M. and Wang, .H, "Detailed Modeling of Soot Particle Nucleation and Growth," Twenty-Third Symposium (International) on Combustion, The Combustion Institute, Pittsburgh, 1990

[59] Richter, H., Grieco, W., and Howard, J., "Formation Mechanisms of Polycyclic Aromatic Hydrocarbons and Fullerenes in Premixed Benzene Flames," Combustion and Flame, The Combustion Institute, 1999

(This page left intentionally blank.)

Appendix A

Cylinder Pressure Traces Various Operating Conditions

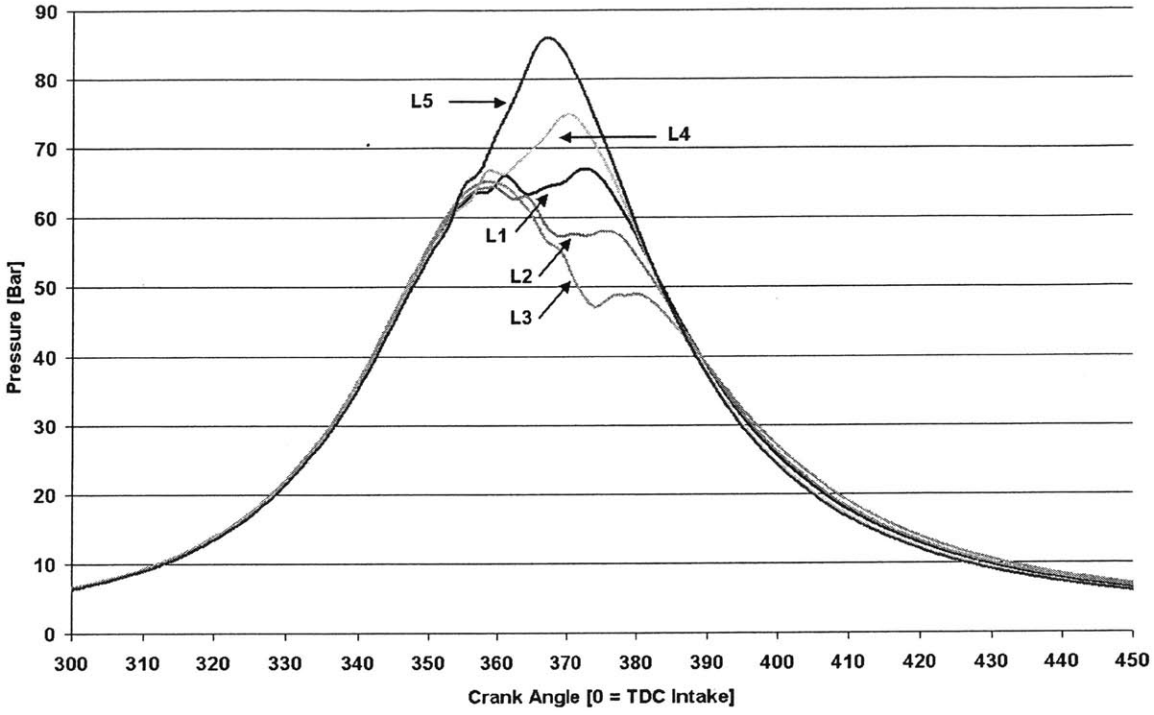

Appendix A.1 Cylinder pressure traces for stock-EGR, low-load conditions with No. 2 diesel.

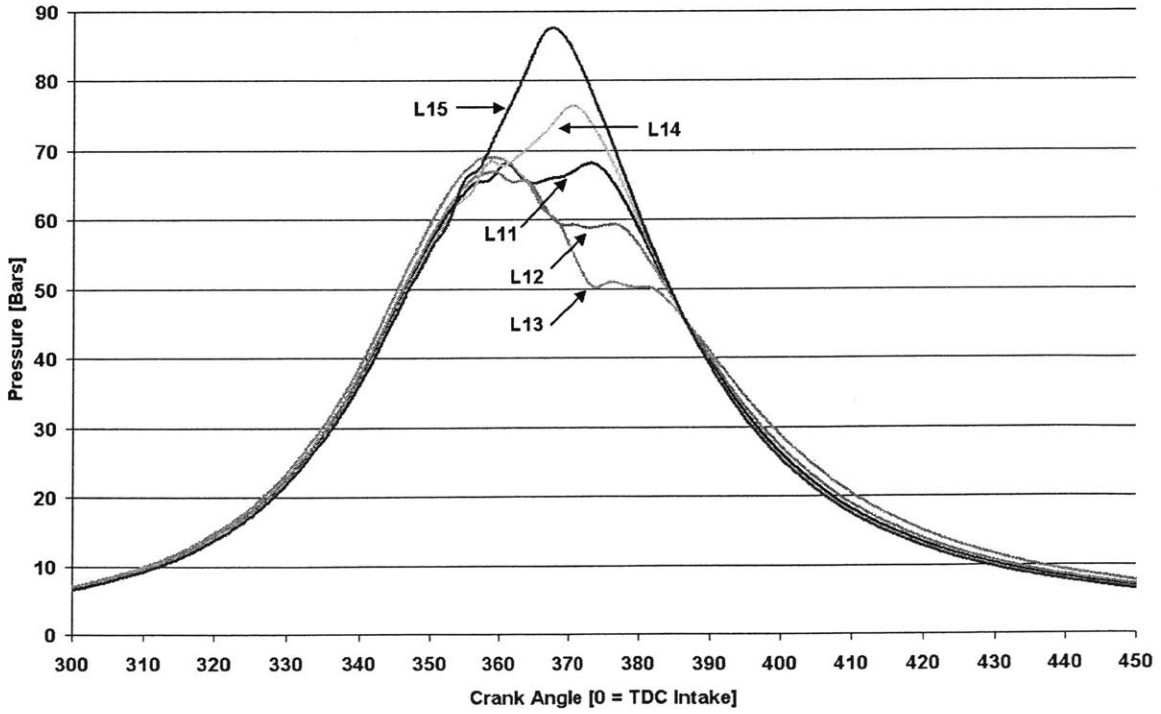

Appendix A.2 Cylinder pressure traces for increased-EGR, low-load conditions with No. 2 diesel.

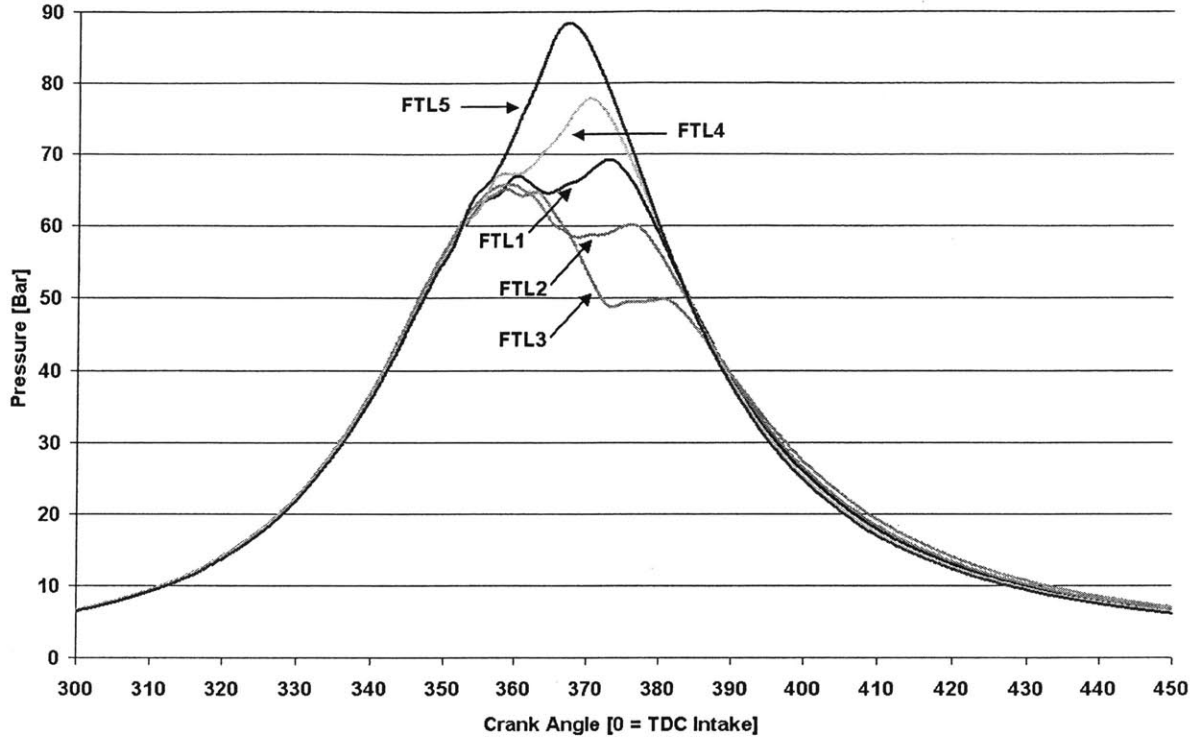

Appendix A.3 Cylinder pressure traces for stock-EGR, low-load conditions with Syntroleum S-2 FT diesel.

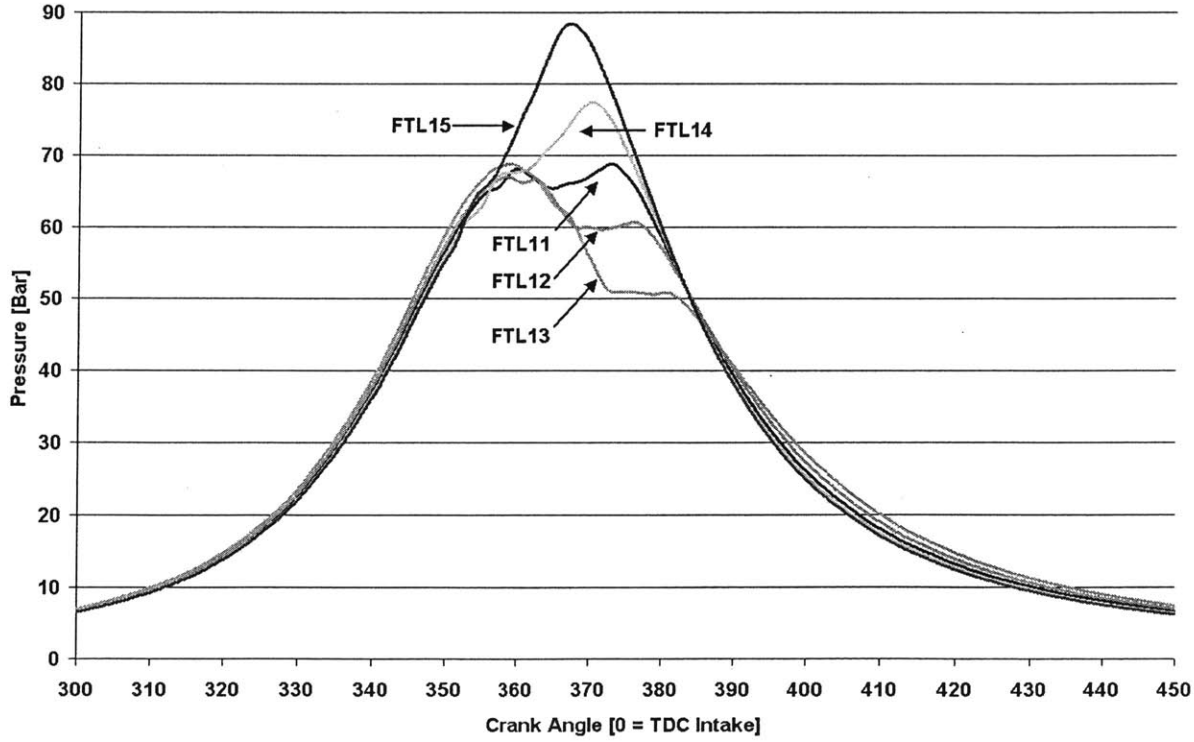

Appendix A.4 Cylinder pressure traces for increased-EGR, low-load conditions with Syntroleum S-2 FT diesel.

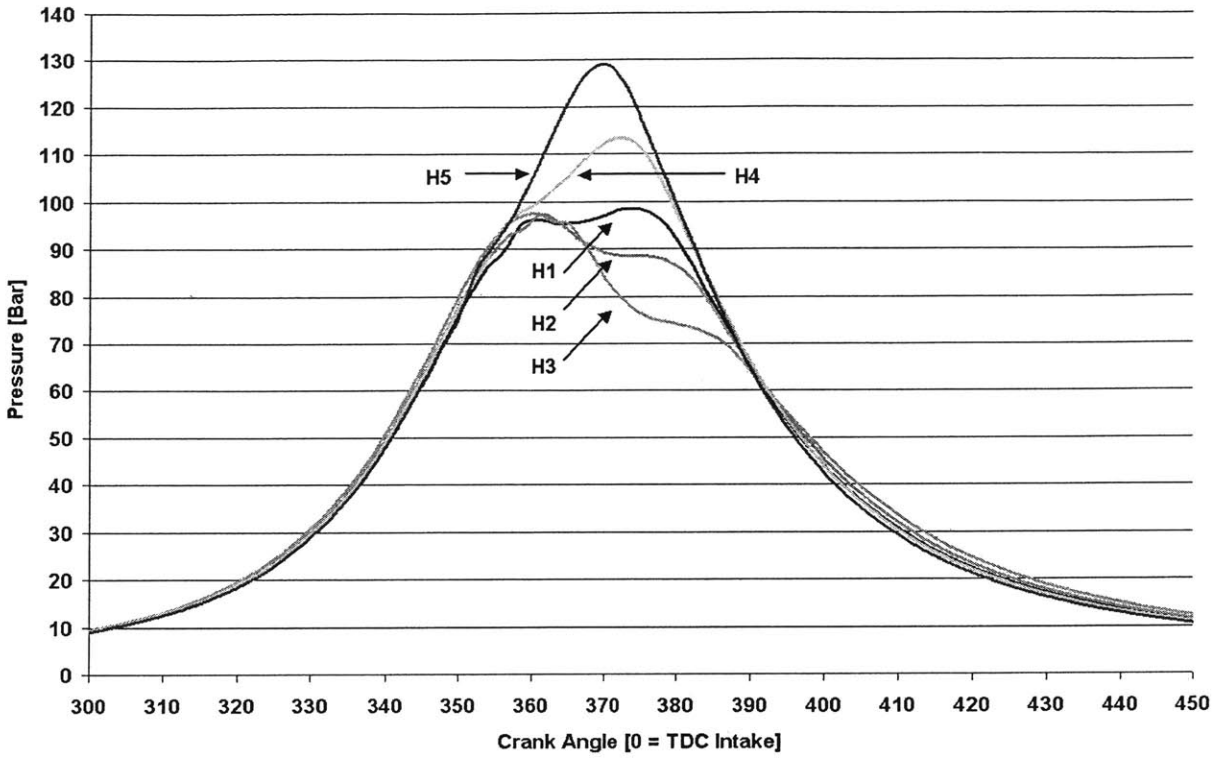

Appendix A.5 Cylinder pressure traces for stock-EGR, high-load conditions with No. 2 diesel.

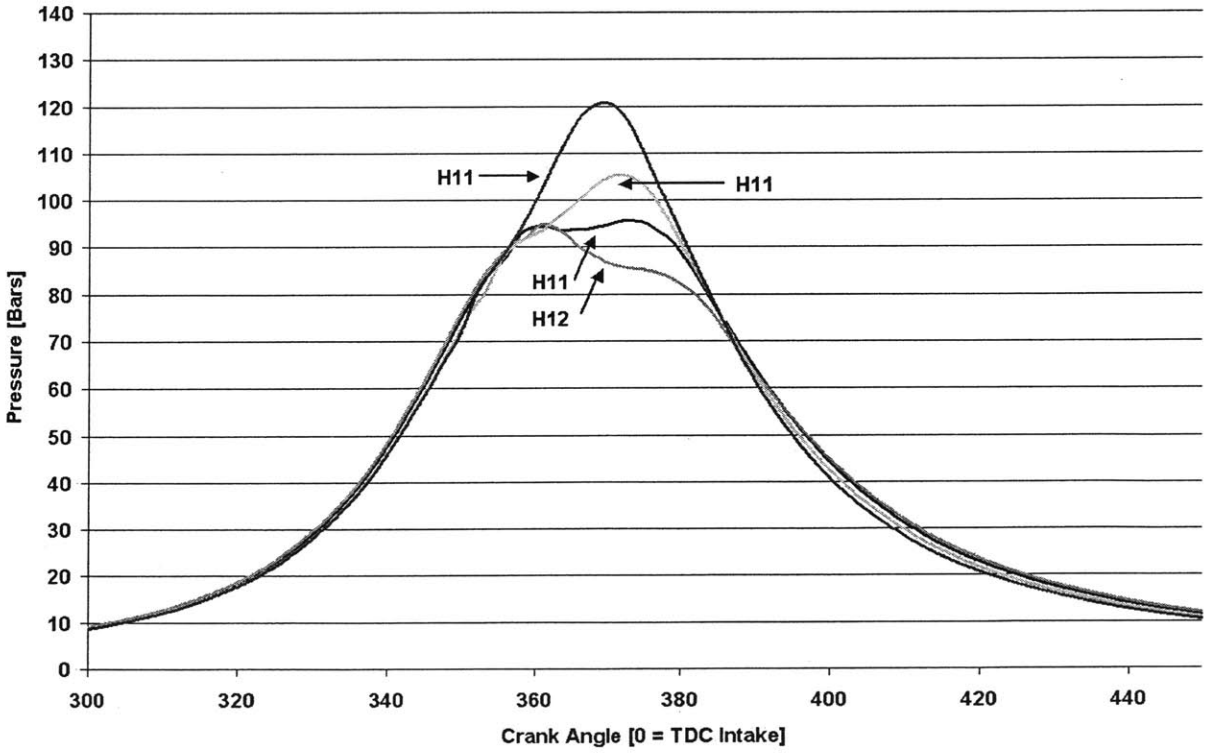

Appendix A.6 Cylinder pressure traces for increased-EGR, high-load conditions with No. 2 diesel.

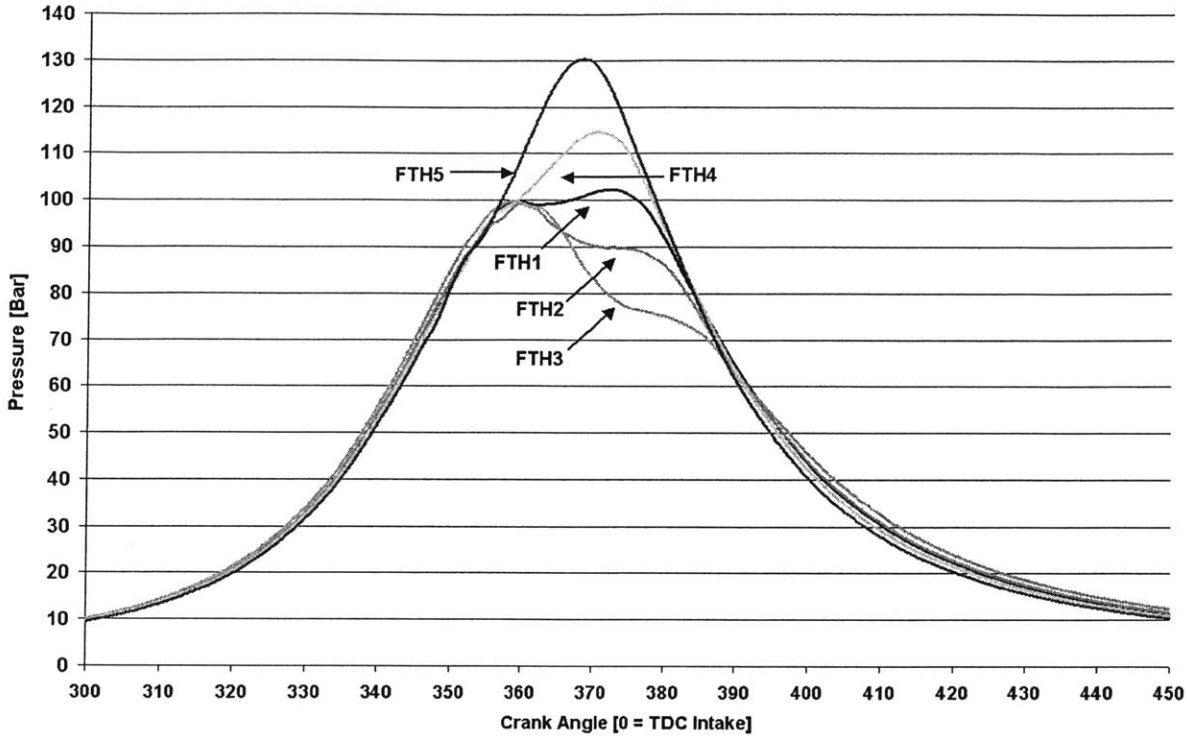

Appendix A.7 Cylinder pressure traces for increased-EGR, high-load conditions with Syntroleum S-2 FT diesel.

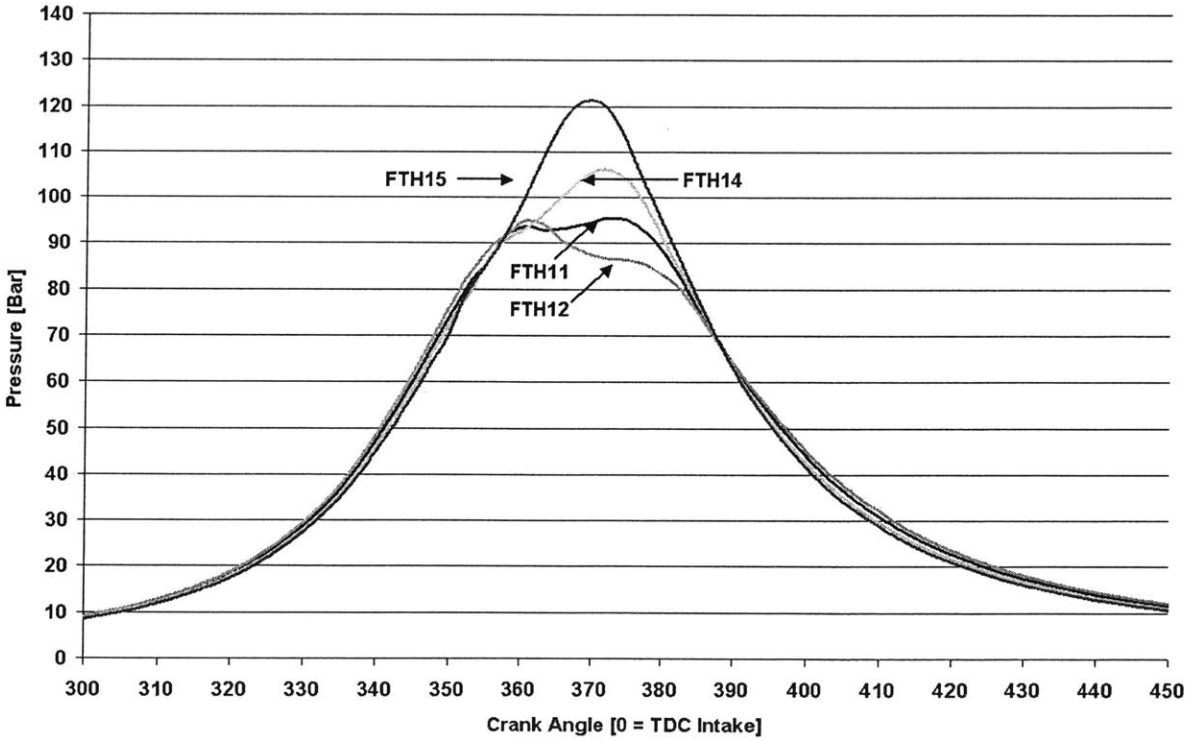

Appendix A.8 Cylinder pressure traces for increased-EGR, high-load conditions with Syntroleum S-2 FT diesel.

Appendix B

Heat Release Curves For All Operating Conditions

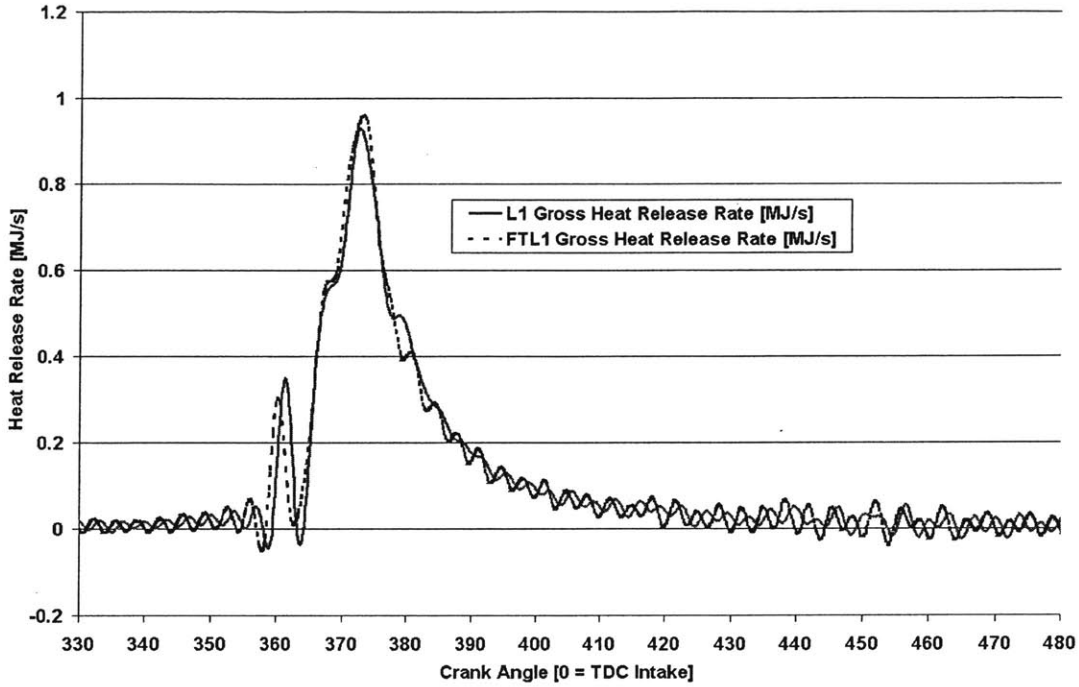

Appendix B.1 Heat release curve for modes L1 (No. 2 diesel) and FTL1 (FT diesel). ~480 kPa BMEP, stock EGR rate, SOI at 1° aTDC.

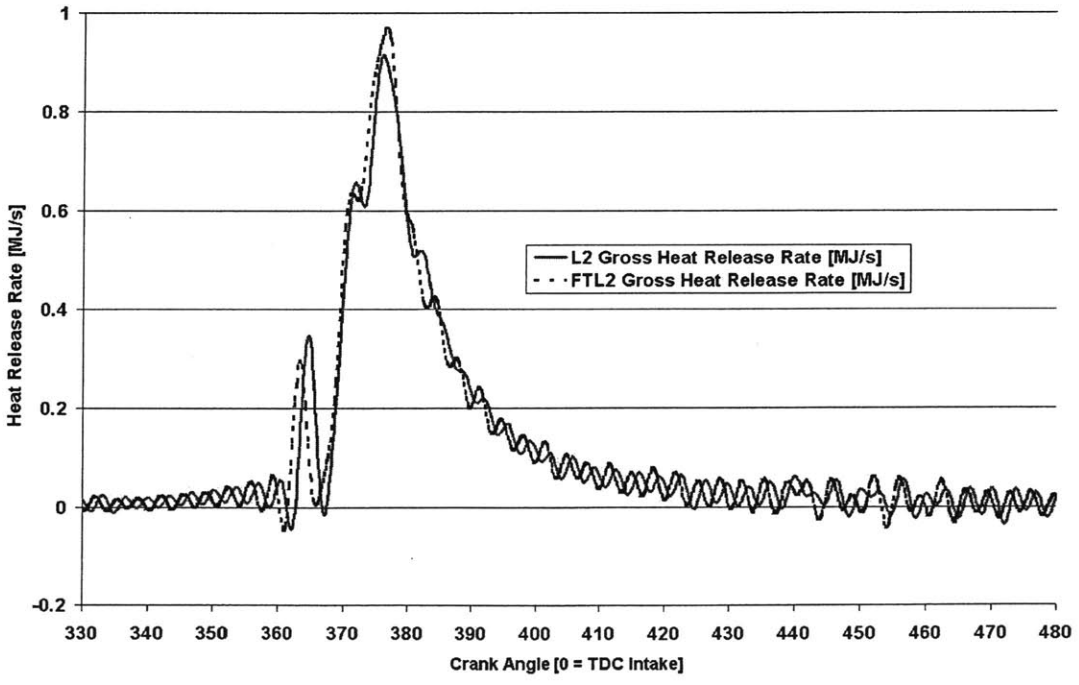

Appendix B.2 Heat release curve for modes L2 (No. 2 diesel) and FTL2 (FT diesel). ~480 kPa BMEP, stock EGR rate, SOI at 4° aTDC.

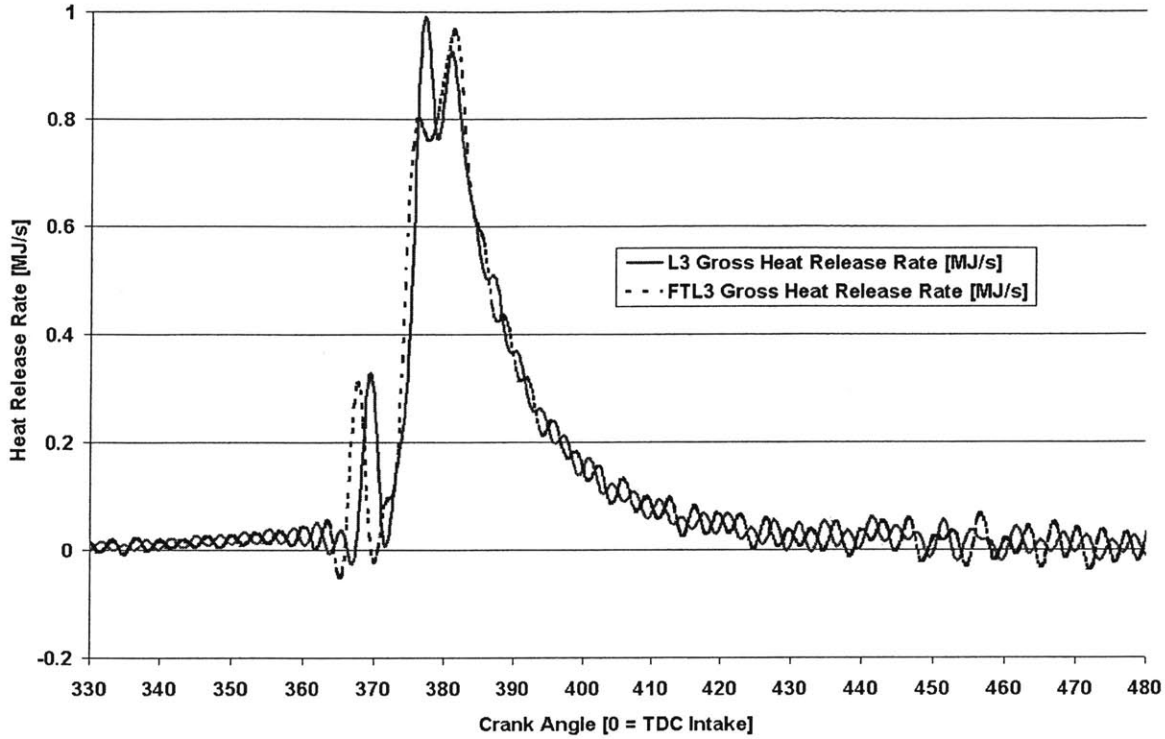

Appendix B.3 Heat release curve for modes L3 (No. 2 diesel) and FTL3 (FT diesel). ~480 kPa BMEP, stock EGR rate, SOI at 8° aTDC.

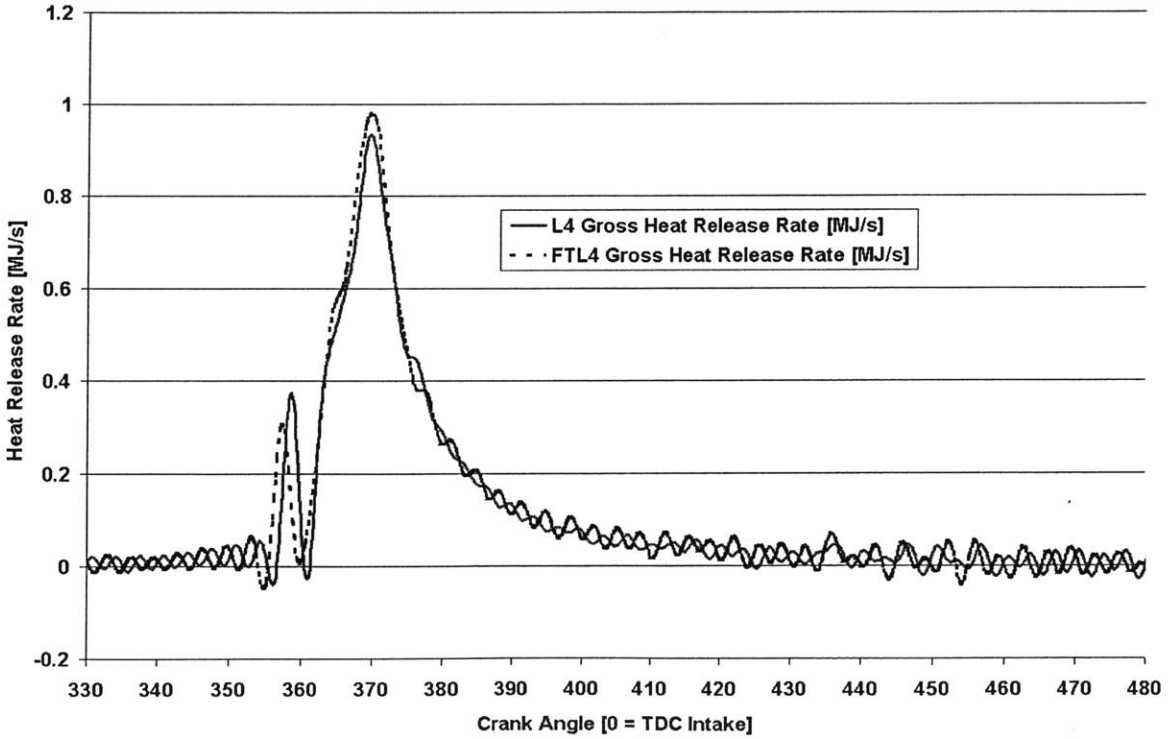

Appendix B.4 Heat release curve for modes L4 (No. 2 diesel) and FTL4 (FT diesel). ~480 kPa BMEP, stock EGR rate, SOI at 2° bTDC.

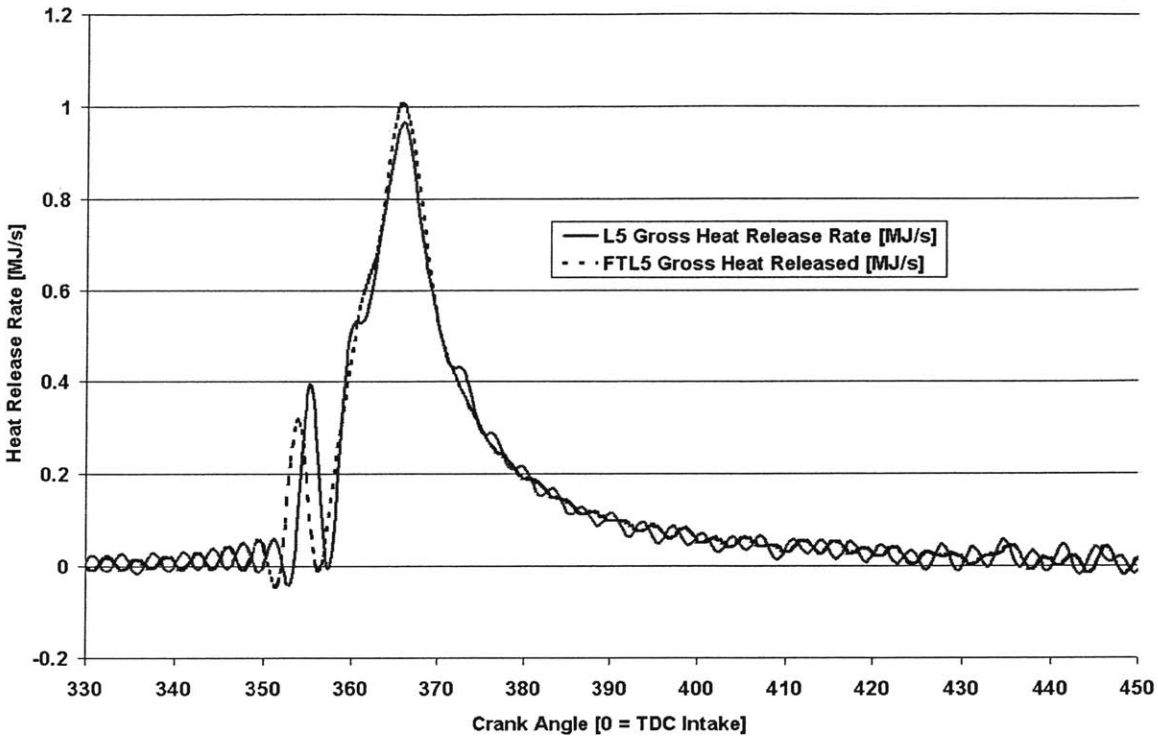

Appendix B.5 Heat release curve for modes L5 (No. 2 diesel) and FTL5 (FT diesel). ~480 kPa BMEP, stock EGR rate, SOI at 6° bTDC.

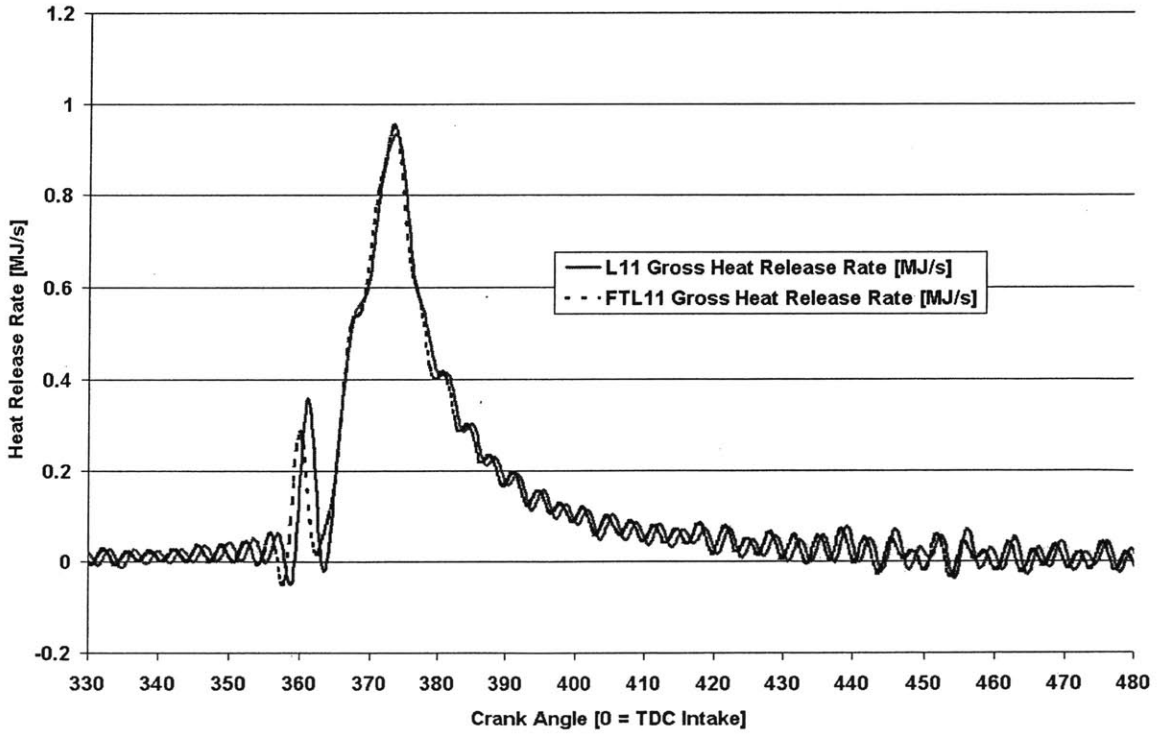

Appendix B.6 Heat release curve for modes L11 (No. 2 diesel) and FTL11 (FT diesel). ~480 kPa BMEP, increased EGR rate, SOI at 1° aTDC.

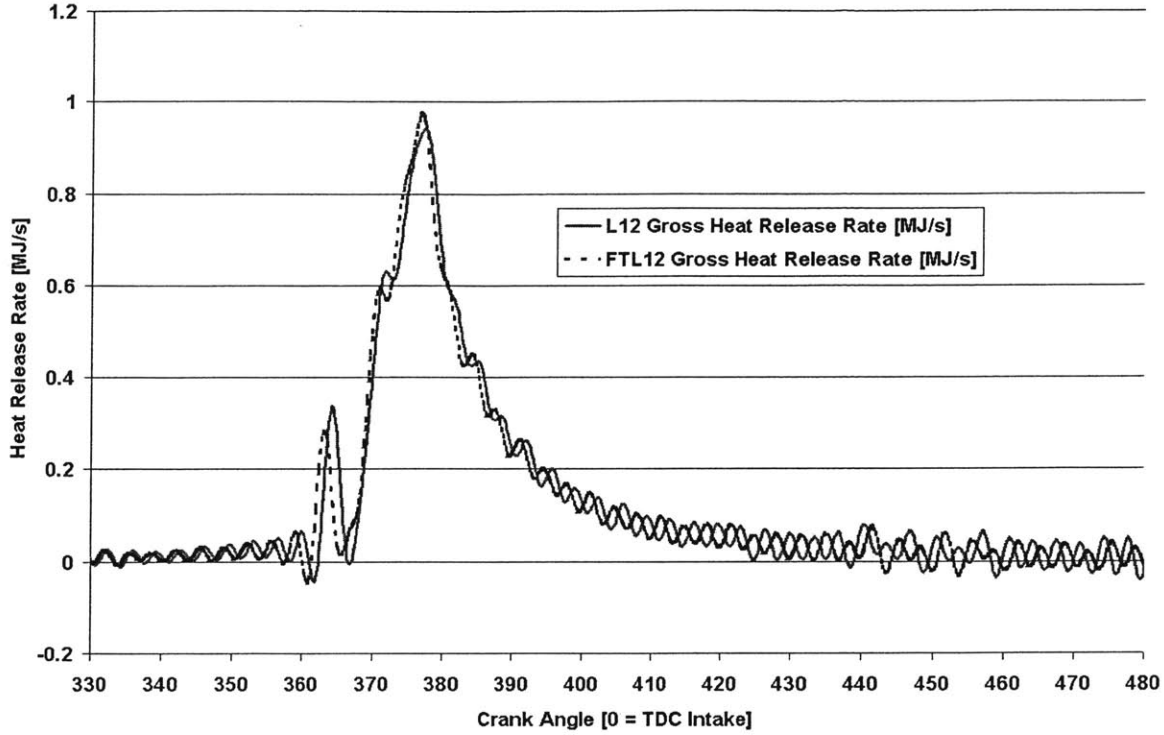

Appendix B.7 Heat release curve for modes L12 (No. 2 diesel) and FTL12 (FT diesel). ~480 kPa BMEP, increased EGR rate, SOI at 4° aTDC.

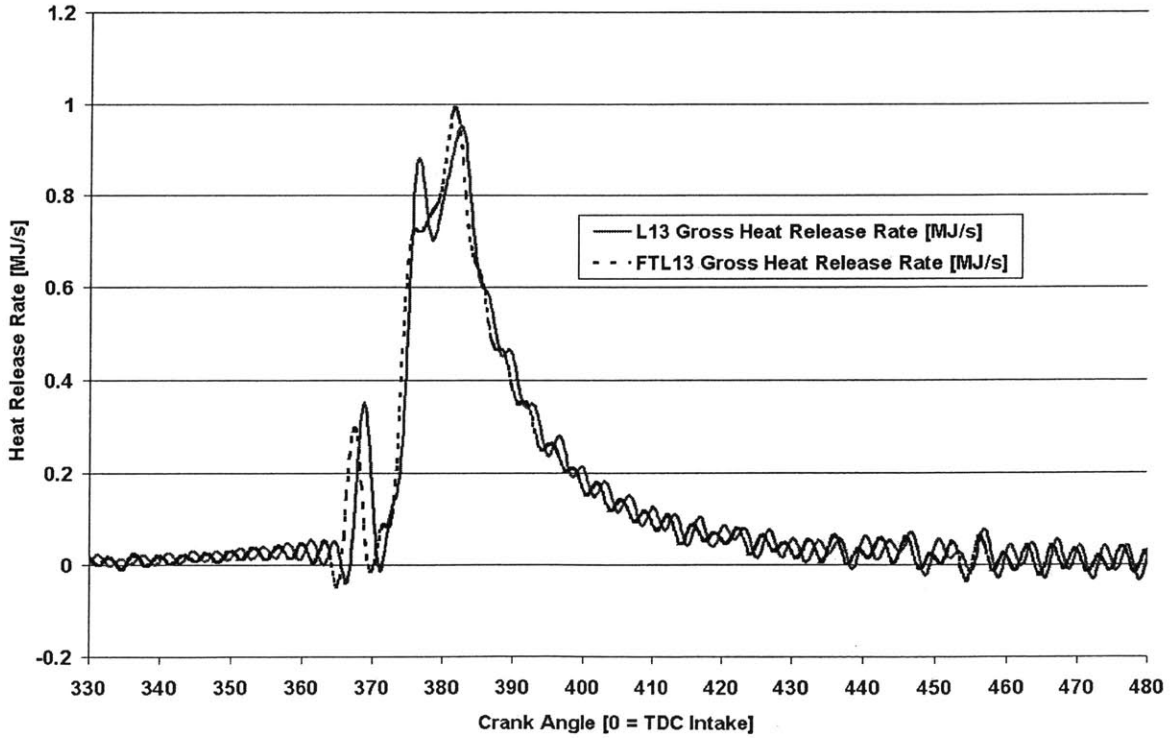

Appendix B.8 Heat release curve for modes L13 (No. 2 diesel) and FTL13 (FT diesel). ~480 kPa BMEP, increased EGR rate, SOI at 8° aTDC.

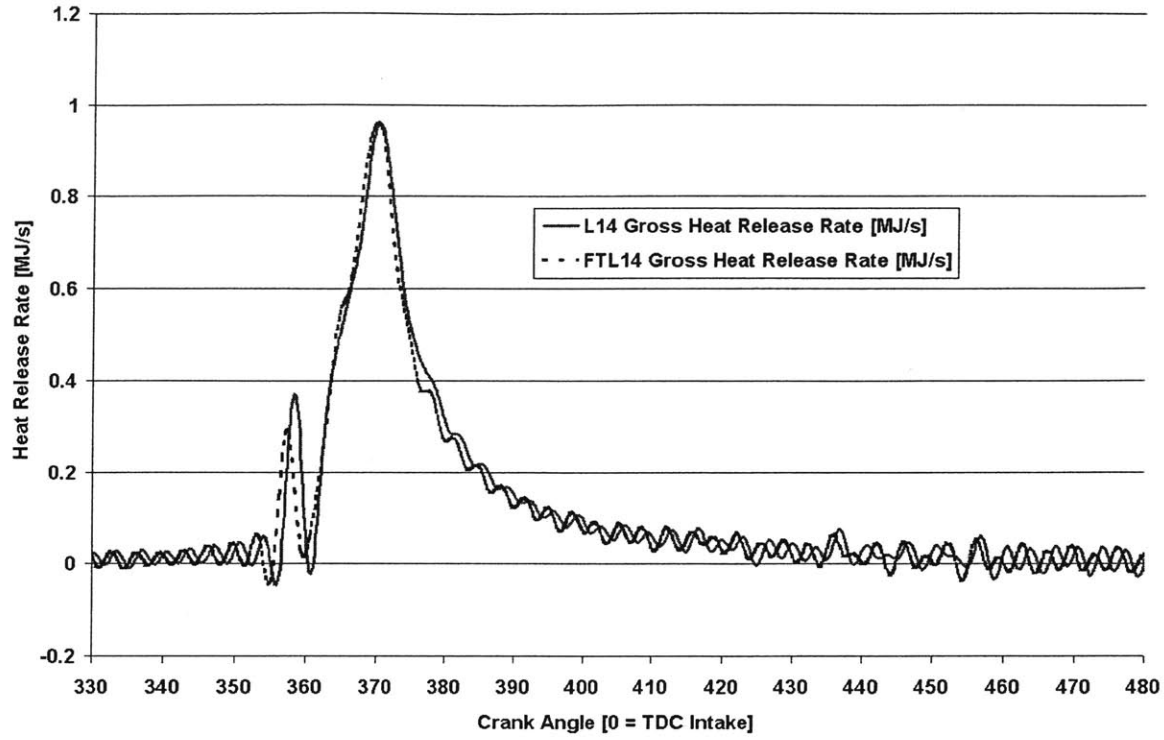

Appendix B.9 Heat release curve for modes L14 (No. 2 diesel) and FTL14 (FT diesel). ~480 kPa BMEP, increased EGR rate, SOI at 2° bTDC.

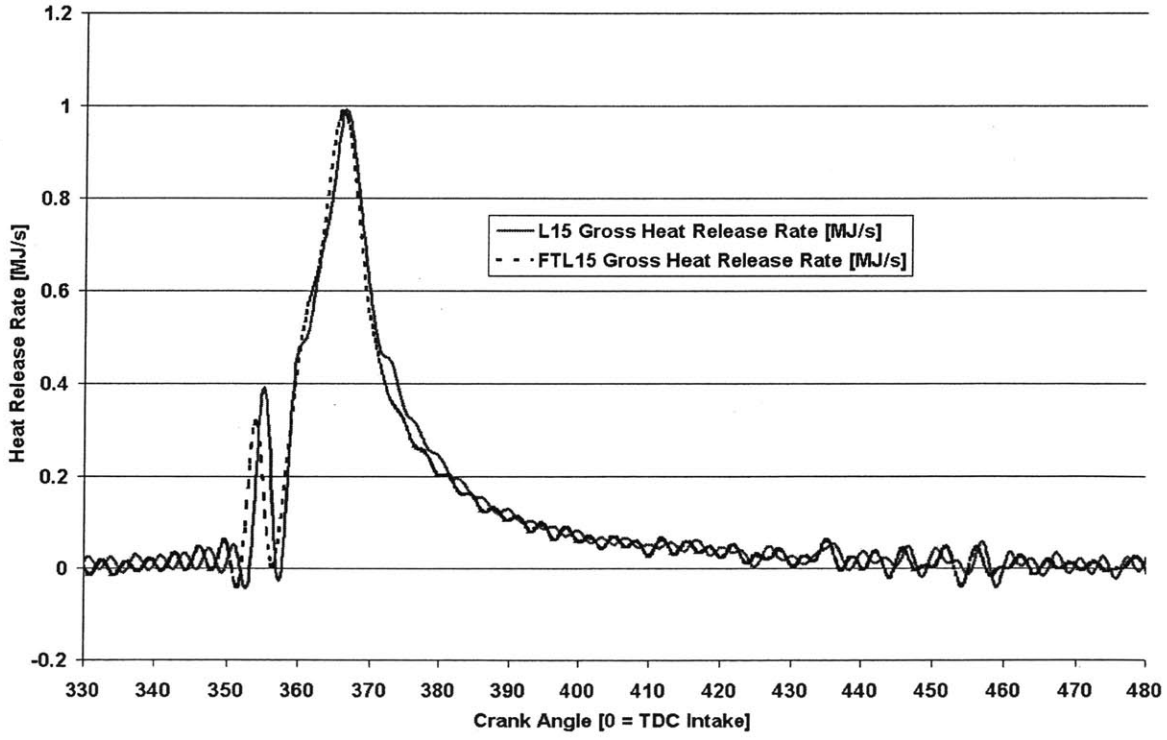

Appendix B.10 Heat release curve for modes L15 (No. 2 diesel) and FTL15 (FT diesel). ~480 kPa BMEP, stock EGR rate, SOI at 6° aTDC.

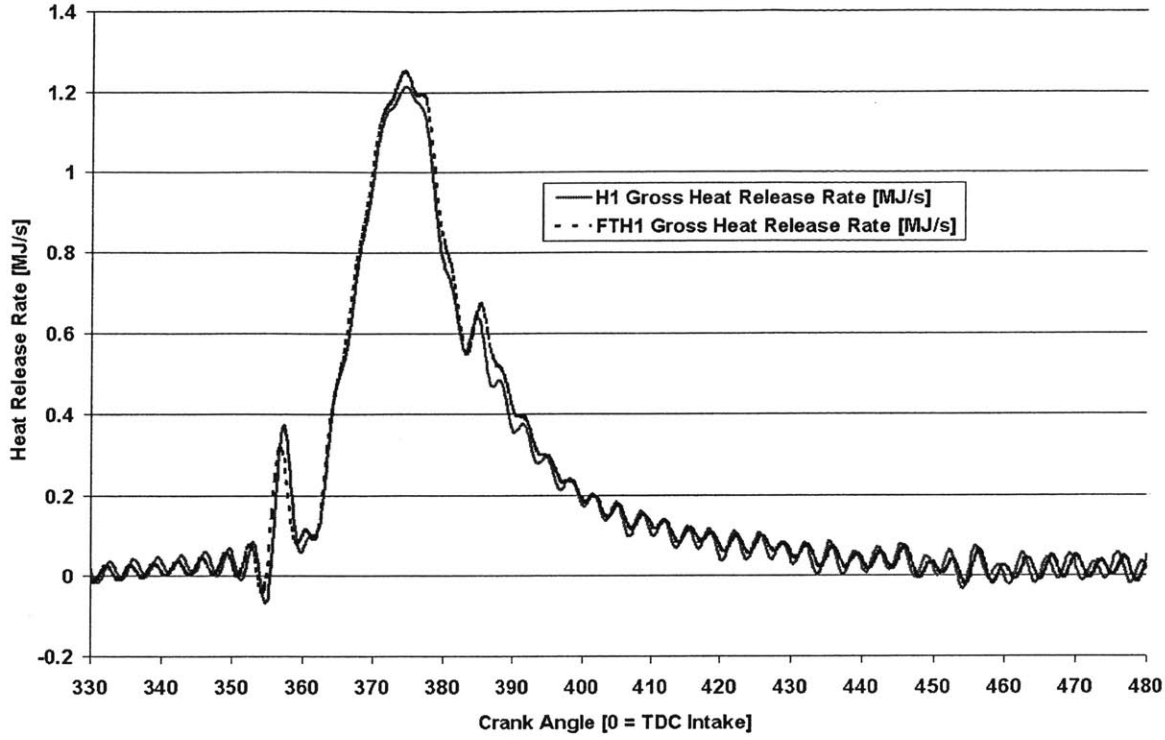

Appendix B.11 Heat release curve for modes H1 (No. 2 diesel) and FTH1 (FT diesel). ~1000 kPa BMEP, stock EGR rate, SOI at 0.5° bTDC.

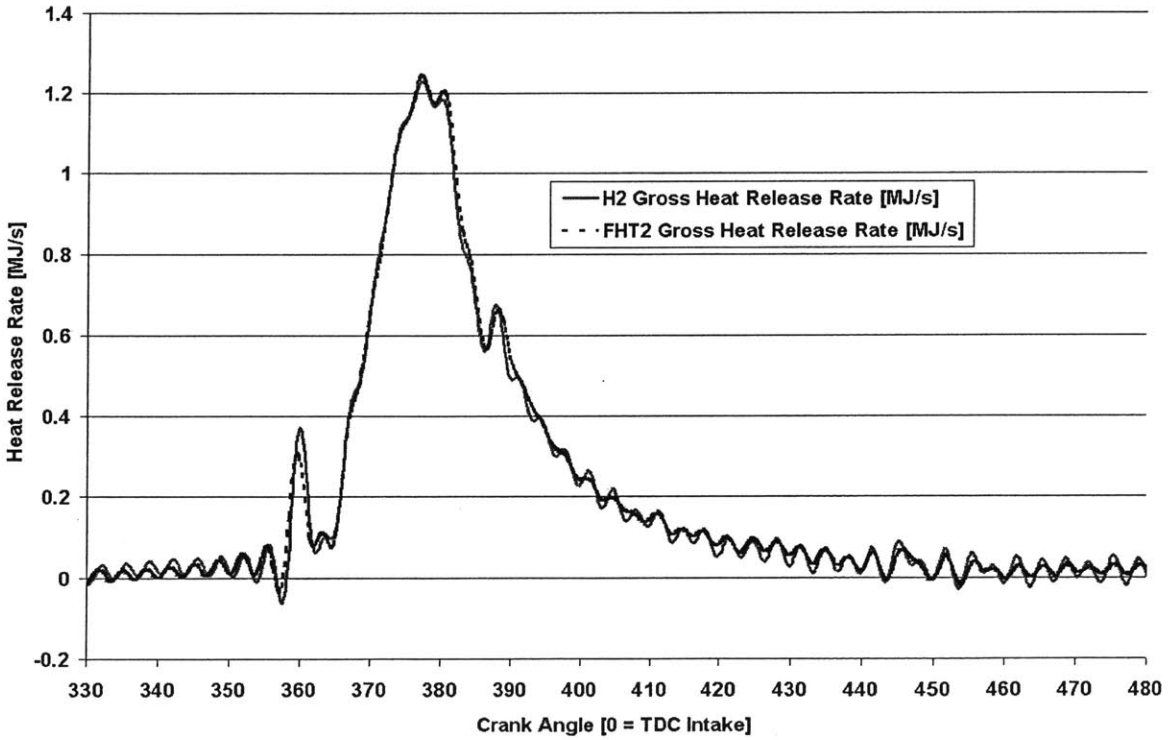

Appendix B.12 Heat release curve for modes H2 (No. 2 diesel) and FTH2 (FT diesel). ~1000 kPa BMEP, stock EGR rate, SOI at 2.5° aTDC.

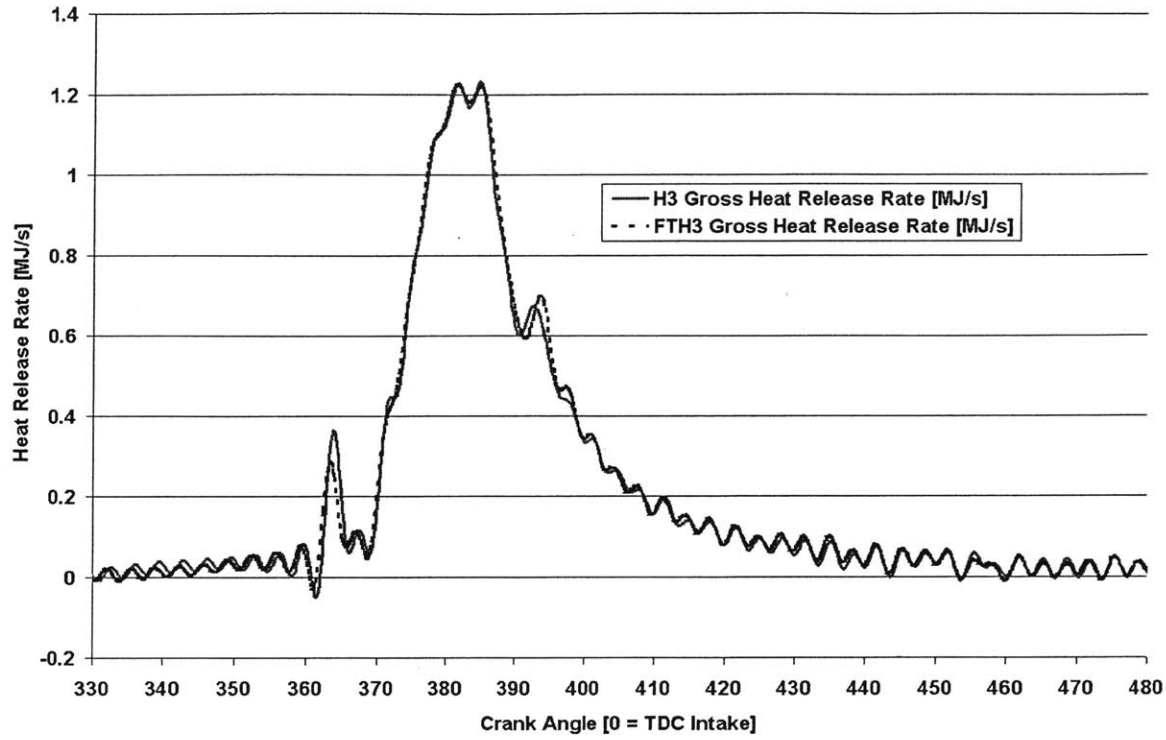

Appendix B.13 Heat release curve for modes H3 (No. 2 diesel) and FTH3 (FT diesel). ~1000 kPa BMEP, stock EGR rate, SOI at 6.5° bTDC.

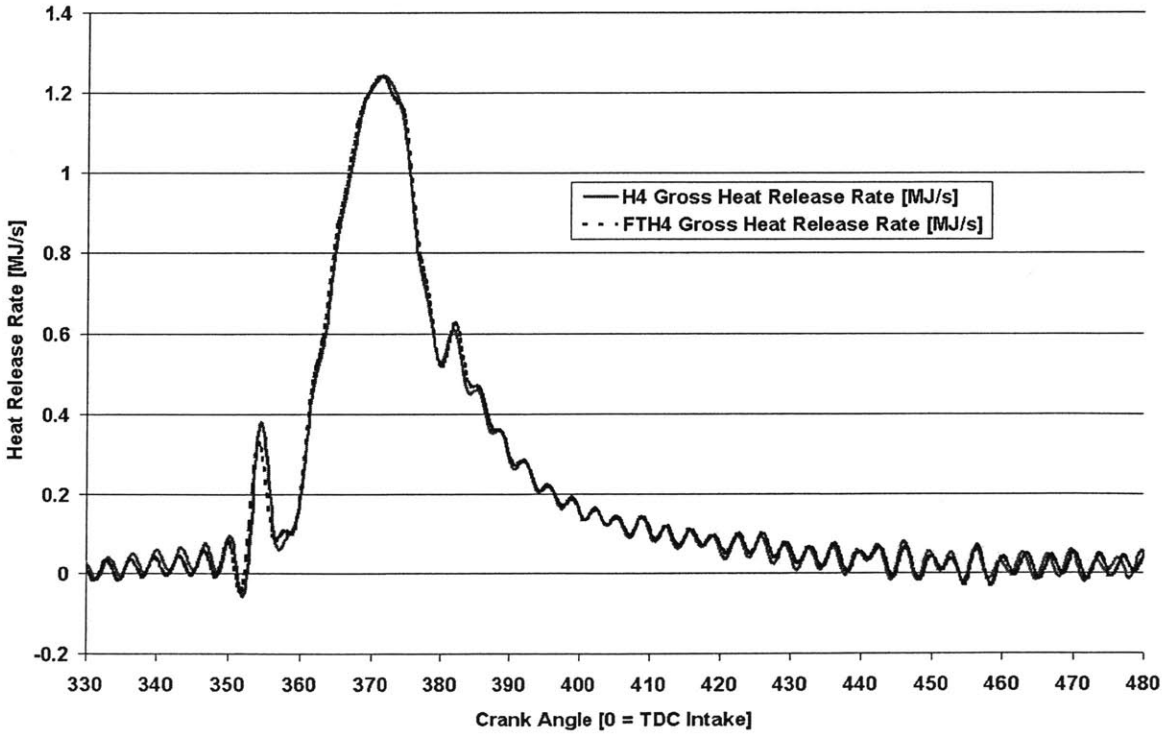

Appendix B.14 Heat release curve for modes H4 (No. 2 diesel) and FTH4 (FT diesel). ~1000 kPa BMEP, stock EGR rate, SOI at 3.5° bTDC.

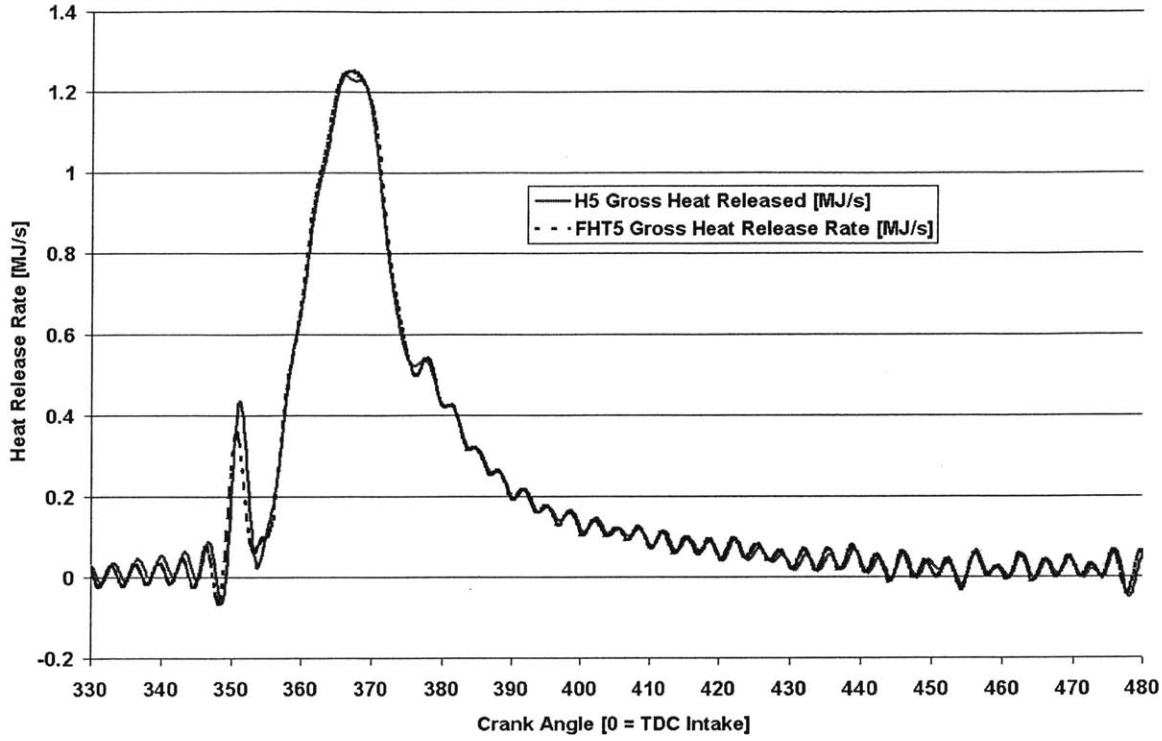

Appendix B.15 Heat release curve for modes H5 (No. 2 diesel) and FTH5 (FT diesel). ~1000 kPa BMEP, stock EGR rate, SOI at 7.5° bTDC.

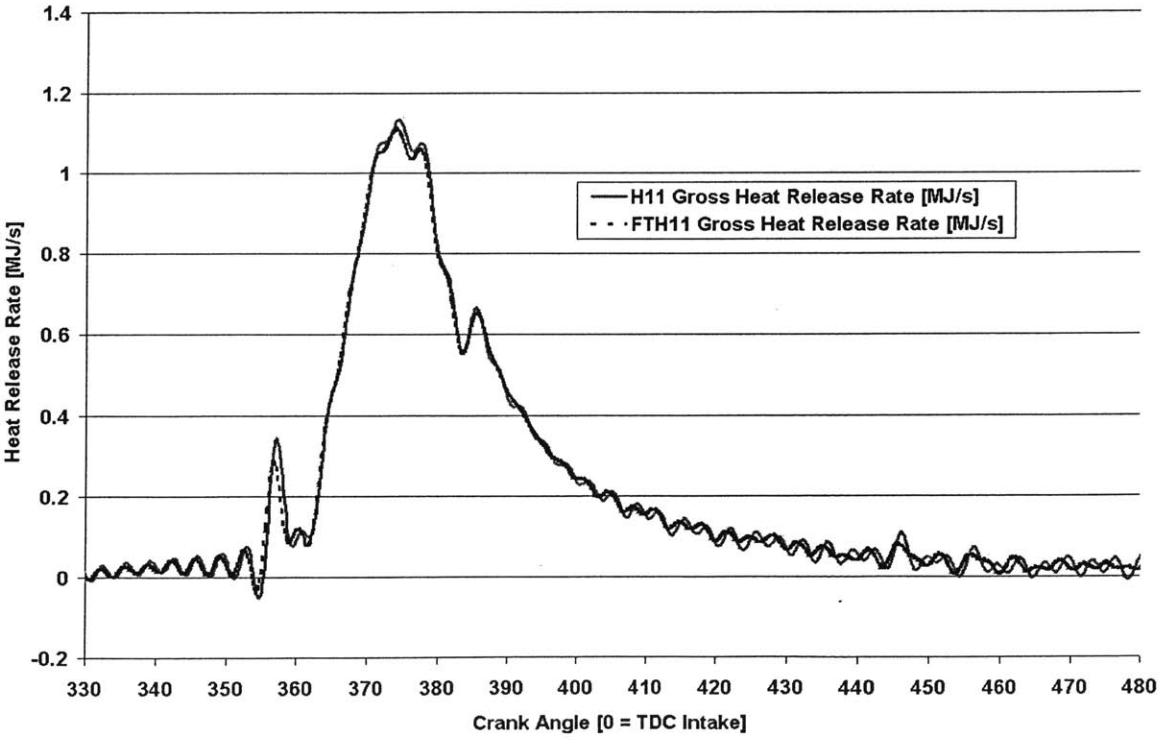

Appendix B.16 Heat release curve for modes H11 (No. 2 diesel) and FTH11 (FT diesel). ~1000 kPa BMEP, increased EGR rate, SOI at 0.5° bTDC.

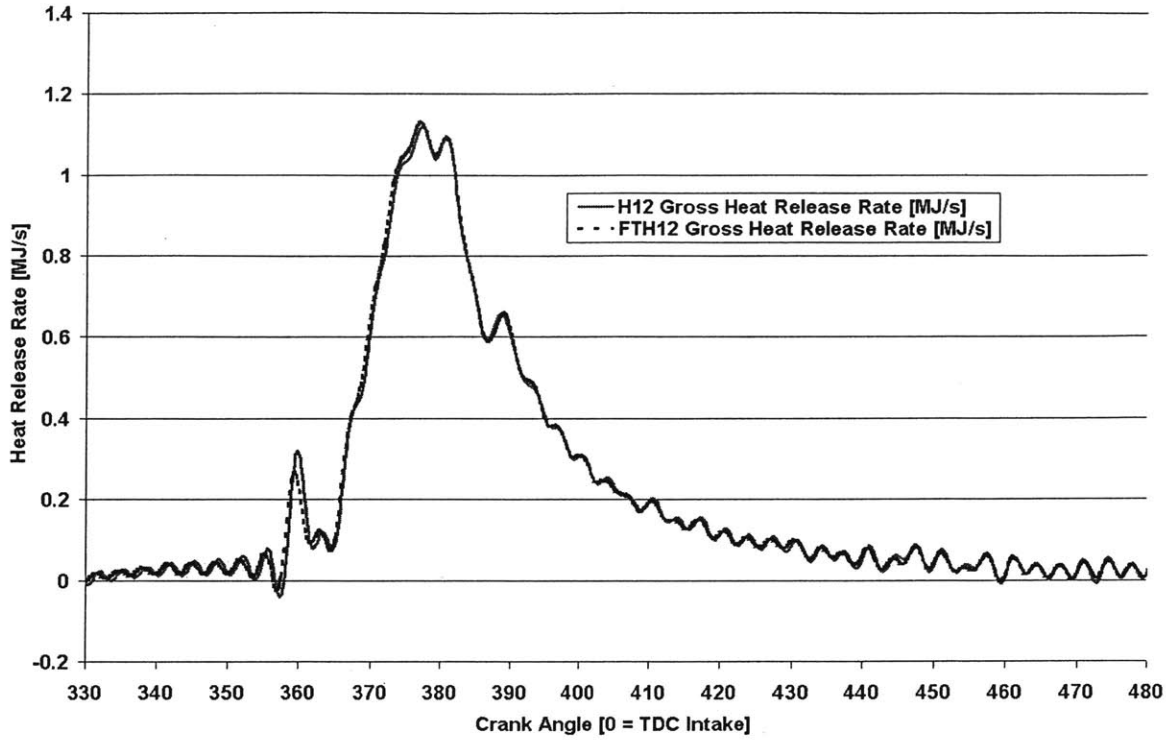

Appendix B.17 Heat release curve for modes H12 (No. 2 diesel) and FTH12 (FT diesel). ~1000 kPa BMEP, increased EGR rate, SOI at 2.5° bTDC.

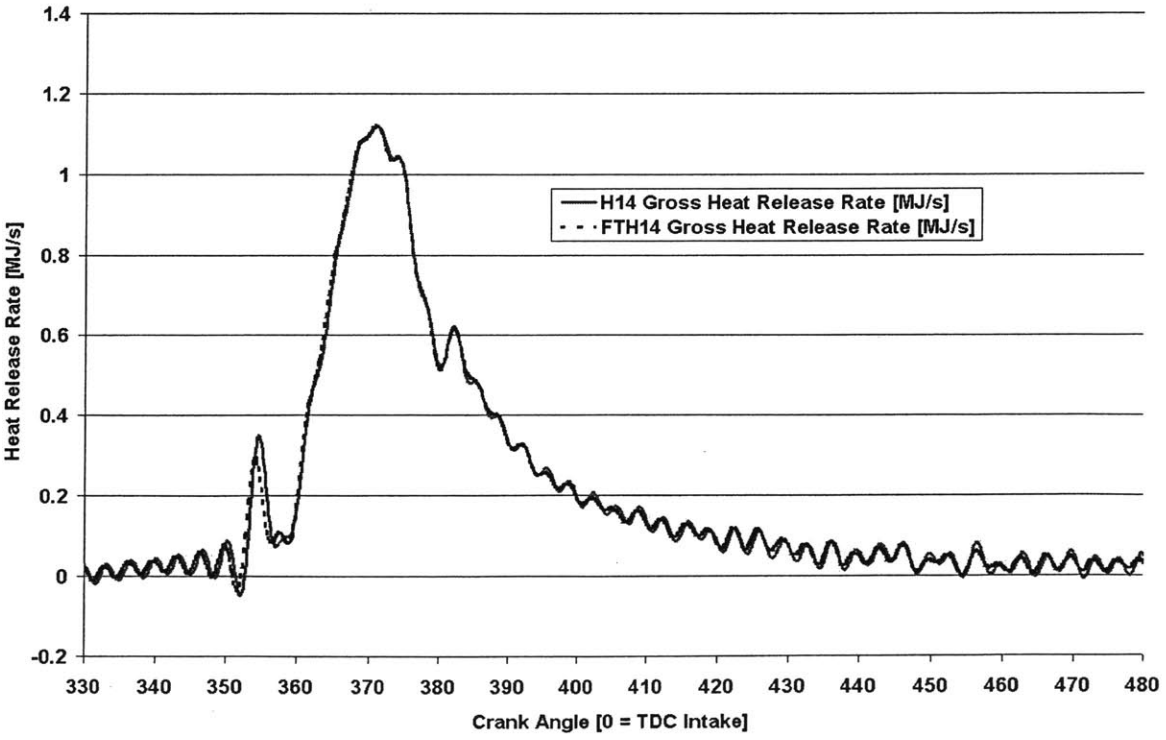

Appendix B.18 Heat release curve for modes H14 (No. 2 diesel) and FTH14 (FT diesel). ~1000 kPa BMEP, increased EGR rate, SOI at 3.5° bTDC.

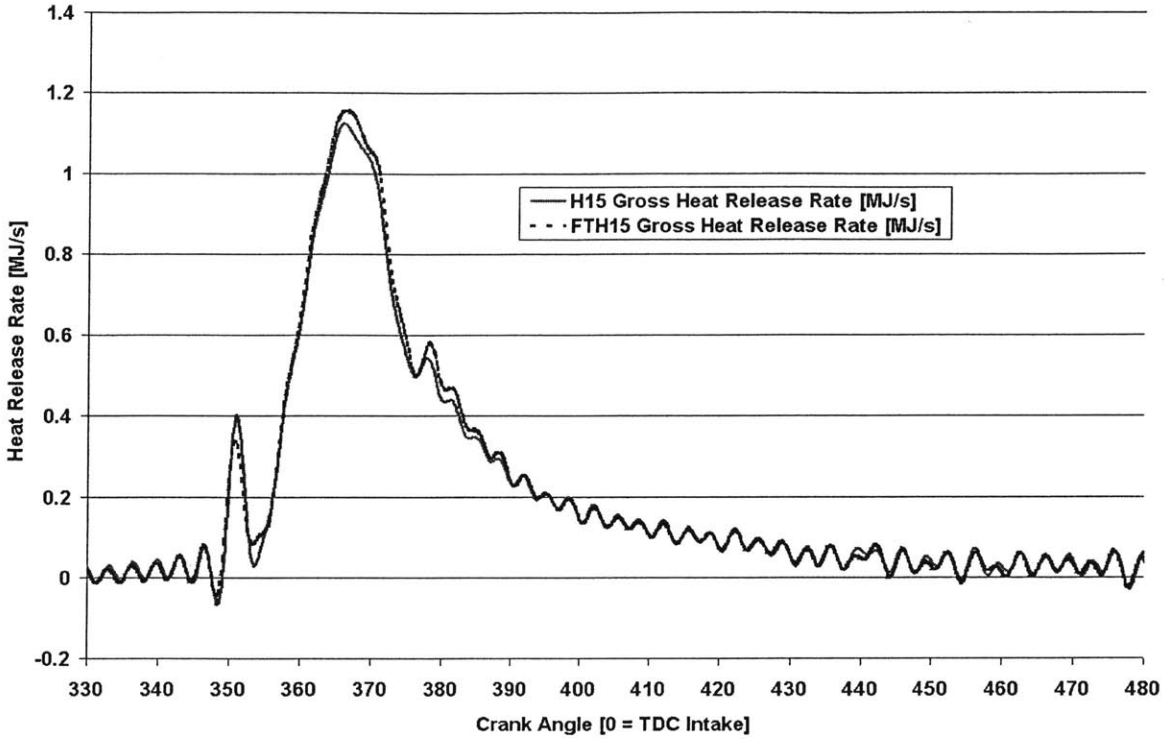

Appendix B.19 Heat release curve for modes H15 (No. 2 diesel) and FTH15 (FT diesel). ~1000 kPa BMEP, increased EGR rate, SOI at 7.5° bTDC.

Appendix C
Adiabatic Flame Temperature Calculations

Adiabatic Flame Temperature Correlation [48]:

Appendix C.1 $$T_{flame-adiabatic} = A\sigma^{\alpha}\exp[\beta(\sigma+\lambda)^2]\pi^x\theta^y\psi^z$$

Nomenclature:

$T_{flame-adiabatic}$ = Adiabatic Flame Temperature

A = Constant

x = Pressure Exponent = $a_1 + b_1\sigma + c_1\sigma^2$

y = Temperature Exponent = $a_2 + b_2\sigma + c_2\sigma^2$

z = Exponent For ψ = $a_3 + b_3\sigma + c_3\sigma^2$

α = Constant

β = Constant

θ = Dimensionless Temperature, $T_{unburned}/T_0$, Where T_0 = 300 K

λ = Constant

π = Dimensionless Pressure, P/P_0, Where P_0 = 101.325 kPa

ψ = H/C Atomic Ratio

ϕ = Fuel/Air Equivalence Ratio

Appendix C.2 Constants for flame temperature correlation.

Constants	$0.3 <= \phi <= 1.0$		$1.0 < \phi <= 1.6$	
	$0.92 <= \theta < 2.00$	$2.00 <= \theta <= 3.20$	$0.92 <= \theta < 2.00$	$2.00 <= \theta <= 3.20$
"A" Constant	2361.7644	2315.7520	916.8261	1246.1778
α	0.1157	-0.0493	0.2885	0.3819
β	-0.9489	-1.1141	0.1456	0.3479
λ	-1.0976	-1.1807	-3.2771	-2.0365
a_1	0.0143	0.0106	0.0311	0.0361
b_1	-0.0553	-0.0450	-0.0780	-0.0850
c_1	0.0526	0.0482	0.0497	0.0517
a_2	0.3955	0.5688	0.0254	0.0097
b_2	-0.4417	-0.5500	0.2602	0.5020
c_2	0.1410	-0.1319	-0.1318	-0.2471
a_3	0.0052	0.0108	0.0042	0.0170
b_3	-0.1289	-0.1291	-0.1781	-0.1894
c_3	0.0827	0.0848	0.0980	0.1037

Using the appropriate constants, the correlation predicts, starting from standard temperature and pressure, and $\phi = 1.0$:

$T_{adiabatic\text{-}No.2} = 2283.3$ K

$T_{adiabatic\text{-}FT} = 2268.1$ K

First-Law Calculation of Adiabatic Flame Temperature:

Equation 3.26 in [2] writes for an adiabatic constant-pressure combustion process:

Appendix C.3 $$[H_P(T) - H_P(T_0)] - [H_R(T) - H_R(T_0)] = Q_{LHV}$$

If the initial state of the reactants is taken at T_0, and knowing the following definition of Q_{LHV}:

Appendix C.4 $$Q_{LHV} = [H_P(T_0) - H_P(T_0)] - [H_R(T_0) - H_R(T_0)]$$

Then the first relation becomes:

Appendix C.5 $$H_P(T) = H_P(T_0)$$

Using values from Appendix C in [1], the following adiabatic flame temperatures results:

$T_{adiabatic\text{-}No.2} = 2479.5$ K

$T_{adiabatic\text{-}FT} = 2481.9$ K

Appendix D
Computer Programs Used to Record and Analyze Data

Appendix D.1 MATLAB program used to filter in-cylinder pressure data.

```
%Function Written To Load High-Speed Data Taken From National Instruments SCXI DAQ System.
%Also, Filters Pressure Data
%High-Speed Data File Format
%Column 1              Column 2                 Column 3
%Pressure           Crankshaft Sensor       Intake Manifold Pressure
% [Bar]                [Volts]                  [PSIG]
%If Data Format Does Not Match Above, Change The Following To Reflect The Proper Column
clear all;
Pcolumn = 1;
Crankcolumn = 2;
MAPcolumn = 3;
fprintf(1, '\n')
filename = input('Enter Name Of High Speed Data File = ','s');
fprintf(1, '\n')
data = load(filename);                                  %Load High-Speed Data File)
Pdata = data(:,Pcolumn);                                %Create Pressure Vector
Crankdata = data(:,Crankcolumn);                        %Create Crankshaft Voltage Vector
MAPdata = data(:,MAPcolumn);                            %Create MAP Vector
clear filename; figure; plot(Pdata); clear w; clear s; clear sl; clear S; clear Sl; format long e;
    Punfiltered = Pdata;                                                    %Store Unfiltered Pressure Data
    %P Is A 1-D Column Vector Containing Pressure.  This Routine Assumes The Data Is Spaced At 1 Second Increments.
    %The Increment Value Can Be Changed.
    N = length(Pdata);                                                      %Finds Number Of Data Points In Pressure File
    t = 0:N-1;                                                              %Time Vector
    % Generate The Ordinates (x-axis) Of  The Plots.  Units Of w (omega) Are 1/s.
    w = (0:N-1);                                                            %Angular Frequency Based On One Revolution
    RPM = input('Enter Engine RPM At This Point = ');
    f = w*RPM/2/60/(2*pi);                                                  %Cyclic Frequency Based On omega And RPM (w = 2*pi*f)
    %Convert From Time To Frequency Domain.
    transform=fft(Pdata);                                                   %Finite Fourier Transform On Data
    unfiltered  = transform;                                                %Store Unfiltered, Transformed Data
    %Frequencies Above/Below The Below Variables high/low Will Be Eliminated.
    high = 47500;                                                           %Upper Limit Of Frequencies
    low = 0;                                                                %Lower Limit Of Frequencies
    %Eliminate Frequencies Above High And Below Low.
    for i=2:(N+1)/2
        if f(i) <= low
            transform(i,:) = 0;
            transform(N+2-i,:) = 0;
        end
        if f(i) >= high
            transform(i,:) = 0;
            transform(N+2-i,:) = 0;
        end
    end
    %Convert From Frequency Domain To Time Domain
    time=ifft(transform);
    %Combine Magnitude And Phase To 'Recreate' P
    Pdata = abs(time).*cos(angle(time)); hold; plot(Pdata,'r');
%data = [Pdata Crankdata MAPdata];
save filtered.txt Pdata -ASCII -TABS
clear data
```

Appendix D.2 Single-zone heat release program. Only the applicable First Law portions of the code are included. Data loading, derivative, output, and other subroutines are left out.

```
C**********************************************************************
C*          Simple Heat Release Analysis Based on First Law          *
C*                          Written By: Dr. Victor Wong
C*                          Modified By: Jeremy T. Llaniguez
C**********************************************************************
logical pcal
dimension psd(3600),hrg(3600),qiallw(3600),volca(3600),
&tbulk(3600),pdsyn(3600),cumhr(3600),hrn(3600),
&dhrg_dt(3600),dhrn_dt(3600),energy(3600),RHS(3600)
common bore,stroke,crl,cr,viarea,vearea,cdin,cdex,rpm,tin,pin,
&     pcrmax,SOImain,charge,fuel,Qlhv,phi
common /filter/ w1,w2,w3,w4,mfl,ktype,hfir
common /mnfold/ pim,tim,pem,tem
common /gas/ rgas, cp, cv, gamma
common /valtim/ caivc,caevo,caeend,caend, castep, cpstep
common /valflo/nin,nex
common /eff/effc,efft,effm
common /burn/casoc,burn90,fpower,qlower,fpc
common /heat/temp,alinr,pspeed,ahdpst,re,prandl,cmuprl,twal, hcoef
common /hwalls/hcst(3),twalli(3),twallp(3),twallh(3)
common /change/cm(3),par(3),parout,ch(3),pah(3),pahout
common /conduc/condin(3),din(3),cndout(3),dout(3),hext(3),text(3)
common /ddd1/caivo,caevc,icycnum,timc,trqini
common /prdata/ca(3600),p(3600),dnl(3600),cca(3600),ps(3600),
&          pfil(3600)
common /ativc/pinit,vinit,tinit,trapm,pi,avpspd,hbore
common /burnsp/cainj,caignd,cabdur,abeta,bbeta,cbeta,c1pmix,
& c2pmix,c1diff,c2diff,c3diff,c4diff,afstoi,betasp,pcal
real Pmax, CApmax(3600)
external pderiv
C
C Read general inputs
C
call readin
C
C Read pressure data
C
call readp
C
C Prepare initial variables used in the calculation
C
      avpspd=stroke*rpm/30.                    !Mean Piston Speed [m/s]
      rgas=8314.3/28.962                       !Universal Gas Constant   [J/kg-K]
      cv=rgas/(gamma-1.)                       !Constant Volume Specific Heat
      cp=gamma*cv                              !Constant Pressure Specific Heat
      pi=3.14159265                            !pi
      ahdpst=pi*bore**2/4.                     !Piston Head Area [m^2]
      alner=pi*bore*stroke*cr/(cr-1.)          !Cylinder Liner Area [m^2]
      hbore=bore/2.                            !Half Of Bore, Radius [m]
      vdispl=pi/4.*bore*bore*stroke            !Displaced Volume [m^3]
      vc=vdispl/(cr-1.)                        !Clearance Volume [m^3]
      fpc=fpower/qlower*120./rpm/float(icycnum)        !Fuel Per Cycle Per Cylinder
```

```
C
C       write (6,*) 'Fuel Energy =',fpower,'kW','Fuel Per Cylinder=',fpc
C
        tstep=castep/rpm/6.                 !Time Steps For Integration
C
C  Add Reference Pressure To Raw Data, Assuming Average p Before IVC = IMP
C
if ((caivc.lt.90.).or.(caivc.gt.270.)) then
write(6,*)'Check intake valve closing timing convention(90-270)'
stop
endif
nivc=ifix(caivc*5.+0.0001)              !IVC Reference
nevo=ifix(caevo*5.+0.0001)              !EVO Reference
sumip=0.                                !Initialize Intake Pressure Variable
C       do 20 i=1,nivc                  !Loop To Average Pressure
        do 20 i = 850,950
20      sumip=sumip+p(i)                !Cumulative Presesure
C       pinavg=sumip/float(nivc)        !Average Pressure
        pinavg=sumip/100
C
C  Calculate Scaled Pressure For Each Crank Angle
C  All Units Should Be In SI, Thus Pressure Should Be In Pascal, Except Jeremy's Data
C
    do 30 i=1,3600                      !Loop To Convert Pressure
 30     ps(i)=(p(i)-pinavg)*1.0e5+pim   !Conversion Calculation
C
C  Get pressure time derivatives
C
    call deriv5p(ps,tstep,3600,psd)
C
C  Set Initial Cylinder Conditions At IVC
C
        call engvol(caivc,vinit,vdot,spdum,alndum)
        pinit=ps(nivc)                  !Pressure At IVC
        pinitkPa = pinit/1000           !Pressure At IVC in kPa
C       tinit=tim                       !Temperature At IVC
C       trapm=pinit*vinit/rgas/tinit    !Trapped Cylinder Mass
        trapm=charge/rpm*60*2/icycnum   !Trapped Mass From Measured Values
        tinit=pinit*vinit/trapm/rgas    !Temperature At IVC with H.T.
        rhoint=trapm/vinit              !Initial Gas Density
        pvgini=pinit*vinit**gamma       !Initial PV^gamma
        write(7,*)
        write(7,950) pinitkPa
        write(7,951) tinit
        write(7,952) vinit
        write(7,953) trapm
        write(7,954) pvgini
950     format('Pressure At IVC [kPa] = ',f12.3)
951     format('Temperature At IVC [K] = ',f6.1)
952     format('Volume At IVC [m^3] = ',e12.3)
953     format('Trapped Mass At IVC [kg] = ',f12.6)
954     format('PV^gamma At IVC = ',f6.3)
C
C  Start cycle calculation loop
C
smwork=0.                               !Initialize Work Variable
```

```
 smhrel=0.                          !Initialize Heat Release Variable
 smhxfer=0.                         !Initialize Heat Transfer Variable
 energy=0.                          !Initialize First Law Energy As Zero
 RHS=0.                             !RHS of First Law (H.T.,Work,Chemical Energy)
 C
 do 40 i=nivc, nevo                 !Heat Release Done During "Closed" System
 theta=ca(i)                        !Index For Current Crank Angle In Loop
 C
 C  Call engvol To Get Various Engine Geometry Information At Each CA
 C
 call engvol(theta,vol,vdot,pspeed,alinr)
 C
 rho=trapm/vol                              !Gas Density At Any Crank Angle
 temp= tinit*ps(i)/pinit*vol/vinit          !Cylinder Average Temperature
 tbulk(i)=temp                              !Bulk Temperature
 C
 C  Calculate Some Heat Transfer Parameters
 C  Heat Transfer Theory Based On Nusselt-Reynolds Correlation:
 C                          Nu = Constant * Re^d * Pr^e
 C  Constant Stored As hcst Array, With All 3 Values = 0.05 (See Input)
 C  Prandtl Number Dependence Removed Below Sine Pr ~ Unity
 C  For More Information, See Ph.D Thesis By Assanis, 1980
 C  Assanis Uses Characteristic Velocity Equation Incorporating Turbulence
 C  Models.  More Simplified Approach Applied Here.
 C
 scale=alinr/pi/bore                        !Characteristic Length Scale
 if (scale.ge.hbore) scale=hbore            !Length Scale Restriction
 vis=3.3e-4*temp**.7                        !NASA Equilibrium Program
 charv=max(abs(pspeed),avpspd/2.)           !Simple Characterisitc Vel.
 re=charv*scale*rho/vis                     !Definition Of Re
 congas=vis*cp/prandl                       !Conductivity Of Gas
 cmuprl=congas/scale                        !Inverse Of RHS Of Nu
 rnuslt=hcst(2)*re**.7                      !Nusselt Number, As Above
 hcoef=cmuprl*rnuslt                        !Solving For h
 C
 C  Calculate Heat Transfer From Various Parts Of Cylinder
 C
 qipist=ahdpst*hcoef*(temp-twallp(2))       !Piston Heat Transfer
 qihead=ahdpst*hcoef*(temp-twallh(2))       !Heat Heat Transfer
 qilinr=alinr*hcoef*(temp-twalli(2))        !Liner Heat Transfer
 qiallw(i)=qipist+qihead+qilinr             !All Wall Heat Transfer
 C
 C  Gamma Correlations
 CSOIindex = ((360-SOImain)*5)              !SOI Index To Heat Release
 Cif (i.lt.SOIindex) then
 Cgamma = 1.415 - (9.595E-05*tbulk(i))
 Cendif
 Cif (i.gt.SOIindex) then
 Cgamma = 1.55
 Cendif
 C       if (i.gt.(nivc+50)) then
 C       gamma = (1.334 - (0.2*phi)) - ((9.43-12.42*phi)*1.0e-5)*tbulk(i)
 C       endif
 Ccv=rgas/(gamma-1.)
 C
 C
```

```
C  Calculate Gross Heat Release
C
hrg(i) = qiallw(i) + ((gamma/(gamma-1.))*ps(i)*vdot) + ((1/(gamma-1))*vol*psd(i))
C
C  Calculate Net Heat Release
C
hrn(i) = hrg(i) - qiallw(i)
C
C  Further Calculations For Various Heat Release Characteristics
C
volca(i)=vol
C
C  pdsyn(i) Is P*dV Term In Burn Rate Analysis Mode
C
pdsyn(i)=ps(i)*vdot                    !P*dV Term
C
smwork=smwork+pdsyn(i)*tstep           !Work
smhrel=smhrel+hrg(i)*tstep             !Heat Release Up To CA
cumhr(i)=smhrel                        !Cumulative Heat Release
smhxfer=smhxfer+qiallw(i)*tstep        !Cumulative Heat Transfer
energy(i)=trapm*cv*tbulk(i)
RHS(i) = (hrg(i)-qiallw(i)-pdsyn(i))*tstep
40      continue
C
C  Calculate Derivatives Of Heat Release Rates
C
call deriv5p(hrg,tstep,3600,dhrg_dt)
call deriv5p(hrn,tstep,3600,dhrn_dt)
C
C  Find where heat release crosses 10%, 50%, and 90%
C
c05par=0.
c10par=0.
c50par=0.
c90par=0.
C
do 45 i=nivc,nevo
hrfrac=cumhr(i)/smhrel
C
C  Find 5% Cross-Over Point
C
if (hrfrac.gt.0.05) then
if (c05par.lt.0.5) ca05=ca(i)
c05par=1.
endif
C
C  Find 10% Cross-Over Point
C
if (hrfrac.gt.0.1) then
if (c10par.lt.0.5) ca10=ca(i)
c10par=1.
endif
C
C  Find 50% Cross-Over Point
C
if (hrfrac.gt.0.5) then
```

```
if (c50par.lt.0.5) ca50=ca(i)
c50par=1.
endif
C
C  Find 90% Cross-Over Point
C
if (hrfrac.gt.0.9) then
if (c90par.lt.0.5) ca90=ca(i)
c90par=1.
endif
45   continue

C
C  Get Pumping Work Integrated Data
C
prewrk=0.
pstwrk=0.
do 60 i=1,nivc
theta=ca(i)
call engvol(theta,vol,vdot,pspeed,alinr)
60        prewrk=prewrk+ps(i)*vdot*tstep
do 70 i=nevo+1,3600
theta=ca(i)
call engvol(theta,vol,vdot,pspeed,alinr)
70   pstwrk=pstwrk+ps(i)*vdot*tstep
C
C  Expressed in kW basis at that rpm (ihp):
C
prewkw=prewrk*rpm/120./1000.
pstwkw=pstwrk*rpm/120./1000.
C
C  Expressed in kW basis at that rpm:
C
work=smwork*rpm/120./1000.
hrel=smhrel*rpm/120./1000.
hxfer=smhxfer*rpm/120./1000.
C
C  Find Ignition Delay
C  Ignition Delay Is Defined As The Time Between The Start Of Injection Of
C  The Main Fuel Pulse And When The Heat Release Goes Through Zero From
C  Being Negative.
C  The Main SOI In The Input File Should Reflect The Cummins Covention Found
C  In CalTerm:  Timing in Degrees Before Top Dead Center [°bTDC]
C
k = 1                                          !Reinitialize Index
C     do j = SOIindex+25,SOIindex,-1           !Backward Search From Ignited Mass
C                    if (hrg(j).LT.hrg(j+1)) then
C                    SOCindex = j
C                    SOC = SOCindex/5
C                    goto 999
C                    endif
C          enddo
C 999    SOImain = 360 - SOImain
C          Delay = SOC - SOImain
SOImain = 360 - SOImain
SOC = ca05
```

```
SOCindex = 5*SOC
Delay = SOC - SOImain
C
C  Calculate The Maximum Pressure, It's Location, And The Corresponding
C  Bulk Temperature Of The Cylinder.  The Maximum Pressure Should Be A Result
C  Of Combustion, And Not Compression From The Piston Only.  Therefore, Search
C  For Maximum Pressure After SOC.
C  It Is Unlikely That The Pressure Derivative Will Be Exactly Zero, So
C  Code Computes Where The Derivative Goes Through Zero, Then Checks The
C  Pressure At These Two Crank Angles.
C  Lastly, The Maximum Pressure Locations Are Compared To The Pressure At
C  TDC.  If TDC Is The Maximum Pressure, Then The Next Maximum Pressure
C  At A Crank Angle Greater Than 360 Is Searched For.  This Is Done Since
C  The Clean-Diesel Engine Is Run With Retarded Timings
C
k = 1                                   !Index For Writting To CApmax
do j = SOCindex, nevo                   !Search Only After Combustion Has Started
if ((psd(j)*psd(j+1).LT.0).and.(ca(j).GT.340)) then
CApmax(k) = (ca(j))                     !Array Of CA Where dP Goes Through Zero.
k = k + 1
CApmax(k) = (ca(j+1))
k = k + 1
endif
enddo
Pmax = 0.                               !Initialization Of Pmax.
do m = 1,k
n = int(CApmax(m) * 5)   !Reference Back To Heat Release Index
if ((ps(n).GT.Pmax).and.(CApmax(m).GT.360)) then
Pmax = (ps(n)+ps(n+1))/2
PmaxCA = CApmax(m) - 0.1
Pmaxloc = n
call engvol(PmaxCA,vol,vdot,pspeed,alinr)
rho=trapm/vol                           !Gas Density At Any Crank Angle
TatPmax=tinit*Pmax/pinit*vol/vinit      !Cylinder Average Temperature
endif
enddo
C
C  The Following Code Takes Care Of Operating Conditions With Large Retards In
C  Timing.  In Pressure Traces With Heavily Retarded Timing, There Is No Real Peak
C  Following TDC.  The Follwing Code Searches Through The dP/dt Array For the Absolute
C  Miniumum Following SOC, And Finds It's Inflection Point, Signaling A Large Change
C  In The Derivative.  This Is Then Defined As The Maximum Cylinder Pressure Follwing
C  Combustion
C
minimum = 0
if ((Pmax.EQ.0).and.(SOC.GT.360)) then  !Conditions For Heavy Retard
do j = SOCindex,SOCindex + 200          !Search Only After SOC
if (psd(j).LT.psd(j+1)) then            !Forward Search For Minimum
Pmax = ps(j)                            !Local Minimum Used
PmaxCA = j/5                            !Engine CA At Local Minimum
Pmaxloc = j                             !Heat Release Index
call engvol(PmaxCA,vol,vdot,pspeed,alinr)
rho=trapm/vol
TatPmax=tinit*Pmax/pinit*vol/vinit
goto 909                                !Stop Forward Search Algorithm
endif
```

```
enddo
909      endif
C
C  Final Heavy-Retard Algorithim For Maximum Pressure.
C  If The Above Code Determines That The Maximum Pressure Occurs Before
C  10% Of The Energy Has Been Released, Choosing That Point Would Not Give
C  A Good Indication Of The Maximum Pressure That A Fuel Packet Would Actually See,
C  As The Fuel Spray Is Most Likely Still Evaporating And The Initital Pre-Mixed
C  Burn Fraction May Not Have Burned (See 1999-01-0519).  Thus, The Following Code
C  Will Then Choose The Pressure And Temperature At The 10% Burn Location.
C
if (PmaxCA.LT.ca10) then
PmaxCA = ca10                                    !Engine CA
j = ca10*5
Pmaxloc = j                                      !Heat Release Index
Pmax = ps(j)
call engvol(PmaxCA,vol,vdot,pspeed,alinr)
rho=trapm/vol
TatPmax=tinit*Pmax/pinit*vol/vinit
endif
PmaxkPa = Pmax/1000
C
C  Compute Various Burn Durations
C
b10t90=ca90-ca10
EOC = ca90
BurnDur = EOC - SOC
```